University of West Bohemia in Pilsen

Faculty of Applied Sciences

DISSERTATION

2021 Ing. Jan Rendl

Západočeská univerzita v Plzni
Fakulta aplikovaných věd

NELINEÁRNÍ DYNAMIKA ROTUJÍCÍCH SOUSTAV S KLUZNÝMI LOŽISKY

Ing. Jan Rendl

Disertační práce
k získání akademického titulu doktor
v oboru Aplikovaná mechanika

Školitel: doc. Ing. Michal Hajžman, Ph.D.
Katedra: Katedra mechaniky

Plzeň 2021

University of West Bohemia in Pilsen
Faculty of Applied Sciences

NONLINEAR DYNAMICS OF ROTATING SYSTEMS WITH JOURNAL BEARINGS

Ing. Jan Rendl

Dissertation
to obtain academic title of Doctor
in the field of the Applied Mechanics

Supervisor: doc. Ing. Michal Hajžman, Ph.D.
Department: Department of Mechanics

Pilsen 2021

Declaration

I declare that this thesis has been composed myself and I have used only the listed sources and publications.

Pilsen, December 20, 2021 Jan Rendl

Acknowledgement

I would like to thank doc. Ing. Michal Hajžman, Ph.D. for exhaustive supervision, numerous comments, consultations, willingness and patience. I would also like to thank Ing. Luboš Smolík, Ph.D., Ing. Štěpán Dyk, Ph.D., doc. Ing. Miroslav Byrtus, Ph.D. and Ing. Radek Bulín, Ph.D. for professional advice and assistance in processing this work and writing of common publications. Many thanks also go to my wife Sandra, family and everyone who supported me during my studies.

Jan Rendl

Contents

1 Introduction and state of the art

Radial journal bearings are widely used in rotating machinery to support high-speed rotating parts with high radial loads and can be found in many applications, from large rotating systems such as turbomachinery [1] to small turbochargers in combustion engines [1, 2]. Fluid film bearings are generally characterised by low friction behaviour, low wear and mainly efficient vibration-damping capabilities. However, the fluid film journal bearings are also known for fluid-induced instability, which causes undamped self-excited vibrations of a supported rotating machine. For this reason, the process of journal bearings design is essential for adequately operating machines in the considered speed range to guarantee a long lifetime. Poorly designed journal bearing in the rotating system is a source of additional financial costs during the operation and in an extreme case could cause fatal damage of machine. Moreover, in many applications, the rotating system behaviour could be significantly changed only with improved bearing construction. The radial journal bearings are generally distinguished [1, 3, 4, 5] to fixed-profile journal bearings (cylindrical, elliptical, offset halves bearings etc.), bearings with pressure dam, tilting pad journal bearings and floating-ring journal bearings.

In the last decades, with the evolution of computational mechanics and modern computers able to perform large numerical operations, the increasing emphasis is focused on computational modelling of rotating systems supported on the journal bearings. In history, the problems were simplified and investigated by reasonable analytical methods based on linear analysis, but comprehensive nonlinear computational models are now being developed to describe the rotor behaviour more realistic.

1.1 State of the art

Computational modelling of rotating systems supported on journal bearings can be generally distinguished into two aims: modelling the rotor and analysing the journal bearing. Both subsystems mutually interact and the coupling is then described by angular speed-dependent visco-elastic dynamic coefficients [1, 4, 6] or nonlinear hydrodynamic force [3, 7].

1.1.1 Rotordynamics

In history, many research and publications such as [3, 4, 5, 6, 8] were dedicated to investigating rotordynamics problems and derivation of mathematical models with various scales of complexity. For comprehensive rotor modelling, the finite element method [3, 4, 6] is used to describe rotationally symmetric and transversally incompressible one-dimensional continuum that satisfies the Bernoulli-Navier hypothesis. On the other hand, discrete models

[3, 6], e.g. Jeffcott rotor, are analysed due to the model simplicity, low computational time costs, and currently eliminating undesirable properties of comprehensive models. In some cases, the simplified discrete model can provide a sufficient approximation of a real system.

1.1.2 Hydrodynamic lubrication

Fundamentals of hydrodynamic lubrication were formulated by Reynolds, who derived a partial differential equation governing the pressure field in thin viscous fluid films in 1886 [9]. Due to the comparatively small bearing clearance to the bearing diameter, the Reynolds equation (the second-order differential equation) was derived under the assumption of constant hydrodynamic pressure across bearing gap height. Thus, the oil film circulation in the bearing gap is simplified to the planar problem. Alternatively, approximate analytical solutions can be used for exceptional cases of bearing aspect ratios (length-to-diameter ratios). For long bearings with aspect ratio $\lambda > 2$, the infinitely long journal bearing (ILJB) approximation [10] can be employed, and for short bearings with $\lambda < 0.5$, the infinitely short journal bearing (ISJB) approximation can be employed [11]. Nevertheless, these approximative solutions do not hold for finite length journal bearings (FLJB) with length-to-diameter ratios in range $0.5 \leq \lambda \leq 2$. An analytical closed-form solution of the entire Reynolds equation has been found lately [12]. However, the most used approach for solving the Reynolds equation is the usage of numerical methods: most notably the finite difference method [13], the finite element method [14, 15] and the finite volumes method [16, 17]. Using numerical methods allows considering various boundary conditions, oil supply through bearing shell [13, 18, 19], temperature-dependent lubrication parameters [13, 14, 19, 20], changes in the bearing shell profiles [14, 18], and many others.

Integrating the hydrodynamic pressure over the bearing surface yields to the hydrodynamic force. The hydrodynamic pressure is generally a function of time, journal position, and speed. Therefore, the hydrodynamic force is nonlinear. This force can be adopted in equations of motion of the rotor [4, 8], but it is far more common, especially in the case of stationary rotating machinery, to replace (approximate) the nonlinear hydrodynamic force by so-called dynamic coefficients. Linearised analytical model of the hydrodynamic force consisted of four elastic and four linear damping coefficients defined in radial and tangential directions was introduced in [21]. The dynamic coefficients can be evaluated numerically as the derivative of the hydrodynamic force concerning the displacement and the velocity of the journal [22]. Furthermore, a cross-coupling term was also defined. The cross-coupling occurs in many types of bearings and can be observed if the bearing is loaded vertically. Then, the journal moves not only vertically but also horizontally.

The journal bearing's dynamic coefficients and other parameters may be estimated employing the ISJB and the ILJB approximations [4]. However, above mentioned approximations may overpredict or underpredict the hydrodynamic force magnitude or linearised dynamic coefficients of the FLJBs. The ISJB and ILJB approximations are more suited for the evaluation of upper or lower limits or determination of trends [23]. Some authors utilised the ISJB and the ILJB approximations as essential closed-form solutions, which were later corrected with corrective factors to apply for the FLJBs. One of the first attempts to correct approximations of journal bearings were proposed in 60s and 70s by authors [24, 25]. A method that allows correction of the ISJB approximation was introduced in [26]. This

method showed good accuracy of the estimated hydrodynamic forces for $\lambda \leq 1.25$. A harmonic combination of both ISJB and ILJB approximations for the calculation of the pressure distribution was proposed in [27]. Later, two analytical models of the hydrodynamic forces were derived [28] based on the ISJB and the ILJB approximations. The approximations were corrected by factors derived based on a numerical solution of the Reynolds equation.

1.1.3 Stability analysis

Knowledge of dynamic coefficients is essential for the stability assessment of journal bearings. Although the occurrence of fluid-film instability has been known since the 20s, it took almost 30 years to develop its proper analytical description. Employing the Routh-Hourwitz criterion, mathematically described conditions that cause the instability were presented in [21]. This concept was later reviewed in [29]. The instability causes self-excited vibrations of the rotor at roughly 0.42X–0.49X of the rotor speed and is known as the oil whirl [8]. Moreover, if the flexibility of a shaft is significant, another phenomenon called oil whip [8] can occur during the operation of the rotor. Hence, the design parameters of fluid film bearings are of crucial importance. Generally, three regimes can be observed during the rotor operation: stable vibrations, fully developed instability and a transient state between the both regimes. A speed at which the rotor becomes unstable will be hereinafter in this thesis called the threshold speed and the corresponding curve depending on the rotor speed, and another parameters will be called the threshold curve.

Muszynska [8] studied the instability of her nonlinear model in detail and proved that the self-excited vibrations can be stable under some circumstances and may even vanish completely if a threshold speed is surpassed. However, if the speed is further increased, the second mode whirl occurs. This phenomenon was also observed experimentally [8]. Finally, methods for the stability assessment of more general nonlinear models are introduced e.g. in [30, 31, 32, 33, 34, 35, 36]. Interestingly, the threshold speeds detected during the run-up and the coast-down operations can be different [20, 37]. This hysteresis behaviour is experimentally repeatable [8] and it is closely related to a subcritical bifurcation profile which can be derived employing the Hopf bifurcation theory [19, 37].

1.1.4 Hydrodynamic lubrication in applications

Journal bearing types

Hydrodynamic lubrication theory introduced for cylindrical radial journal bearings is also extendable on other fixed-profile journal bearings and the tilting pad journal bearings. The various bearing types with corresponding equilibrium loci, linearised dynamic coeeficients are summarised and compared in [38].

Tilting pad journal bearings (TPJB) are widely used to support large rotors such as turbines or generators. Their main advantage is better resistance to oil whirl and whip at high speeds than classical journal bearings. Stability is ensured by pad's tilting, see Fig. 1.1, which keeps the radial component of a hydrodynamic force dominant to the tangential component. In the standard linear rotordynamic formulation, the stability is provided by zero cross-coupling stiffness coefficients. As shown by multiple researchers [39, 40, 41], the actual cross-coupling stiffness is noticeably lower than the direct stiffness rather than zero. Therefore

some instability issues can still occur during the TPJB operation. The effect of non-zero cross-couplings was investigated in [42]. The stability of a nonlinear TPJB model was later examined in [43]. The instability could also occur because of some operational conditions [44] such as a low pad preload, low static load or external excitation.

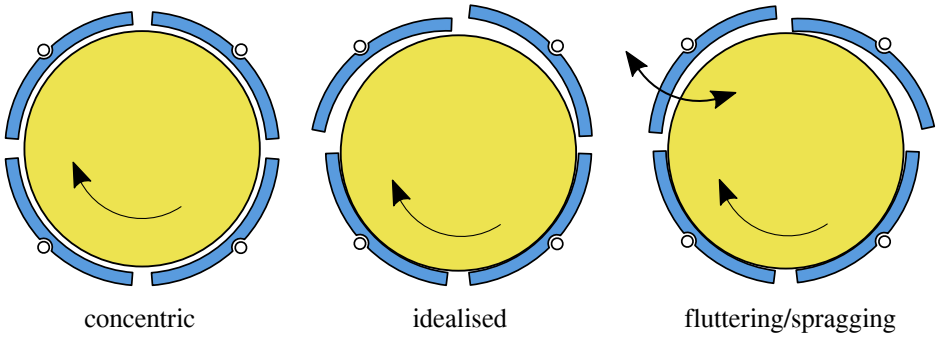

Fig. 1.1: Possible scenarios of TPJB behaviour, adopted from [45]. Last subfigure depicts both fluttering (left-upper pad) and spragging (right-upper pad)

The self-aligning nature of the TPJB also imposes some undesirable phenomena. Under such conditions, the pad may assume a position in which a gap is diverging rather than converging, see Fig. 1.1. The pressure generated close to the pad's leading edge then forces the journal out of its current position, leading to a realignment of the TPJB. This phenomenon is called spragging [46]. Continuous, often unstable vibration of the pad is termed pad fluttering [47]. Pad fluttering affects the level of machine vibrations and shortens the pad's life because the fluttering pad repeatedly hits the journal [46, 48]. A proper design of the TPJB can suppress pad fluttering effectively. The most common practices are pad preloading, shortening pad arcs, or the introduction of pockets or reliefs at pad's edges [45, 46]. More recent works also stress the importance of sufficient supply flow [49].

Historically, the first models of the TPJBs were composed using dynamic coefficients that describe the coupling between shaft and pad by stiffness and damping matrices. This approach is described in [50, 51] for the TPJB with rigid pads, in [52] for the TPJB with flexible pads, and in [53] for the TPJB with the flexible pads and thermo-elastohydrodynamic effects. Nonlinear models have been developed with respect to the class of a particular phenomenon that influences TPJB behaviour. An important field of interest is the influence of pad support or a pivot. The pivot is lined up in a series with the oil film and the flexibilities of both components contribute to the stiffness matrix. In [54], the influence of the pivot stiffness was analysed both analytically and experimentally. The behaviour of various TPJBs under the same operating conditions considering the pad flexibility was compared in [55]. A flexible pivot was introduced in [56] and an adjustable flexible pivot that allows tuning the bearing properties was proposed in [57]. The stiffness and damping coefficients of standard pivot designs employing the Hertzian contact theory were evaluated in [58] and this work was later extended in [59].

Bearing shell texturing

Since the 60s and 70s, researchers started to be interested in bearing shell texturing and micro-texturing. Intensive development in this field of study was initiated by [60] and other authors followed this research direction. Based on numerical simulations performed in the following years to present, it has been concluded that an appropriate arrangement and geometry of textures on the bearing surface can improve tribological performance [61, 62, 63, 64, 65, 66]. Laser surface texturing significantly influences the bearing attitude angle, and the stability of the bearing may be improved [64]. The influence of spherical texture dimensions on the threshold speed was examined for the Jeffcott rotor-bearing system in [67]. It was shown that convex texturing influences rotor dynamic performance dramatically. The stability is also enhanced with increased texture depth [68], whereas there is an optimum texture density corresponding to the maximum threshold speed. The circular and square textures were compared and found out in [69] that the effects of surface texturing on dynamic characteristics depend mainly on the location of texture and not on its geometry. Other studies were focused on analysing the dynamic and stability performance of the hydrodynamic bearing with triangular-shaped textures [70] and herringbone grooves [71, 72, 73].

Experimental studies also revealed that surface texturing could result in lower friction in mixed lubrication [74] and hydrodynamic [75] regimes. Based on measured rotor vibrations in textured bearing in [76], it was demonstrated that lightly- to medium-textured surfaces result in better bearing stability. Fluid film stiffness and damping coefficients were measured in [77] and appropriate texture distribution can have a better vibration-damping effect and provide better stability. A detailed study on the lubrication mechanism and fluid characteristics in typical microcavities was provided in [78]. The computational fluid dynamics (CFD) methods were employed in this theoretical and experimental work. Numerical and experimental results of the effect of spherical textures on dynamic coefficients and threshold speed were compared in [79]. It was proved that surface texturing is an effective method for suppressing the self-excited vibrations of the rotor. In [80], using an experiment in a flexible rotor-bearing system was found that an appropriate depth of micro-texture positively affects bearing dynamic characteristics. Tribological film-asperity interaction and its effect on random excitation during vibrations of rotors supported by journal bearings was investigated in [81]. Large spherical textures and their effect under dynamic operating conditions was studied in [82, 83]. It was shown that the textures allow the reduction in shear viscous force, but on the other hand, increase orbit's amplitude of the shaft under dynamic operation [82]. A parametric study showed that full texturing provides better stability when compared with partial texturing [83].

1.2 Thesis aims and structure

The presented state of the art review in the field of rotating systems with journal bearings reveals and yields several points at which this thesis aims. The main aims of this thesis can be summarised as follows:

- Derivation of a unified and comprehensive model for various bearing types interacting with a rotor through thin fluid film or by solid contacts if the viscous film is interrupted or missing.
- Development of a complex in-house software which can perform static and stability analyses and time domain simulations of the rotors supported on various journal bearing types with emphasis on nonlinear rotor dynamics.
- Determination of threshold speed and investigation of various journal bearing types behaviour in unstable regimes employing different modelling approaches and studying their influence on the system behaviour, including phenomena such as oil whirl, threshold speed hysteresis, pad fluttering etc.
- Implementation of the computational model of textured journal bearing and analysis of texturing impact on the system stability.
- Experimental validation of computationally examined stability of cylindrical and textured journal bearings.

This work is structured into ten chapters. The second and the third chapters are dedicated to the step-by-step derivation of complex journal bearing models and methods for stability examination. The fourth chapter is focused on computational methods, including an analytical approach and mainly numerical method – the finite difference method. Developed in-house software is further used to analyse cylindrical journal bearings in the fifth chapter, fixed-profile journal bearings in the sixth chapter and tilting pad journal bearings in the seventh chapter. All chapters include parameters of the investigated rotor-bearing system, model validation and results of static and dynamic simulations. The first experimental validation is presented in the eighth chapter. The Bently Nevada RK 4 Rotor Kit and corresponding computational model are examined to study the development of unstable behaviour during the run-up and coast-down operations. Textured journal bearings are analysed in the ninth chapter. This chapter also includes the results from experimental measurement and a comparison of the results is provided. Finally, the tenth chapter summarises the conclusions obtained from each part of the proposed thesis. This work also contains several parallel appendices listed at the end of the thesis for better chapters clarity.

2 Hydrodynamic lubrication theory

Hydrodynamic lubrication [13, 14, 20] is fundamental for properly operating journal bearings. Load-carrying oil film supporting a journal arises due to the presence of this phenomenon. The essential condition for inducing hydrodynamic lubrication is the sufficient speed of non-parallel surfaces in wedge form. Other conditions and simplifying assumptions for the derivation of equations describing journal bearing behaviour are presented in this chapter.

Following Sec. 2.1 includes the Reynolds equation, its dimensionless transformation and assumed boundary conditions. Approaches for modelling of cavitation phenomenon are introduced in Sec. 2.2. The linearisation process of nonlinear force coupling calculated in Sec. 2.3 is explained in Sec. 2.4. Finally, stability assessment based on linearised stiffness and damping coefficients is presented in Sec. 2.5.

2.1 Pressure field in bearing gap

The Reynolds equation governs the pressure field. This equation was derived under the following assumptions, well-known as Reynold's theory of hydrodynamic lubrication [13, 14]:

- Surfaces of journal and shell are perfectly smooth and rigid.
- Journal is cylindrical with radius R_R.
- Film thickness is constant in the axial direction.
- Radial clearance c is small compared to nominal shell radius R ($c \ll R$ and $R \approx R_R$).
- Laminar flow of Newtonian fluid is assumed.
- Fluid pressure is constant across the film thickness.
- Gravity and inertia forces acting on the fluid are negligible.
- Oil film curvature is neglected.

The geometric scheme of a radial journal bearing is depicted in Fig. 2.1. The scheme shows two coordinate systems $X_F Y_F Z$ and $X_P Y_P Z$ which are the most used for Reynolds equation derivation [13, 84]. Both coordinate systems are located on the bearing shell. Coordinate system $X_F Y_F Z$ is fixed and its origin lies on the horizontal axis. Origin of coordinate system $X_P Y_P Z$ depends on the journal's position, see radial axis connecting journal centre S_J and

shell centre B in Fig. 2.1. Both systems have the same orientation, but they are only angularly mutually shifted. It allows to use the same notation for spatial coordinates $X_i \in \langle 0, 2\pi R\rangle$, $Y_i \in \langle 0, h_i(X_i)\rangle$ and $Z \in \langle -\frac{L}{2}, \frac{L}{2}\rangle$, where each system is distinguished by subscript $i = F, P$. The advantages of the Reynolds equation formulation in various coordinate systems are further discussed in this work.

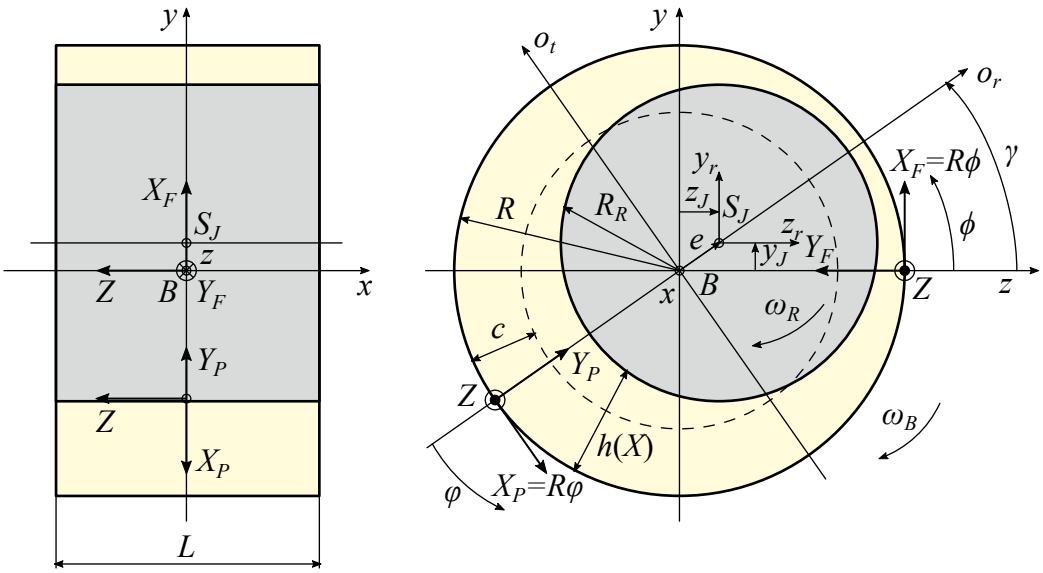

Fig. 2.1: Transverse cross-section of a bearing and coordinate system definition

Based on Reynold's hydrodynamic lubrication theory, the pressure field analysis in the bearing gap is reduced to a planar problem. The Reynolds equation could be derived from force equilibrium in an extracted element of fluid and continuity equation [13, 14, 20, A1] or simplification of Navier-Stokes equations [18, 84]. After derivation, the Reynolds equation has the following general form [13, A1]

$$\frac{\partial}{\partial X_i}\left(\frac{\varrho h_i^3}{\mu}\frac{\partial p_i}{\partial X_i}\right) + \frac{\partial}{\partial Z}\left(\frac{\varrho h_i^3}{\mu}\frac{\partial p_i}{\partial Z}\right) = 6\frac{\partial}{\partial X_i}\left[\varrho h_i\left(u_1 + u_2\right)\right] + 12\frac{\partial}{\partial t}\left(h_i\varrho\right), \tag{2.1}$$

where $p_i = p_i(X_i, Z, t)$ is unknown pressure field, $h_i = h_i(X_i, t)$ is the oil film thickness, X_i, Z are the circumferential and axial coordinates, subscript $i = F, P$ denotes fixed or floating coordinate system, t is time, $\varrho = \varrho\,(X, Z, t)$ is the fluid density, $\mu = \mu\,(X, Z, t)$ is the oil dynamic viscosity and $u_1 = -R\omega_R$ and $u_2 = -R\omega_B$ are circumferential speeds of journal surface and bearing shell by the assumption $R \approx R_R$.

Assumptions of isoviscous and incompressible fluid make it possible to transform the Reynolds equation into this final form [4, 13, A1]

$$\frac{\partial}{\partial X_i}\left(h_i^3\frac{\partial p_i}{\partial X_i}\right) + \frac{\partial}{\partial Z}\left(h_i^3\frac{\partial p_i}{\partial Z}\right) = 6\,\mu\left(u_1 + u_2\right)\frac{\partial h_i}{\partial X_i} + 12\,\mu\frac{\partial h_i}{\partial t}. \tag{2.2}$$

Reynolds equation is simplified [2, 13, 20] for limit cases when the mass flow rate in one direction significantly exceeds the flow in another one. The mass flow rate in circumferential and axial direction depends on the bearing geometry, mainly on aspect ratio $\lambda = L/(2R)$.

Reference [11] mentions the bearing with aspect ratio $\lambda \leq 0.5$ as infinitely short. Infinitely long bearing [2, 10] is distinguished by aspect ratio $\lambda > 1$. Modified Reynolds equations for the infinitely short and infinitely long journal bearings are shown line by line below

$$\frac{\partial}{\partial Z}\left(h_i^3 \frac{\partial p_i}{\partial Z}\right) = 6\,\mu\,(u_1+u_2)\,\frac{\partial h_i}{\partial X_i} + 12\,\mu \frac{\partial h_i}{\partial t}, \tag{2.3}$$

$$\frac{\partial}{\partial X_i}\left(h_i^3 \frac{\partial p_i}{\partial X_i}\right) = 6\,\mu\,(u_1+u_2)\,\frac{\partial h_i}{\partial X_i} + 12\,\mu \frac{\partial h_i}{\partial t}. \tag{2.4}$$

Journal centre position S_J is determined by eccentricity $e(t)$, or relative eccentricity $\varepsilon(t) = e(t)/c$, and attitude angle $\gamma(t)$

$$e(t) = \sqrt{y_J^2(t) + z_J^2(t)}, \tag{2.5}$$

$$\gamma(t) = \begin{cases} \arccos \frac{z_J(t)}{e(t)}, & y_J(t) > 0, \\ 2\pi - \arccos \frac{z_J(t)}{e(t)}, & y_J(t) < 0, \end{cases} \tag{2.6}$$

where $y_J(t), z_J(t)$ are the journal vertical and horizontal displacements in fixed Cartesian coordinate system xyz. Approximated film thickness for cylindrical bearings is calculated in fixed coordinate system $X_F Y_F Z$ as follows [13, A1]

$$h_F(X_F, t) = c - e(t)\cos\left(\frac{X_F}{R} - \gamma(t)\right) = c - e(t)\cos\left(\phi - \gamma(t)\right). \tag{2.7}$$

Angular substitution $\varphi = \pi + \phi - \gamma$ between considered coordinate systems is applied and film thickness in floating coordinate system $X_P Y_P Z$ yields to

$$h_P(X_P, t) = c + e(t)\cos\frac{X_P}{R} = c + e(t)\cos\varphi. \tag{2.8}$$

2.1.1 Reynolds equation in dimensionless form

The Reynolds equation (2.2) is often transformed into dimensionless form [20, 13] applied in computational modelling, especially for numerical solutions. Following dimensionless variables are established

$$h_i = c\,\overline{h}_i, \qquad Z = L\overline{Z}, \qquad X_i = R\psi_i, \quad \text{for} \quad \psi_i = \phi,\, \varphi. \tag{2.9}$$

After substituting (2.9) into the general form of the Reynolds equation (2.2) and necessary algebraic manipulation, it is finally obtained

$$\frac{\partial}{\partial \psi_i}\left(\overline{h}_i^3 \frac{\partial \overline{p}_i}{\partial \psi_i}\right) + \left(\frac{R}{L}\right)^2 \frac{\partial}{\partial \overline{Z}}\left(\overline{h}_i^3 \frac{\partial \overline{p}_i}{\partial \overline{Z}}\right) = -\mathrm{sign}\,(\omega_R + \omega_B)\,\frac{\partial \overline{h}_i}{\partial \psi_i} + \frac{2}{|\omega_R + \omega_B|}\frac{\partial \overline{h}_i}{\partial t}, \tag{2.10}$$

where dimensionless pressure $\overline{p}_i$ occurs

$$\overline{p}_i = \overline{p}_i\left(\psi_i, \overline{Z}, t\right) = \frac{c^2}{6\mu R^2 |\omega_R + \omega_B|}\, p_i(X_i, Z, t). \tag{2.11}$$

2.1.2 Boundary conditions

Unknown pressure field $p_i(X, Z, t)$ governed by the Reynolds equation needs to satisfy prescribed boundary conditions for an explicit definition of a boundary value problem. Given boundary conditions are presented in their nominal values for better clarity. Their dimensionless transformation is possible to perform based on (2.9) and (2.11).

For case of cylindrical bearings, the pressure field $p_i(X, Z, t)$ needs to satisfy circumferential continuity condition field

$$p_i(0, Z, t) = p_i(2\pi R, Z, t). \tag{2.12}$$

Ambient pressure p_{amb} is then supposed at the edges as Dirichlet boundary condition

$$p_i(X_i, -\frac{L}{2}, t) = p_i(X_i, \frac{L}{2}, t) = p_{amb}. \tag{2.13}$$

If there is any area $\Omega_i = \langle \tilde{X}_i \times \tilde{Z}_i \rangle \subset \langle X_i \times Z_i \rangle$ where the oil is supplied with constant pressure p_{sup} through the supply bore or groove, previous boundary conditions are extended by

$$p_i \left(\tilde{X}_i, \tilde{Z}_i, t \right) = p_{sup}. \tag{2.14}$$

2.2 Cavitation

Cavitation occurs when the hydrodynamic pressure in a certain area of the bearing gap drops below the boundary value corresponding to saturated vapour pressure. As a result, a mixture of oil in the fluid phase and gas bubbles of evaporating oil fills the gap in the cavitated region. Cavitation phenomenon and process of its formation is described in detail in [13, 18]. The effect of this phenomenon has to be considered in computational analysis.

The most straightforward computational approach for cavitation modelling is the Gümbel condition or also called the half-Sommerfeld condition [13, 18, 20]. In this case, the pressure field in the bearing gap's divergent part is approximated by ambient pressure p_{amb}

$$p_i(X_i, Z, t) = \begin{cases} p_i(X_i, Z, t), & p_i(X_i, Z, t) \geq p_{amb}, \\ p_{amb}, & p_i(X_i, Z, t) < p_{amb}. \end{cases} \tag{2.15}$$

The Gümbel condition described by (2.15) may be further modified with the substituting the ambient pressure by a constant, which fulfils inequality $p_{sat} < p_{amb}$. This saturation pressure is the approximate pressure of the oil and gas mixture in the bearing gap. The piecewise function has a similar formulation to (2.15)

$$p_i(X_i, Z, t) = \begin{cases} p_i(X_i, Z, t), & p_i(X_i, Z, t) \geq p_{sat}, \\ p_{sat}, & p_i(X_i, Z, t) < p_{sat}. \end{cases} \tag{2.16}$$

2.3 Hydrodynamic force

Load-carrying oil film generates corresponding hydrodynamic force to radial pressure acting on the journal. Particular components of hydrodynamic force acting on the journal are then calculated [1, 4, 20, 84] in radial F_{rad}^{hd} and tangential F_{tan}^{hd} directions from both considered coordinate systems according to Fig. 2.2 as follows

$$F_{rad}^{hd} = F_{rad}^{hd}\left(\varepsilon, \dot{\varepsilon}, \gamma, \dot{\gamma}, \omega_R, \omega_B\right) = -\int_{-\frac{L}{2}}^{\frac{L}{2}} \int_{0}^{2\pi R} p_F(X_F, Z, t)\, \cos\left(\frac{X_F}{R} - \gamma(t)\right) \mathrm{d}X_F\, \mathrm{d}Z = \tag{2.17}$$
$$= \int_{-\frac{L}{2}}^{\frac{L}{2}} \int_{0}^{2\pi R} p_P(X_P, Z, t)\, \cos\frac{X_P}{R}\, \mathrm{d}X_P\, \mathrm{d}Z,$$

$$F_{tan}^{hd} = F_{tan}^{hd}\left(\varepsilon, \dot{\varepsilon}, \gamma, \dot{\gamma}, \omega_R, \omega_B\right) = -\int_{-\frac{L}{2}}^{\frac{L}{2}} \int_{0}^{2\pi R} p_F(X_F, Z, t)\, \sin\left(\frac{X_F}{R} - \gamma(t)\right) \mathrm{d}X_F\, \mathrm{d}Z = \tag{2.18}$$
$$= \int_{-\frac{L}{2}}^{\frac{L}{2}} \int_{0}^{2\pi R} p_P(X_P, Z, t)\, \sin\frac{X_P}{R}\, \mathrm{d}X_P\, \mathrm{d}Z,$$

where the hydrodynamic pressure fulfils the boundary conditions in Sec. 2.1.2 and chosen cavitation modelling approach in Sec. 2.2.

Following transformation is applied to determine the components of the hydrodynamic force in fixed Cartesian coordinate system xyz

$$\begin{bmatrix} F_y^{hd} \\ F_z^{hd} \end{bmatrix} = \begin{bmatrix} \sin\gamma & \cos\gamma \\ \cos\gamma & -\sin\gamma \end{bmatrix} \begin{bmatrix} F_{rad}^{hd} \\ F_{tan}^{hd} \end{bmatrix}. \tag{2.19}$$

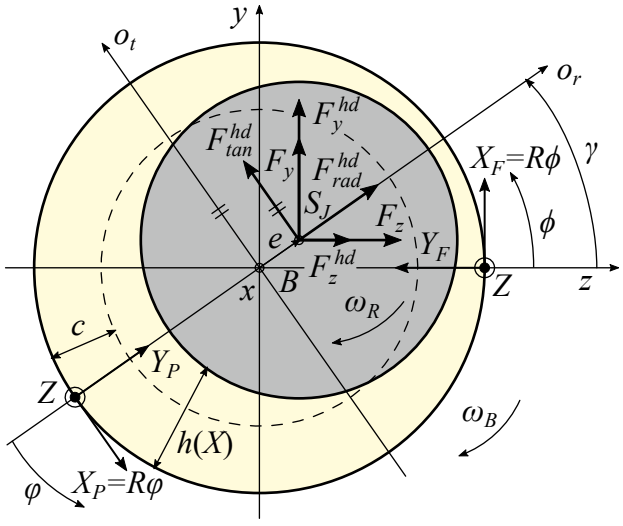

Fig. 2.2: Components of the hydrodynamic force and journal loading forces F_y and F_z

2.4 Hydrodynamic force linearisation

Mutual interaction between the journal and the bearing shell (resp. the bearing pedestal) transmitted through the oil film can be represented by nonlinear force coupling [3, 7], see Sec. 2.3, or described by linearised visco-elastic support [1, 4, 6]. Small journal velocities and displacements from static equilibrium point S of coordinate system $y_r z_r$, see Fig. 2.1, are supposed for sufficient accuracy of established stiffness and damping coefficients of the oil film. Force equilibrium of static loading and hydrodynamic forces determines the equilibrium point where linearisation of force coupling is further performed. The hydrodynamic force components in Cartesian coordinate system xyz are approximated by Taylor series [1, 4] close to the equilibrium point

$$F_y^{hd} = -F_y + \underbrace{\frac{\partial F_y^{hd}}{\partial y_r}\Big|_{\substack{\dot\varepsilon=0\\ \dot\gamma=0}}}_{-k_{yy}} y_r + \underbrace{\frac{\partial F_y^{hd}}{\partial z_r}\Big|_{\substack{\dot\varepsilon=0\\ \dot\gamma=0}}}_{-k_{yz}} z_r + \underbrace{\frac{\partial F_y^{hd}}{\partial \dot y_r}\Big|_{\substack{\dot\varepsilon=0\\ \dot\gamma=0}}}_{-b_{yy}} \dot y_r + \underbrace{\frac{\partial F_y^{hd}}{\partial \dot z_r}\Big|_{\substack{\dot\varepsilon=0\\ \dot\gamma=0}}}_{-b_{yz}} \dot z_r, \tag{2.20}$$

$$F_z^{hd} = -F_z + \underbrace{\frac{\partial F_z^{hd}}{\partial y_r}\Big|_{\substack{\dot\varepsilon=0\\ \dot\gamma=0}}}_{-k_{zy}} y_r + \underbrace{\frac{\partial F_z^{hd}}{\partial z_r}\Big|_{\substack{\dot\varepsilon=0\\ \dot\gamma=0}}}_{-k_{zz}} z_r + \underbrace{\frac{\partial F_z^{hd}}{\partial \dot y_r}\Big|_{\substack{\dot\varepsilon=0\\ \dot\gamma=0}}}_{-b_{zy}} \dot y_r + \underbrace{\frac{\partial F_z^{hd}}{\partial \dot z_r}\Big|_{\substack{\dot\varepsilon=0\\ \dot\gamma=0}}}_{-b_{zz}} \dot z_r, \tag{2.21}$$

where F_y, F_z are the acting forces on the journal in vertical and horizontal direction from Fig. 2.2 and $y_r, z_r, \dot y_r, \dot z_r$ are displacements and velocities of the journal from the equilibrium point. Partial derivatives in (2.20) and (2.21) are expressed [4] as

$$\frac{\partial F_d^{hd}}{\partial y_r} = \frac{\partial F_d^{hd}}{\partial \varepsilon}\frac{\partial \varepsilon}{\partial y_r} + \frac{\partial F_d^{hd}}{\partial \gamma}\frac{\partial \gamma}{\partial y_r}, \qquad \frac{\partial F_d^{hd}}{\partial z_r} = \frac{\partial F_d^{hd}}{\partial \varepsilon}\frac{\partial \varepsilon}{\partial z_r} + \frac{\partial F_d^{hd}}{\partial \gamma}\frac{\partial \gamma}{\partial z_r}, \tag{2.22a}$$

$$\frac{\partial F_d^{hd}}{\partial \dot y_r} = \frac{\partial F_d^{hd}}{\partial \dot\varepsilon}\frac{\partial \dot\varepsilon}{\partial \dot y_r} + \frac{\partial F_d^{hd}}{\partial \dot\gamma}\frac{\partial \dot\gamma}{\partial \dot y_r}, \qquad \frac{\partial F_d^{hd}}{\partial \dot z_r} = \frac{\partial F_d^{hd}}{\partial \dot\varepsilon}\frac{\partial \dot\varepsilon}{\partial \dot z_r} + \frac{\partial F_d^{hd}}{\partial \dot\gamma}\frac{\partial \dot\gamma}{\partial \dot z_r}, \tag{2.22b}$$

where subscript $d = y, z$ and following substitution [4] is used

$$\frac{\partial \varepsilon}{\partial y_r} = \frac{\partial \dot\varepsilon}{\partial \dot y_r} = \frac{\sin\gamma}{c}, \qquad \frac{\partial \varepsilon}{\partial z_r} = \frac{\partial \dot\varepsilon}{\partial \dot z_r} = \frac{\cos\gamma}{c}, \tag{2.23a}$$

$$\frac{\partial \gamma}{\partial y_r} = \frac{\partial \dot\gamma}{\partial \dot y_r} = \frac{\cos\gamma}{\varepsilon c}, \qquad \frac{\partial \gamma}{\partial z_r} = \frac{\partial \dot\gamma}{\partial \dot z_r} = -\frac{\sin\gamma}{\varepsilon c}. \tag{2.23b}$$

Finally, components of hydrodynamic force can be written in matrix form [1, 4, 6]

$$\begin{bmatrix} F_y^{hd} \\ F_z^{hd} \end{bmatrix} = -\begin{bmatrix} F_y \\ F_z \end{bmatrix} - \begin{bmatrix} b_{yy} & b_{yz} \\ b_{zy} & b_{zz} \end{bmatrix} \begin{bmatrix} \dot y_r \\ \dot z_r \end{bmatrix} - \begin{bmatrix} k_{yy} & k_{yz} \\ k_{zy} & k_{zz} \end{bmatrix} \begin{bmatrix} y_r \\ z_r \end{bmatrix}. \tag{2.24}$$

2.5 Stability analysis

Journal bearings are a potential source of self-excited vibrations of rotating systems due to inappropriate design of rotating system's operating conditions, bearing geometry or physical properties of a lubricant. Based on unstable behaviour nature, two different unstable phenomena, oil whirl and oil whip, are distinguished and discussed in detail in [1, 2, 8]. Presented stability analysis aims to establish the threshold speed after whose surpassing unstable behaviour develops.

Routh-Hourwitz criterion [1, 29, 85] is employed to determine the threshold speed. Stability analysis is investigated on the perfectly balanced and symmetrical rigid rotor with mass $2m$, supported on two identical journal bearings. Journal bearings are located at the rotor ends symmetrically to the centre of gravity. The rotor rotates with constant angular velocity ω and is loaded by a radial force acting in the centre of gravity.

Rotor performs only planar motion in the middle plane with supposed small journal velocities and displacements from the static equilibrium point. This assumption allows approximating the hydrodynamic force by linearised stiffness and damping coefficients (2.24). Motion equations of the proposed rotor-bearing system are then derived in matrix form

$$\begin{bmatrix} m & 0 \\ 0 & m \end{bmatrix} \begin{bmatrix} \ddot{y}_r \\ \ddot{z}_r \end{bmatrix} + \begin{bmatrix} b_{yy} & b_{yz} \\ b_{zy} & b_{zz} \end{bmatrix} \begin{bmatrix} \dot{y}_r \\ \dot{z}_r \end{bmatrix} + \begin{bmatrix} k_{yy} & k_{yz} \\ k_{zy} & k_{zz} \end{bmatrix} \begin{bmatrix} y_r \\ z_r \end{bmatrix} = \begin{bmatrix} 0 \\ 0 \end{bmatrix}. \tag{2.25}$$

Using of dimensionless parameters

$$y_r = c\,\overline{y}_r, \qquad z_r = c\,\overline{z}_r, \qquad \overline{t} = \omega\, t, \tag{2.26}$$

where c is the radial clearance, the equations of motion are transformed into dimensionless form

$$\begin{bmatrix} \overline{m} & 0 \\ 0 & \overline{m} \end{bmatrix} \begin{bmatrix} \overline{y}_r^{**} \\ \overline{z}_r^{**} \end{bmatrix} + \begin{bmatrix} \overline{b}_{yy} & \overline{b}_{yz} \\ \overline{b}_{zy} & \overline{b}_{zz} \end{bmatrix} \begin{bmatrix} \overline{y}_r^{*} \\ \overline{z}_r^{*} \end{bmatrix} + \begin{bmatrix} \overline{k}_{yy} & \overline{k}_{yz} \\ \overline{k}_{zy} & \overline{k}_{zz} \end{bmatrix} \begin{bmatrix} \overline{y}_r \\ \overline{z}_r \end{bmatrix} = \begin{bmatrix} 0 \\ 0 \end{bmatrix}, \tag{2.27}$$

where following substitutions are employed

$$Q^{**} = \frac{\mathrm{d}^2 Q}{\mathrm{d}\overline{t}^2}, \qquad Q^{*} = \frac{\mathrm{d}Q}{\mathrm{d}\overline{t}}, \qquad Q = \overline{y}_r, \overline{z}_r, \tag{2.28a}$$

$$\overline{m} = m\,\frac{c\,\omega^2}{mg}, \qquad \overline{b}_{ij} = b_{ij}\,\frac{c\,\omega}{mg}, \qquad \overline{k}_{ij} = k_{ij}\,\frac{c}{mg}, \qquad i,j = y,z. \tag{2.28b}$$

Symbol g denotes gravitational acceleration. After surpassing threshold speed ω_t, rotor undamped orbital motion with angular velocity ω_w starts to develop [29, 85]. Variable $\overline{\omega}_w$ characterises their mutual ratio

$$\overline{\omega}_w = \frac{\omega_w}{\omega}. \tag{2.29}$$

Journal centre trajectory of orbital motion is described by [1, 29, 85]

$$\overline{y}_r = A\,\mathrm{e}^{\mathrm{i}\,\omega_w\, t} = A\,\mathrm{e}^{\mathrm{i}\,\overline{\omega}_w\,\overline{t}}, \qquad \overline{z}_r = B\,\mathrm{e}^{\mathrm{i}\,\omega_w\, t} = B\,\mathrm{e}^{\mathrm{i}\,\overline{\omega}_w\,\overline{t}}, \tag{2.30}$$

where A, B are the dimensionless amplitudes in corresponding directions and i is the imaginary unit. Substituting (2.30) into (2.27) leads to system of equations

$$\begin{bmatrix} -\overline{m}\,\overline{\omega}_w^2 + \overline{k}_{yy} + \mathrm{i}\,\overline{\omega}_w\,\overline{b}_{yy} & \overline{k}_{yz} + \mathrm{i}\,\overline{\omega}_w\,\overline{b}_{yz} \\ \overline{k}_{zy} + \mathrm{i}\,\overline{\omega}_w\,\overline{b}_{zy} & -\overline{m}\,\overline{\omega}_w^2 + \overline{k}_{zz} + \mathrm{i}\,\overline{\omega}_w\,\overline{b}_{zz} \end{bmatrix} \begin{bmatrix} A \\ B \end{bmatrix} = \begin{bmatrix} 0 \\ 0 \end{bmatrix}, \tag{2.31}$$

where non-trivial solution is found [1, 29, 85]. After algebraic manipulation of imaginary and real part of the determinant in (2.31), final formulae are obtained

$$\overline{k}_{eq} = \frac{\overline{k}_{yy}\overline{b}_{zz} + \overline{k}_{zz}\overline{b}_{yy} - \overline{k}_{yz}\overline{b}_{zy} - \overline{k}_{zy}\overline{b}_{yz}}{\overline{b}_{yy} + \overline{b}_{zz}} = \overline{m}\,\overline{\omega}_w^2, \tag{2.32}$$

$$\overline{\omega}_w^2 = \frac{\left(\overline{k}_{eq} - \overline{k}_{yy}\right)\left(\overline{k}_{eq} - \overline{k}_{zz}\right) - \overline{k}_{yz}\overline{k}_{zy}}{\overline{b}_{yy}\overline{b}_{zz} - \overline{b}_{yz}\overline{b}_{zy}}, \tag{2.33}$$

where $\overline{k}_{eq}$ is the dimensionless equivalent stiffness of the corresponding auxiliary system with one degree of freedom. Using backward substitution (2.29) into (2.32) and identifying $\omega = \omega_t$ results to

$$\omega_t = \sqrt{\frac{g\,\overline{k}_{eq}}{c\,\overline{\omega}_w^2}} = \sqrt{\frac{k_{eq}}{m\,\overline{\omega}_w^2}}. \tag{2.34}$$

The threshold speed depends on rotor speed ω, stiffness k_{ij} and damping b_{ij} coefficients. However, an implicit form of threshold speed calculation (2.34) makes it impossible to perform a direct solution and the threshold speed evaluation as the intersection of $\omega_t = \omega_t(\omega)$ with the synchronous line ω is required.

3 Complex bearing systems

Hydrodynamic lubrication theory presented in the previous chapter can be generalised for complex bearing systems such as tilting pad journal bearings (TPJBs) and other types of bearings with fixed geometry. The particular types of bearings are depicted in Fig. 3.1. The small white circles denote pivot positions for individual pads of tilting pad journal bearings and the shell curvature centre for other bearings. A mathematical model describing the tilting pad journal bearing can also be employed to model the bearings with fixed-profile geometry assuming several simplifications.

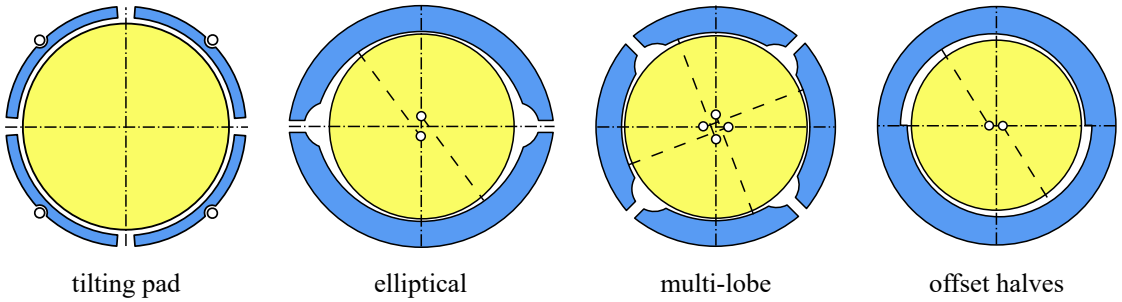

Fig. 3.1: Various bearing types

Governing equations of bearing with fluid-structure interaction in simplistic formulation of the mathematical model without compromising its nonlinear properties are described in detail in Sec. 3.1. Analytical formulation of hydrodynamic forces with assumed boundary conditions are further presented in Sec. 3.2.

3.1 Governing equations

A symmetric flexible rotor supported on the TPJBs can be decomposed into mutually interacting subsystems – a rotor and movable pads. Equations of motion of such a system can be expressed in the block matrix form as follows (arguments are omitted for simplicity)

$$\begin{bmatrix} \mathbf{M}_r & \mathbf{0} \\ \mathbf{0} & \mathbf{M}_p \end{bmatrix} \begin{bmatrix} \ddot{\mathbf{q}}_r \\ \ddot{\mathbf{q}}_p \end{bmatrix} + \begin{bmatrix} \mathbf{B}_r + \omega \mathbf{G}_r & \mathbf{0} \\ \mathbf{0} & \mathbf{0} \end{bmatrix} \begin{bmatrix} \dot{\mathbf{q}}_r \\ \dot{\mathbf{q}}_p \end{bmatrix} + \\ + \begin{bmatrix} \mathbf{K}_r + \omega \mathbf{C}_r & \mathbf{0} \\ \mathbf{0} & \mathbf{0} \end{bmatrix} \begin{bmatrix} \mathbf{q}_r \\ \mathbf{q}_p \end{bmatrix} = \begin{bmatrix} \mathbf{f}_{g,r} \\ \mathbf{f}_{g,p} \end{bmatrix} + \begin{bmatrix} \mathbf{f}_{un} \\ \mathbf{0} \end{bmatrix} + \begin{bmatrix} \mathbf{f}_{c,r} \\ \mathbf{f}_{c,p} \end{bmatrix}, \quad (3.1)$$

where subscripts $i = r, p$ correspond to rotor and pads subsystems, respectively. Vector $\mathbf{q}_i = \mathbf{q}_i(t) \in \mathbb{R}^{N_i,1}$ is a vector of generalised coordinates with N_i being the total number of degrees of freedom (DoF) of the i-th subsystem. Matrices $\mathbf{M}_r$, $\mathbf{B}_r$, $\mathbf{G}_r$, $\mathbf{K}_r$, $\mathbf{C}_r \in \mathbb{R}^{N_r,N_r}$ are constant matrices of mass, damping, gyroscopic effects, stiffness and circulation of the rotor. Matrix $\mathbf{M}_p \in \mathbb{R}^{N_p,N_p}$ incorporates the mass properties of the pads. Each subsystem is subjected to a gravitational load which is included in vector $\mathbf{f}_{g,i} \in \mathbb{R}^{N_i,1}$. The rotor can be excited by out-of-balance forces introduced in vector $\mathbf{f}_{un} = \mathbf{f}_{un}(t) \in \mathbb{R}^{N_r,1}$. Mutual interaction of the subsystems is described by coupling forces $\mathbf{f}_{c,i}\left(\mathbf{q}_r, \mathbf{q}_p, \dot{\mathbf{q}}_r, \dot{\mathbf{q}}_p\right) \in \mathbb{R}^{N_i,1}$ which involves hydrodynamic forces generated in oil films, coupling forces between the pads and the ground and elastic forces due to contacts between subsystems.

Here, an angular misalignment of a journal to the pads is neglected, i.e. the journal is assumed parallel to the pad in the axial direction. Hence the TPJBs can be considered planar, and the total number of DoF of the pad system is $N_p = 3N$ where N is the number of the pads. N_r depends on a used rotor model – it can be relatively high, e.g. for the rotor subsystem modelled by a finite element method (FEM), or relatively low for the rigid rotor.

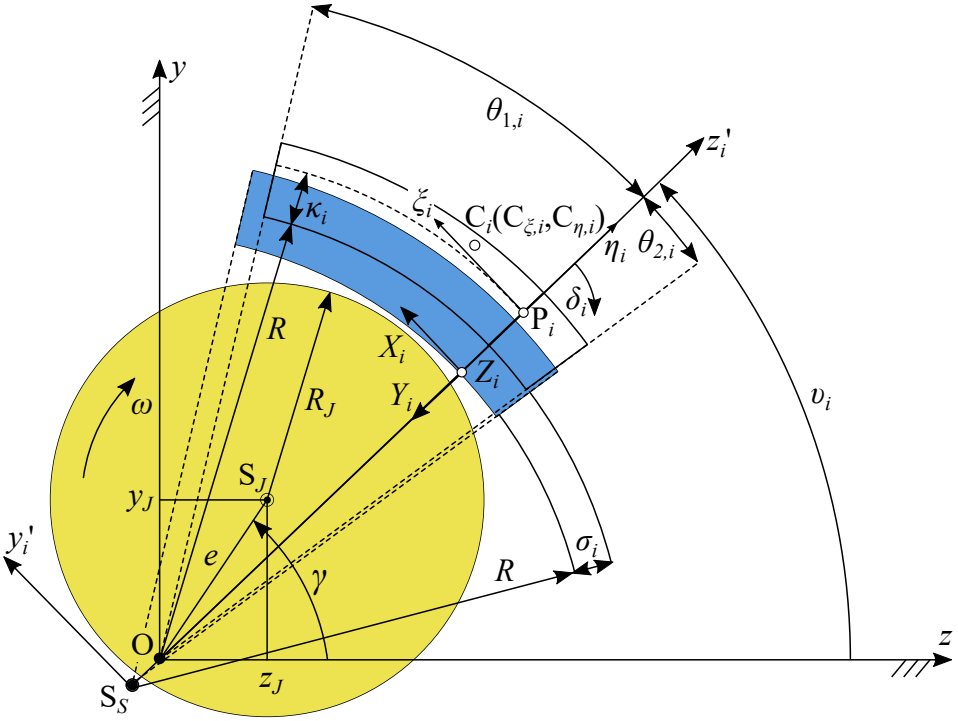

Fig. 3.2: Scheme of the used coordinate systems and general TPJB geometry parameters. The initial (untilted) position of the pad is depicted (uncolored) and the preloaded position is highlighted in blue

For simplicity, a simple 2 DoF model of the rotor supported on the TPJB with N rigid pads is further supposed. This model can be also used to describe the TPJB in the system with a flexible rotor. A scheme of the considered system with essential dimensions and coordinate systems is depicted in Fig. 3.2. The journal rotates with angular speed ω and its centre position S_J is defined in fixed Cartesian coordinate system yz by vector $\mathbf{q}_r(t) = [y_J(t),\, z_J(t)]^T$. Each pad has 3 DoF: rotational $\delta_i(t)$, radial $\eta_i(t)$ and tangential $\xi_i(t)$ defined with respect to pivot position P_i in fixed auxiliary coordinate system $\xi_i\eta_i$. Vector of

generalised coordinates of all pads is $\mathbf{q}_p(t) = [\delta_1, \eta_1, \xi_1, \ldots, \delta_N, \eta_N, \xi_N]^T$. The pivot position in the fixed Cartesian system is defined by attitude angle υ_i and radial distance κ_i between the inner surface of the pad and the pivot. Centre of gravity C_i in coordinate system $\xi_i\eta_i$ has the following coordinates: $\mathrm{C}_i = [C_{\xi,i}, C_{\eta,i}]^T$. The pad can be preloaded, i.e. the radial clearance between the pad and the journal can be adjusted. The radial preload is described by distance σ_i.

Each pad has its local coordinate system $y_i'z_i'$ which is fixed to the pad and whose orientation is obvious from Fig. 3.2. These pad coordinate systems are used to formulate equations that describe hydrodynamic lubrication in the oil film [20]. Angles $\theta_{1,i}$ and $\theta_{2,i}$ denote leading and trailing edges of the pad with respect to the origin of the pad coordinate system $y_i'z_i'$.

The usage of the coordinate system fixed to the pad allows describing bearing gap $h_i = h_i(X_i, t)$ at the i-th pad as a gap of the cylindrical bearing, see Sec. 2.1

$$h_i(X_i, Z_i, t) = c - e_i'(t) \cos\left(\frac{X_i}{R} - \gamma_i'(t)\right), \tag{3.2}$$

where $c = R - R_J$ is the nominal (machined) radial clearance, $e_i'(t)$ and $\gamma_i'(t)$ are the journal eccentricity and attitude angle in the pad coordinate system $y_i'z_i'$ which are given as

$$e_i'(t) = \sqrt{{y_{J,i}'}^2(t) + {z_{J,i}'}^2(t)}, \qquad \gamma_i'(t) = \begin{cases} \arccos \frac{z_{J,i}'(t)}{e_i'(t)}, & y_{J,i}'(t) > 0, \\ 2\pi - \arccos \frac{z_{J,i}'(t)}{e_i'(t)}, & y_{J,i}'(t) < 0, \end{cases} \tag{3.3}$$

where journal position $y_{J,i}'$, $z_{J,i}'$ is expressed in the pad coordinate system $y_i'z_i'$. These local coordinates can be transformed from the global coordinate system using the following transformation

$$\begin{bmatrix} y_{J,i}'(t) \\ z_{J,i}'(t) \end{bmatrix} = \begin{bmatrix} -\left(R + \kappa_i - \sigma_i + \eta_i(t)\right) \sin \delta_i(t) - \xi_i(t) \\ \left(\sigma_i - \eta_i(t)\right) - \left(R + \kappa_i - \sigma_i + \eta_i(t)\right) \left(1 - \cos \delta_i(t)\right) \end{bmatrix} + \begin{bmatrix} \cos\left(\upsilon_i - \delta_i(t)\right) & -\sin\left(\upsilon_i - \delta_i(t)\right) \\ \sin\left(\upsilon_i - \delta_i(t)\right) & \cos\left(\upsilon_i - \delta_i(t)\right) \end{bmatrix} \begin{bmatrix} y_J(t) \\ z_J(t) \end{bmatrix}. \tag{3.4}$$

System of motion equations of the considered system with N pads has a formal structure proposed in (3.1). The acting forces are depicted in Fig. 3.3. The inertia terms of the second and higher orders are neglected due to their supposed small values, and the final equations of motion can be written in the form

$$m_J\, \ddot{y}_J = -m_J g + \Delta m E\, \omega^2 \cos(\omega\, t) + \sum_{i=1}^{N} F_{hd,i}^{y}, \tag{3.5}$$

$$m_J\, \ddot{z}_J = \Delta m E\, \omega^2 \sin(\omega\, t) + \sum_{i=1}^{N} F_{hd,i}^{z}, \tag{3.6}$$

$$I_{P,i}\, \ddot{\delta}_i + m_{s,i}\, C_{\xi,i}\, \ddot{\eta}_i - m_{s,i}\, C_{\eta,i}\, \ddot{\xi}_i + b_{t,i}\, \dot{\delta}_i + k_{t,i}\, \delta_i = \\ = -m_{s,i}\, g \left[C_{\xi,i} \sin\left(\upsilon_i - \delta_i\right) - C_{\eta,i} \cos\left(\upsilon_i - \delta_i\right)\right] - F_{hd,i}^{y'} \left(R + \kappa_i\right), \tag{3.7}$$

$$m_{s,i}\,\ddot{\eta}_i + m_{s,i}\,C_{\xi,i}\,\ddot{\delta}_i + b_{rad,i}\,\dot{\eta}_i + k_{rad,i}\,\eta_i = -m_{s,i}\,g\sin\left(\upsilon_i - \delta_i\right) - F^{z'}_{hd,i}, \tag{3.8}$$

$$m_{s,i}\,\ddot{\xi}_i - m_{s,i}\,C_{\eta,i}\,\ddot{\delta}_i + b_{tan,i}\,\dot{\xi}_i + k_{tan,i}\,\xi_i = -m_{s,i}\,g\cos\left(\upsilon_i - \delta_i\right) - F^{y'}_{hd,i}, \tag{3.9}$$

where $i = 1, \ldots, N$ is the index of the pad, m_J is the journal mass, g is the gravitational constant, ΔmE is the static unbalance, $F^{y}_{hd,i}$, $F^{z}_{hd,i}$ are the components of the hydrodynamic force generated in the oil film between the journal and the i-th pad. These components acting on the journal can be transformed from the auxiliary coordinate system to the global coordinate system as follows

$$\begin{bmatrix} F^{y}_{hd,i} \\ F^{z}_{hd,i} \end{bmatrix} = \begin{bmatrix} \cos\left(\upsilon_i - \delta_i\right) & \sin\left(\upsilon_i - \delta_i\right) \\ -\sin\left(\upsilon_i - \delta_i\right) & \cos\left(\upsilon_i - \delta_i\right) \end{bmatrix} \begin{bmatrix} F^{y'}_{hd,i} \\ F^{z'}_{hd,i} \end{bmatrix}, \tag{3.10}$$

where the components of hydrodynamic force $F^{y'}_{hd,i}$, $F^{z'}_{hd,i}$ are calculated in the pad coordinate system $y'_i z'_i$ and act on the journal. It is assumed that the hydrodynamic force acting on the journal exerts equal and opposite force also on the pad, i.e. there is no transport moment due to the oil film. This assumption is satisfied well for systems with small clearances. The components of the hydrodynamic force acting on the pad are schematically depicted in Fig. 3.3 by dashed lines based on the application of Newton's third law.

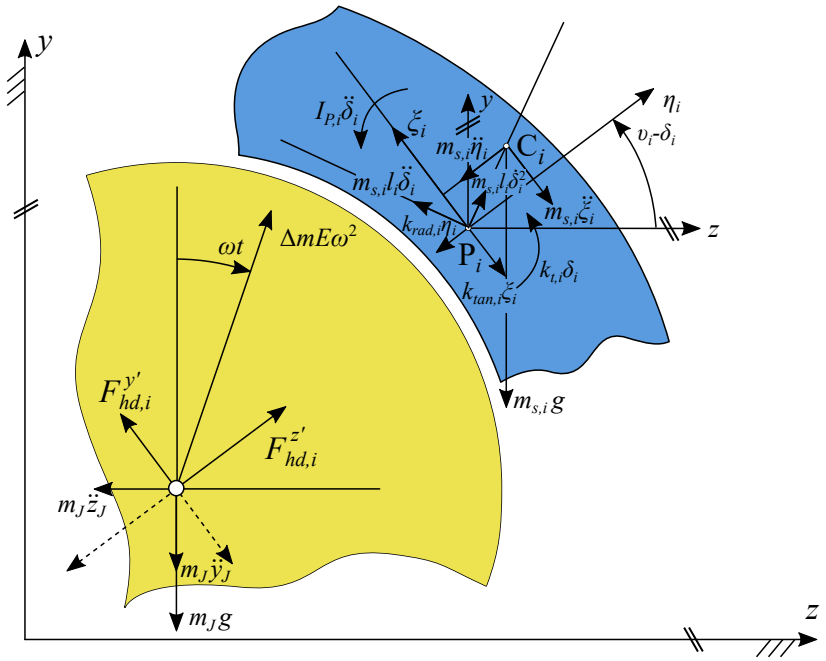

Fig. 3.3: Scheme of force balance contains gravitational forces $m_Jg, m_{s,i}g$, out-of-balance force $\Delta mE\omega^2$, inertial forces ($m_J\ddot{y}_J, m_J\ddot{z}_J$ are acting on the journal and $I_{P,i}\ddot{\delta}_i, m_{s,i}\ddot{\eta}_i, m_{s,i}\ddot{\xi}_i, m_{s,i}l_i\dot{\delta}_i^2, m_{s,i}l_i\ddot{\delta}_i$ are acting on the i-th pad) and elastic forces due to the pivot deformation $k_{t,i}\delta_i, k_{rad,i}\eta_i, k_{tan,i}\xi_i$. Damping forces $b_{t,i}\dot{\delta}_i, b_{rad,i}\dot{\eta}_i, b_{tan,i}\dot{\xi}_i$ are not depicted here for clarity but they are supposed in the same directions as the elastic force due to the pivot deformation. The components of the hydrodynamic force $F^{y'}_{hd_i}, F^{z'}_{hd_i}$ acting on the journal are depicted by solid lines. The dashed lines depict the components of the hydrodynamic force acting on the pad

Each pad is characterised by mass $m_{s,i}$ and moment of inertia $I_{P,i}$ relative to the pivot. The flexibility of the pivot is described by stiffness and damping in the directions of the corresponding generalised coordinates. The equations of motion (3.8) and (3.9) can be omitted if the radial and tangential motions of the pad are negligible. Visco-elastic properties of the pivot have an essential role in the TPJB dynamics, particularly at relatively high rotor speeds and under high loads [54]. The dynamic pivot stiffness is in the series with the dynamic stiffness of the oil film. Hence it strongly influences the total dynamic stiffness of the journal-housing coupling.

There are several types of pivot designs that differ according to the connection between pad and housing: rocker-backed pivots and spherical pivots, including a sphere in a sphere, a sphere in a cylinder, and a sphere on a flat plate [58]. Other constructions such as flexure pivots [86] use pads and housing made of one piece where the flexibility of relatively thin pivot allows the pad tilting. The corresponding stiffness and damping coefficients can be estimated based on detailed FEM models or simplified contact models such as the Hertzian contact [56].

The contact can also occur between the journal and the i-th pad. In a case of missing load-carrying oil film between the journal and the i-th pad, the fluid-structure interaction is substituted by an elastic force which is transmitted if

$$\exists! X_i \in \langle -R\,\theta_{2,i}, R\,\theta_{1,i}\rangle : h_i\left(X_i, t\right) = 0, \tag{3.11}$$

where $h_i\left(X_i, t\right)$ is the bearing gap between the journal and i-th pad. Coupling forces acting on the journal are then given by the following relations

$$F_{cf,i}^{y'} = -k_c \left|\Delta_{pen,i}\right|^{n_c} \sin\varphi_i, \tag{3.12}$$

$$F_{cf,i}^{z'} = -k_c \left|\Delta_{pen,i}\right|^{n_c} \cos\varphi_i, \tag{3.13}$$

which are formulated in the pad coordinate system and where k_c is the contact stiffness and n_c is the force exponent. It is assumed that the contact occurs close to the pad edges [87]. Penetration depth $\Delta_{pen,i}$ and attitude angle φ_i are then calculated as follows

$$\Delta_{pen,i} = \begin{cases} h_i\left(R\,\theta_{1,i}, t\right), & X_i \in \langle 0,\, R\,\theta_{1,i}\rangle, \\ h_i\left(-R\,\theta_{2,i}, t\right), & X_i \in \langle -R\,\theta_{2,i},\, 0\rangle, \end{cases} \tag{3.14}$$

$$\varphi_i = \begin{cases} \theta_{1,i}, & X_i \in \langle 0,\, R\,\theta_{1,i}\rangle, \\ -\theta_{2,i}, & X_i \in \langle -R\,\theta_{2,i},\, 0\rangle. \end{cases} \tag{3.15}$$

The mathematical model for the bearing with fixed geometry is obtained by omitting (3.7)–(3.9), i.e. reducing the degrees of freedom. However, the coordinate and force transformations are still valid.

3.2 Analytical formulation of hydrodynamic forces

Lateral forces acting on the journal due to hydrodynamic pressure $p_i = p_i\left(X_i, Z_i, t\right)$ generated between the journal and the i-th pad are evaluated using following integrals

$$F_{hd,i}^{y'} = -\int_{-\frac{L}{2}}^{\frac{L}{2}} \int_{-R\theta_{2,i}}^{R\theta_{1,i}} p_i(X_i, Z_i, t)\, \sin\frac{X_i}{R}\, \mathrm{d}X_i\, \mathrm{d}Z_i, \tag{3.16}$$

$$F_{hd,i}^{z'} = -\int_{-\frac{L}{2}}^{\frac{L}{2}} \int_{-R\theta_{2,i}}^{R\theta_{1,i}} p_i(X_i, Z_i, t)\, \cos\frac{X_i}{R}\, \mathrm{d}X_i\, \mathrm{d}Z_i, \tag{3.17}$$

where X_i, Z_i are the circumferential and axial coordinates, respectively, which are defined in a coordinate system fixed to the inner surface of the i-th pad, see Fig. 3.2. Constant L is the axial length of the bearing and angles $\theta_{1,i}$ and $\theta_{2,i}$ are defined in Fig. 3.2.

Pressure $p_i\left(X_i, Z_i, t\right)$ is governed by the Reynolds equation, whose exact form depends on simplifying assumptions, see Sec. 2.1. The hydrodynamic pressure also depends on working conditions of the TPJB. Some of these conditions can be expressed in the form of boundary conditions. Pressures at pad edges are usually prescribed as constants using the Dirichlet boundary conditions

$$p_i\left(R\theta_{1,i}, Z_i, t\right) = p_{sup}, \tag{3.18}$$

$$p_i\left(-R\theta_{2,i}, Z_i, t\right) = p_{amb}, \tag{3.19}$$

$$p_i\left(X_i, -\frac{L}{2}, t\right) = p_{amb}, \tag{3.20}$$

$$p_i\left(X_i, \frac{L}{2}, t\right) = p_{amb}, \tag{3.21}$$

where p_{sup} and p_{amb} are supply and ambient pressures, respectively. Condition (3.18) is usually used if the oil is supplied employing pressurised supply or leading edge groove methods.

Cavitation phenomenon occurs when hydrodynamic pressure drops rapidly in a certain area of the oil film. The corresponding Gümbel condition can be written in the form

$$\forall p_i(X_i, Z_i, t) < p_{sat} \Rightarrow p_i(X_i, Z_i, t) = p_{sat}, \tag{3.22}$$

where p_{sat} is the saturation pressure in the cavitated area. The saturation pressure can be approximated with the ambient pressure if the fluid inertia is neglected [20].

TPJBs are often used to support large machinery where the laminar flow assumption might be inappropriate. The transition from laminar to turbulent flow occurs if [20]

$$Re = \frac{R\,\omega\,c\,\rho}{\mu} \geq 1000, \tag{3.23}$$

where Re is the bearing Reynolds number and ρ is the lubricant density. If condition (3.23) is fulfilled, the Reynolds equation should be modified with turbulent coefficients which characterise flow in the X_i and Z_i directions and are functions of the local Reynolds number [20].

4 Computational methods

Previously derived mathematical models and formulae in chapters 2 and 3 can be solved employing various computational methods.

Analytical solution of the limit cases of the Reynolds equation, hydrodynamic force calculation and determination of stiffness and damping oil film coefficients are written in Sec. 4.1. In addition, this section contains so-called corrected models of hydrodynamic forces and dynamic coefficients for finite length journal bearings.

Despite the derived analytical solution of the Reynolds equation and formulation of pressure field in the closed-form [12], numerical methods are widely used in journal bearing analyses. The finite difference method is introduced in Sec. 4.2. Modelling methodology, which incorporates oil supply bores and grooves to the computational model, is also summarised in Sec. 4.2.

4.1 Analytical method

4.1.1 Pressure field calculation

The Reynolds equation is simplified to final forms (1) and (2) for the limit cases of the infinitely short (IS) and the infinitely long (IL) bearings. The Reynolds equation derived in the floating coordinate system comes with the benefits of applying Booker's integrals [88] during the integration, which yields to pressure field solution. After several algebraic manipulations, pressure fields are finally derived into closed-form [2, 84, A1]

$$p_P^{IS}(\varphi, Z) = p_{amb} + \frac{3\,\eta\,c}{h_P^3}\left(Z^2 - \frac{L^2}{4}\right)\left[K\varepsilon\sin\varphi + 2\,\dot{\varepsilon}\cos\varphi\right], \tag{4.1}$$

$$p_P^{IL}(\varphi) = p_0 + 6\eta R^2\left[\frac{\dot{\varepsilon}}{\varepsilon}\frac{h_P^2 + c^2\,(1+\varepsilon)^2}{h_P^2\,c^2\,(1+\varepsilon)^2} - K\frac{\varepsilon\,(2+\varepsilon\cos\varphi)\sin\varphi}{h_P^2\,(2+\varepsilon^2)}\right], \tag{4.2}$$

where $K = (2\dot{\gamma} - \omega)$, $\omega = \omega_R + \omega_B$ and p_0 is the assumed pressure in the largest bearing gap.

4.1.2 Hydrodynamic force calculation

Calculated pressure fields are further integrated based on (1) and (2) to obtain the hydrodynamic force components. Employing Booker's integrals allows calculating the hydrodynamic force in the closed-form [28, 84] with assumed Gümbel condition (2.15). Following formulae

of the hydrodynamic force components in radial (rad) and tangential (tan) direction are adopted from [28] where reverse journal rotation direction is supposed concerning Fig. 2.1, i.e. $u = R\omega = u_1 + u_2 = R\left(\omega_R + \omega_B\right)$. Hydrodynamic force components for the limit cases of journal bearings adopted from [28] are written as follows

$$F_{rad}^{hd,IS} = -\mu RL\left(\frac{L}{c}\right)^2\left[|\omega - 2\dot{\gamma}|\frac{\varepsilon^2}{\left(1-\varepsilon^2\right)^2} + \frac{\pi\left(1+2\varepsilon^2\right)\dot{\varepsilon}}{2\left(1-\varepsilon^2\right)^{5/2}}\right], \tag{4.3}$$

$$F_{tan}^{hd,IS} = \mu RL\left(\frac{L}{c}\right)^2\left[\left(\omega - 2\dot{\gamma}\right)\frac{\pi\varepsilon}{4\left(1-\varepsilon^2\right)^{3/2}} + \frac{2\varepsilon\dot{\varepsilon}}{\left(1-\varepsilon^2\right)^2}\right], \tag{4.4}$$

$$F_{rad}^{hd,IL} = -6\mu RL\left(\frac{R}{c}\right)^2\left[|\omega - 2\dot{\gamma}|\frac{2\varepsilon^2}{\left(2+\varepsilon^2\right)\left(1-\varepsilon^2\right)} + \frac{\pi\dot{\varepsilon}}{\left(1-\varepsilon^2\right)^{3/2}}\right], \tag{4.5}$$

$$F_{tan}^{hd,IL} = 6\mu RL\left(\frac{R}{c}\right)^2\left[\left(\omega - 2\dot{\gamma}\right)\frac{\pi\varepsilon}{\left(2+\varepsilon^2\right)\left(1-\varepsilon^2\right)^{1/2}} + \frac{4\dot{\varepsilon}}{\left(1+\varepsilon\right)\left(1-\varepsilon^2\right)}\right], \tag{4.6}$$

where $\omega = \omega_R + \omega_B$. Derived formulae of hydrodynamic force can be applied for the infinitely short bearings with aspect ratio $\lambda \leq 0.5$ [11] and theinfinitely long bearings with aspect ratio $\lambda > 1$ [2]. However, these formulae (4.3)–(4.6) are not suitable for application out of supposed aspect ratio and evaluation of hydrodynamic force could cause some inaccuracies.

Hydrodynamic forces for the case of the finite length bearings are calculated by multiplication of formulae (4.3)–(4.6) by correction polynomial functions [28]. Coefficients of presented functions were obtained by linear regression method [28] of the results from the numerical solution of the general Reynolds equation. Corrected components of the hydrodynamic force are considered in the following forms [28]

$$F_{rad}^{hd,IScor} = C_{rad}^{IS}\,F_{rad}^{hd,IS} = \left(f_1^{IS}\varepsilon^3 + f_2^{IS}\varepsilon^2 + f_3^{IS}\varepsilon + f_4^{IS}\right)F_{rad}^{hd,IS}, \tag{4.7}$$

$$F_{tan}^{hd,IScor} = C_{tan}^{IS}\,F_{tan}^{hd,IS} = \left(g_1^{IS}\varepsilon^2 + g_2^{IS}\varepsilon + g_3^{IS}\right)F_{tan}^{hd,IS}, \tag{4.8}$$

$$F_{rad}^{hd,ILcor} = C_{rad}^{IL}\,F_{rad}^{hd,IL} = \left(f_1^{IL}\varepsilon^3 + f_2^{IL}\varepsilon^2 + f_3^{IL}\varepsilon + f_4^{IL}\right)F_{rad}^{hd,IL}, \tag{4.9}$$

$$F_{tan}^{hd,ILcor} = C_{tan}^{IL}\,F_{tan}^{hd,IL} = \left(g_1^{IL}\varepsilon^2 + g_2^{IL}\varepsilon + g_3^{IL}\right)F_{tan}^{hd,IL}, \tag{4.10}$$

where ε is the relative eccentricity and particular polynomial functions $f_i^{IS} = f_i^{IS}(\lambda)$, $f_i^{IL} = f_i^{IL}(\lambda)$ for $i = 1,2,3,4$ and $g_i^{IS} = g_i^{IS}(\lambda)$, $g_i^{IL} = g_i^{IL}(\lambda)$ for $i = 1,2,3$ are listed in Appendix A.

Coefficients of polynomial functions were established by linear regression method for the same journal rotation direction as components of hydrodynamic force (4.3)–(4.6). For this reason, the hydrodynamic force for the finite length bearings will be further supposed in this form and necessary transformation for the reverse rotation direction, see Fig. 2.1, is discussed in Sec. 4.1.4.

4.1.3 Determination of stiffness and damping oil film coefficients

Particular stiffness and damping oil film coefficients are calculated from partial derivatives (2.22) of the hydrodynamic force. Dynamic coefficients for the infinitely short and long bearings are primarily introduced in dimensionless forms [4, 20] or depending on Sommerfeld number [1, 38]. Sommerfeld number is a characteristic variable summarising all design parameters into one number. Appendix A includes dynamic coefficients for the infinitely short

and long bearing in dimensional form as the author's research output. A similar procedure is then applied for corrected components of hydrodynamic force (4.7)–(4.10). Approximate dynamic coefficients in the closed-form for the finite length bearings were not previously investigated and this work was published in [A2] as original research in this field of study. MATLAB symbolic solver was mainly used for derivation of dynamic coefficients. Final formulae consider only the reverse rotation direction with respect to Fig. 2.1.

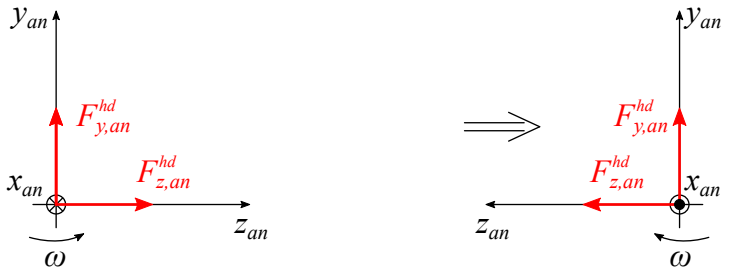

(a) Coordinate system orientation

(b) Coordinate system orientation after unification of journal rotation direction with Fig. 2.1

Fig. 4.1: Hydrodynamic force transformation

4.1.4 Hydrodynamic force transformation

Coordinate system $x_{an}y_{an}z_{an}$ with corresponding rotation direction was used for analytical derivation of the hydrodynamic force and linearised stiffness and damping coefficients. This coordinate system is depicted in Fig. 4.1a. A scheme depicted in Fig. 4.1b results from matching the rotation direction with Fig. 2.1. Comparing both figures gives the following relations

$$x \equiv -x_{an}, \qquad y \equiv y_{an}, \qquad z \equiv -z_{an} \tag{4.11}$$

and in plane yz and $y_{an}z_{an}$ yields

$$F^{hd}_{y} = F^{hd}_{y,an}, \qquad F^{hd}_{z} = -F^{hd}_{z,an}, \quad \text{resp.} \quad F^{hd}_{rad} = F^{hd,i}_{rad,an}, \qquad F^{hd}_{tan} = -F^{hd,i}_{tan,an}, \tag{4.12}$$

where $i = IS, IL, IScor, ILcor$ and index an denotes the variables expressed in coordinate system $x_{an}y_{an}z_{an}$ with journal rotation based on Fig. 4.1a. Linearised dynamic coefficients are estimated in the static equilibrium point where loading and hydrodynamic forces are equal. With respect to (2.24) and (2.25), the hydrodynamic force components calculated based on linearised dynamic coefficients are written below in matrix forms for both rotation directions [1]

$$\begin{bmatrix} F^{hd}_{y} \\ F^{hd}_{z} \end{bmatrix} = -\begin{bmatrix} b_{yy} & b_{yz} \\ b_{zy} & b_{zz} \end{bmatrix} \begin{bmatrix} \dot{y} \\ \dot{z} \end{bmatrix} - \begin{bmatrix} k_{yy} & k_{yz} \\ k_{zy} & k_{zz} \end{bmatrix} \begin{bmatrix} y \\ z \end{bmatrix}, \tag{4.13}$$

$$\begin{bmatrix} F^{hd}_{y,an} \\ -F^{hd}_{z,an} \end{bmatrix} = -\begin{bmatrix} b^{an}_{yy} & b^{an}_{yz} \\ -b^{an}_{zy} & -b^{an}_{zz} \end{bmatrix} \begin{bmatrix} \dot{y}_{an} \\ \dot{z}_{an} \end{bmatrix} - \begin{bmatrix} k^{an}_{yy} & k^{an}_{yz} \\ -k^{an}_{zy} & -k^{an}_{zz} \end{bmatrix} \begin{bmatrix} y_{an} \\ z_{an} \end{bmatrix}. \tag{4.14}$$

Comparing both equations (4.13) and (4.14) and substituting (4.11), mutual transformations of dynamic coefficients between both supposed rotation directions [1] yields

$$b_{yy} = b_{yy}^{an}, \qquad b_{yz} = -b_{yz}^{an}, \qquad b_{zy} = -b_{zy}^{an}, \qquad b_{zz} = b_{zz}^{an}, \tag{4.15a}$$

$$k_{yy} = k_{yy}^{an}, \qquad k_{yz} = -k_{yz}^{an}, \qquad k_{zy} = -k_{zy}^{an}, \qquad k_{zz} = k_{zz}^{an}. \tag{4.15b}$$

4.2 Numerical method – finite difference method

4.2.1 Pressure field calculation

The numerical solution of the Reynolds equation can be performed by employing the finite difference method [13, 14, 20, 84]. Method implementation is the same for both coordinate systems $X_F Y_F Z$ a $X_P Y_P Z$ and both forms of Reynolds equations (2.2) and (2.10). Here, the dimensional form of the Reynolds equation is further assumed and unique notation $X = X_F, X_P$ is used.

A uniform mesh of nodes $(i, j) \in \langle 1, M{+}1\rangle \times \langle 1, N\rangle$, where $M, N \in \mathbb{N}$, covers the bearing shell with steps $\Delta X, \Delta Z$ between the nodes, see Fig. 4.2. Partial derivatives are approximated by central finite differences [89]

$$\frac{\partial p}{\partial X} = \frac{p_{i+1,j} - p_{i-1,j}}{2\Delta X}, \qquad \frac{\partial^2 p}{\partial X^2} = \frac{p_{i+1,j} - 2p_{i,j} + p_{i-1,j}}{\Delta X^2}, \tag{4.16a}$$

$$\frac{\partial p}{\partial Z} = \frac{p_{i,j+1} - p_{i,j-1}}{2\Delta Z}, \qquad \frac{\partial^2 p}{\partial Z^2} = \frac{p_{i,j+1} - 2p_{i,j} + p_{i,j-1}}{\Delta Z^2}, \tag{4.16b}$$

where $p_{i,j}$ is unknown nodal pressure. The Reynolds equation is approximated in each node of inner mesh $(i, j) \in \langle 2, M\rangle \times \langle 2, N-1\rangle$ by linear combination based on the five-point computational stencil [13, 14, 20, 84] depicted in Fig. 4.2

$$a_{i,j}\, p_{i+1,j} + b_{i,j}\, p_{i-1,j} + c_{i,j}\, p_{i,j} + d_{i,j}\, p_{i,j+1} + e_{i,j}\, p_{i,j-1} = f_{i,j}, \tag{4.17}$$

where $a_{i,j}, \ldots, f_{i,j}$ are the coefficients of linear combination. Each coefficient is described in detail in [A1]. System of algebraic equations (4.17) for inner nodes can be written into compact matrix form

$$\mathbf{A}^{(\mathrm{FDM})}\mathbf{p}^{(\mathrm{FDM})} = \mathbf{f}^{(\mathrm{FDM})}, \tag{4.18}$$

where $\mathbf{A}^{(\mathrm{FDM})} \in \mathbb{R}^{M(N-2),M(N-2)}$ is the sparse, diagonal, positive definite coefficient matrix, $\mathbf{p}^{(\mathrm{FDM})} \in \mathbb{R}^{M(N-2)}$ is the vector of unknown nodal pressures and $\mathbf{f}^{(\mathrm{FDM})} \in \mathbb{R}^{M(N-2)}$ is the vector of values which are determined on the right-hand side of Reynolds equation (2.2) and by boundary conditions (2.12) and (2.13).

System of the algebraic equations can be solved directly (Gauss elimination method) or iteratively (Gauss-Seidel iterative method [90]). Successive OverRelaxation method (SOR) is often employed for better convergence of iteration procedure [18, 90] where the solution in the iteration step $(k{+}1)$ is known as

$$\mathbf{p}_{k+1}^{(\mathrm{FDM})} = (\mathbf{D} + w\mathbf{L})^{-1}\left[(1-w)\,\mathbf{D} - w\mathbf{U}\right]\mathbf{p}_k^{(\mathrm{FDM})} + w\left[(\mathbf{D} + w\mathbf{L})^{-1}\,\mathbf{f}^{(\mathrm{FDM})}\right], \tag{4.19}$$

where $\mathbf{D}, \mathbf{L}, \mathbf{U}$ are the diagonal, lower and upper triangular matrix below and above main diagonal of matrix $\mathbf{A}^{(\mathrm{FDM})}$, $\mathbf{p}_k^{(\mathrm{FDM})}$ is the solution from previous iteration and w is the relaxation parameter which takes place in the range $w \in \langle 1, 2)$ [18]. SOR method comes into the Gauss-Seidel method for parameter value $w = 1$. Stopping criteria of iteration procedure are defined by the maximum number of iterations n_{max} and accepted tolerance ε_{SOR} of solution difference between individual iterations calculated based on the Euclidian vector norm

$$k \leq n_{max}, \qquad \|\mathbf{p}_{k+1}^{(\mathrm{FDM})} - \mathbf{p}_k^{(\mathrm{FDM})}\| < \varepsilon_{SOR}. \tag{4.20}$$

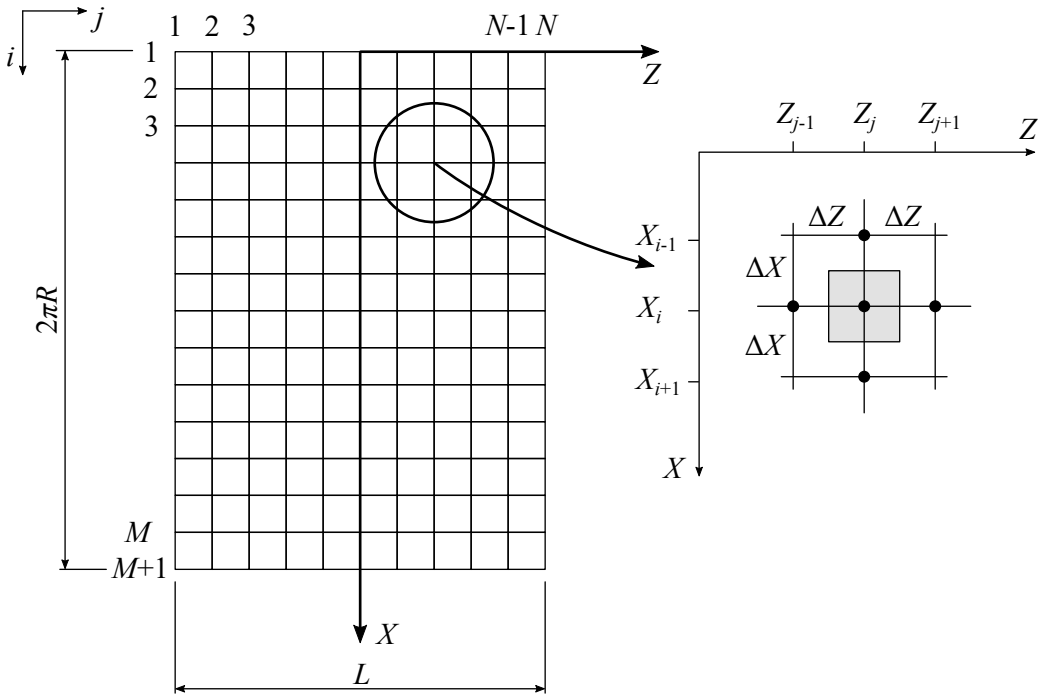

Fig. 4.2: Computational mesh and five-point stencil applied in the finite difference method

4.2.2 Bearing oil supply bores and grooves

Bearing shells contain various oil supply bores and grooves [13, 19, 38]. In the case of the finite difference method, the computational model of the journal bearing can be extended by supply boundary conditions. Constant supply pressure is supposed in the whole area of the bore or groove with prescribed geometry. The borders then define the inner nodes and the indices of the bore/groove in the computational mesh can be easily distinguished [A3]. The transformation between default vector of nodal pressure $\mathbf{p}^{(\mathrm{FDM})} = [p_{1,2}, \ldots, p_{M,N-1}]^T$ and new sorted vector $\tilde{\mathbf{p}}^{(\mathrm{FDM})}$ is performed using orthonormal permutation matrix $\mathbf{T}$ as follows

$$\mathbf{p}^{(\mathrm{FDM})} = \mathbf{T}\,\tilde{\mathbf{p}}^{(\mathrm{FDM})}, \tag{4.21}$$

where $\tilde{\mathbf{p}}^{(\mathrm{FDM})} = \left[\mathbf{p}_Z^T, \mathbf{p}_N^T\right]^T$ contains two subvectors $\mathbf{p}_Z$ of prescribed nodal pressures and unknown nodal pressures $\mathbf{p}_N$.

Substituting (4.21) into (4.18) and multiplication by $\mathbf{T}^T$ yields to

$$\underbrace{\begin{bmatrix} \tilde{\mathbf{A}}_{11} & \tilde{\mathbf{A}}_{12} \\ \tilde{\mathbf{A}}_{21} & \tilde{\mathbf{A}}_{22} \end{bmatrix}}_{\tilde{\mathbf{A}}=\mathbf{T}^T\mathbf{A}^{(\mathrm{FDM})}\mathbf{T}} \underbrace{\begin{bmatrix} \mathbf{p}_Z \\ \mathbf{p}_N \end{bmatrix}}_{\tilde{\mathbf{p}}^{(\mathrm{FDM})}} = \tilde{\mathbf{f}} = \mathbf{T}^T\mathbf{f}^{(\mathrm{FDM})}. \tag{4.22}$$

The Reynolds equation has to be solved only for nodes with unknown pressure and the final system of equations is described by the following equation with prescribed supply pressure on the right-hand side

$$\tilde{\mathbf{A}}_{22}\mathbf{p}_N = \tilde{\mathbf{f}} - \tilde{\mathbf{A}}_{21}\mathbf{p}_Z. \tag{4.23}$$

A direct or iterative solver can be applied to solve this final system of equations. The developed methodology for computational modelling of the supply bores and grooves is more suitable for fixed coordinate system X_FY_FZ because the permutation matrix $\mathbf{T}$ of nodes indices is constant and independent of journal position. On the other hand, for the floating coordinate system X_PY_PZ using, the permutation matrix needs to be rearranged based on new detected supply nodes for each change of journal position.

4.2.3 Hydrodynamic force calculation

After employing the finite difference method for the Reynolds equation solution, a discontinuous pressure field is obtained and a numerical solution of integrals (2.17) and (2.18) has to be applied for hydrodynamic force calculation. Calculated nodal pressures fulfil cavitation boundary condition (2.15) or (2.16).

Approximate calculation of definite integral is based on the trapezoidal rule [89] written in the summary form

$$\begin{aligned} F_{rad}^{hd} &\approx \sum_{j=1}^{N}\sum_{i=1}^{M} q(i,j)\, p_P|_{i,j}\, \Delta X_P \Delta Z \cos\left(\frac{X_P|_i}{R}\right) = \\ &= -\sum_{j=1}^{N}\sum_{i=1}^{M} q(i,j)\, p_F|_{i,j}\, \Delta X_F \Delta Z \cos\left(\frac{X_F|_i}{R} - \gamma\right), \end{aligned} \tag{4.24}$$

$$\begin{aligned} F_{tan}^{hd} &\approx \sum_{j=1}^{N}\sum_{i=1}^{M} q(i,j)\, p_P|_{i,j}\, \Delta X_P \Delta Z \sin\left(\frac{X_P|_i}{R}\right) = \\ &= -\sum_{j=1}^{N}\sum_{i=1}^{M} q(i,j)\, p_F|_{i,j}\, \Delta X_F \Delta Z \sin\left(\frac{X_F|_i}{R} - \gamma\right), \end{aligned} \tag{4.25}$$

where $q(i,j)$ is the size parameter of area with constant nodal pressure $p_{i,j}$. The size parameter is a piecewise function

$$q(i,j) = \begin{cases} 0.5 & \text{for } i = 1,\ldots,M \text{ and } j = 1, N, \\ 1 & \text{else.} \end{cases} \tag{4.26}$$

4.2.4 Determination of stiffness and damping oil film coefficients

Hydrodynamic force is linearised in a static equilibrium position defined by relative eccentricity $\varepsilon^r(y^r, z^r)$ and attitude angle $\gamma^r(y^r, z^r)$. The perturbation method [13, A3] is used to provide partial derivatives (2.22) of hydrodynamic force and determine linearised stiffness and damping coefficients.

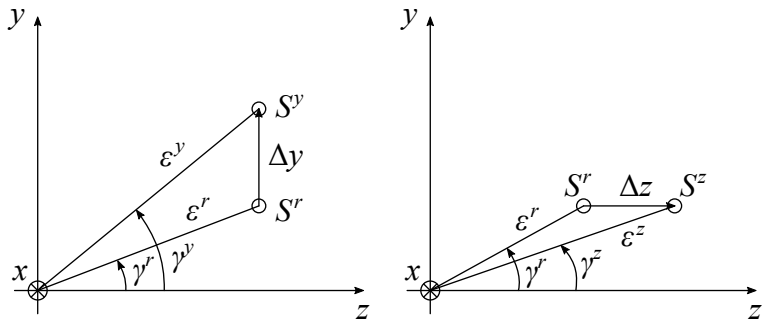

(a) Vertical displacement y (b) Horizontal displacement z

Fig. 4.3: Journal displacement from static equilibrium position S^r

In the first step, journal is moved by small distance Δy, and Δz, from static equilibrium point S^r and the hydrodynamic force is calculated in new positions, see Fig. 4.3. The stiffness coefficients are expressed as [A3]

$$k_{yy} = -\frac{F_y^{hd}\left(\varepsilon^y, 0, \gamma^y, 0, \omega_R, \omega_B\right) - F_y^{hd}\left(\varepsilon^r, 0, \gamma^r, 0, \omega_R, \omega_B\right)}{\Delta y}, \tag{4.27}$$

$$k_{yz} = -\frac{F_y^{hd}\left(\varepsilon^z, 0, \gamma^z, 0, \omega_R, \omega_B\right) - F_y^{hd}\left(\varepsilon^r, 0, \gamma^r, 0, \omega_R, \omega_B\right)}{\Delta z}, \tag{4.28}$$

$$k_{zy} = -\frac{F_z^{hd}\left(\varepsilon^y, 0, \gamma^y, 0, \omega_R, \omega_B\right) - F_z^{hd}\left(\varepsilon^r, 0, \gamma^r, 0, \omega_R, \omega_B\right)}{\Delta y}, \tag{4.29}$$

$$k_{zz} = -\frac{F_z^{hd}\left(\varepsilon^z, 0, \gamma^z, 0, \omega_R, \omega_B\right) - F_z^{hd}\left(\varepsilon^r, 0, \gamma^r, 0, \omega_R, \omega_B\right)}{\Delta z}. \tag{4.30}$$

Oil film damping coefficients are determined similarly by giving small velocity $\dot{y}$ and $\dot{z}$ to the journal which remains in static equilibrium point S^r. Transversal velocities are transformed into cylindrical velocities $\dot{\varepsilon}^y(\dot{y}, 0)$, $\dot{\varepsilon}^z(0, \dot{z})$ a $\dot{\gamma}^y(\dot{y}, 0)$, $\dot{\gamma}^z(0, \dot{z})$. Change of hydrodynamic force components yields to

$$b_{yy} = -\frac{F_y^{hd}\left(\varepsilon^r, \dot{\varepsilon}^y, \gamma^r, \dot{\gamma}^y, \omega_R, \omega_B\right) - F_y^{hd}\left(\varepsilon^r, 0, \gamma^r, 0, \omega_R, \omega_B\right)}{\dot{y}}, \tag{4.31}$$

$$b_{yz} = -\frac{F_y^{hd}\left(\varepsilon^r, \dot{\varepsilon}^z, \gamma^r, \dot{\gamma}^z, \omega_R, \omega_B\right) - F_y^{hd}\left(\varepsilon^r, 0, \gamma^r, 0, \omega_R, \omega_B\right)}{\dot{z}}, \tag{4.32}$$

$$b_{zy} = -\frac{F_z^{hd}\left(\varepsilon^r, \dot{\varepsilon}^y, \gamma^r, \dot{\gamma}^y, \omega_R, \omega_B\right) - F_z^{hd}\left(\varepsilon^r, 0, \gamma^r, 0, \omega_R, \omega_B\right)}{\dot{y}}, \tag{4.33}$$

$$b_{zz} = -\frac{F_z^{hd}\left(\varepsilon^r, \dot{\varepsilon}^z, \gamma^r, \dot{\gamma}^z, \omega_R, \omega_B\right) - F_z^{hd}\left(\varepsilon^r, 0, \gamma^r, 0, \omega_R, \omega_B\right)}{\dot{z}}. \tag{4.34}$$

For the application of the perturbation method on various bearings with different geometry and nominal dimensions, given journal displacements Δy, Δz and velocities $\dot{y}$, $\dot{z}$ are calculated from dimensionless variables

$$\Delta y = c\,\Delta\overline{y}, \qquad \Delta z = c\,\Delta\overline{z}, \qquad \dot{y} = c\,\dot{\overline{y}}, \qquad \dot{z} = c\,\dot{\overline{z}}, \tag{4.35}$$

where c is the radial clearance.

5 Cylindrical bearing

Mathematical models and considered computational methods introduced in chapters 2 and 4 were implemented into in-house software written in MATLAB. This software was developed to investigate the rotor-bearing system with parameters defined in Sec. 5.1 and all presented results shown in the following sections were calculated using this software. First, properties of the finite difference method (FDM) are analysed in Sec. 5.2 and computational costs of various computational approaches are discussed in Sec. 5.3. Analytically examined threshold speeds together with stiffness and damping coefficients are shown in Sec. 5.4. Sec. 5.5 contains results of numerical integration of motion equations and threshold speed detection from obtained time series. The influence of static unbalance on the nonlinear steady-state responses is investigated in Sec. 5.6.

5.1 Test bearing

A simple 2 DoF symmetrical rigid rotor supported on two identical plain journal bearings is considered and bearings with various aspect ratios $\lambda = L/(2R)$ are studied. The bearing gap is filled up by lubricant ISO VG 46 and the Gümbel condition is used for cavitation modelling. The rotating system is loaded in the vertical direction $-y$ ($F_z = 0$) by the gravitational load. Nominal parameters of the analysed system are listed in Tab. 5.1. All numerical analyses were performed on the standard workstation[1].

Parameter	Symbol	Nominal value	Unit
Bearing shell radius	R	50	mm
Aspect ratio	λ	0.5, 1, 1.5	-
Radial clearance	c	0.8	mm
Rotor speed	n	100 – 15000	rpm
Lubricant dynamic viscosity ($\approx$ 40 °C)	μ	0.04	Pa·s
Rotor mass	$2m$	30	kg
Gravitational acceleration	g	9.81	m·s^{-2}
Ambient pressure	p_{amb}	0	Pa

Tab. 5.1: Parameters of investigated bearings

[1]Intel Core i7-7700 CPU 3.6 GHz, 64 GB RAM

5.2 Properties of the finite difference method

Employing of the finite difference method for solution of the Reynolds equation and hydrodynamic force calculation in two different coordinate systems is presented in Sec. 4.2. Mutual comparison of obtained results is shown for static equilibrium points of the bearing with aspect ratio $\lambda = 0.5$ (Tab. 5.1).

Static equilibrium points defined by relative eccentricity ε and attitude angle γ result from the force balance described by following nonlinear system of equations

$$-mg + F_y^{hd}(\varepsilon, \gamma, n_i) = 0, \qquad F_z^{hd}(\varepsilon, \gamma, n_i) = 0, \tag{5.1}$$

where n_i is the rotor speed from range in Tab. 5.1 with the speed-step 25 rpm.

Calculated static equilibrium points are depicted in Fig. 5.1. The simulations were performed on the computational mesh of 91×21 nodes and discretised Reynolds equation (4.18) was solved directly with coefficient matrix $\mathbf{A}^{(\mathrm{FDM})}$ inversion. MATLAB function `fsolve` was employed for solution of the system of nonlinear equations (5.1).

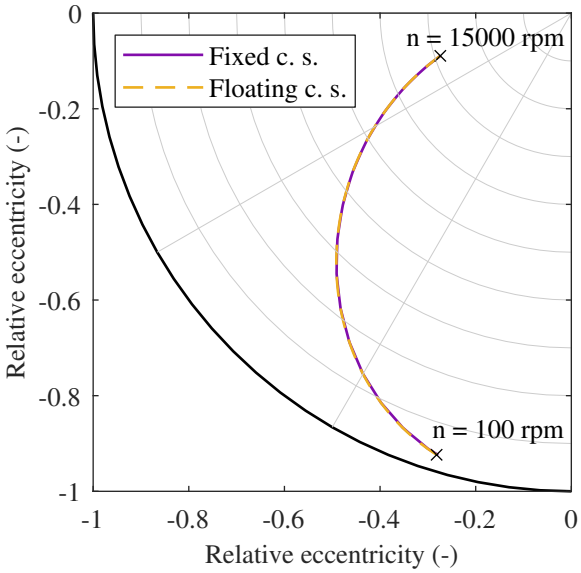

Fig. 5.1: Comparison of static equilibrium points

For better results interpretation, the static equilibrium points are depicted in detail in Fig. 5.2. Fig. 5.2a shows increments of attitude angle as a function of rotor speed. There are significant jumps in the increments of attitude angle for the case of the fixed coordinate system. Investigated speed range on the X-axis is replaced by the corresponding calculated attitude angle for rotor speed n_i, see Fig. 5.2b. Fig. 5.2b also contains highlighted black vertical lines which represent circumferential angles of the computational mesh. It is apparent from the attached figures that the jumps occur at the moment when static equilibrium points circumferentially cross each angular level of the computational mesh. Calculated results in the floating coordinate system stay smooth. Observed jumps in the static equilibrium points also occur in estimated oil film stiffness and damping coefficients [A4]. An increasing number of nodes in circumferential direction [A4] decrease the absolute difference of jumps in

attitude angle but increase the occurrence of this phenomenon. However, finer mesh extends the computational time. It can be concluded that the derived mathematical model in the floating coordinate system $X_P Y_P Z$ is more suitable for numerical analyses rather than in the fixed coordinate system $X_F Y_F Z$ if supply bores in the bearing shell are not supposed.

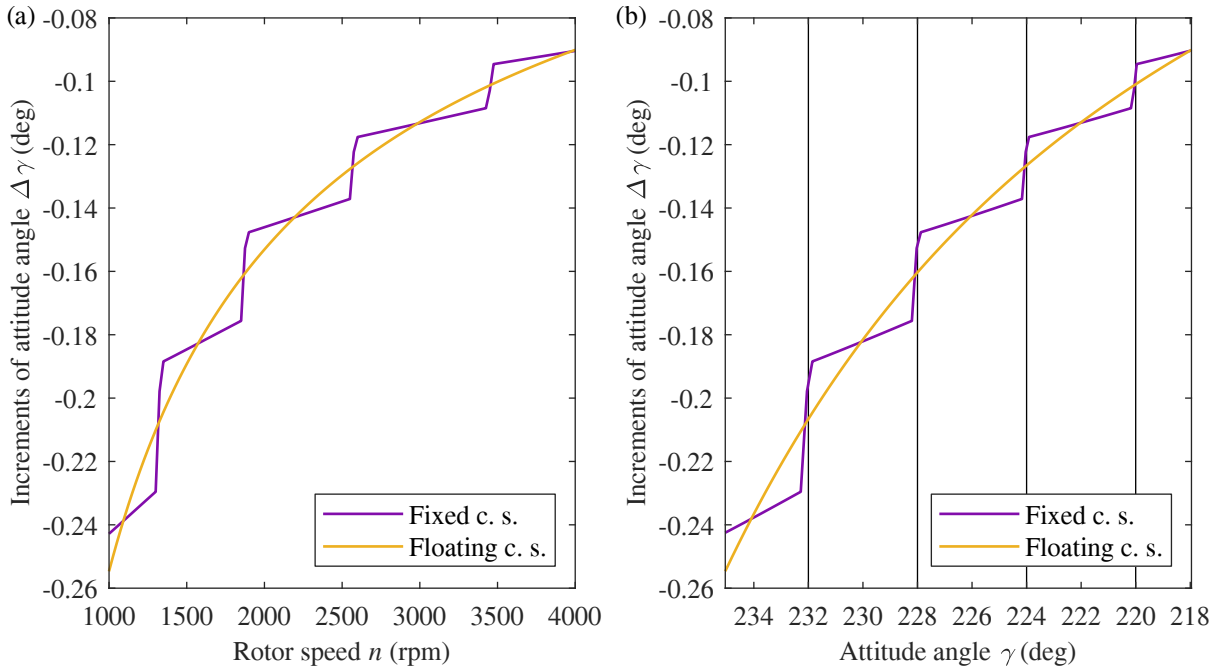

Fig. 5.2: Analysis of static equilibrium points – attitude angle

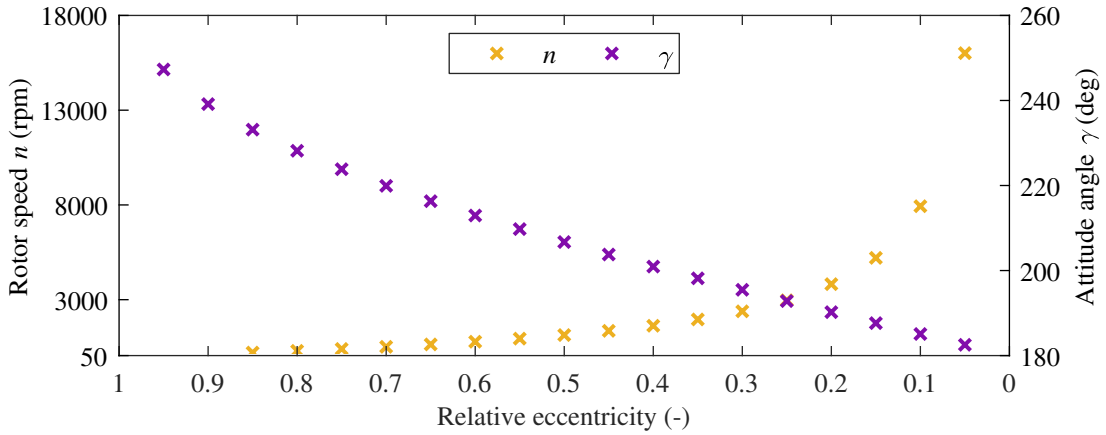

Fig. 5.3: Static equilibrium points – rotor speed and attitude angle

5.3 Comparison of calculation time

The critical side of numerical simulations is CPU time demands and calculation accuracy. Therefore, the test bearing with aspect ratio $\lambda = 1$ was herein analysed and an inverse approach of static equilibrium points determination was used, i.e. unknown rotor speed n and attitude angle γ was found based on prescribed relative eccentricity $\varepsilon_i \in \langle 0.5, 0.95 \rangle$. Hydrodynamic pressure and force evaluation were performed in the floating coordinate system $X_P Y_P Z$ using the finite difference method. Results of the system of nonlinear equations are depicted in Fig. 5.3.

For objective comparison of computational time costs of various calculation approaches, hydrodynamic pressure and hydrodynamic force were evaluated in previously determined static equilibrium points. All presented simulations were repeated five times and the final median value of computational time was established to eliminate inaccuracy in time measurement.

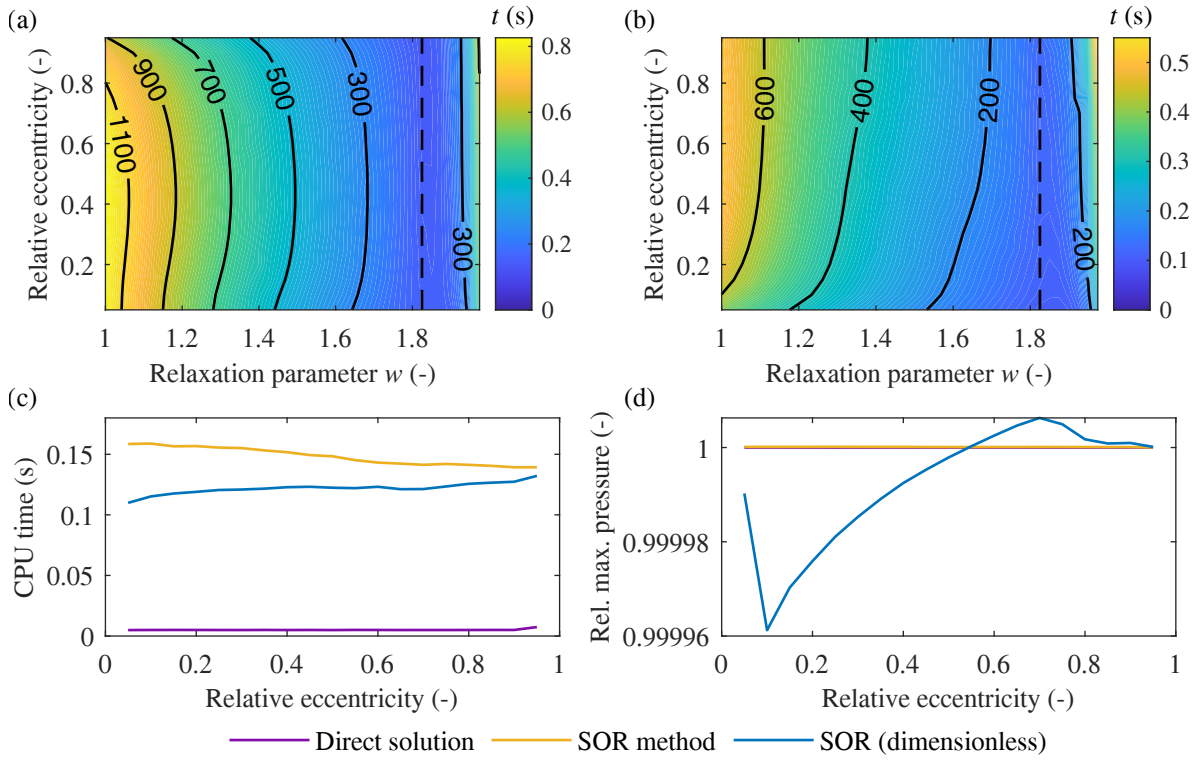

Fig. 5.4: Comparison of computational time – hydrodynamic pressure

Hydrodynamic pressure was calculated using the finite difference method by both direct and iterative solutions of the Reynolds equation in the dimensional and dimensionless forms. In the case of the SOR method, the influence of the relaxation parameter w on the computational time was studied. The simulations were performed on the computational mesh with 91×21 nodes. Fig. 5.4a depicts a colourmap of the computational time for the SOR method and the dimensional form of the Reynolds equation. The results for the SOR method and dimensionless form of the Reynolds equation are shown in Fig. 5.4b. Black contour lines in both subfigures represent the number of iterations until the stopping criteria were met.

The stopping criteria were defined as follows: $n_{max} = 1 \cdot 10^5$ iterations for both models and various tolerances $\varepsilon_{SOR} = 1 \cdot 10^{-2}$ for dimensional and $\varepsilon_{SOR} = 1 \cdot 10^{-5}$ for dimensionless case. The best time was achieved for the relaxation parameter $w \approx 1.825$ for both cases (black dashed lines). The reference [18] mentions that the optimal value of the relaxation parameter concerning the computational time is close to $w_{opt} \approx 1.7$. A mutual comparison of elapsed times is depicted in Fig. 5.4c, where the results of the SOR method with the best achieved time are used (black dashed lines in Fig. 5.4a,b). Obviously, the fastest method is the direct solution, although the pressure peak accuracy is comparable for all methods, see Fig. 5.4d. Pressure peaks are transformed and depicted relatively to the pressure peak results of direct solution.

Fig. 5.5 shows a comparison of computational time for evaluation of the hydrodynamic force which consists of two steps of pressure calculation p and its numerical integration F. First, the hydrodynamic pressure is calculated with the most effective method, i.e. direct solution of the discretised Reynolds equation. Particular parts of the bar charts then show the time of each solution step. Particular numerical integration is several orders times faster than hydrodynamic pressure calculation. For speeding up numerical simulations in developed in-house software, the source codes were compiled to the `mex` format [91]. Using this procedure saved 13 % in total of elapsed time and the best simulation time is $4.6 \cdot 10^{-3}$ s.

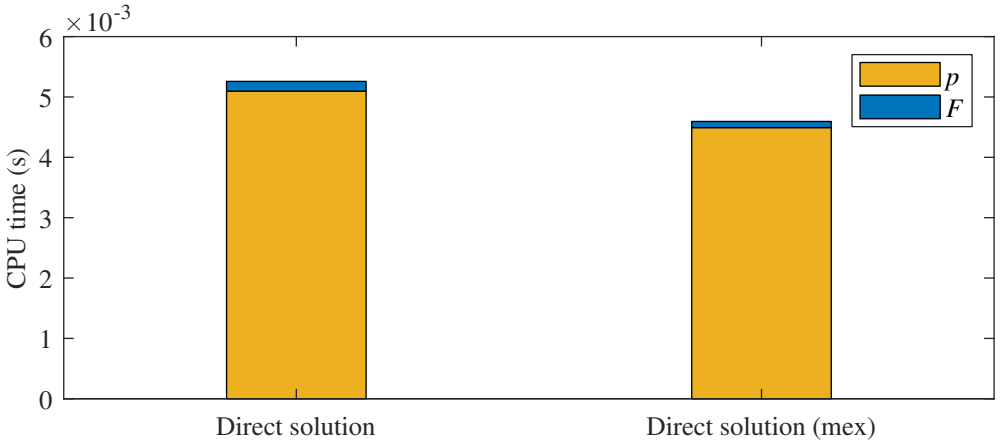

Fig. 5.5: Comparison of computational time – hydrodynamic force

5.4 Stability analysis

Stability and modal analyses are fundamental analyses for the design of the rotor system supported on journal bearings. Journal bearings are characterised by rotor speed-dependent linearised stiffness and damping coefficients [1, 4, 6, 38]. Linearised coefficients can be determined by analytical models (Sec. 4.1) for plain journal bearings or by numerical methods (Sec. 4.2) for complex bearings geometry. Derived models and developed methods are applied and analysed on the bearings with various aspect ratios λ.

Static equilibrium points in the bearing gap for all investigated cases $\lambda = 0.5, 1, 1.5$ (Tab. 5.1) are depicted in sequence in Fig. 5.6. The finite difference method and corrected analytical models of the infinitely short and long bearing provide similar static loci for all

analysed bearings. However, significant differences are apparent after using the infinitely long bearing model for limit case $\lambda = 0.5$ and vice versa, the infinitely short bearing model for $\lambda = 1.5$, because of their inappropriate application in this aspect ratio range. Nevertheless, obtained results for the infinitely short or long bearing models will correspond nicely with the finite difference method after moving towards the suggested aspect ratio.

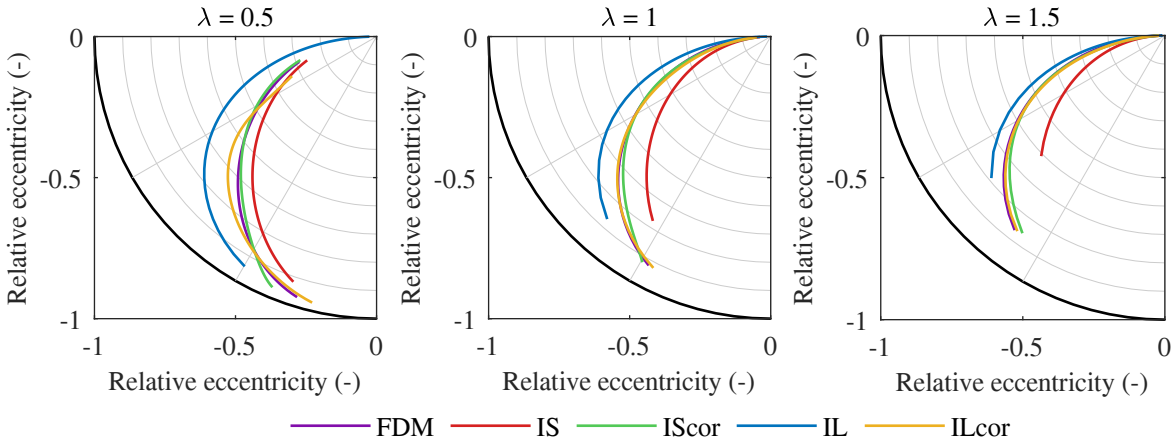

Fig. 5.6: Comparison of static equilibrium points for aspect ratio $\lambda = 0.5, 1, 1.5$

Evaluated linearised dynamic coefficients in static equilibrium points are shown in Fig. 5.7 – Fig. 5.9 as a function of relative eccentricity. Coefficients $\overline{k}_{ij}$ and $\overline{b}_{ij}$ are transformed into dimensionless quantities (2.28) and vertical axes are restricted for better results interpretation.

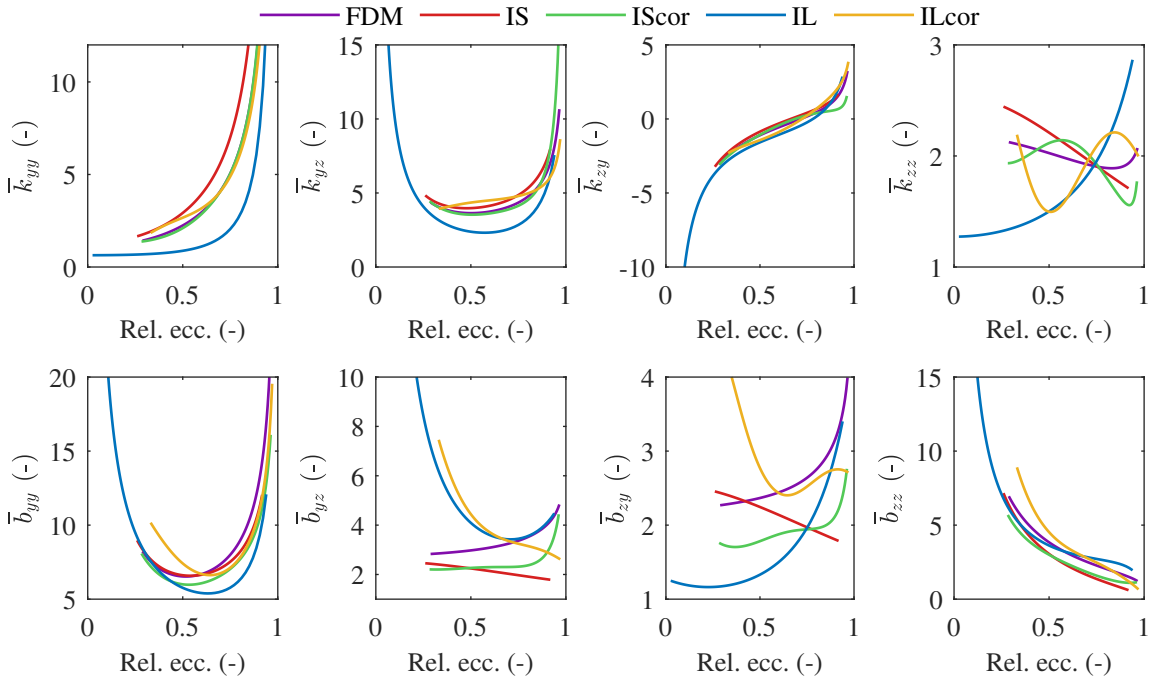

Fig. 5.7: Comparison of stiffness and damping coefficients for aspect ratio $\lambda = 0.5$

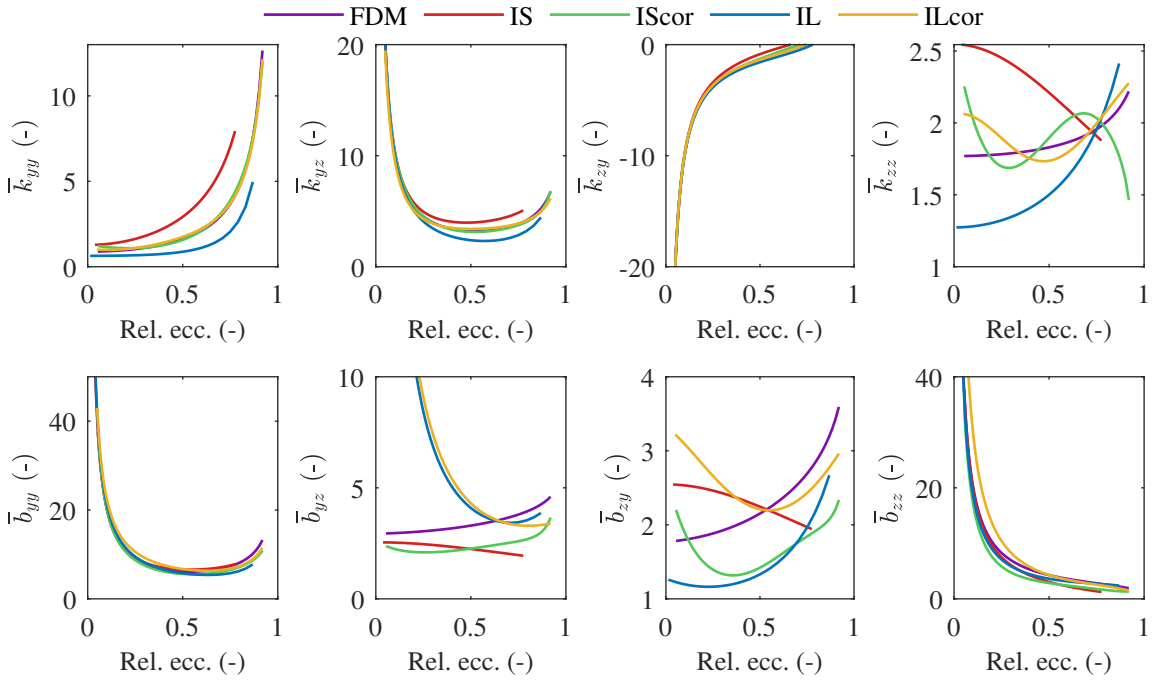

Fig. 5.8: Comparison of stiffness and damping coefficients for aspect ratio $\lambda = 1$

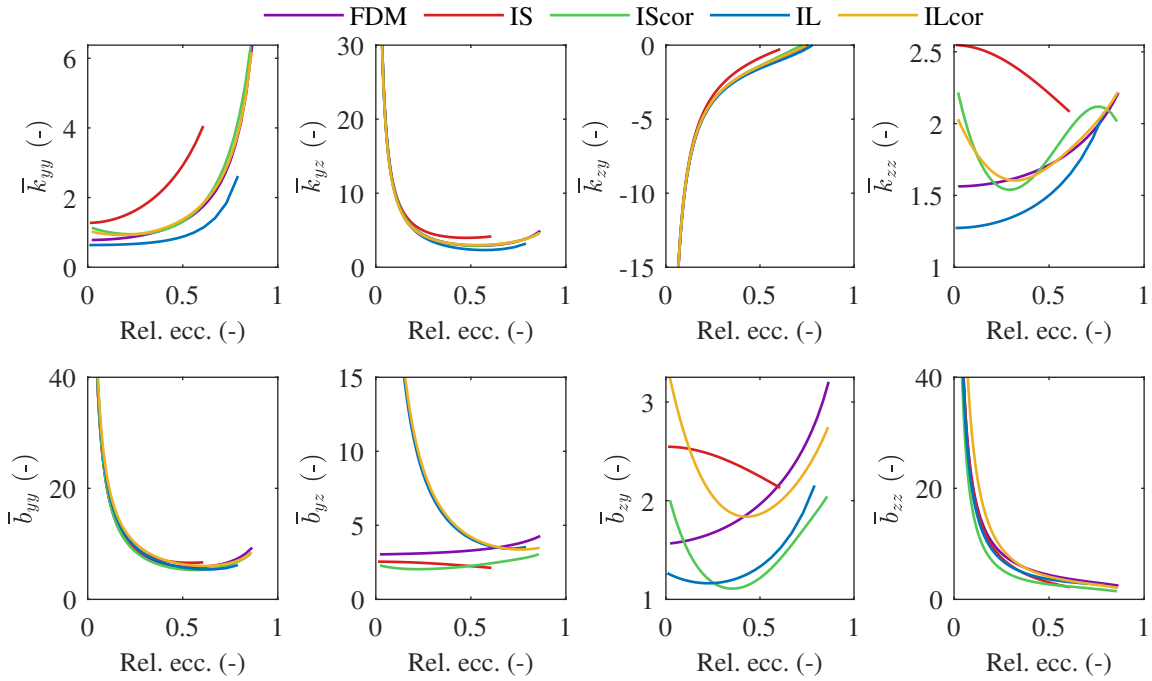

Fig. 5.9: Comparison of stiffness and damping coefficients for aspect ratio $\lambda = 1.5$

Stiffness coefficients $\overline{k}_{ij}$ for $ij = yy, yz, zy$ qualitatively and quantitatively correspond well for all aspect ratios λ and computational models except for IS model for $\lambda = 1.5$ and IL model for $\lambda = 0.5$. In the case of $\lambda = 1$, the IS and IL models are still comparable with the finite difference method. Differences in the dynamic coefficients between the models are mainly caused by different static equilibrium points (Fig. 5.6). Significant qualitative discrepancies in coefficient $\overline{k}_{zz}$ are still reasonable because this coefficient does not affect the main load in the vertical direction.

Similar conclusions as for stiffness coefficients $\overline{k}_{ij}$ can be also stated for damping coefficients $\overline{b}_{ij}$ evaluated by all proposed methods. However, cross-coupling damping coefficients $\overline{b}_{yz}$ and $\overline{b}_{zy}$ determined from the IL and ILcor models significantly differ from the other models for $\varepsilon < 0.5$.

It can be concluded, computational model IScor provides comparable results as finite difference method in the whole investigated range of rotor speed and aspect ratio λ. Therefore, applying the other models for journal bearing analyses out of the supposed aspect ratio should be employed only in substantiated cases.

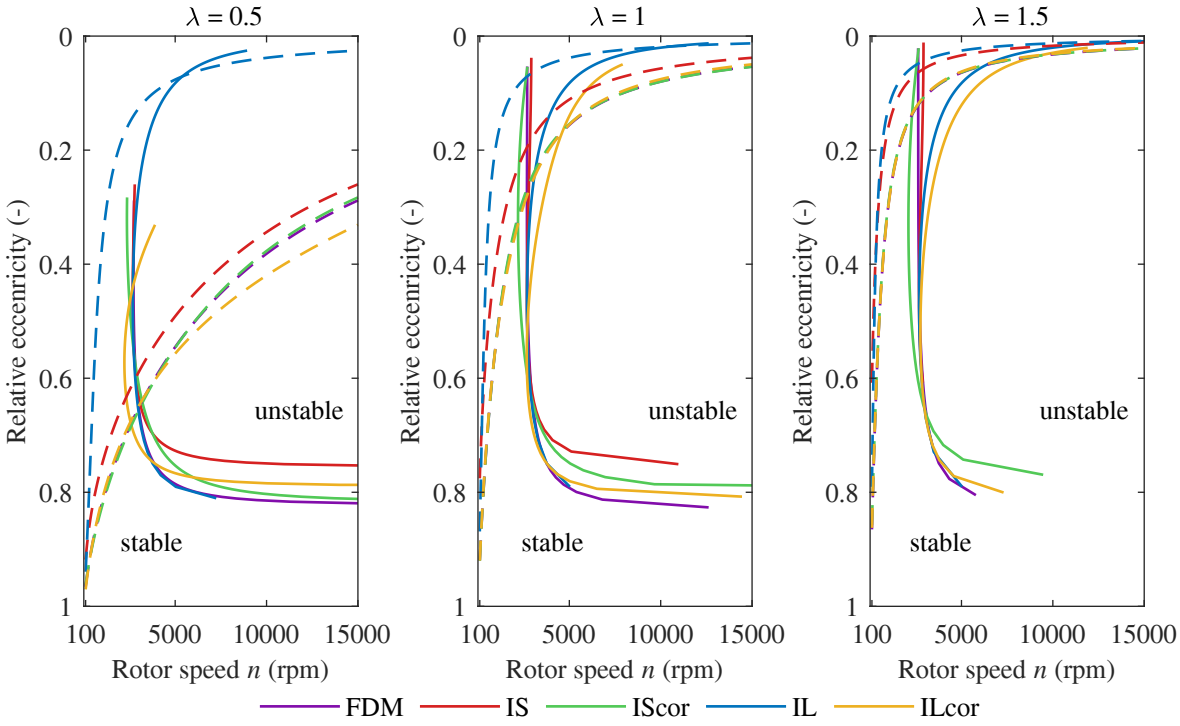

Fig. 5.10: Comparison of threshold speed curves for aspect ratio $\lambda = 0.5, 1, 1.5$

After surpassing threshold speed, the rotor becomes unstable and starts to perform the undamped orbital motion. Threshold speed can be easily determined (2.34) using linearised dynamic coefficients. Fig. 5.10 shows the comparison of calculated threshold speed for all investigated bearing aspect ratios λ. Each subfigure consists of a solid line, which distinguishes area to stable (left) and unstable (right) parts, and a dashed line of the relative eccentricity of static equilibrium points obtained from static analysis (Fig. 5.6). Both curves are a function of rotor speed. The mutual intersection of stability borderline and relative eccentricity curve represents threshold speed ω_t. Presented results confirm the previous statement that IS and IScor models are suitable to apply for a relatively wide range of aspect ratios. Model IScor

predicts unstable behaviour development at lower rotor speed for a higher aspect ratio than other models. Threshold speed curves (stability borderline) obtained by computational models IL and ILcor differ from others solutions if relative eccentricity $\varepsilon \leq 0.5$, see cross-coupling damping coefficients $\overline{b}_{yz}$ and $\overline{b}_{zy}$.

Fig. 5.11 depicts computational time necessary for the determination of linearised dynamic coefficients. Each case of aspect ratio is distinguished by a different colour. The vertical axis is transformed into a logarithmic scale for better results interpretation. The finite difference method is much higher time demanding than analytical methods because the pressure field and the hydrodynamic force are calculated three times in the determination of the coefficients by a perturbation method, see Sec. 4.2.

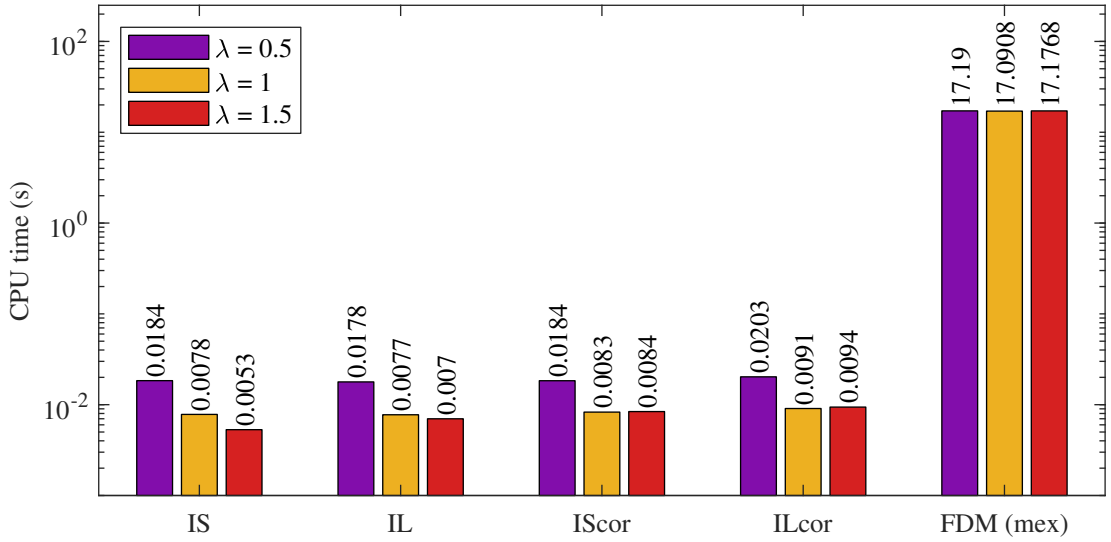

Fig. 5.11: Comparison of calculation time for linearised dynamic coefficients determination

5.5 Stability analysis in the time domain

Another way of rotor system stability analysis is the investigation of its behaviour in the time domain. Equations of motion of analysed system are written with respect to Fig. 2.1 and Fig. 2.2 in this form

$$\begin{bmatrix} m & 0 \\ 0 & m \end{bmatrix} \begin{bmatrix} \ddot{y}_S \\ \ddot{z}_S \end{bmatrix} = \begin{bmatrix} -mg \\ 0 \end{bmatrix} + \begin{bmatrix} F_y^{hd} \\ F_z^{hd} \end{bmatrix}, \qquad \mathbf{M}\ddot{\mathbf{q}}(t) = \mathbf{f}_g + \mathbf{f}_{hd}\left(\mathbf{q}, \dot{\mathbf{q}}, t\right), \tag{5.2}$$

where $\mathbf{M}$ is the mass matrix, $\ddot{\mathbf{q}}(t), \dot{\mathbf{q}}(t), \mathbf{q}(t)$ are the vectors of generalised acceleration, velocity and displacement and $\mathbf{f}_g, \mathbf{f}_{hd}$ are the vectors of gravitational load and hydrodynamic force. The system of the second-order ordinary differential equations (5.2) is for the reason of numerical integration transformed into the state-space $\mathbf{u}(t) = \left[\dot{\mathbf{q}}(t)^T, \mathbf{q}(t)^T\right]^T \in \mathbb{R}^{4,1}$ [6, A3] with using of identity $\mathbf{M}\dot{\mathbf{q}}(t) - \mathbf{M}\dot{\mathbf{q}}(t) = \mathbf{0}$ and its association to (5.2). After mathematical manipulation, this yields to

$$\dot{\mathbf{u}}(t) = \mathbf{A}\mathbf{u}(t) + \mathbf{b}(t), \tag{5.3}$$

where $\mathbf{A} \in \mathbb{R}^{4,4}$ is the system matrix and $\mathbf{b} \in \mathbb{R}^{4,1}$ is the vector of the right-hand side with following components

$$\mathbf{A} = \begin{bmatrix} \mathbf{0} & \mathbf{0} \\ \mathbf{E} & \mathbf{0} \end{bmatrix}, \qquad \mathbf{b}(t) = \begin{bmatrix} \mathbf{M}^{-1} \left(\mathbf{f}_g + \mathbf{f}_{hd} \left(\mathbf{q}, \dot{\mathbf{q}}, t \right) \right) \\ \mathbf{0} \end{bmatrix}. \tag{5.4}$$

$\mathbf{E}$ is the identity matrix. The system of the first-order ordinary differential equations (5.3) is extended by initial conditions $\mathbf{u}(0) = \left[\mathbf{0}^T, \mathbf{q}(0)^T \right]^T$.

Two different run-up times $t_1 = 5$ s and $t_2 = 10$ s were assumed for rotor stability analyses. Run-up simulations with prescribed constant angular acceleration were performed for various nominal values of journal bearing design parameters, i.e. lubricant dynamic viscosity, rotor mass, radial clearance and bearing width. Bearing default parameters were set up according to Tab. 5.1 with aspect ratio $\lambda = 1$ except chosen varying-parameter. Investigated range of varying-parameters is summarised in Tab. 5.2. Intervals are divided into 30 discrete steps. Minimum and maximum rotor speed was chosen concerning the results from Fig. 5.10 where the threshold speed was found close to 3000 rpm.

Parameter	Symbol	Min. value	Max. value	Units
Radial clearance	c	0.4	1	mm
Lubricant dynamic viscosity	μ	0.01	0.065	Pa·s
Jounal mass	m	3	25	kg
Aspect ratio	λ	0.5	1.5	-
Rotor speed	n	2000	4000	rpm

Tab. 5.2: Various design parameters of investigated bearings

Threshold speed detection from the time series is performed using developed in-house software. Fig. 5.12 shows chosen time series of journal centre trajectory of balanced rotor for run-up time $t_1 = 5$ s. The finite difference method was used for the hydrodynamic force calculation. The journal centre follows equilibrium locus (series of static equilibrium points from static analysis in Fig. 5.6) until the first threshold speed ω_t is not reached during the run-up. After surpassing this speed ω_t, the rotor losses stability and starts to oscillate with increasing lateral displacements around its static equilibrium point. The hydrodynamic force stabilises this phenomenon until the second threshold speed ω_g, when the stabilising effect is lost and lateral displacements significantly increase, and the instability is fully developed. The described behaviour during oil whirl instability development is depicted in detailed subfigures in Fig. 5.12 with both detected threshold speeds ω_t and ω_g by in-house software.

Threshold speed ω_t is automatically found by in-house software when following implemented condition for consecutive local extrema of relative eccentricity time series is met

$$\omega_t = \omega_i \quad \Leftrightarrow \quad |\varepsilon_{i+1} - \varepsilon_i| \geq \Delta\varepsilon, \tag{5.5}$$

where ε_i is the local extreme value of relative eccentricity $\varepsilon(t)$ in the i-th time step of the simulation, ω_i is the journal angular velocity at this time step and $\Delta\varepsilon$ is chosen tolerance of relative eccentricity increment. Threshold speed ω_g reflects the point, when maximum gradient of relative eccentricity time series is determined $\omega_g = \max\{(\mathrm{d}\varepsilon/\mathrm{d}t)\,|_i\}$.

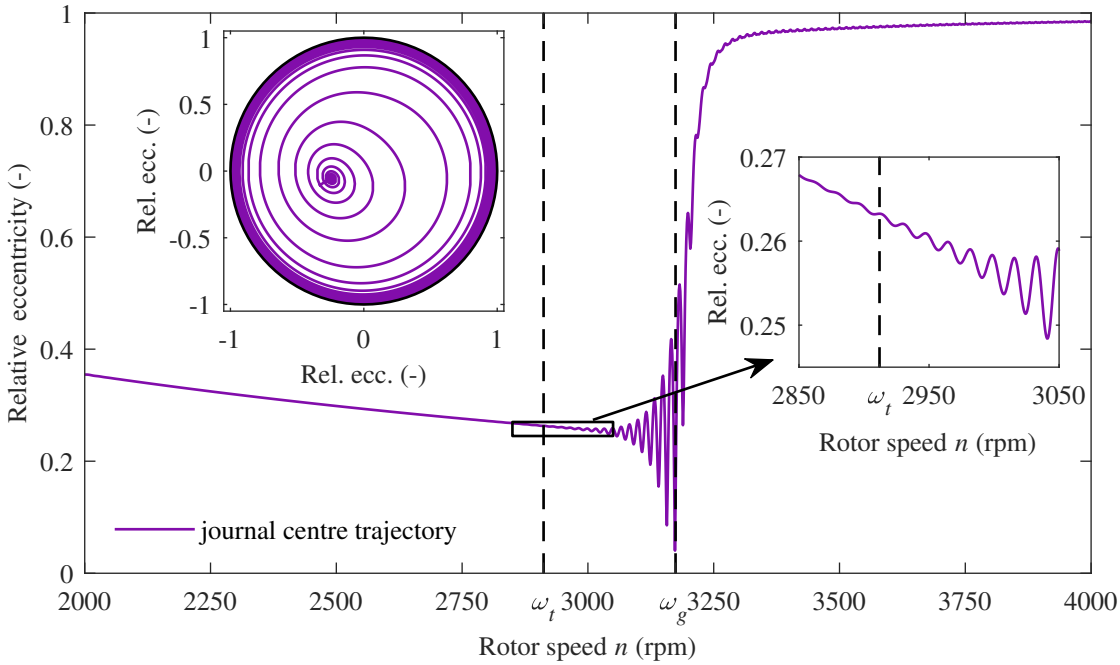

Fig. 5.12: Journal centre trajectory during run-up

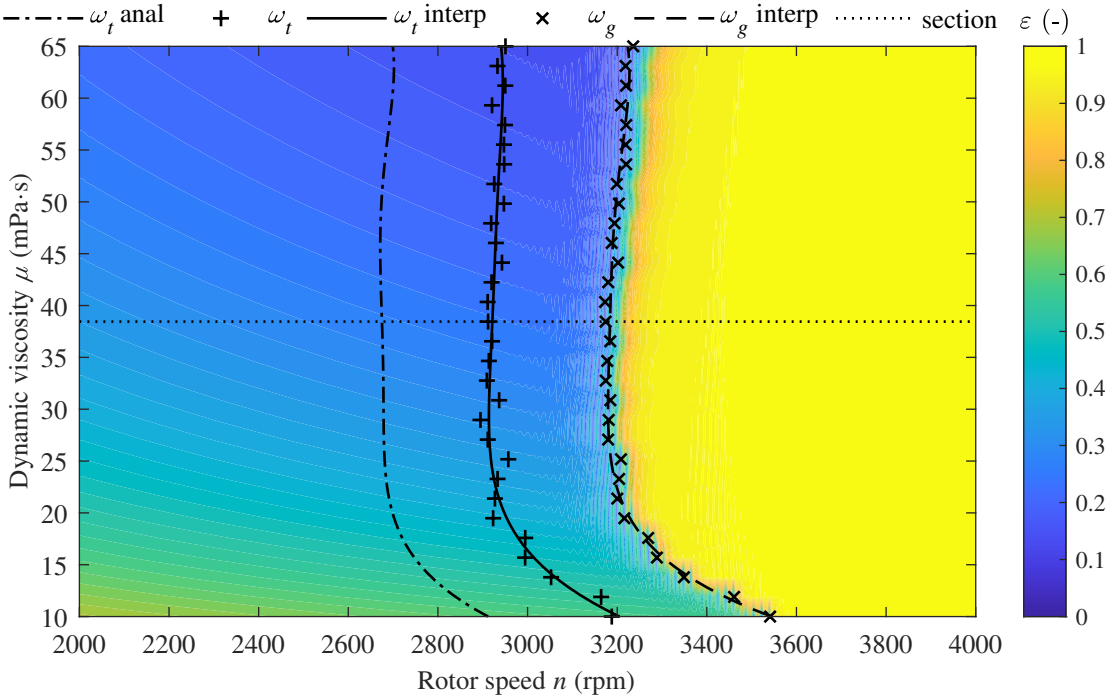

Fig. 5.13: Instability development and detected threshold speeds

Sensitivity analysis of lubricant dynamic viscosity on the detected threshold speeds for run-up time $t_1 = 5$ s are depicted in the colourmap of relative eccentricity in Fig. 5.13. Each horizontal section corresponds to time series for nominal value from the parametric study. The section highlighted by the dotted line is analysed in detail in Fig. 5.12. All detected

threshold speeds are denoted by markers and interpolated by the fifth-degree polynomial function to eliminate numerical inaccuracies and estimate threshold speed between discrete points. Threshold speeds calculated based on stability criterion (2.34) (Sec. 2.5 and Sec. 5.4) employing linearised dynamic coefficients are interpolated by the same polynomial function and depicted by dash-dotted line.

Numerical simulations with various design parameters from Tab. 5.2 were performed with MATLAB solver `ode15s`, which is based on the Runge-Kutta algorithm suitable for stiff problems. The initial condition for numerical integration of the equation of motion was set to static equilibrium point for the first rotor speed from investigated range and zero initial velocity. Hydrodynamic forces were calculated in each time step of integration with IS, IScor, ILcor models and by finite difference method.

Fig. 5.14 – Fig. 5.17 show detected threshold speeds as a function of various design parameters, rotor speed and the results are distinguished by the employed computational method. Detection of the thresholds speeds ω_t was performed for all sensitivity analyses and computational methods consistently with stopping criterion $\Delta\varepsilon = 1 \cdot 10^{-9}$ and the same degree of approximation polynomial function (the 5th degree). For better clarity, each subfigure consists of interpolated detected threshold speeds and the analytically estimated threshold speed curve based on stiffness and damping coefficients. The presented figures show that instability arises at higher rotor speed ω_t in case of faster run-up (lower run-up time), and all depicted curves detected from the time series do not qualitatively differ from the analytical calculation. Interestingly, numerical and analytical results should be identical for an infinitely long run-up time. Region width between initial ω_t and fully developed ω_g instability continually decreases with increasing run-up time. Fig. 5.17 depicts detected thresholds speeds for various aspect ratios λ. The results are comparable to Fig. 5.10. In all presented figures, discrepancies at the ends of the design parameter range are caused by approximation procedure. Obtained results for the ILcor computational models significantly differ from other presented models and fluid-induced instability was not even developed in many investigated cases.

Particular sensitivity analyses of the bearing with the same aspect ratio λ are mutually equivalent with respect to the Sommerfeld number calculated based on [3, 4] as follows

$$S = \frac{1}{\mu\,\omega}\frac{mg}{2LR}\left(\frac{c}{R}\right)^2. \tag{5.6}$$

Dependence of the Sommerfeld number on the dimensionless detected threshold speeds $\omega\sqrt{c/g}$ and different computational methods is depicted in Fig. 5.18. Fore better diagram clarity, only the analytically established threshold speeds ω_t and detected threshold speeds ω_g are shown for particular computational methods and sensitivity analyses. Different lengths of depicted curves are caused by various nominal values of parameter from investigated range. Obviously from Fig. 5.18, the IScor computational model predicts the losses of stability earlier than other methods, see also the previous results in Fig. 5.14 – Fig. 5.16. Otherwise, the ILcor bearing model estimates instability threshold for higher Sommerfeld numbers similarly to the IS model and the finite difference method. The results also confirm the statement [3] that the journal bearings with the same Sommerfeld number and aspect ratio have similar behaviour. Minor results discrepancies between the sensitivity analyses are affected by detection accuracy and postprocessing approximation (Fig. 5.13).

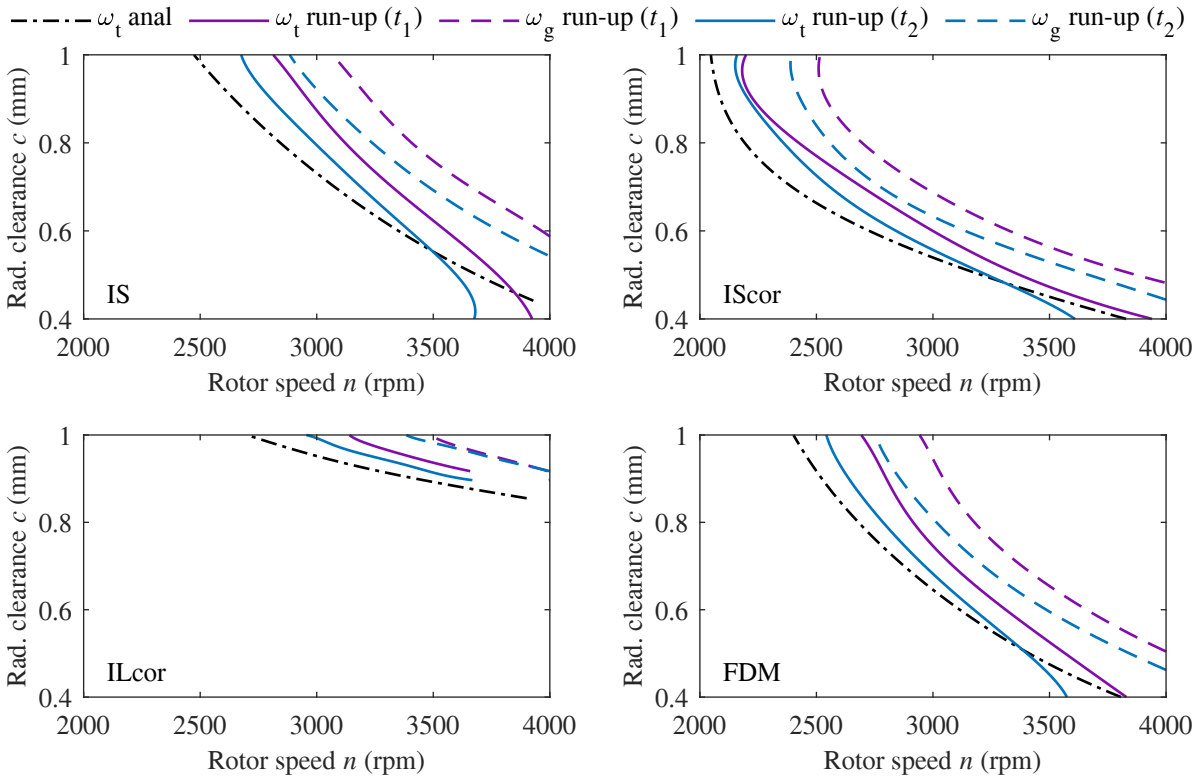

Fig. 5.14: Detected threshold speed for various radial clearances

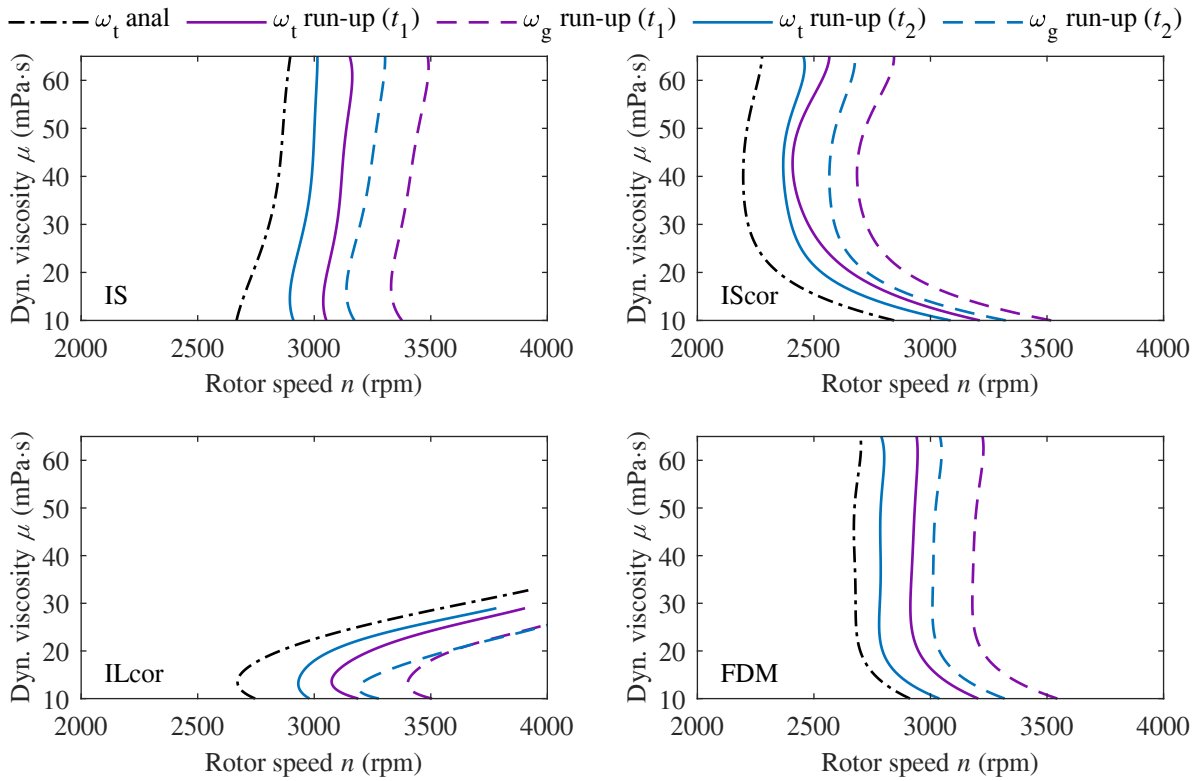

Fig. 5.15: Detected threshold speed for various dynamic viscosities

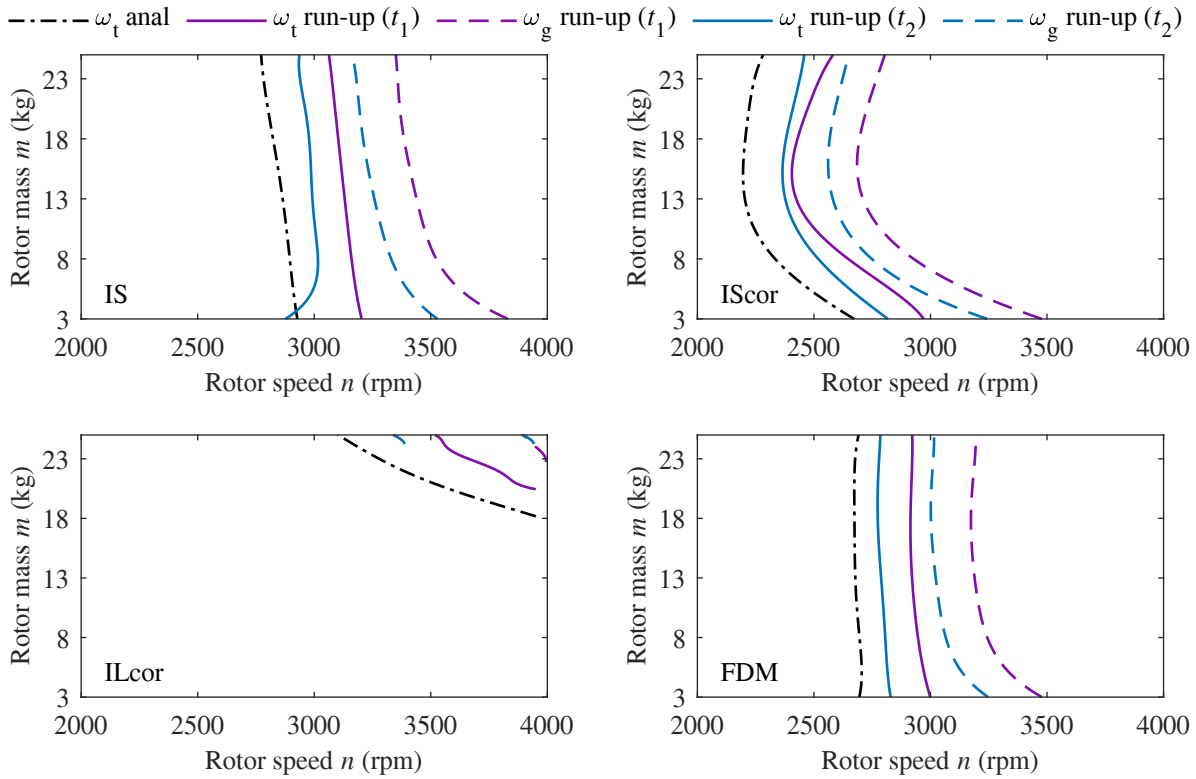

Fig. 5.16: Detected threshold speed for various rotor masses

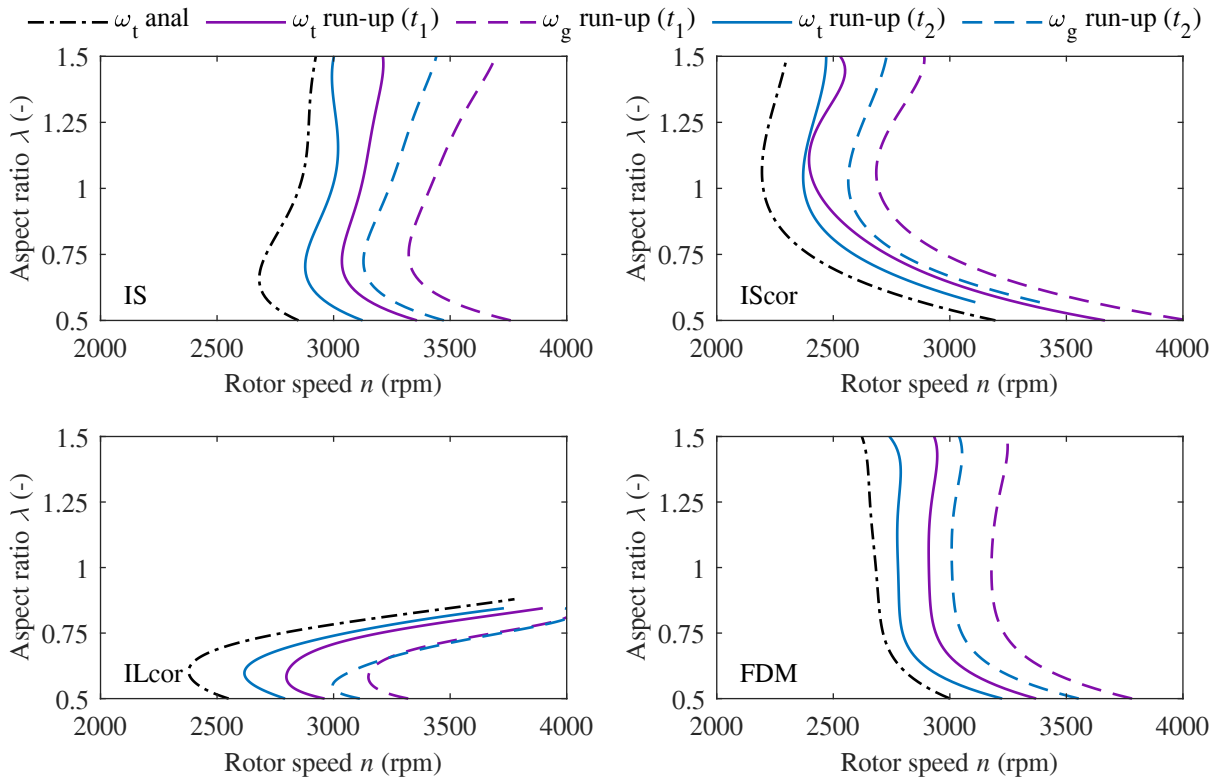

Fig. 5.17: Detected threshold speed for various aspect ratios

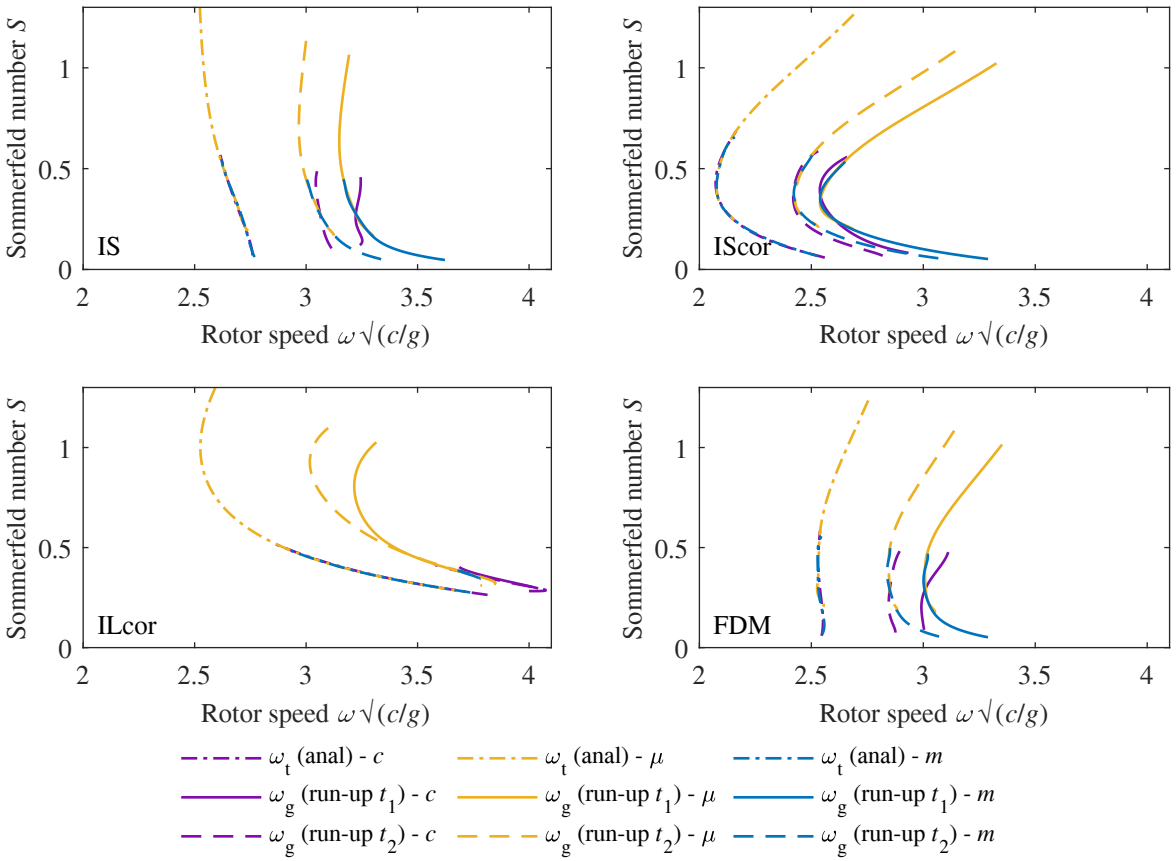

Fig. 5.18: Detected threshold speeds for various Sommerfeld numbers

5.6 Influence of unbalance

The hydrodynamic forces in journal bearings were evaluated using IS and IScor models and the finite difference method. Parameters of the considered 2 DoF rotor-bearing system with various static bearing loads (corresponding rotor mass) and static unbalances are listed in Tab. 5.3.

The system's response was simulated 10 s long for each speed from the investigated speed range with speed-step 50 rpm. The transient response to the initial conditions in time interval $t \in \langle 0, 5 \rangle$ s was omitted. The initial conditions were set to the estimated static equilibrium point resulting from the static analyses and zero initial velocity. The obtained results are depicted in Fig. 5.19 – Fig. 5.24. Results of each investigated case consist of a bifurcation diagram to depict the local extremes of the response and corresponding spectrogram resulting from fast Fourier transform using tool `autofft` [92]. The bifurcation diagrams show local maxima (red), local minima (black) and static equilibrium points (yellow). The spectrograms are depicted in the logarithmic scale for better diagram clarity. Only the horizontal rotor response is depicted due to similar behaviour in both directions.

In the case of heavily loaded bearing in Fig. 5.19 – Fig. 5.21, there is an apparent region between approx. 6000 and 7000 rpm with 0.5X subharmonic component. The width of this region and oscillations increase with the increasing magnitude of static unbalance. The IS model predicts this behaviour for all considered static unbalances. The period-doubling

bifurcation does not appear for static unbalance U_1 and the IScor model, and for both static unbalances U_1, U_2 and the finite difference method. Here, the subharmonic periodic motion excited due to applied out-of-balance force is suppressed by the damping effect of the hydrodynamic force. Employed hydrodynamic force models mainly differ in cross-coupling damping coefficients in Fig. 5.8. The hydrodynamic force calculated using the finite difference method has the most significant damping impact and invoked oscillations are apparent only for static unbalance U_3.

The oil whirl starts to develop after surpassing the threshold speed, see the results for zero static unbalance U_0. The self-excited transient response (limit cycles) has a subsynchronous component ca. 0.4X until fully developed instability is reached. Then, the journal performs the orbital motion over the full bearing clearance circle. Contrary to the IS and IScor models, using the finite difference method causes this transient region with the quasiperiodic motion to begin at lower rotor speed with increasing static unbalance than for a perfectly balanced system. Interestingly for the employed IScor model, the synchronous 1X component disappeared when the fluid-induced instability developed for all static unbalances. In all diagrams, increased oscillations at ca. 3000 rpm are caused by the resonance of excitation frequency and natural frequency of the rotor-bearing system.

Parameter	Symbol	Nominal value	Unit
Bearing shell radius	R	50	mm
Bearing length	L	50	mm
Radial clearance	c	0.125	mm
Rotor speed	n	1000 – 11000	rpm
Lubricant dynamic viscosity	μ	0.02	Pa·s
Ambient pressure	p_{amb}	0	Pa
Journal static load	W_i	2.24, 11.2	kN
Journal static unbalance	U_i	0, 3435, 6870, 8588	g·mm

Tab. 5.3: Parameters of investigated rotor-bearing system

The results for lightly loaded journal bearings are depicted in Fig. 5.22 – Fig. 5.24. The threshold speed is ca. 1000 rpm lower for a perfectly balanced lightly loaded journal than in the previous study. In all considered cases, there is no transient region with dominant subharmonic component 0.4X resulting from the force balance of the static load, hydrodynamic force, and inertia forces. The self-excited vibrations typically developed after surpassing the threshold speed are apparent only in the case of static unbalance U_1 and all considered hydrodynamic force models. For the static unbalances U_2, U_3 and analytical force models, the unstable behaviour occurs at a higher rotor speed than expected.

The response in the instability region is quasiperiodic rather than a limit cycle. The instability is not developed in the case of static unbalance U_3 and calculated force based on the IS model. The journal oscillates only with synchronous component 1X corresponding to the excitation frequency. Period-doubling bifurcation before reaching the threshold speed is more significant for a lightly loaded system because the magnitude of the out-of-balance force is considerably higher than the static load. The responses obtained using the finite difference

method are qualitatively different for static unbalances U_2 and U_3 compared to analytical hydrodynamic force models. Despite the spectrograms showing dominant subsynchronous harmonic component 0.5X starting at 6000 rpm, which could be initially classified as oil whirl motion, the corresponding bifurcation diagrams exhibit period-doubling behaviour due to the out-of-balance force presence.

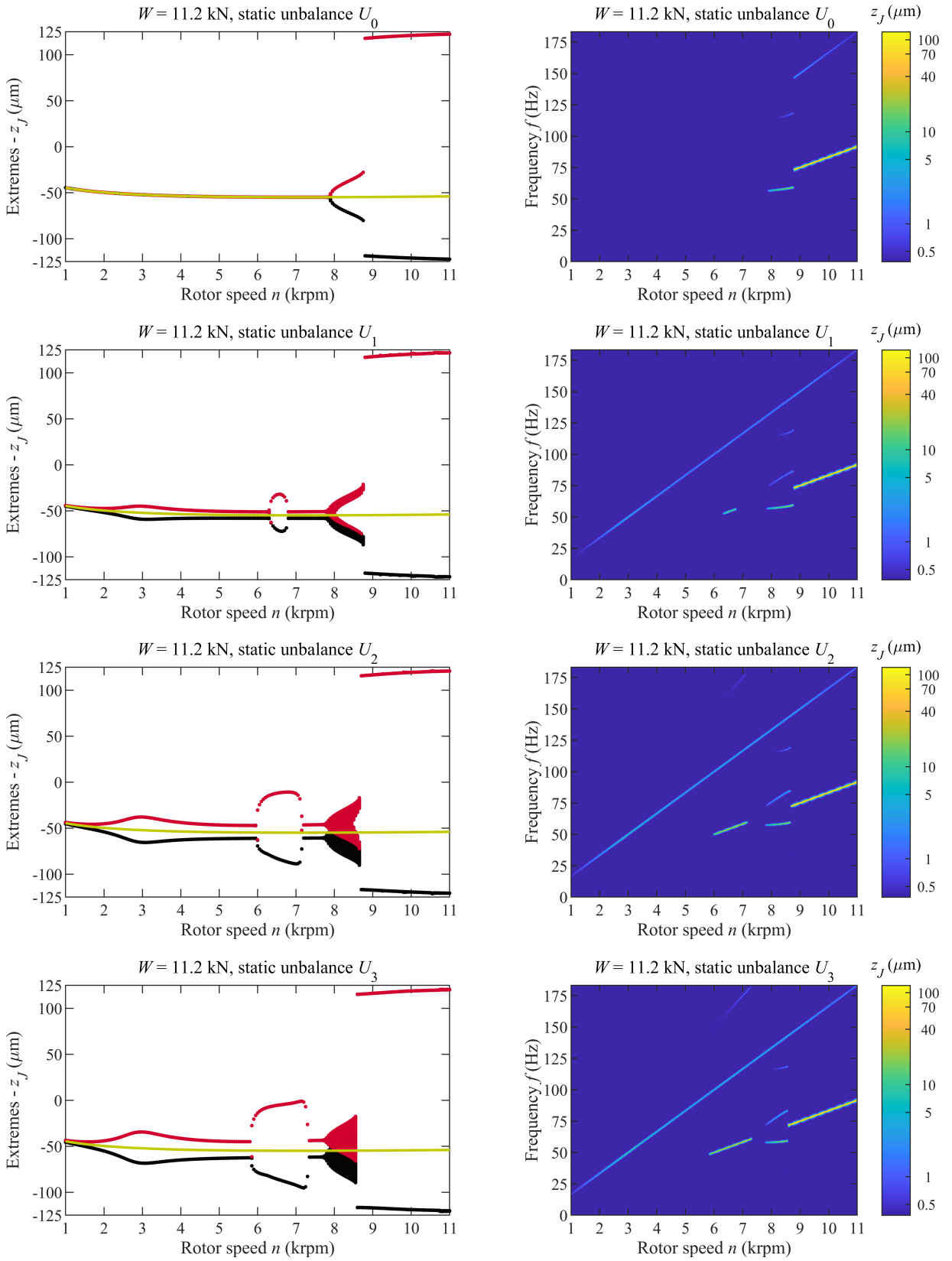

Fig. 5.19: Bifurcation diagrams and spectrograms of the nonlinear steady-state horizontal response to harmonic excitation by various static unbalances and static load 11.2 kN. The hydrodynamic forces are evaluated using the IS model

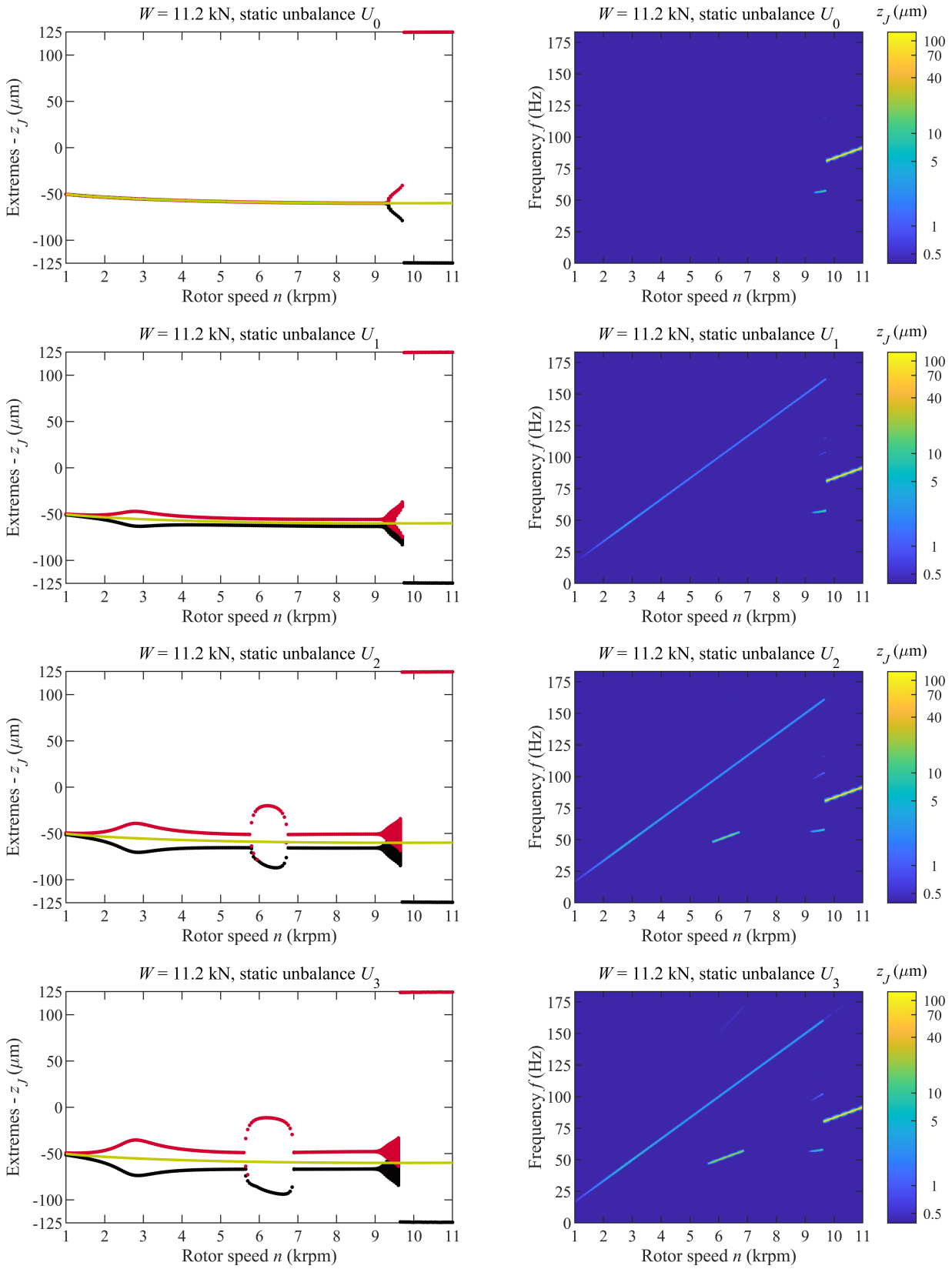

Fig. 5.20: Bifurcation diagrams and spectrograms of the nonlinear steady-state horizontal response to harmonic excitation by various static unbalances and static load 11.2 kN. The hydrodynamic forces are evaluated using the IScor model

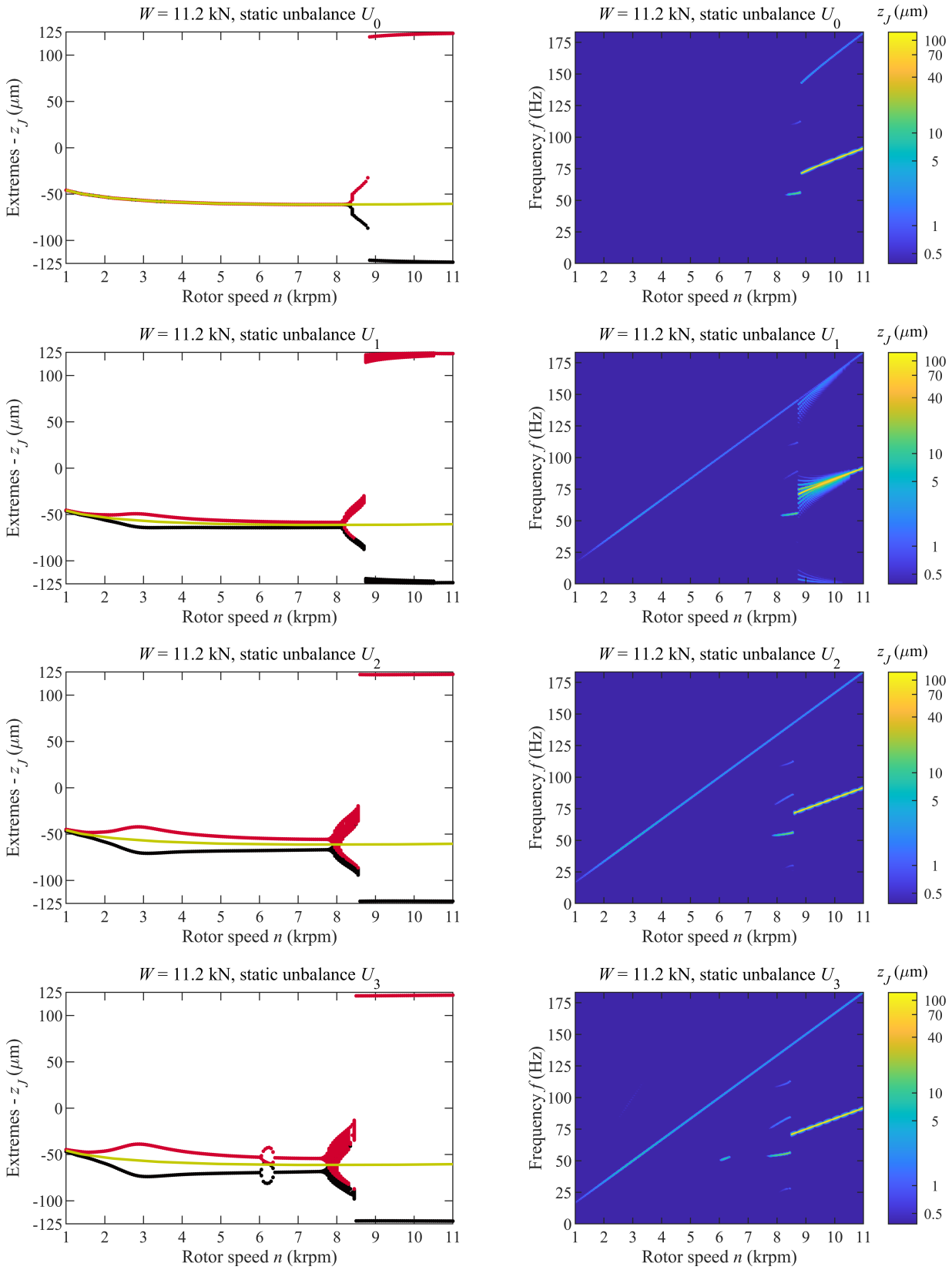

Fig. 5.21: Bifurcation diagrams and spectrograms of the nonlinear steady-state horizontal response to harmonic excitation by various static unbalances and static load 11.2 kN. The hydrodynamic forces are evaluated using the finite difference method

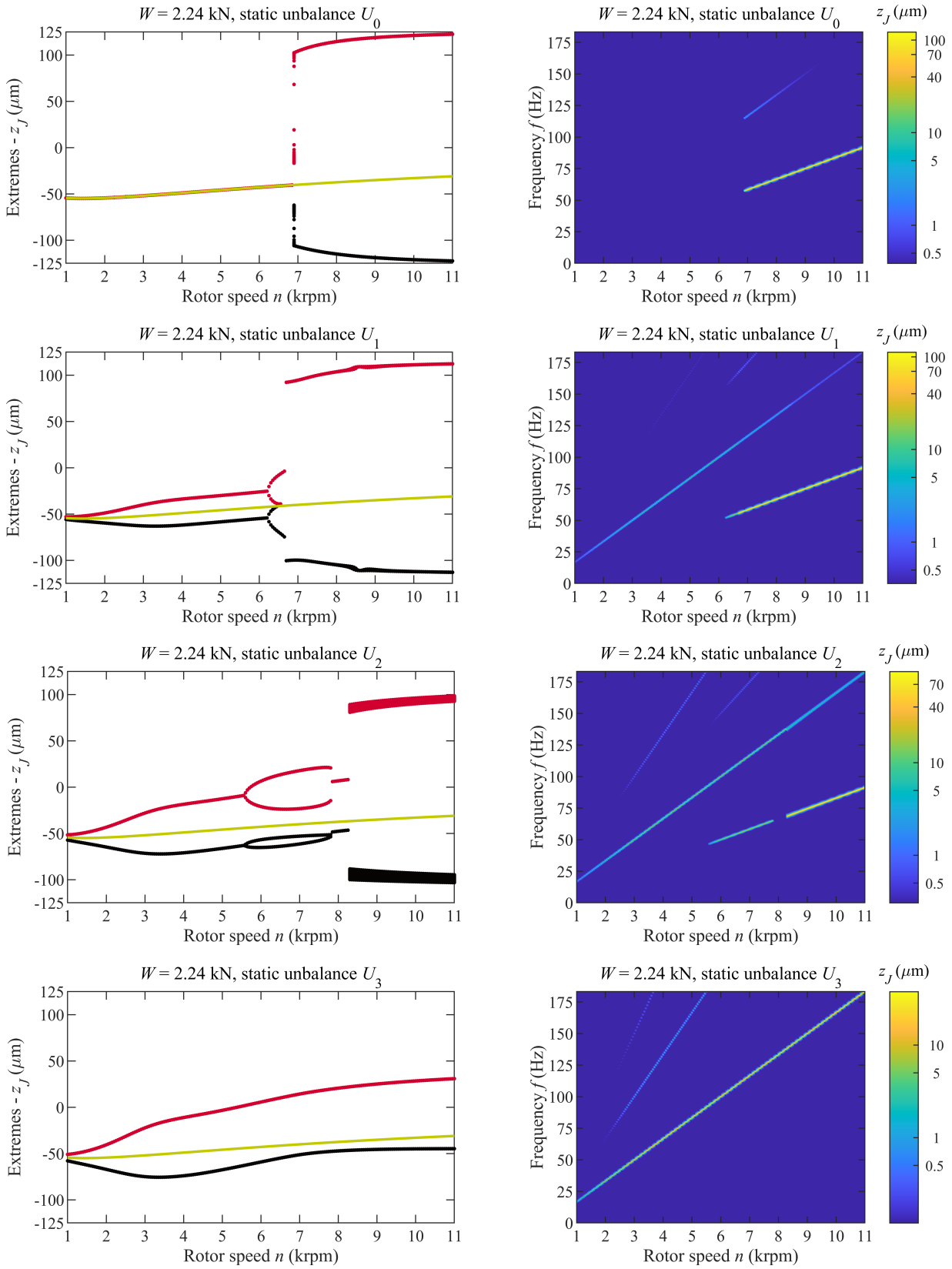

Fig. 5.22: Bifurcation diagrams and spectrograms of the nonlinear steady-state horizontal response to harmonic excitation by various static unbalances and static load 2.24 kN. The hydrodynamic forces are evaluated using the IS model

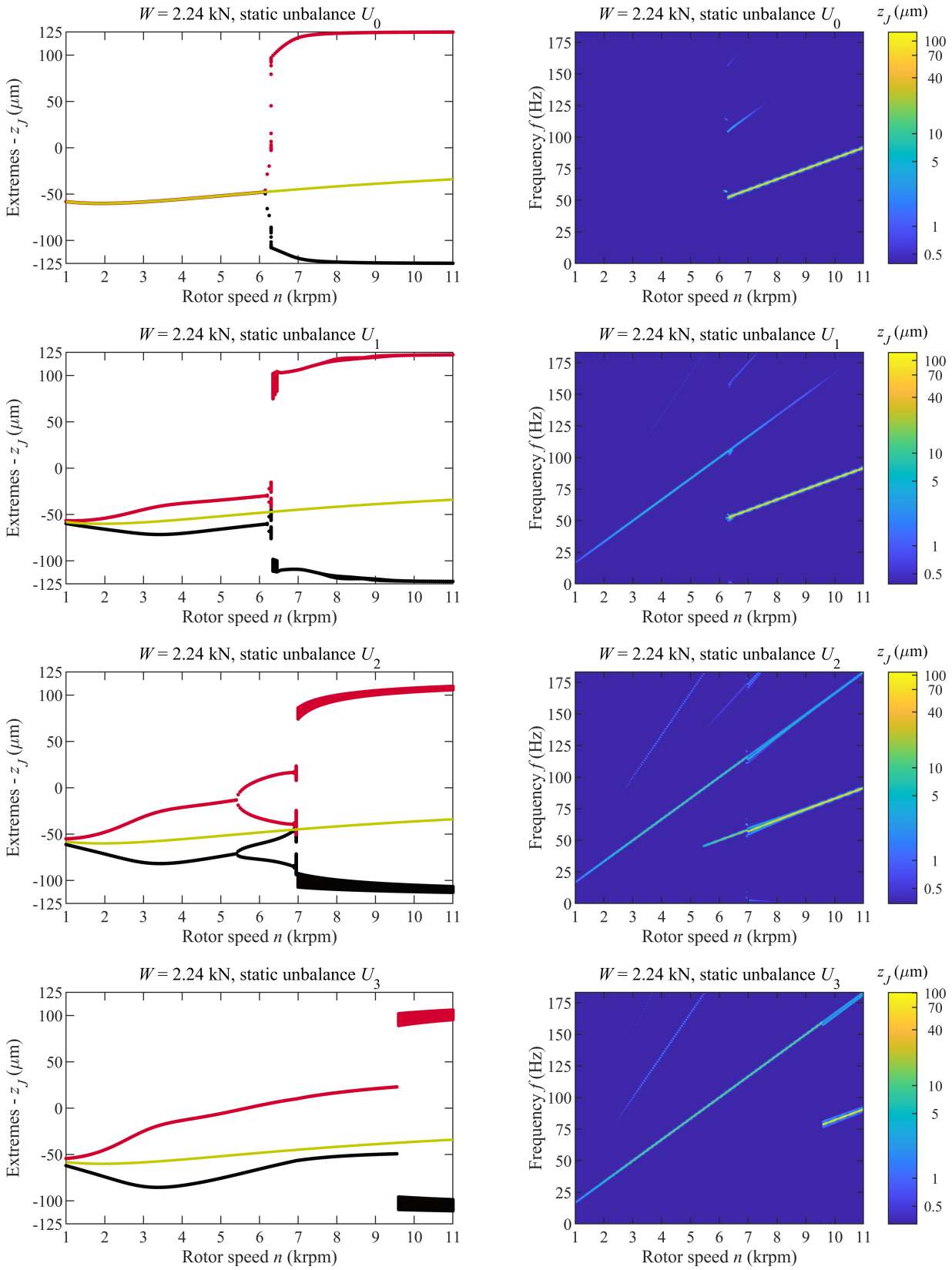

Fig. 5.23: Bifurcation diagrams and spectrograms of the nonlinear steady-state horizontal response to harmonic excitation by various static unbalances and static load 2.24 kN. The hydrodynamic forces are evaluated using the IScor model

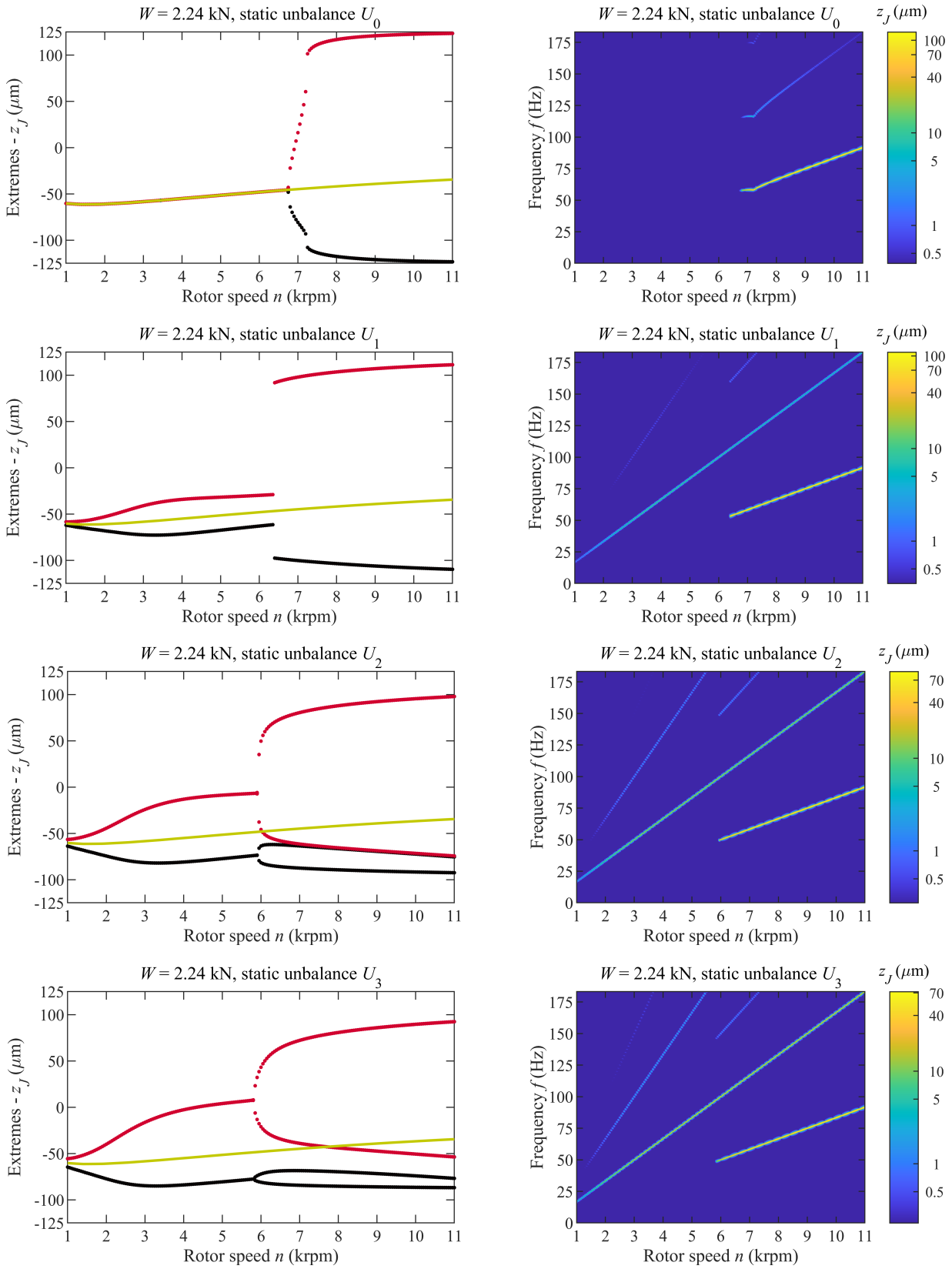

Fig. 5.24: Bifurcation diagrams and spectrograms of the nonlinear steady-state horizontal response to harmonic excitation by various static unbalances and static load 2.24 kN. The hydrodynamic forces are evaluated using the finite difference method

6 Fixed-profile journal bearings

The fixed-profile journal bearings with properly designed bearing shell preload or/and offset can reduce the destabilising effect introduced by the tangential hydrodynamic forces (or cross-coupling stiffness). This chapter is focused on the modelling of elliptical (lemon) and offset halves bearings based on the generalised mathematical model described in detail in Chap. 3. First, the parameters of the considered 2 DoF rotor-bearing system are introduced in Sec. 6.1. Then, validation of computational model implementation is provided in Sec. 6.2. Next, the influence of bearing preloads and offsets on the journal behaviour is examined using the static analysis and the dynamic response on the out-of-balance force in Sec. 6.3, respectively in Sec. 6.4. Finally, the conclusions are summarised in Sec. 6.5.

6.1 Test bearings

A simple 2 DoF rigid rotor-bearing system with various static unbalances is assumed. The parameters of considered elliptical (cases 1–2) and offset halves (cases 3–4) journal bearings with two axial grooves in the horizontal dividing plane are written in Tab. 6.1 and Tab. 6.2. Assumed static bearing loads refer to the different mass of supported rotor on the fixed-profile journal bearings. The investigated system is described by equations of motion in forms (3.5)–(3.6).

Developed software in MATLAB presented for cylindrical bearings was generalised for fixed-profile journal bearings applications. The in-house software is based on the finite difference method used for hydrodynamic pressure calculation and hydrodynamic force evaluation with assumed Gümbel cavitation condition. MATLAB `fsolve` function with the Levenberg-Marquardt algorithm was employed for static analysis. The solution of ordinary differential equations was performed using `ode15s` solver for stiff problems with relative error tolerance 10^{-6} and absolute error tolerance 10^{-8}. The tolerances were set based on the convergence tests.

Parameter	Symbol	Value	Unit
Journal radius	R_J	49.875	mm
Bearing shell radius	R	50	mm
Bearing length	L	50	mm
Rotor speed	n	1000 – 14000	rpm
Lubricant dynamic viscosity	μ	0.02	Pa·s
Ambient and supply pressure	p_{amb}	0	Pa
Journal static load	W_i	2.24, 11.2	kN
Journal static unbalance	U_i	0, 3435, 6870	g·mm

Tab. 6.1: Parameters of the studied fixed-profile bearings, adopted from [38]

Parameter	Case 1	Case 2	Case 3	Case 4
Assembled radial clearance (μm)	62.5	93.75	62.5	93.75
Bearing shell angle (deg)	170	170	170	170
Bearing shell preload (μm)	62.5	31.25	0	0
Bearing shell offset (μm)	0	0	62.5	31.25

Tab. 6.2: Parameters considered during case studies, adopted from [38]

6.2 Model validation

Results of static analysis obtained for case 1 (Tab. 6.2) using developed in-house software were validated by reference data [38]. The reference data include static equilibrium points (relative eccentricity and attitude angle) and stiffness and damping coefficients.

The results of static equilibrium points for various static bearing loads are depicted in Fig. 6.1. Journal relative eccentricity and attitude angle are transformed to the Cartesian coordinates and shown versus the dimensionless Sommerfeld number calculated based on (5.6). The static equilibrium points are particularly overcovered because some of the operating condition parameters yield to the same Sommerfeld number. The solid yellow line represents the results for lightly loaded bearing (W_1) and the blue dashed line shows the results for the higher bearing load (W_2). The absolute errors between calculated and adopted reference data from [38] are significant but still reasonable up to ca. 6 μm in the horizontal direction mainly for a lower Sommerfeld number, i.e. lightly loaded bearing or heavy rotor operating at higher rotor speeds. However, the differences in the vertical journal positions are almost negligible, with the maximum error lower than ca. 0.75 μm. The journal is pushed away from the bearing vertical axis of symmetry and the static equilibrium locus is more elliptical than the reference locus.

Linearised stiffness $\overline{k}_{ij}$ and damping $\overline{b}_{ij}$ coefficients determined in the static equilibrium points are depicted in Fig. 6.2 for the reference data and case 1 with both static loads W_1 and W_2. The coefficients were transformed into dimensionless quantities based on (2.28) and the vertical axes were restricted for better results interpretation. The nominal differences between

the results are minor. The occurred jumps in the calculated data obtained by the finite difference method are analysed and discussed in Sec. 5.2. The most significant differences are apparent for diagonal coefficient $\overline{k}_{zz}$. These quantitative discrepancies are caused by different horizontal journal positions in the corresponding static locus compared to the reference locus, see Fig. 6.1.

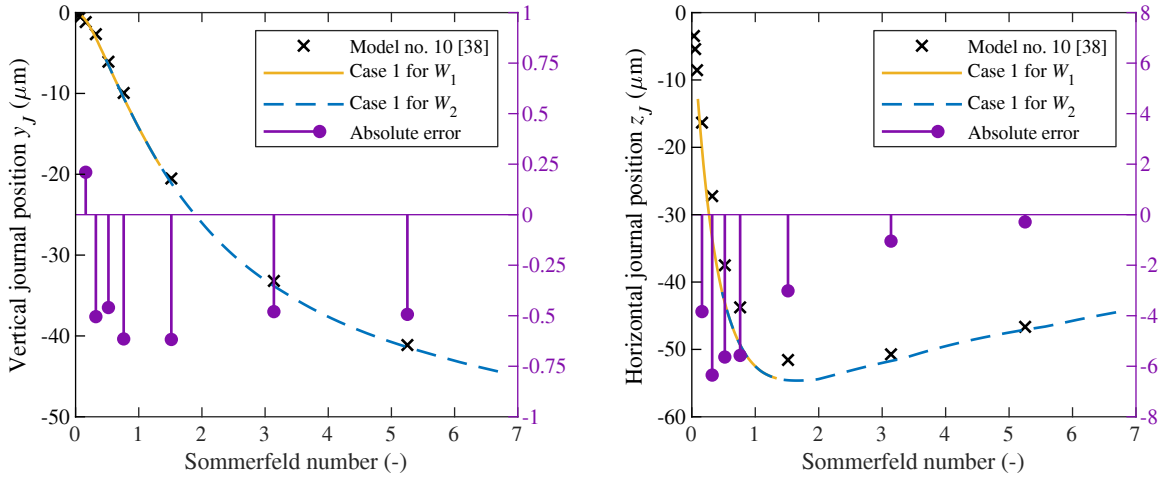

Fig. 6.1: Journal relative eccentricity and attitude angle for case 1 with various static loads

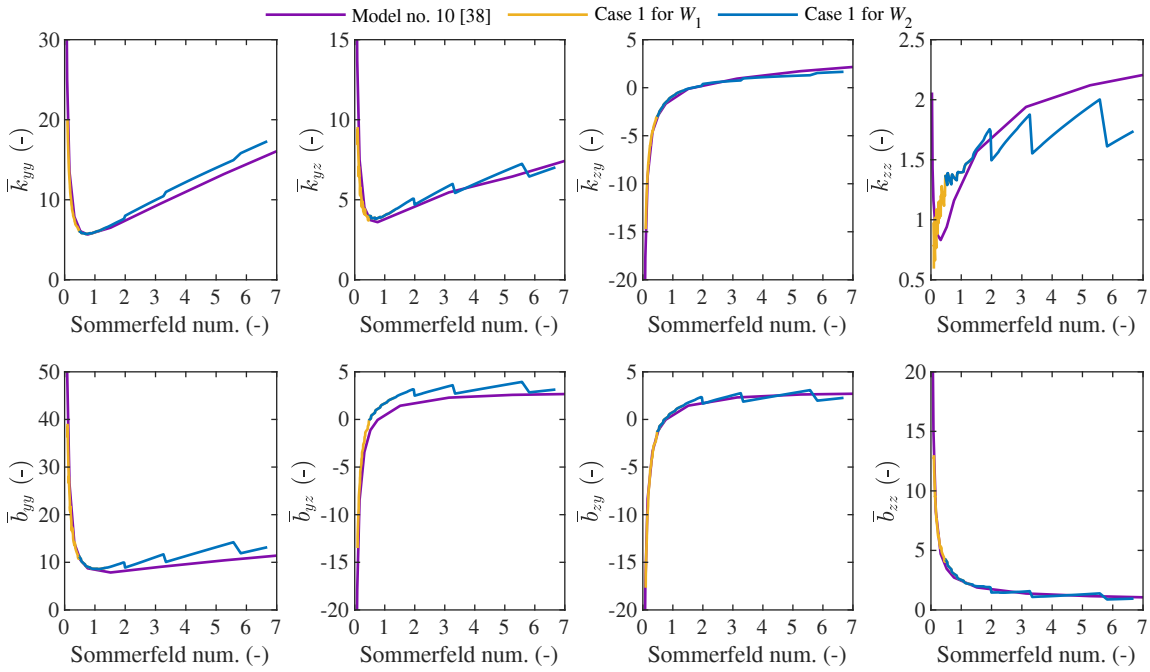

Fig. 6.2: Dimensionless linearised stiffness and damping coefficients for case 1

6.3 Static analysis

The static analysis results for all considered cases 1–4 and both static journal loads are depicted in Fig. 6.3. The force balance solved during the analysis consists only of static journal loads and the hydrodynamic force with omitted all the time-dependent terms. Each subfigure depicts by black line the assembled clearance of elliptical and offset bearing with various preloads and offsets.

Different journal static loads are distinguished by the solid yellow line for lightly loaded bearing and the blue dashed line for higher static journal load. The black crosses depict the start and the end of each equilibrium locus. The equilibrium loci are particularly overcovered due to similar Sommerfeld numbers.

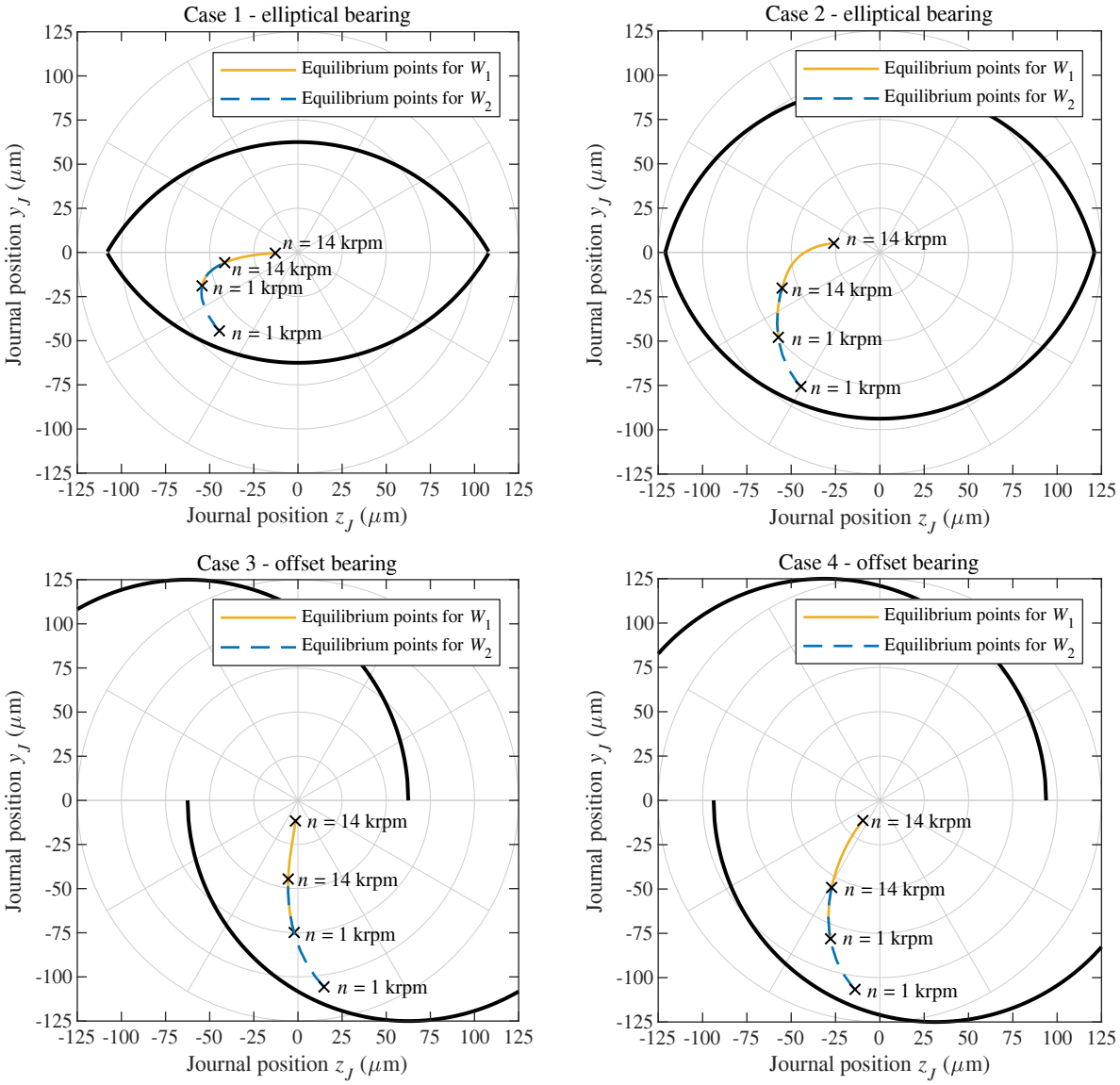

Fig. 6.3: Static equilibrium points for cases 1–4 and various static journal loads

In the case of elliptical bearing with smaller preload (case 2), the lightly loaded journal crosses the horizontal dividing axis compared to case 1 and cylindrical plain journal bearings investigated in Chap. 5.

The excessive offset (horizontal preload) in the offset bearing (cases 3–4) causes the journal trajectory to be more vertically straight with increasing rotor speed. There is a significant contribution of the horizontal hydrodynamic force from the pressure field covering the upper shell for the lightly loaded journal operating at higher rotor speed. If the journal is close to the bearing centre, the horizontal hydrodynamic force generated from the pressure field at the upper and bottom shells are almost equal and the resulting trajectory is close to vertical.

6.4 Dynamic analysis

The nonlinear steady-state responses of the system (cases 1–4) to harmonic excitation due to applied static unbalances from Tab. 6.1 were simulated for 10 s. Parameters of the investigated systems are written in Tab. 6.1 and Tab. 6.2. Particular simulations were performed in the listed range of rotor speed with speed-step 50 rpm, and the transient response to the initial conditions (estimated equilibrium points and zero initial velocity) in time interval $t \in \langle 0, 5 \rangle$ s was omitted. The presented results are depicted for each case study in Fig. 6.4 – Fig. 6.9 in the form of bifurcation diagrams – local maxima (red), local minima (black) and static equilibrium points (yellow) – and spectrograms in the logarithmic scale in the range 2.5 decades. The spectrograms were created using tool `autofft` [92]. Each figure contains the results for both static journal loads and all considered static unbalances.

6.4.1 Case 1

The results for the elliptical bearing with characteristic dimensionless preload 0.5 are summarised in Fig. 6.4. For applied zero static unbalance U_0, the self-excited (fluid-induced) instability appears for the heavily loaded bearing at a higher rotor speed 12400 rpm compared to 11000 rpm for the lightly loaded bearing. Interestingly, the invoked oscillations have different subsynchronous components: ca. 0.51X for the lightly loaded bearing and ca. 0.36X for the heavily loaded one. Applied out-of-balance force corresponding to static unbalances U_1 and U_2 on the lightly loaded journal have significant impact on the response with apparent period-doubling bifurcation occurring at 9550 rpm respectively 10900 rpm.

For the heavily loaded unbalanced journal, the response is quasiperiodic after surpassing the threshold speed. The quasiperiodic motion disappears and changes to 11-periodic motion when rotor speed 13400 rpm is reached for the static unbalance U_2. The journal trajectories (orbits) with corresponding Poincaré maps are shown for chosen rotor speeds in Fig. 6.5. The simulation time was extended up to 40 s for chosen rotor speeds to visualise the Poincaré maps of obtained orbits. Above mentioned 11-periodic motion is depicted for 13700 rpm.

Although the maximum vertical assembled clearance is 62.5 μm, journal oscillations magnitude apparent from the bifurcation diagrams remain under 30 μm in the whole investigated speed range for all considered journal static loads and static unbalances.

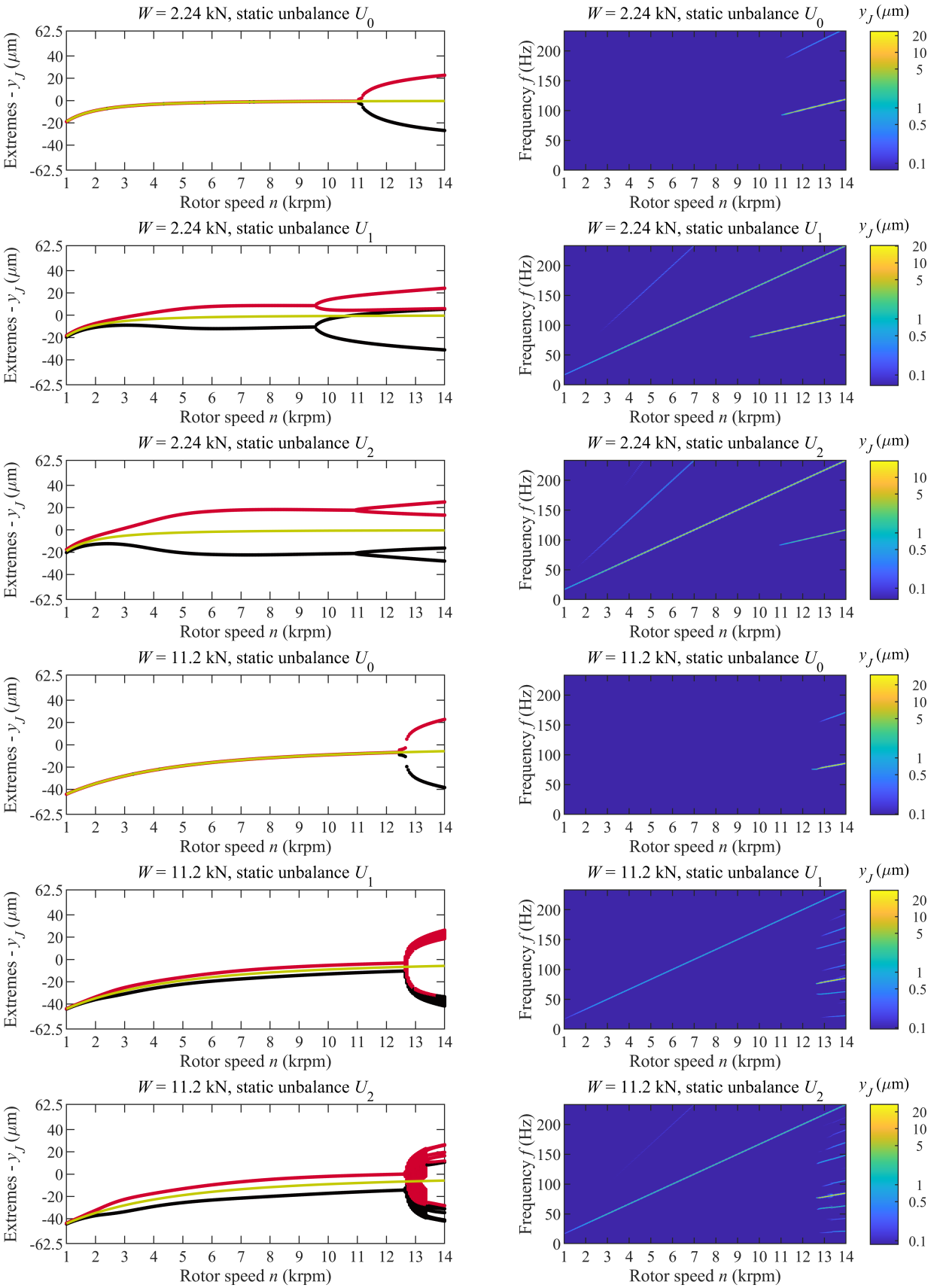

Fig. 6.4: Case 1 – Bifurcation diagrams and spectrograms of the vertical response to harmonic excitation by various static unbalances and both static loads

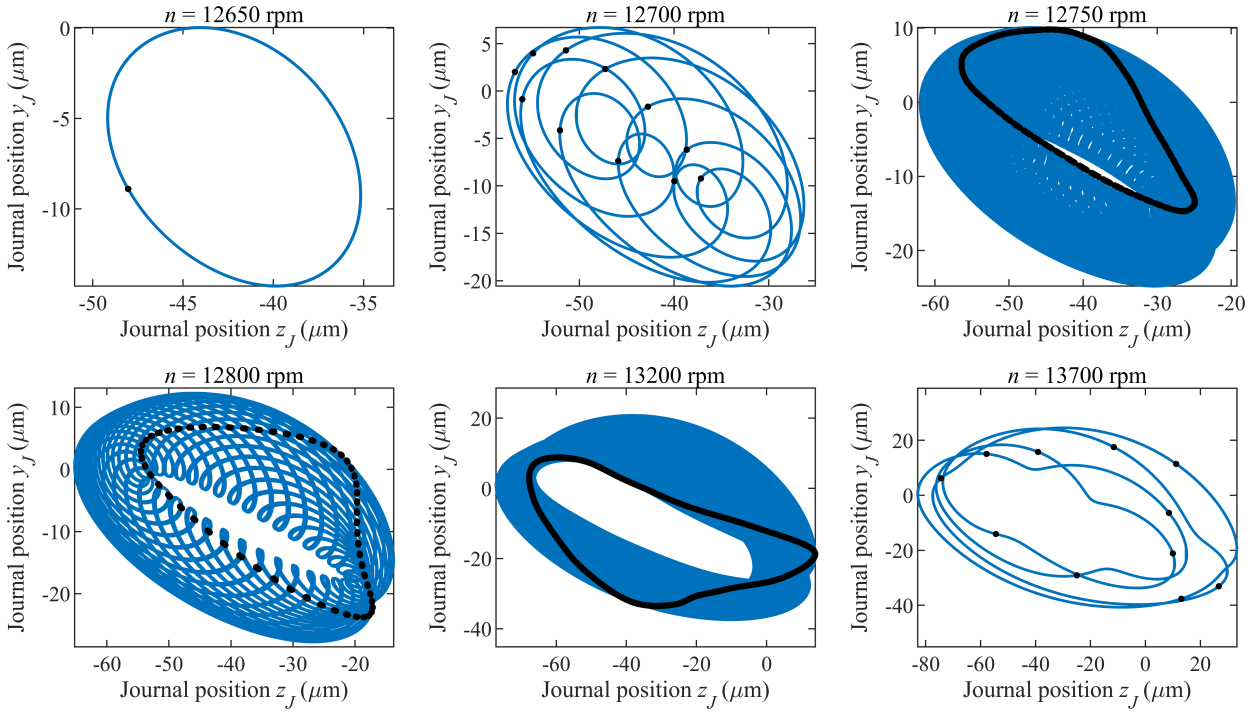

Fig. 6.5: Case 1 – Journal orbits and Poincaré maps (black points) for static load 11.2 kN and static unbalance U_2

6.4.2 Case 2

The elliptical bearing with dimensionless preload 0.25 has a lower stabilising effect than bearing with excessive preload (case 1), see Fig. 6.6. The fluid-induced instability of a perfectly balanced rotor occurs at 8400 rpm for the lightly loaded bearing and 6950 rpm for the heavily loaded bearing. Contrary to the constant subsynchronous component 0.5X for the lightly loaded bearing, the subsynchronous component for the heavily loaded bearing is variable in the range ca. 0.42X–0.47X with increasing rotor speed. Period-doubling bifurcation appears for lightly loaded bearings due to applied out-of-balance force. The multiple period-doubling is visible at 12650 rpm for static unbalance U_2.

Similar to case 1, the heavily loaded journal response to harmonic excitation is quasiperiodic after surpassing the threshold speed. The quasiperiodic motion has a dominant subsynchronous variable component in the range ca. 0.42X–0.47X corresponding to unstable orbital motion. However, there are apparent (mainly for unbalance U_2) irregular changes from the quasiperiodic motion to N-periodic motion and vice versa. The quasiperiodic motion disappears at 12500 rpm and the new branch of the 2-periodic limit cycle is found for static unbalance U_2. Qualitative changes of the response distinguishable from the bifurcation diagram are emphasised by Poincaré maps for chosen rotor speeds shown in Fig. 6.7. There is a short period-doubling bifurcation around 6000 rpm for unbalanced rotor U_2. This phenomenon was also observed in the cylindrical bearings with a highly unbalanced journal in Sec. 5.6.

The journal vertically oscillates almost over the entire assembled bearing gap compared to the bearing with an excessive preload.

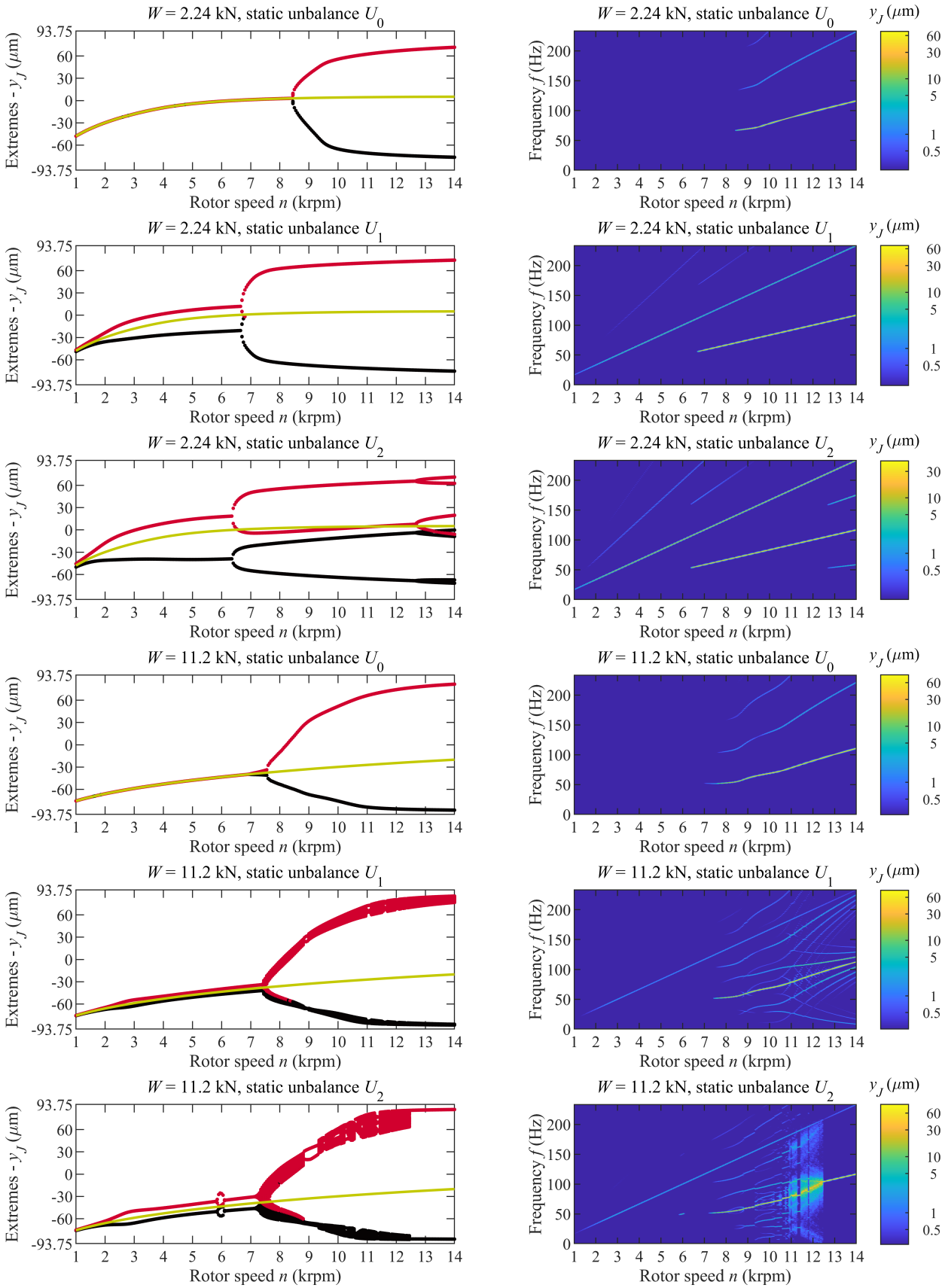

Fig. 6.6: Case 2 – Bifurcation diagrams and spectrograms of the vertical response to harmonic excitation by various static unbalances and both static loads

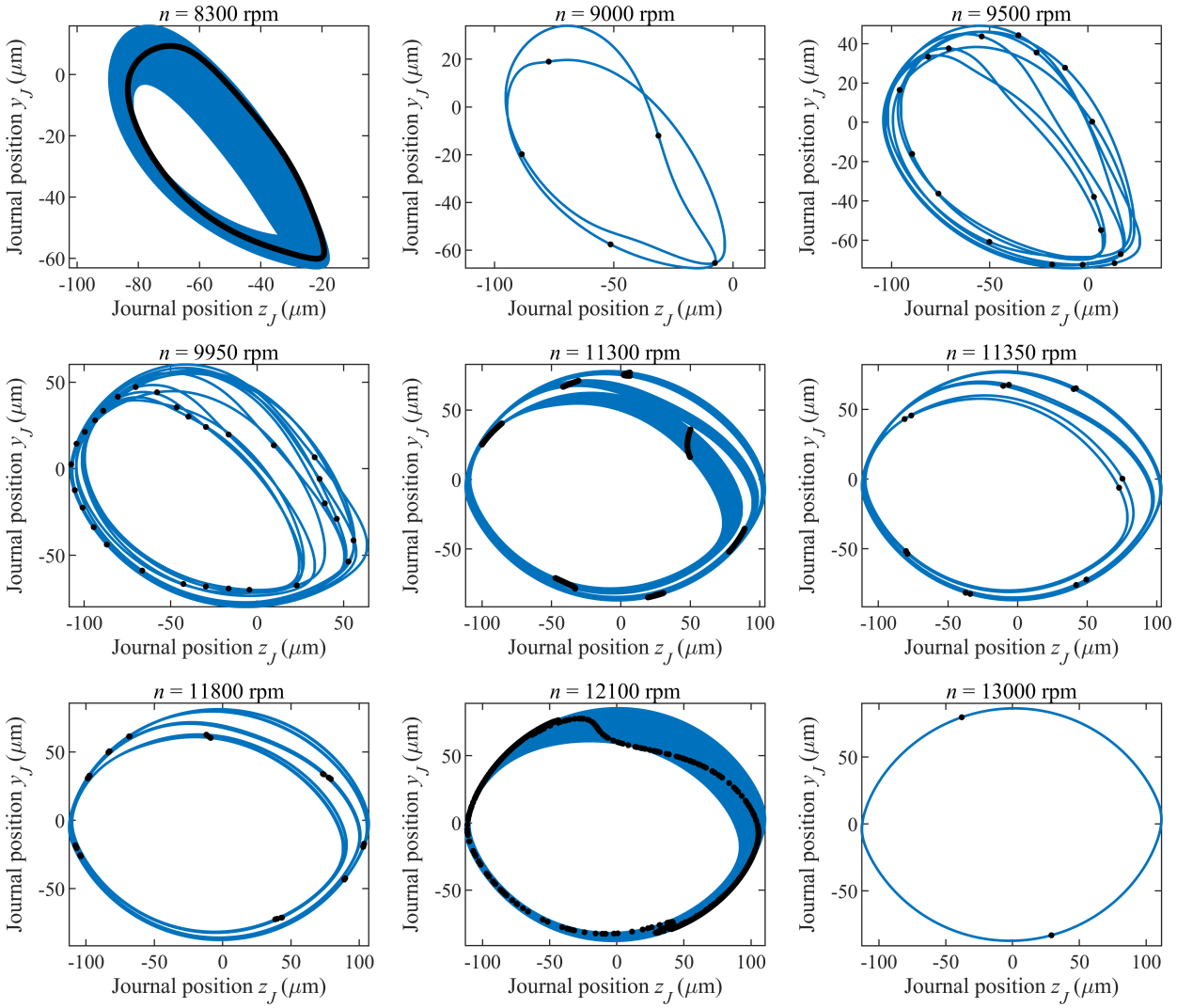

Fig. 6.7: Case 2 – Journal orbits and Poincaré maps (black points) for static load 11.2 kN and static unbalance U_2

6.4.3 Case 3

The lightly loaded rotor supported on the offset halves bearing with excessive horizontal offset is stable in the whole considered speed range, see Fig. 6.8. Thus, fluid-induced instability is not developed either if out-of-balance excitation is applied. As a result, visible oscillations have only harmonic 1X component corresponding to the excitation frequency.

In the case of heavily loaded bearing, the self-excited vibrations start to develop at 9150 rpm. The motion is characterised by a subsynchronous component that changes linearly with increasing rotor speed from ca. 0.34X to 0.4X of rotor speed. Subsynchrounous component in this range was also studied in [93]. Response of the unbalanced rotor is quasiperiodic after surpassing the threshold speed. Then, the quasiperiodic motion changes to the 3-periodic motion at 13450 rpm for static unbalance U_2. The period-doubling bifurcation due to out-of-balance force present is developed around 7000 rpm.

Excessive horizontal offset causes the same way as in case 1 that the journal horizontally oscillates only up to ca. 60 % of the maximum assembled clearance.

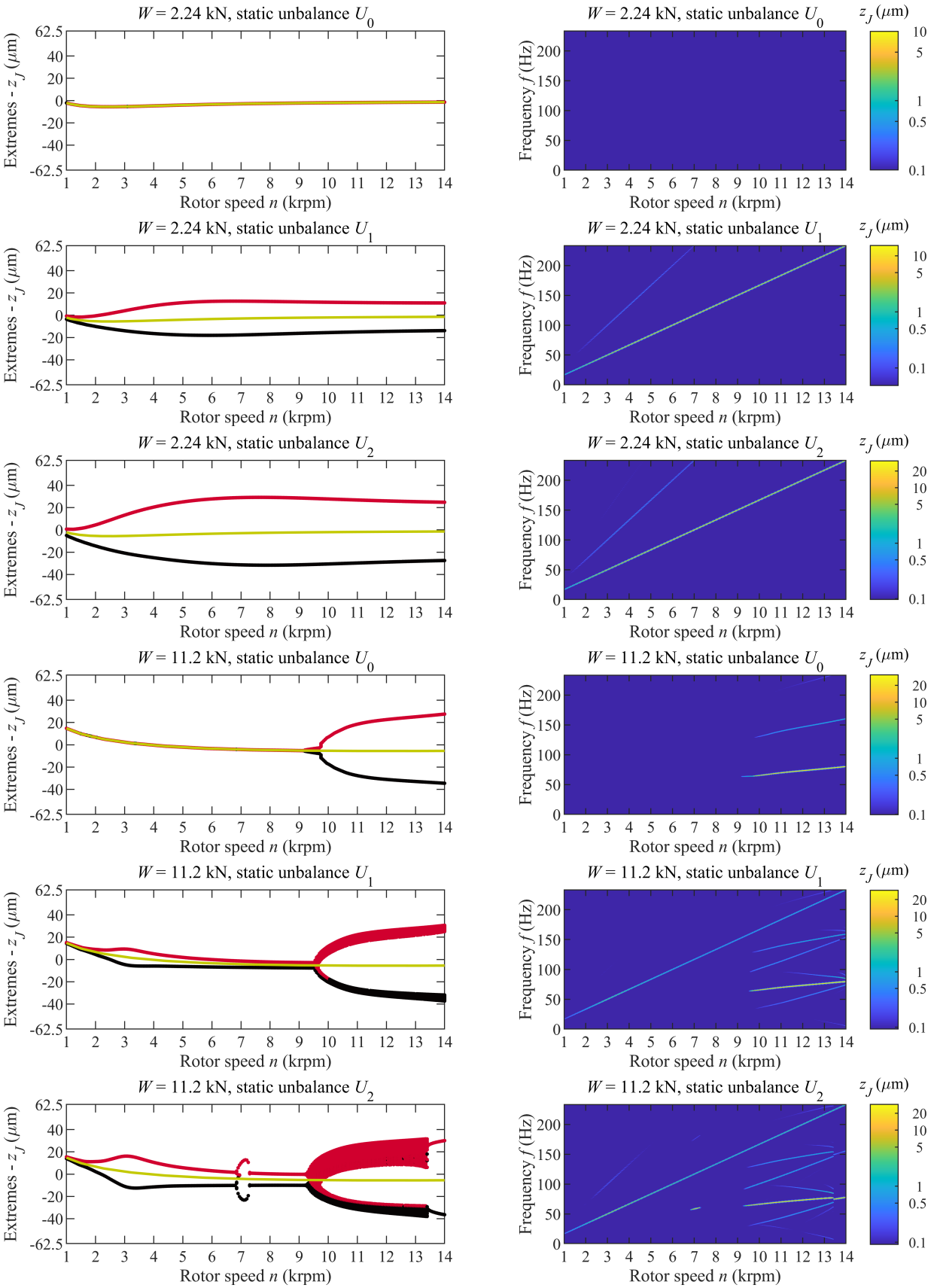

Fig. 6.8: Case 3 – Bifurcation diagrams and spectrograms of the horizontal response to harmonic excitation by various static unbalances and both static loads

6.4.4 Case 4

The results of the steady-state dynamic response of the rotor supported on the offset bearing with dimensionless offset 0.25 are depicted in Fig. 6.9. Contrary to case 3, the perfectly balanced lightly loaded rotor-bearing system with offset bearing loses stability at 7900 rpm. In addition, applying out-of-balance force causes period-doubling bifurcation at a higher rotor speed than the established threshold speed.

Interestingly, the self-excited vibrations of a perfectly balanced heavy rotor start to develop at a similar rotor speed (7850 rpm) as in the case of the lightly loaded offset bearing. Similarly to previous cases, the journal response to the harmonic excitation is quasiperiodic after surpassing the threshold speed. For applied static unbalance U_2, there is an apparent period-doubling bifurcation between 6000–6500 rpm.

6.5 Results summary

The general approach for modelling complex bearing systems introduced in Chap. 3 was simplified to analyse the fixed-profile journal bearings, specifically elliptical and offset halves journal bearings.

The in-house software created by the author in MATLAB was validated with reference data of elliptical journal bearings with parameters adopted from [38]. The validation yields similar journal vertical equilibrium points results and linearised stiffness and damping coefficients as reference data. Differences in the horizontal equilibrium points were more significant but still reasonable.

Next, validated software was further used to perform the static and dynamic analyses of considered cases with various preloads and offsets. In addition, two different static bearing loads with corresponding rotor mass were assumed. Finally, the steady-state journal response was simulated for a perfectly balanced rotor and chosen static unbalances. The results are shown in the form of bifurcation diagrams, spectrograms and Poincaré maps visualising particular results. Based on the performed analyses, the results can be summarised as follows:

- The lightly loaded journal crosses the horizontal dividing plane of the elliptical journal bearing with a smaller preload for higher rotor speed.
- The journal trajectory in the offset bearing with excessive offset is rather vertical than elliptical. In addition, this bearing has the most stabilising effect because the fluid-induced instability was observed only for the heavily loaded bearing.
- Excessive preload and offset cause the journal to not perform the orbital motion over the entire bearing assembled clearance when the fluid-induced instability is developed, neither if out-of-balance is applied.
- The response of the heavy rotor to harmonic excitation is quasiperiodic after surpassing the established threshold speed. Therefore for cases 1–3, there are apparent changes between a quasiperiodic motion to N-periodic motion and vice versa.

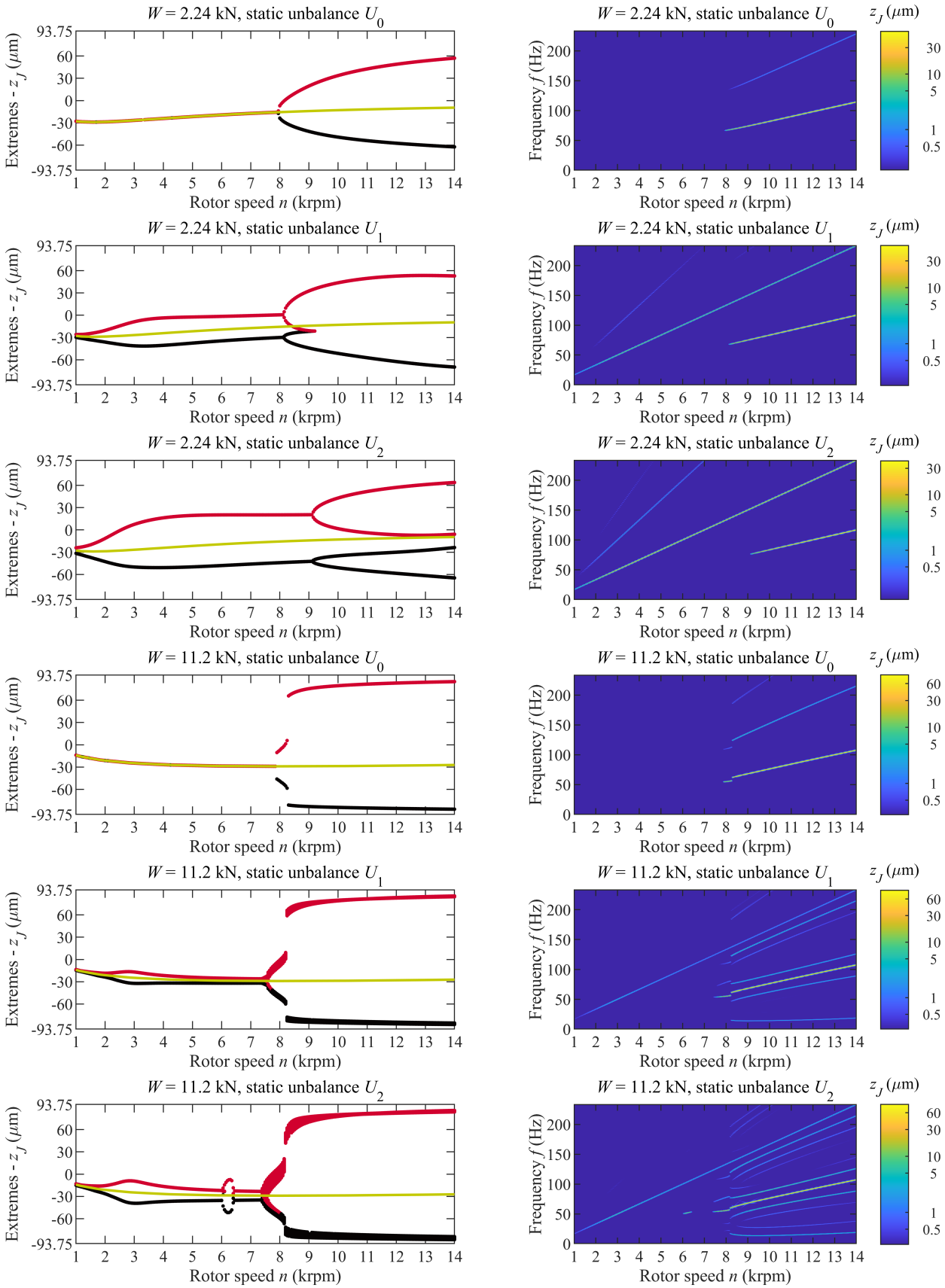

Fig. 6.9: Case 4 – Bifurcation diagrams and spectrograms of the horizontal response to harmonic excitation by various static unbalances and both static loads

7 Tilting pad journal bearing

This chapter is focused on the detailed investigation of the nonlinear dynamics of four segment tilting pad journal bearing (TPJB) employing mathematical model derived in Chap. 3. First, chosen tilting pad journal bearing is introduced in Sec. 7.1. Then, validation of model implementation is provided in Sec. 7.2. Results of static analysis are shown in Sec. 7.3. Next, demonstration and analysis of the bearing behaviour under out-of-balance excitation are performed in Sec. 7.4. Finally, conclusions are summarised in the last Sec. 7.5.

7.1 Test bearing

Four-segment TPJBs in a load-between pads (LBP) configuration have two upper pads which are almost unloaded during operation, and thus they might be susceptible to pad fluttering. Here, the TPJB adopted from [44] presented in Fig. 7.1 and Tab. 7.1 is studied. This TPJB has low Reynolds and reduced Reynolds numbers which render turbulence and fluid inertia effects negligible [20, 94]. Further, it is assumed that the supported rotor is rigid to avoid phenomena resulting from rotor elasticity. In such a case, the rotor has only 2 DoF (horizontal and vertical displacements), and equations of motion can be formally written in the form (3.5)–(3.9).

The computational model was implemented in MATLAB in developed in-house software. For the solution of nonlinear algebraic equations during the process of static equilibrium points determination, `lsqnonlin` function with the Levenberg-Marquardt algorithm was employed. The solution of a set of ordinary differential equations was performed using `ode15s` solver for stiff problems with relative error tolerance 10^{-6} and absolute error tolerance 10^{-8} based on the convergence tests. The solution strategy and the order of calculation steps inside of the used solver are described in detail in Appendix B. Hydrodynamic pressure calculation and hydrodynamic force evaluation is performed using the finite difference method.

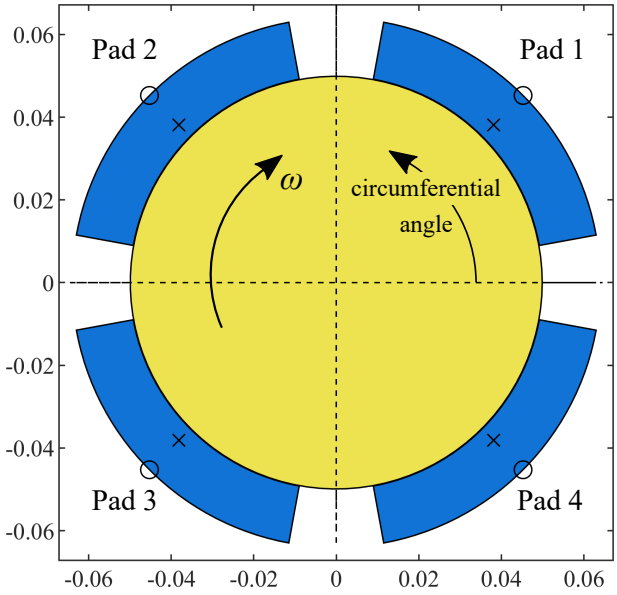

Fig. 7.1: A scheme of the TPJB studied in cases 1–4 [44]. Pivots are situated at 45, 135, 225 and 315 deg (measured from the horizontal axis). Pads centres of mass are denoted by crosses (x) and pivots by circles (o)

Parameter	Value	Unit
Journal radius	49.9	mm
Journal weight (static load)	19.6	kN
Journal static unbalance	$5 \cdot 10^{-3}$	$\mathrm{kg} \cdot \mathrm{m}$
Maximum speed	13000	rpm
Pad inner radius	50	mm
Pad axial length	100	mm
Pad thickness	14	mm
Pad material density	8400	$\mathrm{kg} \cdot \mathrm{m}^{-3}$
Pivot radius	64	mm
Pivot ratio	0.5	
Lubricant dynamic viscosity	$19 \cdot 10^{-3}$	$\mathrm{Pa} \cdot \mathrm{s}$
Lubricant density	860	$\mathrm{kg} \cdot \mathrm{m}^{-3}$
Ambient and supply pressure	0	Pa
Reynolds number [20]	307.3	
Reduced Reynolds number [94]	0.62	

Tab. 7.1: Parameters of the studied TPJB, adopted from [44]. The pivot ratio is the fraction of the distance between the leading edge and the pad pivot point to the complete pad arc length

Parameter	Val. 1	Val. 2	Case 1	Case 2	Case 3	Case 4
Assembled radial clearance (μm)	100	50	100	100	80	100
Pad angle (deg)	80	80	69.3	69.3	69.3	69.3
Pad inner radius (mm)	50	50	50	50.025	50	50
Pad preload (μm)	0	50	0	25	20	0
Pivot radial stiffness (N·m^{-1})	rigid	rigid	rigid	rigid	rigid	$1{\cdot}10^9$

Tab. 7.2: Parameters considered during case studies, adopted from [38, 44]

7.2 Model validation

The proposed model was validated by comparing the computed journal static equilibrium points with reference data adopted from [38].

Fig. 7.2a and Fig. 7.2b compare the computed results with the reference data transformed into dimensional quantities. The absolute errors are almost negligible in both validation cases. The maximum error 0.44 μm was found at 3940 rpm for validation case 1.

Corresponding pad tilting angles are shown in Fig. 7.2c and Fig. 7.2d. Reference data [38] do not include pad tilting angles for direct comparison. However, the tilting angles of the preloaded pads from Fig. 7.2d correspond well with the results presented in [95]. A notable difference in the tilting angle of pad 1 is due to no preload in validation case 1. If pad 1 is unpreloaded, it assumes the position depicted in Fig. 1.1, in which the gap between the journal and the pad is diverging. The hydrodynamic pressure is then predominantly determined by the boundary conditions. Here, the pressure is zero due to the zero boundary conditions and the tilting angle of the pad is restricted only by contact forces.

Typical pressure distributions at the individual pads are depicted in Fig. 7.3. The pressure distributions in validation case 1 (Fig. 7.3a) are described more in detail:

- Pad 1 is unloaded, and the pressure distribution is determined predominantly by the boundary conditions. The tilting angle of the pad is restricted by the elastic forces described by (3.12) and (3.13).
- Two peaks are formed close to the trailing edge of pad 2. The pressure distribution on this is symmetric with respect to $Z_i = 0$.
- The pressure distribution on bottom pads 3 and 4 are similar. The pressure peaks lie approximately in the centre of the pad surface. The maximum pressure is considerably higher than on pad 2 because the bottom pads support most of the applied static load. The load capacity of the bottom pads is almost equal.

Naturally, the maximum pressure at individual pads differs with the rotor speed and the pad preload. When the pad preload is increased, the pressure distribution on pads 1 and 2 further develops as shown in Fig. 7.3b, where new pressure fields form on upper pads. Pressure on the upper pads is distributed similarly to the bottom pads, but its maximum is an order of magnitude lower than on the bottom pads. These pressure distributions correspond well with the results presented in [95].

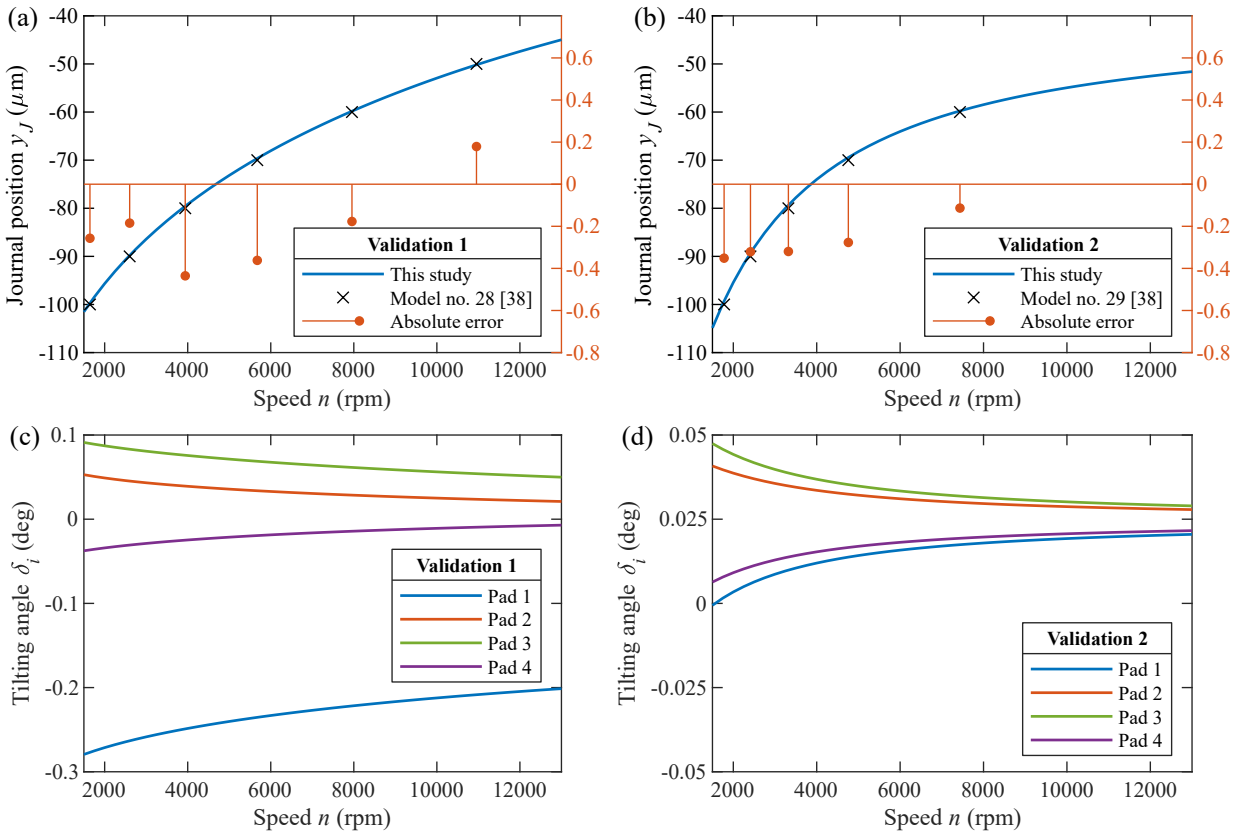

Fig. 7.2: Journal eccentricity and tilting angles of the pads for validation cases 1 and 2

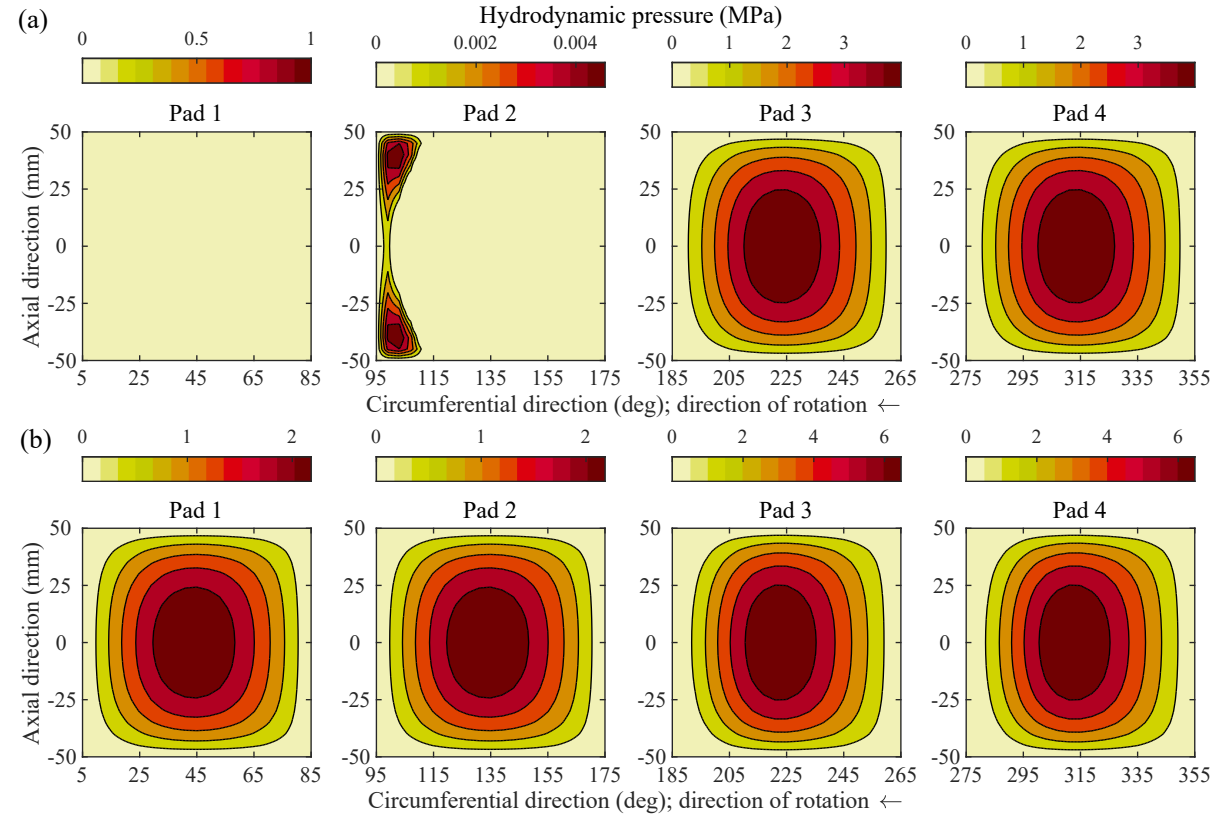

Fig. 7.3: Pressure distributions on the pads for validation cases 1 (a) and 2 (b) at rotor speed 5000 rpm

7.3 Static analysis

The analysis of the journal and pad equilibrium points provides essential information about the bearing operating eccentricity, and it is a reasonable estimation of static gaps during run-ups and coast-downs. In the static analysis, all the time-dependent terms in the hydrodynamic forces are neglected as well as inertial, out-of-balance and damping forces. For cases 1–3, a system of equations (3.5)–(3.7) with a total 6 DoF $(2+4\cdot1)$ was solved. In case 4, the system of equations was extended by (3.8) and the number of DoF raised to 10 $(2+4\cdot2)$. The results of the analysis are depicted in Fig. 7.4.

The left part of this figure depicts the bearing equilibrium locus for cases 1–4. The static equilibrium points are shown for each 500 rpm from the investigated speed range. Tilting angles of the individual pads depending on the rotor speed are shown in the figure's right part. In all cases, the tilting of the pads allows for the journal eccentricity to exceed the assembled bearing clearance at low rotor speeds. This phenomenon is the most significant in case 4 where the radial flexibility of pivot mounting is assumed, see Fig. 7.4. In the TPJBs with the flexible pivots in the LBP configuration, the bottom pads are radially compressed out of the bearing centre and then tilted according to the load direction.

Furthermore, the bearing equilibrium loci are almost vertical in all cases which corresponds well with [38]. It suggests that the direct stiffness is dominant over the cross-coupling stiffness at most rotor speeds. The only deviation was observed in case 3 (preloaded pads with the reduced assembled clearance), where the bearing equilibrium locus starts to follow the elliptic trajectory after reaching approximately 11000 rpm, see detail in Fig. 7.4c. This change is caused due to a significant change in the pressure field distribution on pad 2, which starts pushing the journal horizontally away from the bearing's centerline.

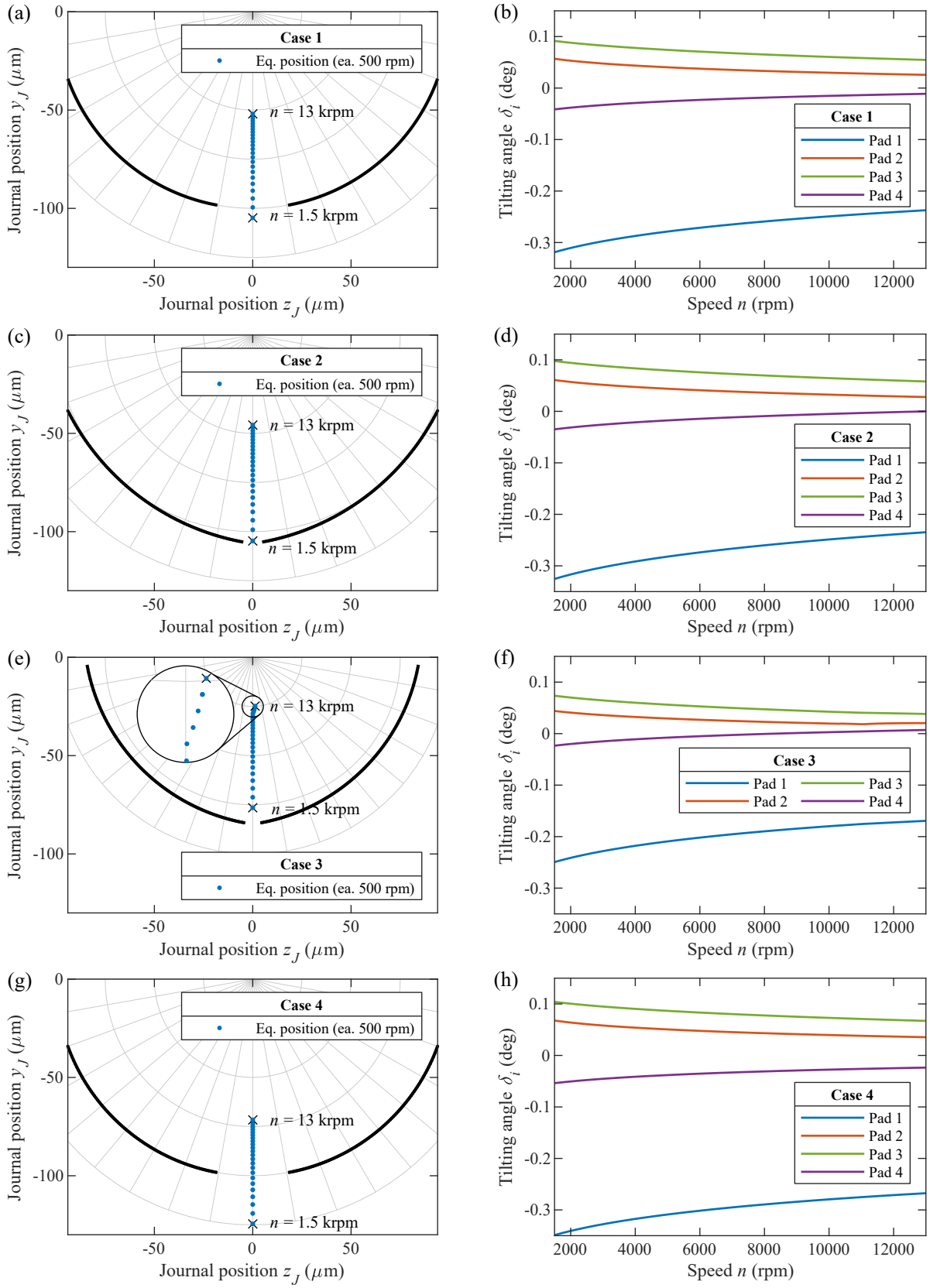

Fig. 7.4: Results of static analysis of load cases 1–4 defined in Tab. 7.2. Pads on the left side of this figure are in untilted configuration and are depicted only for illustration of the assembled radial clearances and pad preloads

7.4 Analysis of the TPJB dynamics

The response of the system to the out-of-balance force is analysed in the range of rotor speeds $n \in \langle 1500, 13000 \rangle$ rpm with the speed-step 100 rpm. The results of the static analysis are used as initial conditions for simulations, and the equations of motion are solved at each speed for $t \in \langle 0, 10 \rangle$ s. The interval $t \in \langle 0, 5 \rangle$ s is omitted because some simulations contain the transient response to the initial conditions up to 4 s long. The rest of the results is then analysed as follows:

- The motions of the journal and all four pads are analysed using the fast Fourier transform in tool `autofft` [92] and the results are depicted as spectrograms. This diagram allows identifying qualitative changes in the response with changing rotor speed. The spectrograms are depicted in Figs. 7.5, 7.9, 7.11, 7.13 and 7.14.

- For more precise insight into the dynamic behaviour of the system, bifurcation diagrams are constructed in Figs. 7.6, 7.10, 7.12, 7.15 and 7.16. These diagrams depict local extremes at the particular rotor speed employing different colours for local maxima (red) and minima (black). The figures also include static equilibrium points (yellow). The bifurcation diagrams help to analyse the steady-state response and distinguish between regions with periodic, quasiperiodic and chaotic motions.

- Fig. 7.7a shows the evolution of phase portraits of the pad tilting motion with the increasing rotor speed. The phase portraits use the results calculated with extended time interval $t \in \langle 0, 20 \rangle$ s.

- For a better interpretation of the phase portraits, the largest Lyapunov exponents $\lambda_{\max}$ of the corresponding motions are estimated using the procedure proposed in [96]. This analysis was performed in cooperation with Ing. Luboš Smolík, Ph.D. The magnitude of $\lambda_{\max}$ quantifies the mean exponential rate of divergence or convergence of neighbouring orbits in phase space [96]. In terms of information theory, $\lambda_{\max}$ defines a rate at which the future behaviour of the time series cannot be predicted based on the initial state [96]. Hence, $\lambda_{\max}$ is expressed in bits/s.

  - $\lambda_{\max} < 0$ suggests that the time series corresponds with a fixed point trajectory.
  - $\lambda_{\max} = 0$ marks the marginally stable time series, which suggest the existence of a limit cycle, a limit torus or a similar trajectory.
  - $\lambda_{\max} > 0$ indicates the nontrivial and potentially chaotic time series. Although high magnitudes of $\lambda_{\max}$ suggest chaotic nature of the attractor, its exact form depends on other Lyapunov exponents. It was demonstrated in [96] that $\lambda_{\max} > 0$ can correspond with either the strange attractor, chaos or hyperchaos.

- Furthermore, the snapshots visualised in Fig. 7.8 contain pad tilting angles and acting moments developed due to impacts or the hydrodynamic forces. A sign convention of the acting moments corresponds to the pad angle orientation depicted in Fig. 3.2.

7.4.1 Case 1

The dominant response of the journal and bottom pads 3 and 4 is synchronous (1X), see Fig. 7.5. The 1X component is caused due to the out-of-balance force. The second harmonic (2X) is also present, but approximately two orders of magnitude smaller than 1X. The 2X component stems from the nonlinearity of the system, and it is also caused due to the out-of-balance force.

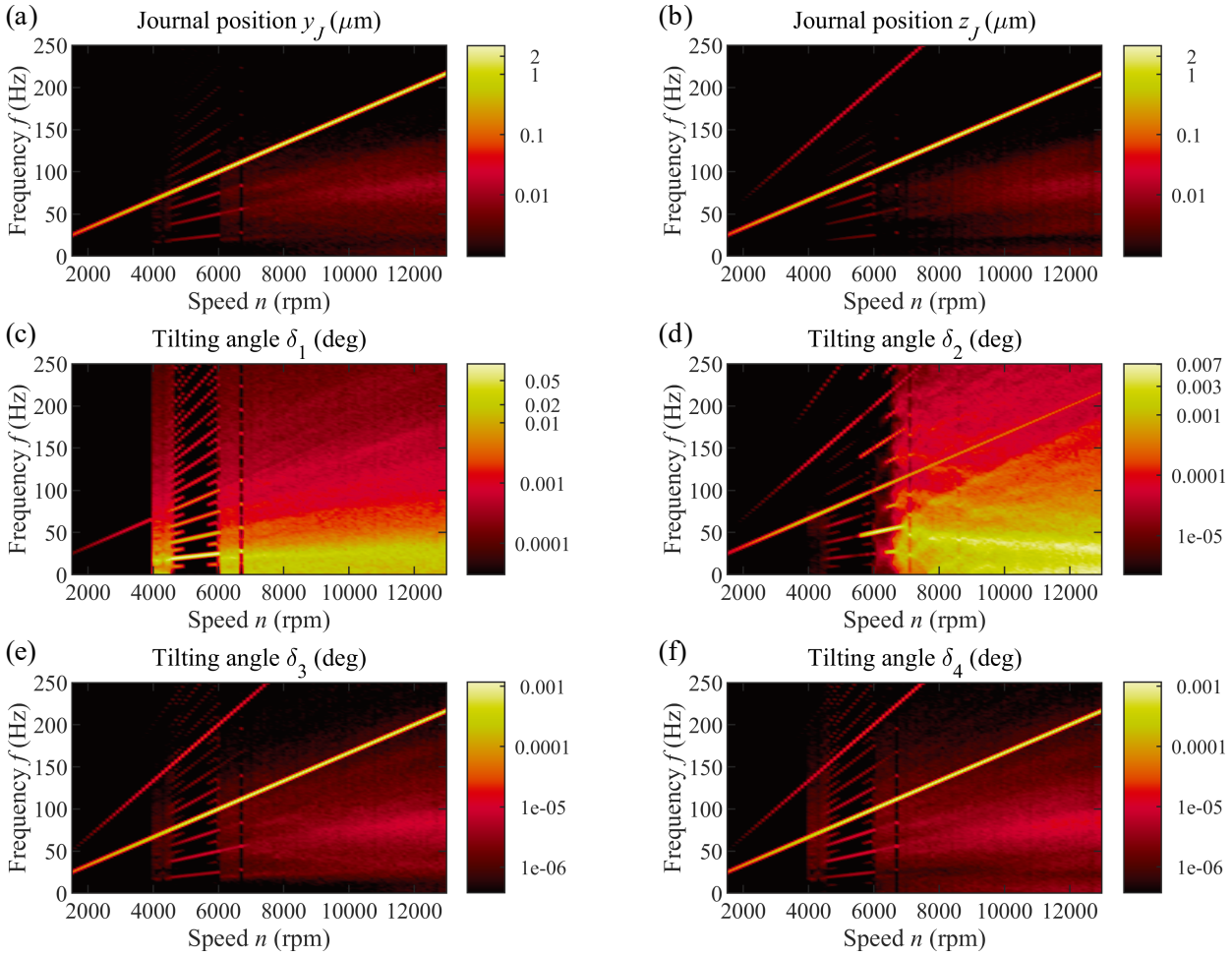

Fig. 7.5: Case 1 – Spectrograms of the nonlinear steady-state response to harmonic excitation of TPJB without preload

The response of upper pads 1 and 2 differs significantly from the response of the bottom pads.

The motion of pad 1 can be classified as chaotic almost in the whole investigated speed range. The chaotic nature of this motion arises from repeated single-sided impacts of the pad's edge to the journal. At lower speeds (4000 rpm), a single-sided contact occurs, while for increasing rotor speed, the pad hits the journal in two sections of its phase trajectory in Fig. 7.7a. This observation is confirmed by depicted time series in the left column of Fig. 7.8. Increasing rotor vibrations at 4000 rpm induce distinguishable motion of pad 1 due to solid structure impact at the leading edge, see positive moment impulse values. This moment

impulse invokes the pad's tilting motion and causes formation of the hydrodynamic pressure in the convergent bearing gap close to the trailing edge for higher rotor speed. In the case of existing hydrodynamic pressure pressure at the trailing pad half, the moment induced by the hydrodynamic force is applied. A broadband response with maximum magnitudes around 15–20 Hz is dominating in the spectrogram, see Fig. 7.5c. These magnitudes are likely present due to the natural frequency of the system. The 1:4 resonance occurs in the interval 4500–6000 rpm, which is also reflected in estimated Lyapunov exponents in Fig. 7.7c. The estimated Lyapunov exponent at 6000 rpm is considerably higher (1.7 ± 2.01 bit/s) than at 5000 rpm (0.5 ± 0.07 bit/s), suggesting a transient zone (TR) between periodic (PM) and chaotic (CH) motion. This zone is indistinct in the bifurcation diagram in Fig. 7.6c but is noticeable in the spectrogram in Fig. 7.5c.

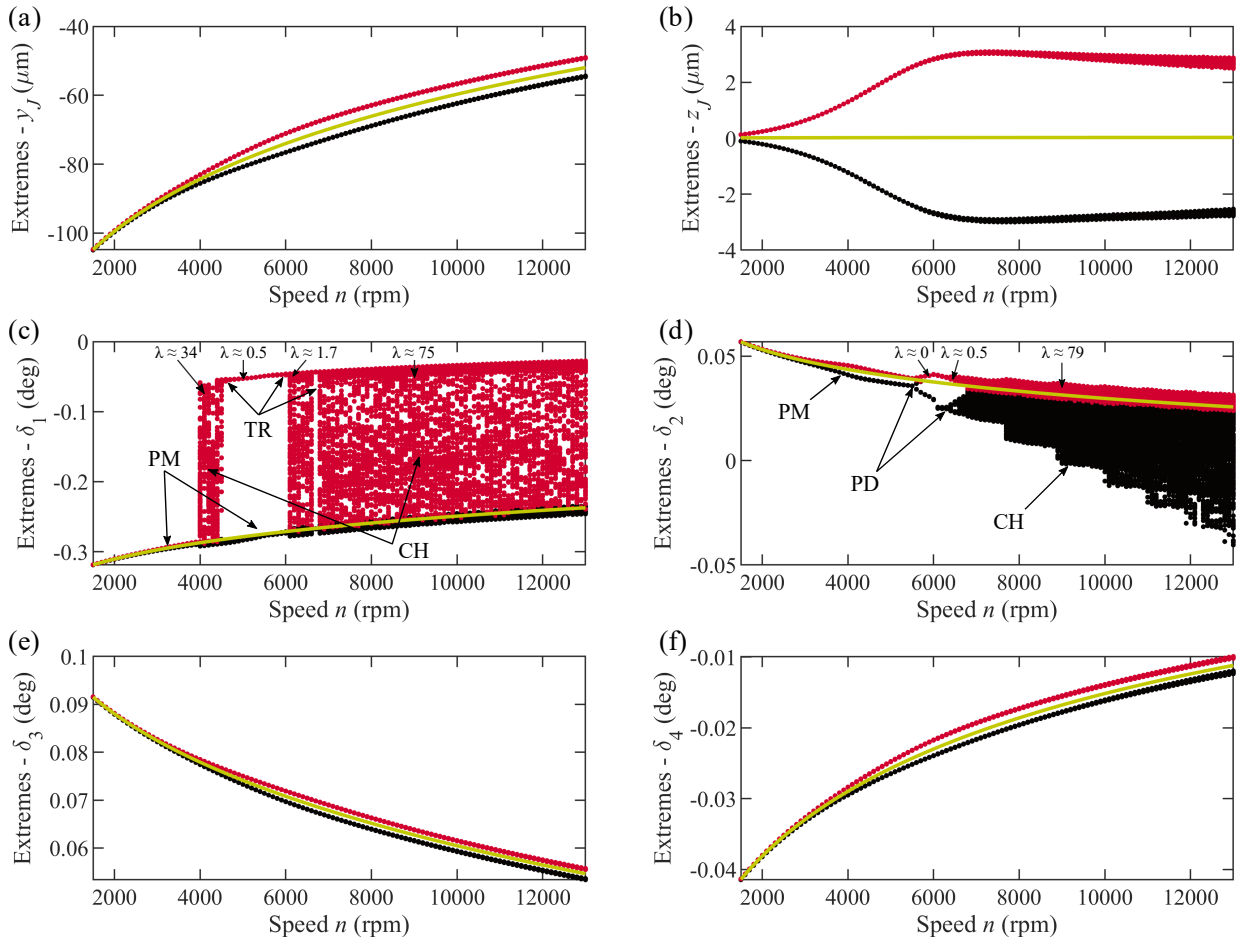

Fig. 7.6: Case 1 – Bifurcation diagrams and static equilibrium points of TPJB without preload

The response of pad 2 can be divided into three main regions with qualitatively different behaviour. At the low rotor speeds, the response is synchronous with negligible harmonics and subharmonics due to the nonlinearity. The period-doubling occurs after approximately 5500 rpm and 6400 rpm. The period-doubling events are apparent from the formation of subsynchronous components 0.5X and 0.25X in spectrogram, see Fig. 7.5d, as well as from the bifurcation diagram depicted in Fig. 7.6d. Period-doubling event is evident from the

phase portrait in Fig. 7.7b at 6500 rpm but corresponding Lyapunov exponent indicate possible quasiperiodic motion rather than a limit cycle. After surpassing 6700 rpm, the pad motion becomes chaotic, see Lyapunov exponents in Fig. 7.7d, with cascading increments in oscillations minima in Fig. 7.6d which depend on the journal position. The synchronous periodic response of lightly loaded pad 2 at lower rotor speed is induced by fluctuating hydrodynamic pressure developed in the trailing pad half due to rotor vibrations. Larger rotor vibrations at higher rotor speeds cause scenarios when the hydrodynamic pressure disappears and the resultant moment equal zero, see Fig. 7.8. Interestingly, small moment fluctuation due to the pressure field change, e.g. in case of 6000 rpm, does not influence pad inclination angle. Contrary to pad 1, the coupling between the journal and pad 2 is still ensured by the hydrodynamic force only and solid structure impact does not occur.

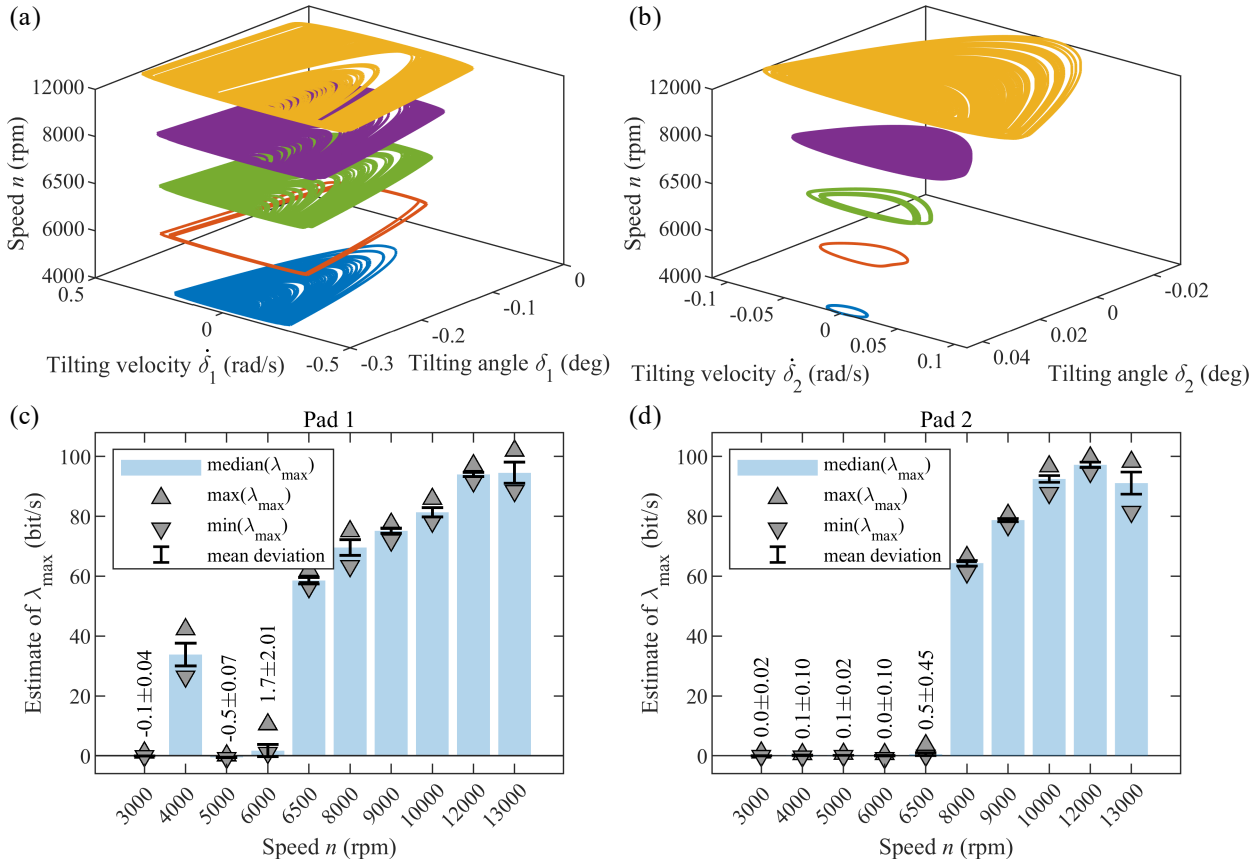

Fig. 7.7: Case 1 – Evolution of phase portraits of pads 1 (a) and 2 (b) with the increasing rotor speed and estimated Lyapunov exponents based on [96]

Based on the performed numerical analyses and presented results, the upper pad's motion can be classified as pad fluttering discussed in [46]–[48]. Classification of the observed subsynchronous self-excited vibration as pad fluttering is motivated by the in-depth time series insight of pad motion.

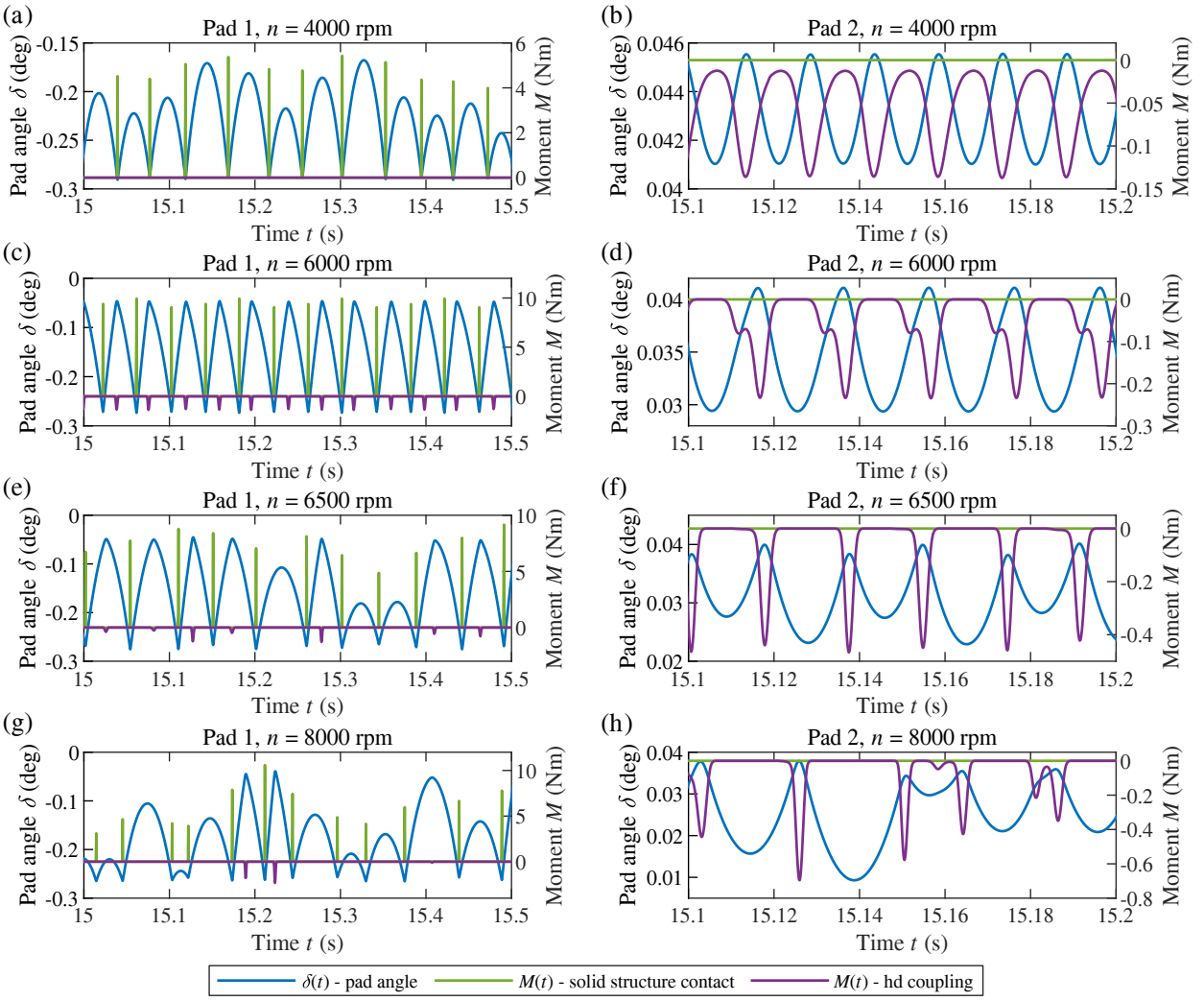

Fig. 7.8: Case 1 – Tilting angles of pads 1 and 2 and nominal moments of elastic and hydrodynamic forces

7.4.2 Case 2

The preloaded set-up in case 2 strengthens the interaction between the subsystems. Although the dominant response of the journal and the bottom pads (3 and 4) is synchronous (1X), Fig. 7.9 shows that asynchronous components appear in all spectrograms. Interestingly, these asynchronous components are a combination of the upper pad responses. The asynchronous components significantly affect the circularity of the journal trajectory in the horizontal direction at higher rotor speed. This phenomenon is further transferred through the oil-films to the oscillations of bottom pads, see Fig. 7.10.

The response of the upper pads can be divided into many different regions which exhibit the period-doubling or chaotic behaviour. The motion of pad 1 irregularly changes from chaotic motion to periodic motion region and vice versa, see Fig. 7.10. These changes occur when the conditions for 1:5 and 1:6 resonances are met.

Analogically to case 1, the motion of pad 2 can be classified as a periodic motion with the distinguishable period-doubling at 5200 rpm and with the additional short period-doubling

at 6100 rpm and 6400 rpm. After surpassing 6600 rpm, the chaotic motion develops. At even higher speeds, the motion is very similar to that of pad 1 and exhibits irregular changes between chaotic behaviour and limit cycles due to internal resonances.

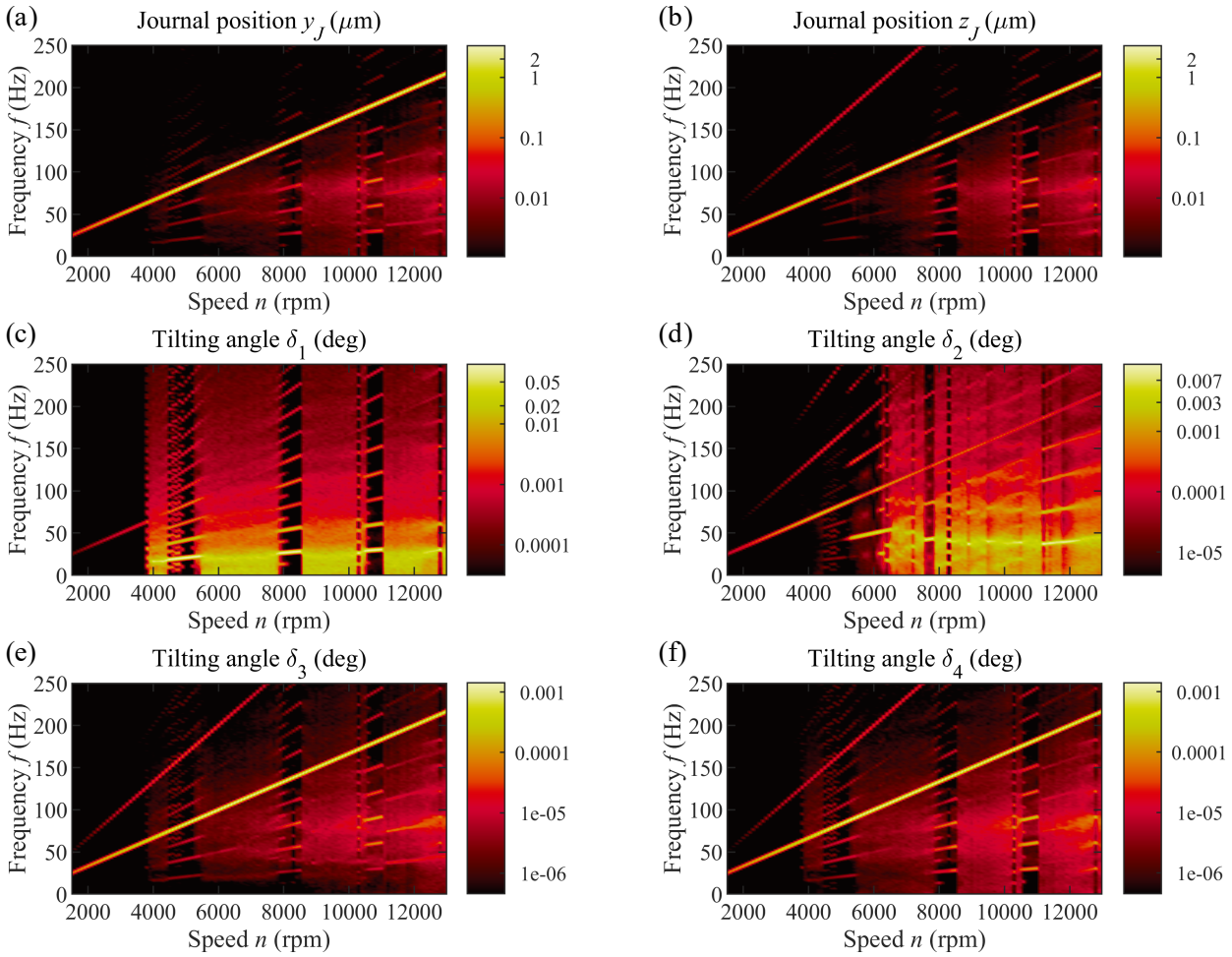

Fig. 7.9: Case 2 – Spectrograms of the nonlinear steady-state response to harmonic excitation of TPJB with preload

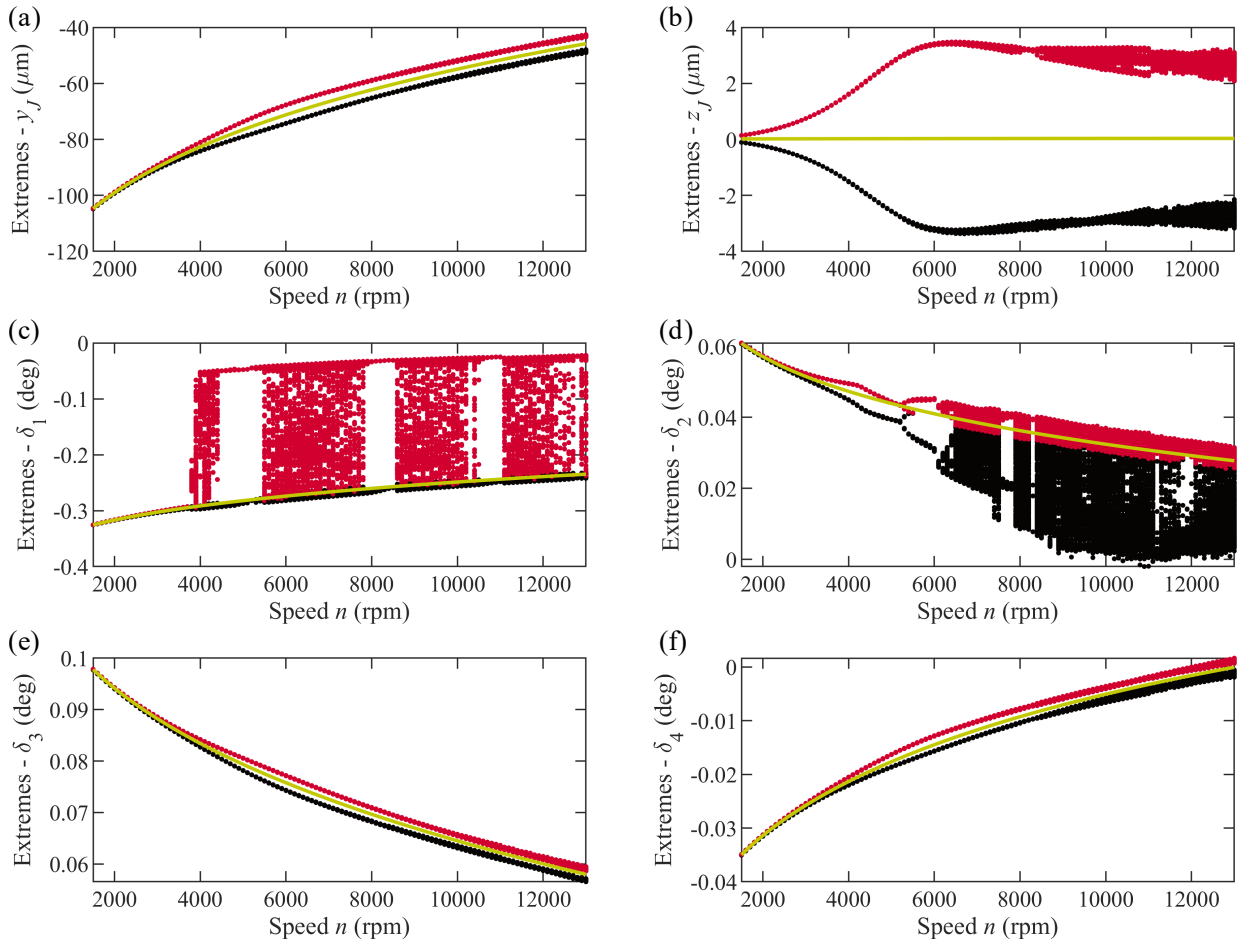

Fig. 7.10: Case 2 – Bifurcation diagrams and static equilibrium points of TPJB with preload

7.4.3 Case 3

Mutual subsystems interaction is more significant due to the decreased assembled clearance than it was observed in case 2, see visible asynchronous components in all spectrograms in Fig. 7.11. Similarly to case 2, upper pad 1 response irregularly changes from chaotic motion to periodic motion region and vice versa after surpassing 4000 rpm. Shaft orbit circularity is also affected at higher rotor speed.

There is a dominant periodic motion of the second pad with period-doubling at 6100 rpm. This observation confirms the statement from [44], where TPJB system with this preload is stable at 6000 rpm compared to case 1 without preload. Another period-doublings exhibit in two regions 6600–7100 rpm and 8000–8400 rpm. Chaotic motion develops after surpassing 8400 rpm and changes between chaotic behaviour and internal resonances 1:5, 1:6 and 1:7 are apparent as well as in the response of the first pad.

The chaotic motion of the upper pads completely disappears at approx. 12000 rpm, see Fig. 7.11. The disappearance of the chaotic behaviour at high speeds can be attributed to the changes in the trajectory of the static equilibrium points, which is described in detail in Sec. 7.3. The bifurcation diagram in Fig. 7.12d shows that the envelopes of the local extremes reflect changes of the static equilibrium points from approx. 11000 rpm. Interestingly, the first

pad's dynamic response differs from the observation based on the static equilibrium analyses. Regarding rotor speeds below 12000 rpm, the limit cycles are formed around the theoretical static equilibrium, since after crossing 12000 rpm, the limit cycle is formed probably around different equilibrium branch, see Fig. 7.12c. This branch was not revealed during the static equilibria analysis.

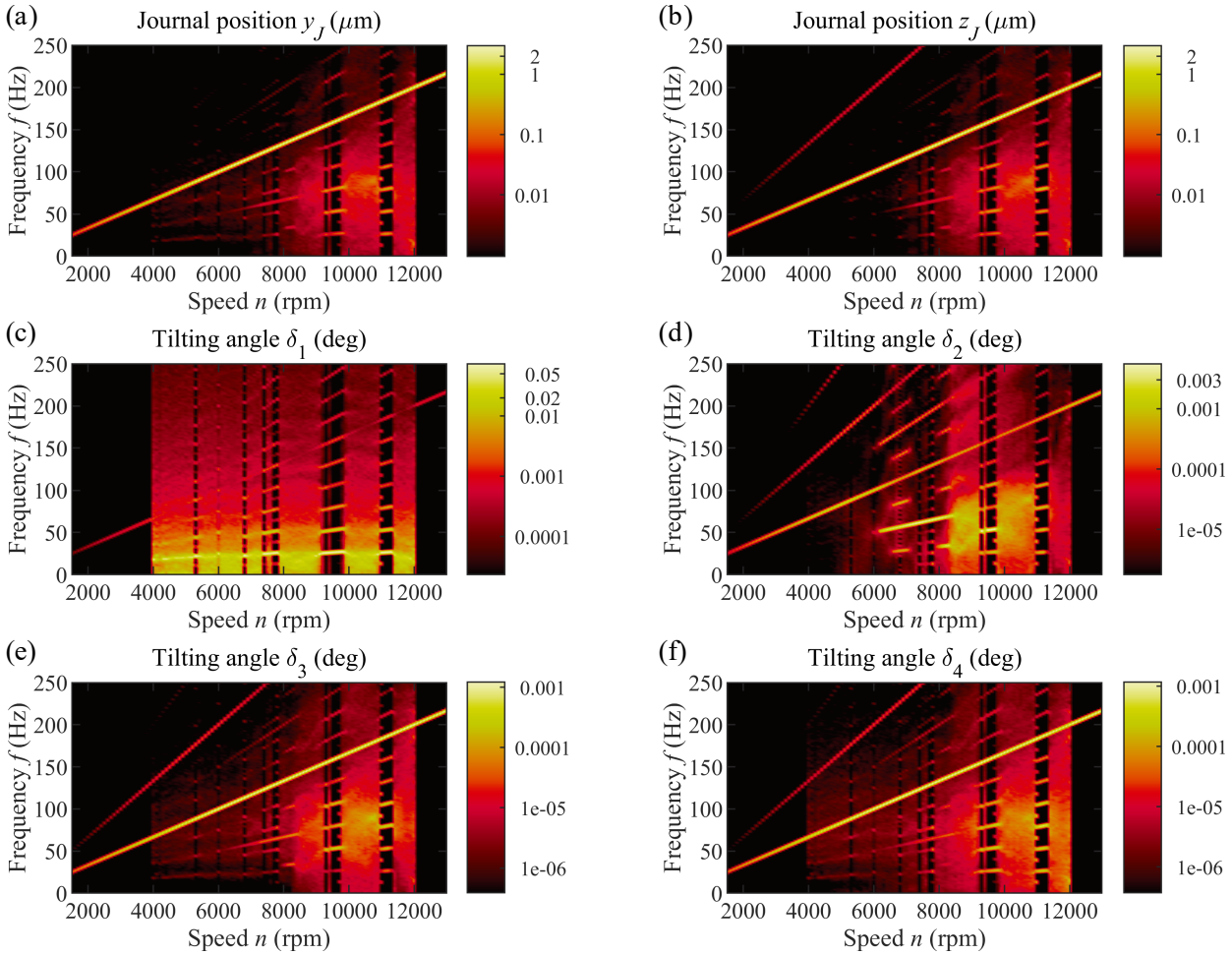

Fig. 7.11: Case 3 – Spectrograms of the nonlinear steady-state response to harmonic excitation of TPJB with preload

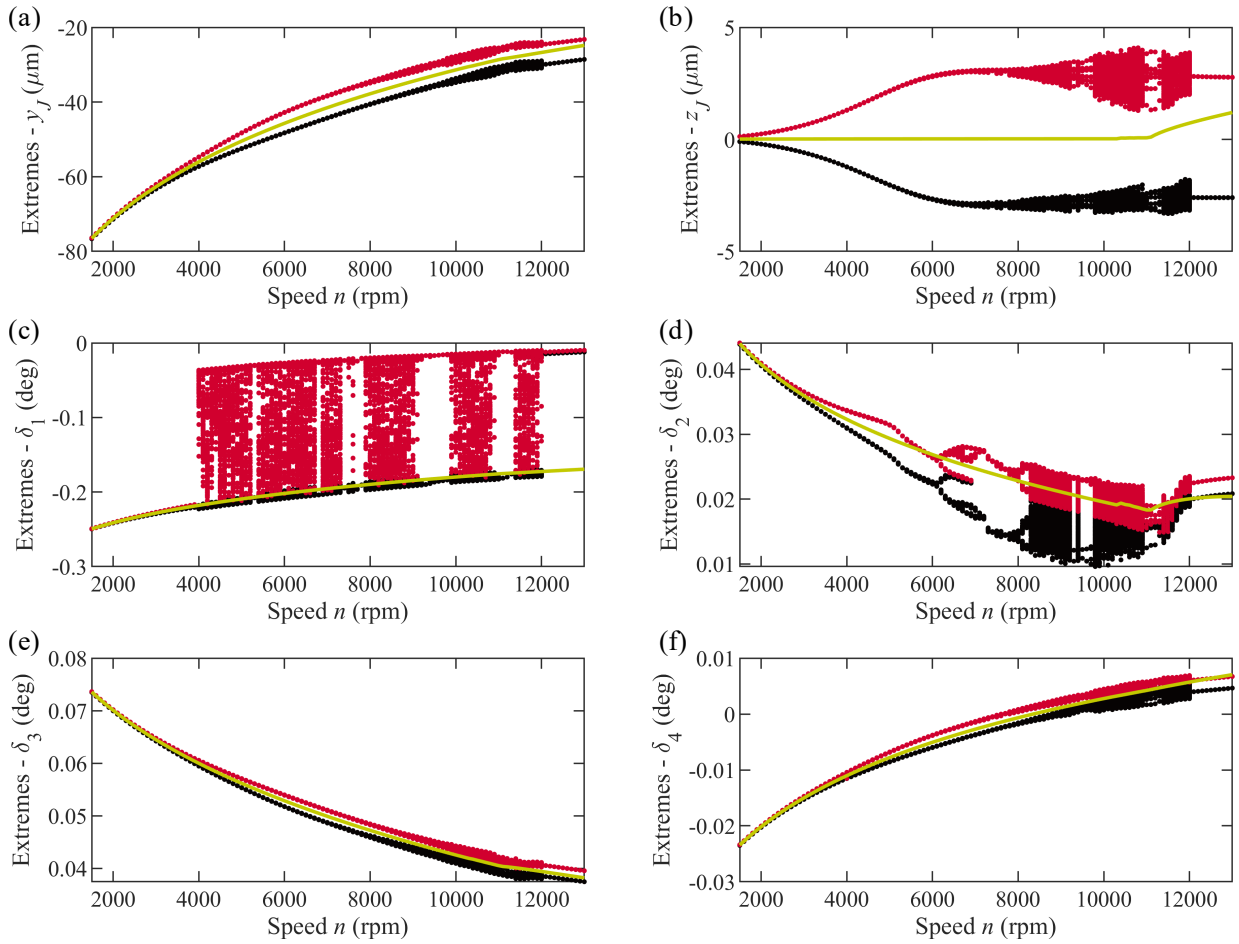

Fig. 7.12: Case 3 – Bifurcation diagrams and static equilibrium points of TPJB with preload

7.4.4 Case 4

Here, the results are supplemented with spectrograms and bifurcation diagrams for the additional radial motion of the pads due to radial flexibility of pivot mounting, see Fig. 7.14 and Fig. 7.16. The journal displacements and the tilting angles shown in Figs. 7.13 and 7.15 do not significantly qualitatively differ from the results presented in case 1. Therefore, the discussion regarding case 1 more or less applies also to this case: the dominant response of the journal and the bottom pads (3 and 4) is synchronous (1X); the upper pads exhibit the chaotic behaviour with clearly-separated intervals of period-doubling motion. The bifurcation diagrams in Figs. 7.15 and 7.16 reveal that there is a resonance peak close to rotor speed 5000 rpm. This resonance is due to the pivot radial stiffness.

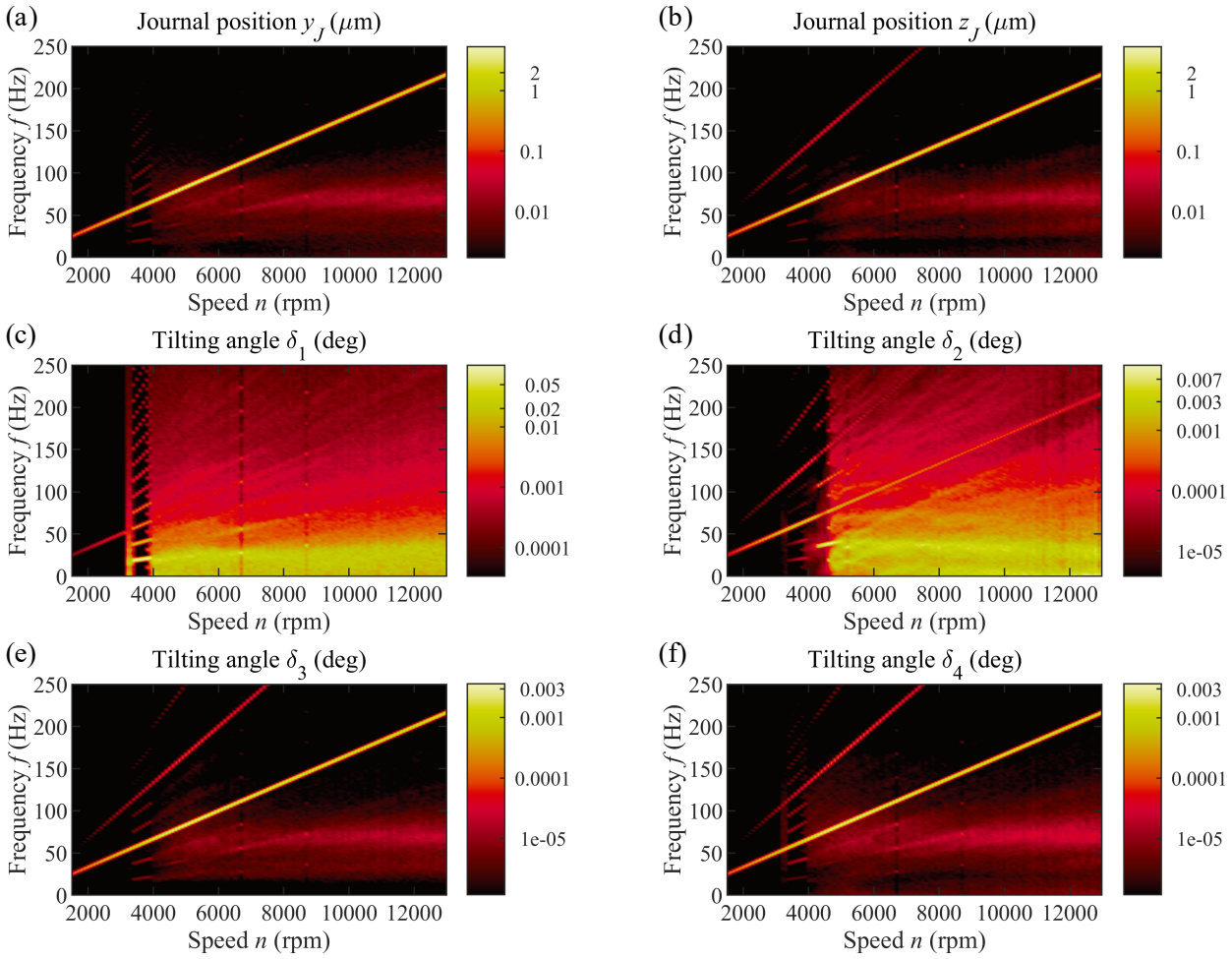

Fig. 7.13: Case 4 – Spectrograms of the nonlinear steady-state response to harmonic excitation of TPJB with flexible radial pivot mounting – journal displacement and tilting angles

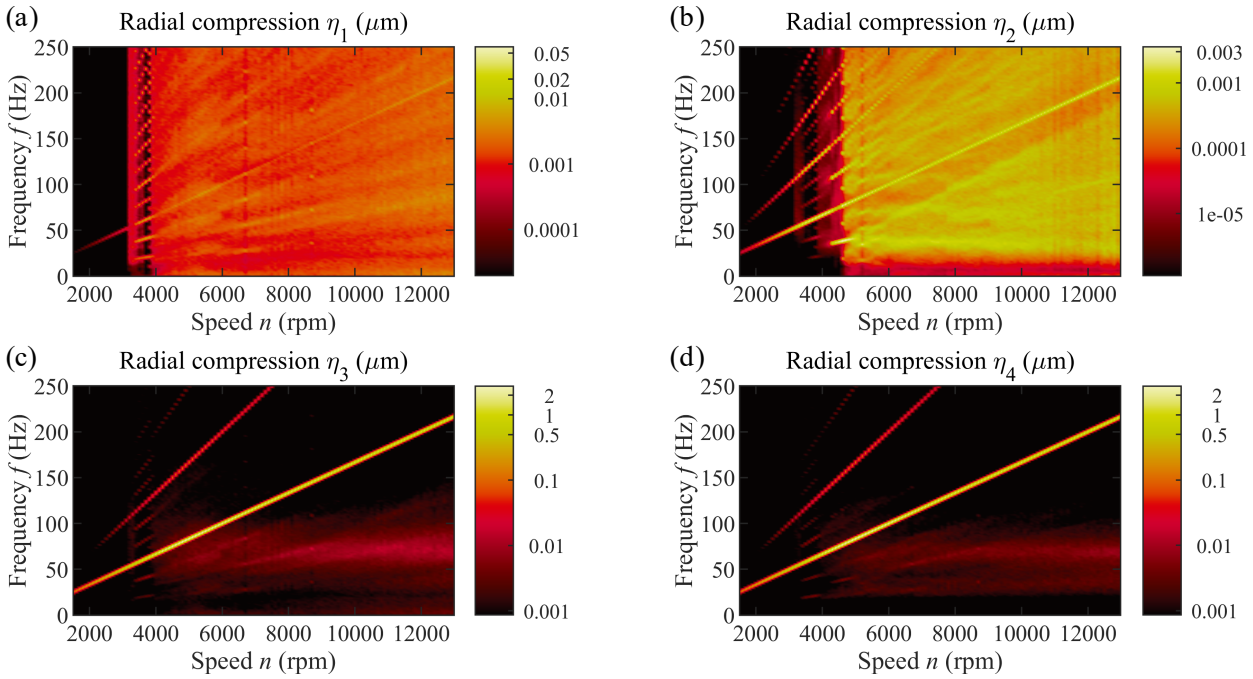

Fig. 7.14: Case 4 – Spectrograms of the nonlinear steady-state response to harmonic excitation of TPJB with flexible radial pivot mounting – radial compression of pads

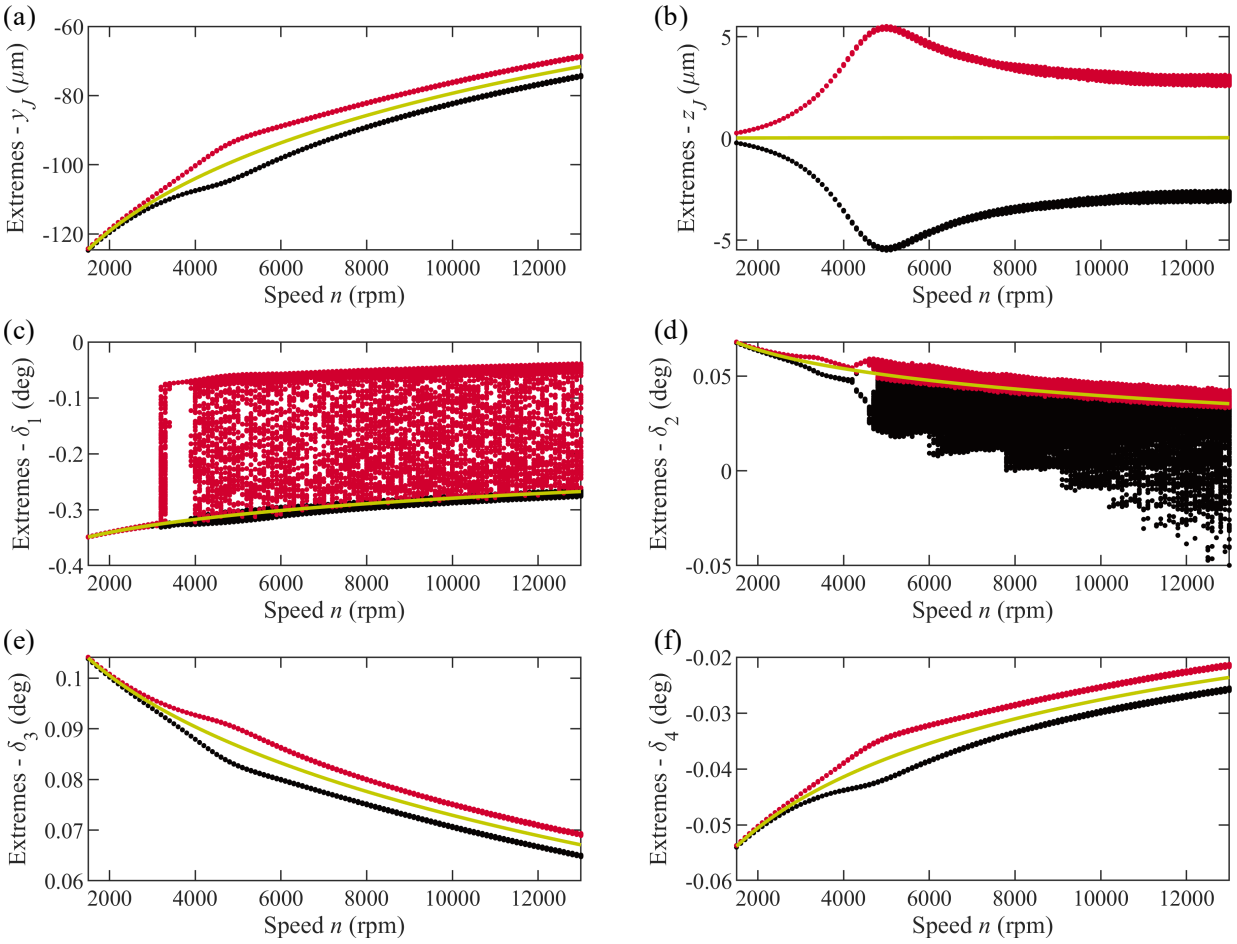

Fig. 7.15: Case 4 – Bifurcation diagrams and static equilibrium points of TPJB with flexible radial pivot mounting – journal displacement and tilting angles

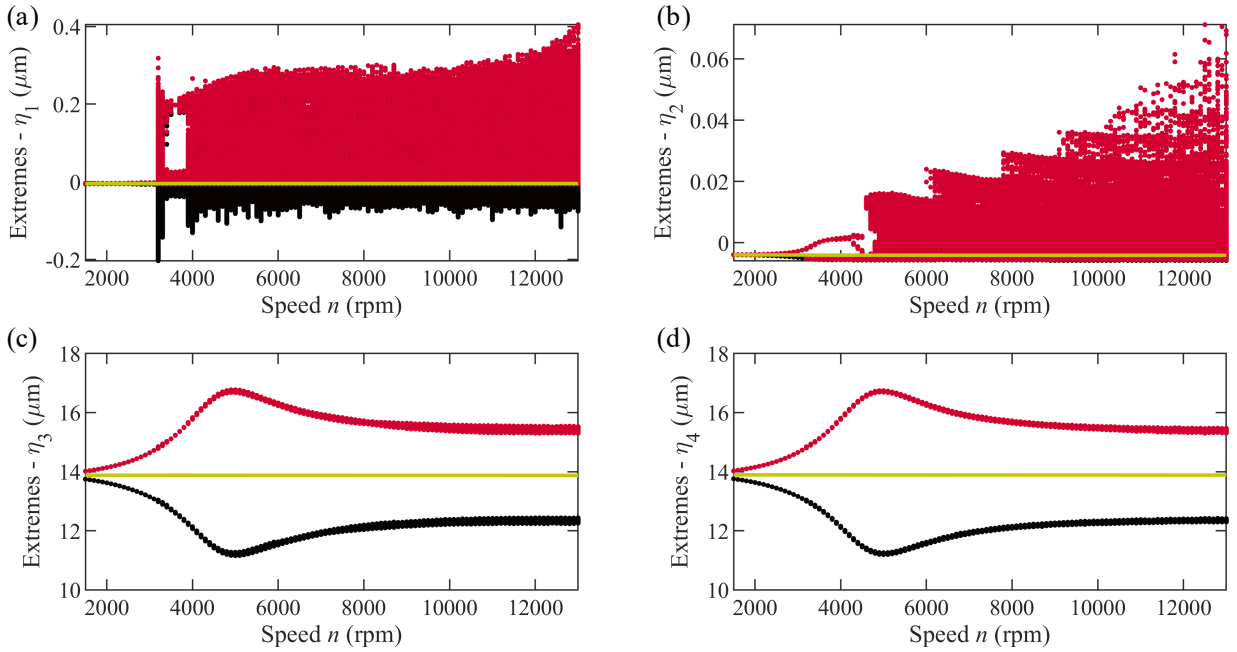

Fig. 7.16: Case 4 – Bifurcation diagrams and static equilibrium points of TPJB with flexible radial pivot mounting – radial compression of pads

7.5 Results summary

The proposed approach for modelling of tilting pad journal bearings presented in Chap. 3 was validated by comparison with the data published in [38] with virtually the same results as those published.

Furthermore, the dynamics of a four-segment TPJB in load-between pads (LBP) configuration was analysed using the proposed concept of the TPJB model. It was demonstrated that the proposed concept is capable of predicting nonlinear behaviour, including period-doubling and chaotic motions. A broad spectrum of tools was used to analyse a complex pad's motion: spectrograms, bifurcation diagrams, Lyapunov exponents, phase trajectories and waveforms of the interaction forces. The results can be summarised as follows:

- The motion of the journal and bottom pads is synchronous with the rotor speed. However, excessive pad preload can also induce asynchronous motions to these subsystems.
- The excessive pad preload strengthen interactions between individual subsystems. If preloaded upper pads exhibit the period-doubling or chaotic motion, these motions are also visible in the journal and bottom pad's response. Interestingly, if each upper pad oscillates differently, both these oscillations are superimposed to the motions of the remaining subsystems.
- The motion of the upper pads depends on the position of pivots. Here, single-sided impacts of the pad's edge to the journal developed, which led to the interesting nonlinear behaviour. In addition to the chaotic broadband motion, many internal resonances, including 1:4, 1:5, 1:6 and 1:7 were examined.
- Decreased assembled clearance has a stabilising effect on lightly loaded pad 2. Subsynchronous vibrations occur at a higher rotor speed compared to other case studies.
- The upper pad's motion was classified as pad fluttering based on in-depth time series insight of pad motion and acting hydrodynamic and elastic forces. Pad fluttering disappears at relative eccentricities lower than 0.34. This behaviour is enabled due to a new equilibrium branch of pad 1 that was not found during the static analysis. Such behaviour is essential for high-speed applications because it suggests that the TPJBs may be operated above pad fluttering regimes. However, the threshold value 0.34 can vary with particular system parameters.

8 Application – Rotor Kit

The threshold speed for the fluid-induced rotor instability (oil whirl) can be identified as the speed at which the rotor vibrations significantly increase during a run-up or the speed at which the rotor vibrations significantly decrease during a coast-down. However, the threshold speeds detected during the run-up and the coast-down are not the same.

Therefore, this hysteresis phenomenon is investigated in this chapter both experimentally and computationally. The Bently Nevada RK 4 Rotor Kit was used to study the hysteresis phenomenon experimentally and computationally using an in-house software with a solver based on the finite element method for rotor dynamics and a solver based on the finite difference method for hydrodynamic lubrication in the journal bearing.

8.1 Rotor Kit description

The Rotor Kit was assembled in the configuration shown in Fig. 8.1. The shaft with the attached disc is supported on a journal bearing located at the non-drive end and on a sliding bearing at the drive end of the rotor. The shaft is also supported on preload frame with four radial springs, and a bellows coupling links the shaft and the motor. The investigated journal bearing has four inlet bores located at 45, 135, 225 and 315 deg with respect to the horizontal divided plane. The bearing is supplied by constant pressure. Detailed parameters of subsystems and dimensions are described in the following section.

8.2 Mathematical model and Rotor Kit parameters

The mechanically isolated rotating system consisted of a flexible shaft and a rigid disc was assumed. The finite element method [6] was employed for the derivation of equations of motion of this system with the following assumptions: the flexible shaft is rotationally symmetric and transversally incompressible one-dimensional continua that satisfies the Bernoulli-Navier hypothesis. The motions of the shaft and the disc are described by lateral vibrations v, w and two Euler angles θ, ψ. The global system of equations of motion defined in the fixed Cartesian system xyz is written in the matrix form

$$\mathbf{M}^{(\mathrm{FEM})}\ddot{\mathbf{q}}(t) + \left(\mathbf{B}^{(\mathrm{FEM})} + \omega\mathbf{G}^{(\mathrm{FEM})}\right)\dot{\mathbf{q}}(t) + \mathbf{K}^{(\mathrm{FEM})}\mathbf{q}(t) = \mathbf{f}_g^{(\mathrm{FEM})}, \tag{8.1}$$

where ω is the angular speed of the shaft, $\mathbf{q}(t) = [\ldots, v_k, w_k, \theta_k, \psi_k, \ldots]^T$ is the vector of generalized coordinates, $\dot{\mathbf{q}}(t), \ddot{\mathbf{q}}(t)$ are time vectors of velocity and acceleration. Symmetric matrices $\mathbf{M}^{(\mathrm{FEM})}, \mathbf{B}^{(\mathrm{FEM})}, \mathbf{K}^{(\mathrm{FEM})}$ are the mass, damping and stiffness matrices of the rotor,

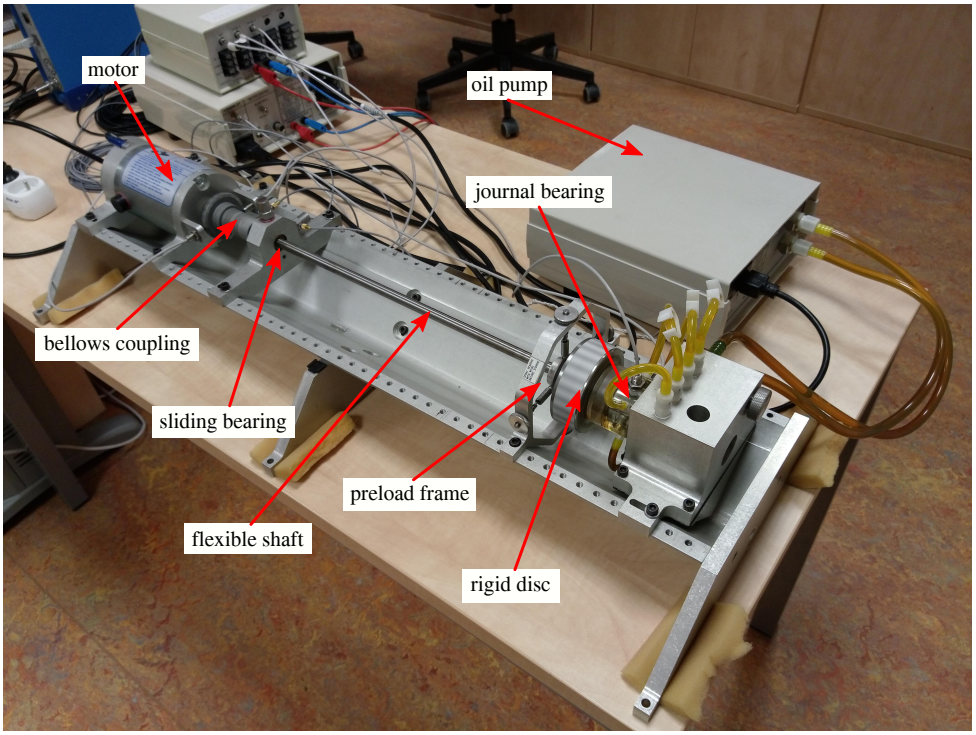

Fig. 8.1: The Bently Nevada RK 4 Rotor Kit

respectively. Antisymmetric matrix $\mathbf{G}^{(\mathrm{FEM})}$ is the matrix of gyroscopic effects and $\mathbf{f}_g^{(\mathrm{FEM})}$ is the vector of gravitational load. Damping matrix $\mathbf{B}^{(\mathrm{FEM})}$ can be expressed as

$$\mathbf{B}^{(\mathrm{FEM})} = \alpha \mathbf{M}^{(\mathrm{FEM})} + \beta \mathbf{K}^{(\mathrm{FEM})}, \tag{8.2}$$

where α and β are the Rayleigh's damping coefficients.

Derived equations of motion in (8.1) represent the motion of isolated rotating system without coupling with the ground. The coupling with the ground can be described by a visco-elastic joint or by nonlinear hydrodynamic forces acting in journal bearings. In the case of the visco-elastic joint, its inertia, damping and stiffness can be considered. These parameters are expressed in the form of coupling matrices $\mathbf{M}_c$, $\mathbf{B}_c$, $\mathbf{K}_c$ which can be assembled into global matrices as

$$\mathbf{M} = \mathbf{M}^{(\mathrm{FEM})} + \mathbf{M}_c, \quad \mathbf{B} = \mathbf{B}^{(\mathrm{FEM})} + \mathbf{B}_c, \quad \mathbf{K} = \mathbf{K}^{(\mathrm{FEM})} + \mathbf{K}_c. \tag{8.3}$$

Finally, equations of motion of the rotating system supported on the journal bearings and/or the visco-elastic couplings are written in general matrix form

$$\mathbf{M}\ddot{\mathbf{q}}(t) + (\mathbf{B} + \omega \mathbf{G})\,\dot{\mathbf{q}}(t) + \mathbf{K}\mathbf{q}(t) = \mathbf{f}_g + \mathbf{f}_{\mathrm{hd}}(\mathbf{q}, \dot{\mathbf{q}}, t). \tag{8.4}$$

A detailed scheme of the Rotor Kit with dimensions and used finite element discretisation is depicted in Fig. 8.2. The bellows coupling is modelled as a subsystem with lumped mass and isotropic bending stiffness. The preload frame and the rigid disc are attached in nodes 6 and 7, respectively. The shaft made of regular steel is supported on the investigated journal bearing in node 9. Temperature influence on dynamic lubricant viscosity was neglected and isoviscous

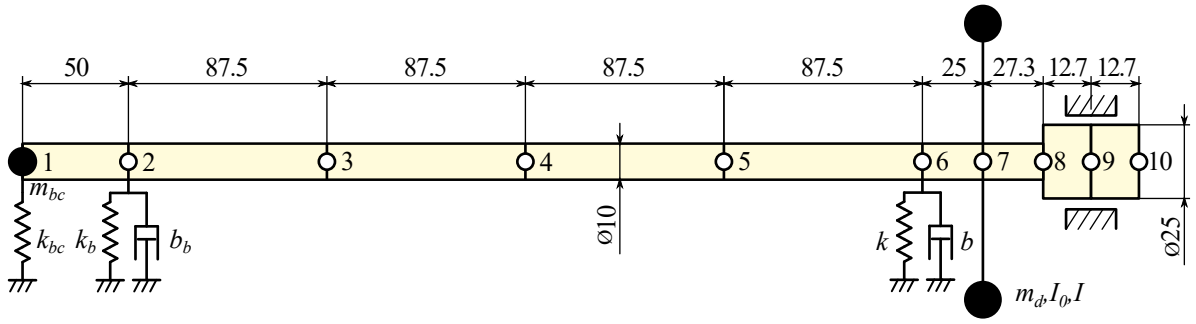

Fig. 8.2: A computational scheme Rotor Kit and nodes for a finite element discretisation

distribution in the whole bearing was used in computational analyses. Characteristic journal bearing static load was calculated from the force balance on the rigid shaft with the disc supported only on the rigid supports at the isotropic sliding bearing and journal bearing positions. Gravitational load acted at the centre of gravity of the system and the bellows coupling was replaced by external force. All of the presented parameters are summarised in Tab. 8.1.

For numerical simulations, the system of equations (8.4) is transformed to the set of the first-order differential equations with state-space vector $\mathbf{u}(t) = \left[\dot{\mathbf{q}}(t)^T, \mathbf{q}(t)^T\right]^T \in \mathbb{R}^{80,1}$ as follows

$$\dot{\mathbf{u}}(t) = \mathbf{A}(t)\mathbf{u}(t) + \mathbf{b}(t), \tag{8.5}$$

where system matrix $\mathbf{A}(t)$ and right-hand side vector $\mathbf{b}(t)$ have following form

$$\mathbf{A}(t) = \begin{bmatrix} -\mathbf{M}^{-1}\left(\mathbf{B} + \omega\mathbf{G}\right) & -\mathbf{M}^{-1}\mathbf{K} \\ \mathbf{E} & \mathbf{0} \end{bmatrix}, \qquad \mathbf{b}(t) = \begin{bmatrix} \mathbf{M}^{-1}\left(\mathbf{f}_g + \mathbf{f}_{hd}\left(\mathbf{q}, \dot{\mathbf{q}}, t\right)\right) \\ \mathbf{0} \end{bmatrix}. \tag{8.6}$$

Extensive rotating systems with many degrees of freedom and nonlinearities are subjected to the modal reduction method to reduce computational demands during numerical integration.

Stability analysis classified based on complex eigenvalues and eigenvectors which come from solving a modal analysis problem allows considering detailed modelling of the investigated comprehensive rotating systems. Contrary, the stability analysis performed based on previously presented Routh-Hourwitz criterion in Sec. 2.5 is more suitable for a simplified rigid rotor-bearing model. Eigenvalue problem is generally described by

$$\left[\lambda_\nu(\omega)\mathbf{E} - \mathbf{A}(\omega)\right]\mathbf{v}_\nu(\omega) = \mathbf{0}, \tag{8.7}$$

where matrix $\mathbf{A}$ includes linearised stiffness and damping coefficient at the established static equilibrium points of the investigated journal bearing in global submatrices $\mathbf{K}, \mathbf{B}$, respectively. Eigenvalues are given as a complex number dependent on the shaft angular speed

$$\lambda_\nu(\omega) = \alpha_\nu(\omega) \pm \mathrm{i}\beta_\nu(\omega), \tag{8.8}$$

where imaginary part $\beta_\nu(\omega)$ represents the ν-th eigenfrequency, $\alpha_\nu(\omega)$is the real part of each eigenvalue, which classifies the stability, and damping and i is the imaginary unit.

Parameter	Symbol	Value	Unit
Steel density	ϱ	7800	$\mathrm{kg{\cdot}m^{-3}}$
Young modulus	E	210	GPa
Poisson's ratio	ν	0.3	-
Rayleigh's coefficient	α	2.618	$\mathrm{s^{-1}}$
Rayleigh's coefficient	β	$2.122 \cdot 10^{-5}$	s
Rigid disc mass	m_d	800	g
Rigid disc axial moment of inertia	I_0	$5.525 \cdot 10^{-4}$	$\mathrm{kg{\cdot}m^2}$
Rigid disc lateral moment of inertia	I	$3.1792 \cdot 10^{-4}$	$\mathrm{kg{\cdot}m^2}$
Bellows coupling mass	m_{bc}	65	g
Bellows coupling bending stiffness	k_{bc}	$1 \cdot 10^4$	$\mathrm{N{\cdot}m^{-1}}$
Sliding bearing stiffness	k_b	$1 \cdot 10^5$	$\mathrm{N{\cdot}m^{-1}}$
Sliding bearing damping	b_b	$1 \cdot 10^2$	$\mathrm{N{\cdot}s{\cdot}m^{-1}}$
Radial preload frame stiffness	k	$4 \cdot 10^3$	$\mathrm{N{\cdot}m^{-1}}$
Equivalent stiffness	k_s	$5 \cdot 10^3$	$\mathrm{N{\cdot}m^{-1}}$
Bearing length	L	25.4	mm
Bearing shell radius	R	12.7	mm
Radial clearance	c	0.2	mm
Lubricant dynamic viscosity	μ	27.5	mPa·s
Ambient pressure	p_a	1.0	bar
Saturation pressure	p_{cav}	0.98	bar
Supply pressure	p_{sup}	1.225	bar
Bore diameter	d_b	3.0	mm
Bearing static load	W	-9.1223	N

Tab. 8.1: Parameters of the Rotor Kit

Modal damping factor $D_\nu(\omega)$ is used for the stability identification and for a comparison of the magnitude of growth/decay at the same time. The modal damping factor results from this fraction

$$D_\nu(\omega) = -\frac{\alpha_\nu(\omega)}{|\lambda_\nu(\omega)|}. \tag{8.9}$$

The stability is then evaluated using following rules

- $\forall\nu$: $D_\nu(\omega) \geq 0$, then the system is stable, and
- $\exists\nu$: $D_\nu(\omega) < 0$, then the system is unstable.

The precession direction in each node is determined from corresponding eigenvectors and the determination procedure is described in detail in [6, A5].

8.3 Experimental measurement

The system described in the previous sections was tested first and then its response was simulated. The test was performed as follows. The Rotor Kit was operated at slow speed 300 rpm at the beginning, then its speed was gradually increased, and after reaching 5000 rpm, its speed was gradually decreased. This process was executed with various acceleration and deceleration ramps ranging from 25 rpm·s^{-1} to 250 rpm·s^{-1}. Each operation case was repeated three times. The speed at which the rotor loses the stability, i.e. the threshold speed for the instability, was detected in all operation cases. The experimental measurements were performed in cooperation with Ing. Luboš Smolík, Ph.D.

The threshold speed can be computed analytically or numerically using various criteria, including the Routh-Hourwitz criterion or stability analysis based on eigenvalues. However, identifying the exact threshold speed experimentally may be difficult. Even a stable rotor performs some motions due to a residual unbalance and external forces [4, 8]. Because of this, a procedure of subsynchronous order tracking given below was used in order to estimate threshold speed.

First, the short-time Fourier transform (STFT) with parameters specified in Tab. 8.2 was performed using tool `autofft` [92]. A flat-top window function with significant spectral leakage was employed, which decreases the uncertainty of the instantaneous magnitude of the subsynchronous response at the cost of a reduced frequency resolution. A maximum magnitude in the frequency range 0.35X–0.55X of the rotor speed was then tracked together with the rotor speed and the threshold speed was estimated at a point where the magnitude changes most significantly. Extremes of measured relative journal vertical displacement and a typical resulting track with a magnitude profile are depicted in Fig. 8.3.

Parameter	Value	Unit
Sampling frequency	6.4	kHz
Segment length	0.2	s
Segment overlapping	80	%
Time-weighting function	flat-top	
Averaging	none	

Tab. 8.2: Parameters of the short-time Fourier transform

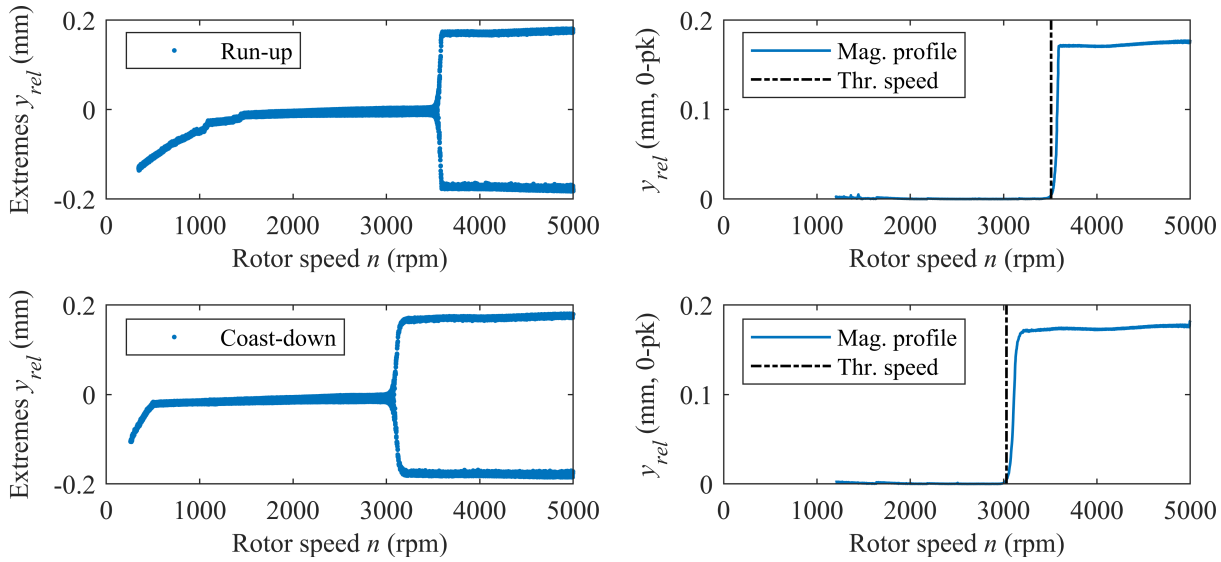

Fig. 8.3: Extremes of relative journal vertical displacement and threshold speed detection in experimental measurement

8.4 Results

In order to perform simulations, in-house software based on proposed computational methods was created in MATLAB. Except for the complex model depicted in Fig. 8.2, a simplified 2 DoF model of a rigid journal supported on the journal bearing was also implemented and the bearing was loaded by nominal value from Tab. 8.1. The journal was additionally attached to the ground by isotropic spring support with stiffness k_s. This coupling represents the flexibility of the reduced system and its nominal value is close to the preload frame stiffness.

First, stability analysis of the complex model was performed. Corresponding Campbell diagram is depicted in Fig. 8.4. The frequency range is limited to 350 Hz. For better diagram clarity, the damping factor D_ν is restricted to 0.99 to avoid depicting overdamped eigenmodes. Each branch consists of different markers for precession distinguishing, and all branches are labelled by corresponding shaft mode. There is an apparent unstable conical mode which begins at ca. 3650 rpm. For the simplified 2 DoF model, the Routh-Hourwitz criterion is sufficient to estimate threshold speed, but stability analysis based on calculated eigenvalues can also be performed.

Equations of motion for both computational models were integrated numerically employing MATLAB solver `ode15s` and simulated responses were processed the same way as experimental data. All experimental data and results of numerical simulations are summarised in Fig. 8.5. The comprehensive model was modally reduced to the lowest 10 eigenmodes for numerical integration.

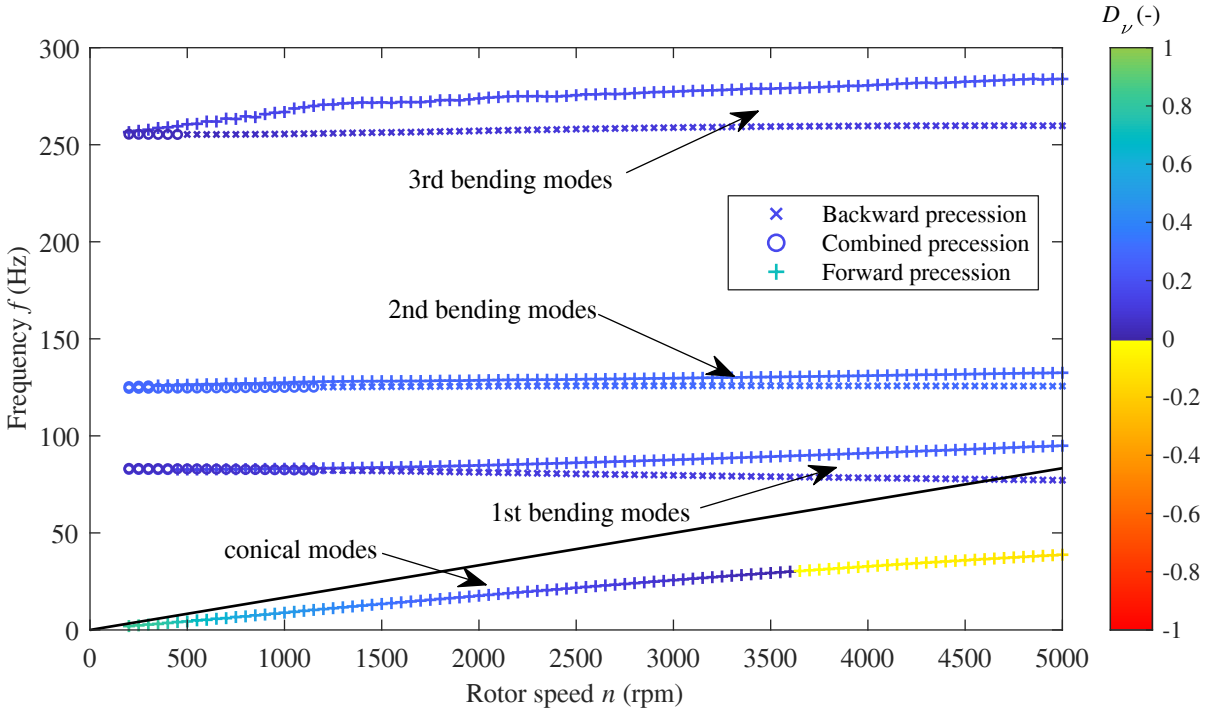

Fig. 8.4: Campbell diagram for complex model of Rotor Kit resulting from computational analysis

The subfigure in Fig. 8.5 for numerical results contains analytically estimated threshold speeds (dash-dot line). The subfigures demonstrate that the instability occurs at a lower rotor speed during the coast-down operation and at a higher speed during the run-up. The width of the hysteresis loop is comparable between experimental and simulated results. Interestingly, the relationship between the width and the angular acceleration is close to linear and the width is almost symmetrically distributed around analytically estimated threshold speeds. However, the computationally examined nominal threshold speeds significantly differ from the experimental measurement.

This discrepancy might be caused by fluctuating oil supply pressure, temperature-dependent lubricant parameters, neglecting the journal bearing misalignment and insufficiently accurate identifying of Rotor Kit parameters, e.g. the parameters of sliding bearing and bellows coupling. In addition, the preload frame and its preload control might significantly affect the journal bearing loading. The preload magnitude is manually controlled by tightening the lock nut. It was an effort to set the preload to zero in both directions by minimal tension of the radial springs.

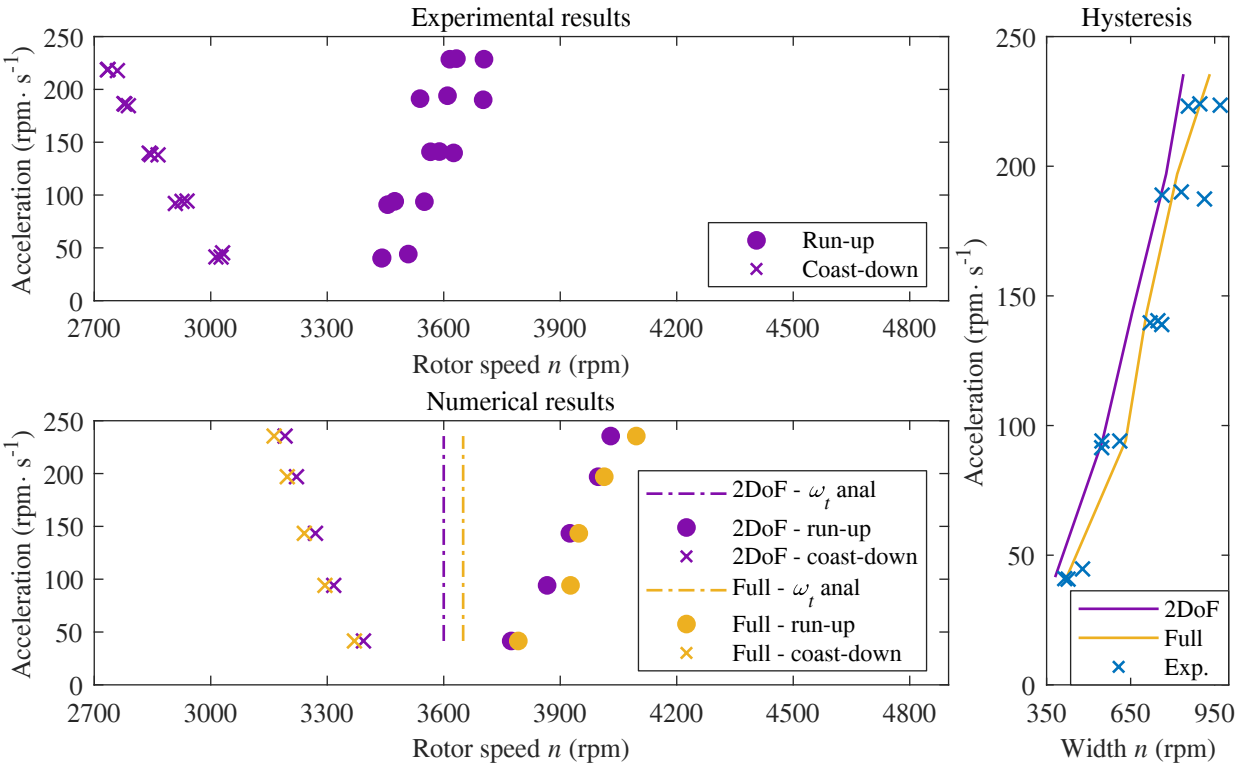

Fig. 8.5: Threshold speed comparison for both experimental and numerical results

9 Application – textured bearings

The stability of a rotating system supported on journal bearings can be improved by suitable texturing of the bearing shell. However, the texturing can also impact bearing temperature, formation of cavitation in the bearing gap and tribological characteristics such as friction losses, wear etc.

This chapter is divided into two main parts. The first part in Sec. 9.1 is focused on mathematical modelling of a textured bearing and the study of the influence of employed numerical methods on computational analysis results. Then in Sec. 9.2, established theoretical conclusions and developed computational models are validated by experimental measurements of the textured bearing of the created test rig. Concluding remarks from numerical simulations and experimental measurements are summarised in Sec. 9.3.

9.1 Computational analysis

This section introduces a computational model for a simulation of dynamics of a rotor supported on the textured journal bearing shown in Fig. 9.1. Considered 2 DoF model is supposed to emphasise the influence of textures on the system stability and currently eliminate the following undesirable effects of comprehensive models, e.g. rotor flexibility, gyroscopic effects, etc.

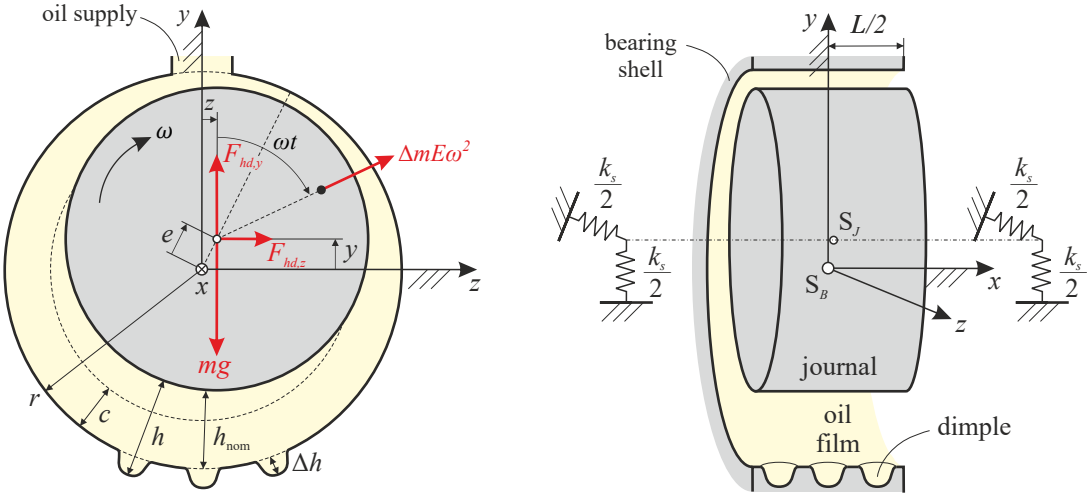

Fig. 9.1: Geometry of a generic journal bearing with a textured shell

9.1.1 Mathematical modelling

A simple rotor of effective mass m depicted in Fig. 9.1 is supported on a textured journal bearing which rotates at prescribed angular speed ω. The rotor is subjected to hydrodynamic forces, out-of-balance forces and gravity load. If angular misalignment of the rotor is negligible, its motion can be described by the following equations

$$\begin{bmatrix} m & 0 \\ 0 & m \end{bmatrix} \begin{bmatrix} \ddot{y}(t) \\ \ddot{z}(t) \end{bmatrix} + \begin{bmatrix} k_s & 0 \\ 0 & k_s \end{bmatrix} \begin{bmatrix} y(t) \\ z(t) \end{bmatrix} = \begin{bmatrix} -m\,g \\ 0 \end{bmatrix} + \begin{bmatrix} \Delta m E \omega^2 \cos(\omega\,t) \\ \Delta m E \omega^2 \sin(\omega\,t) \end{bmatrix} + \begin{bmatrix} F_{hd,y} \\ F_{hd,z} \end{bmatrix}, \quad (9.1)$$

where k_s is the equivalent stiffness of the system, which includes the stiffness of auxiliary bearings, shaft and coupling of the shaft to a drive, parameter ΔmE is the static unbalance of the rotor, g is the gravitational acceleration and $F_{hd,y}$, $F_{hd,z}$ are components of the hydrodynamic force. In reality, the auxiliary bearings also induce some damping. This damping is neglected in this work because it is challenging to evaluate it accurately, unlike the equivalent stiffness.

A laminar flow of isoviscous incompressible Newtonian fluid and texturing only on the bearing shell is supposed for pressure field calculation and hydrodynamic force evaluation. Contrary to a plain journal bearing, the film height presence in the Reynolds equation governing the pressure field in the textured bearing is a sum of nominal gap $h_{nom} = h_{nom}(X, t)$ for cylindrical bearing (2.7) and local deviation $\Delta h = \Delta h(X, Z)$ due to texture. It is assumed that local deviation Δh is at least C^1 continuous. This condition means that all dimples are reasonably smooth, i.e. there are no step changes in the bearing gap. If such changes are present, pressure terms in the Reynolds equation have to be modified, see [79].

For providing stability assessment by Routh-Hourwitz criterion, the investigated system's static analysis is first performed to determine equilibrium points and estimate linearised dynamic coefficients in these positions. Following system of nonlinear equations is obtained by omitting all time-dependent terms from (9.1)

$$\begin{bmatrix} k_s & 0 \\ 0 & k_s \end{bmatrix} \begin{bmatrix} y_S \\ z_S \end{bmatrix} = \begin{bmatrix} -m\,g \\ 0 \end{bmatrix} + \begin{bmatrix} F_{hd,y} \\ F_{hd,z} \end{bmatrix}, \quad (9.2)$$

where y_S, z_S are the static equilibrium points. Assuming that the journal is in the equilibrium point (y_r, z_r), its motion close to the equilibrium point can be approximated with

$$\begin{bmatrix} m & 0 \\ 0 & m \end{bmatrix} \begin{bmatrix} \ddot{y}_r \\ \ddot{z}_r \end{bmatrix} + \begin{bmatrix} b_{yy} & b_{yz} \\ b_{zy} & b_{zz} \end{bmatrix} \begin{bmatrix} \dot{y}_r \\ \dot{z}_r \end{bmatrix} + \begin{bmatrix} k_{yy} + k_s & k_{yz} \\ k_{zy} & k_{zz} + k_s \end{bmatrix} \begin{bmatrix} y_r \\ z_r \end{bmatrix} = \begin{bmatrix} 0 \\ 0 \end{bmatrix}, \quad (9.3)$$

where y_r, z_r are small displacements from the equilibrium point, and k_{ij}, b_{ij} are linear coefficients that approximate oil film stiffness and damping, respectively.

9.1.2 Bearing parameters

Theoretical results are provided for a journal bearing whose parameters are summarised in Tab. 9.1. Four examined different bearing layouts, including a plain shell and three textured shells, are introduced in Tab. 9.1 and Fig. 9.2a–d. In all three cases, textures are located in the lower half of the bearing and are denoted as follows:

- Layout Q2: the texture covers the convergent area of the bearing gap in the second quadrant,
- Layout Q3: the texture is located in the third quadrant where the maximum hydrodynamic pressure is expected,
- Layout Q23: the texture covers the lower half of the bearing.

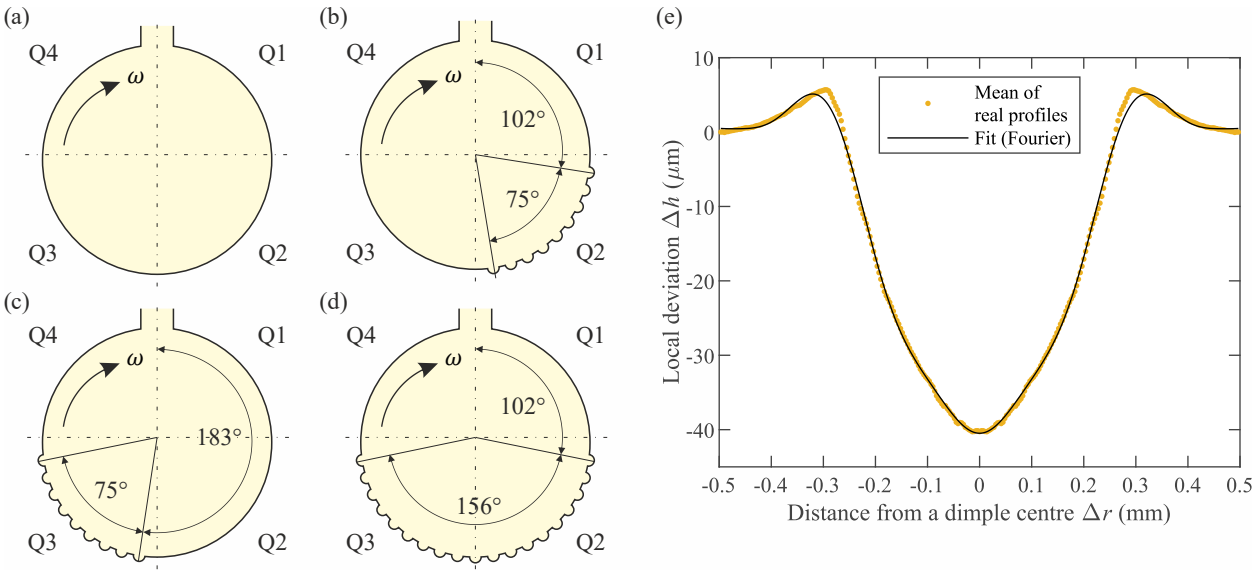

Fig. 9.2: Considered bearing layouts: a) plain bearing, b) layout Q2, c) layout Q3, d) layout Q23, e) composite and approximated dimple profiles

The textures consist of axisymmetric dimples produced by mechanical indentation with a steel ball. This procedure results in dimples with a profile shown in Fig. 9.2e. The composite profile is the average from measured profiles which is than converted to a symmetric curve. The profile can be further approximated by a Fourier series

$$\begin{aligned}\Delta h \approx &-13.66 - 22.7\cos\left(\frac{20}{3}\Delta r\right) - 6.385\cos\left(\frac{40}{3}\Delta r\right) + 3.533\cos\left(\frac{60}{3}\Delta r\right)\\ &+ 0.02469\cos\left(\frac{80}{3}\Delta r\right) - 1.298\cos\left(\frac{100}{3}\Delta r\right),\end{aligned} \tag{9.4}$$

where Δh [μm] is a local deviation of the bearing gap and Δr [mm] is a distance from the dimple centre.

Parameter	Value	Unit
Bearing inner diameter	37.933	mm
Bearing length	20	mm
Radial clearance	55	μm
Nominal load	11.87	N
Maximum speed	20000	rpm
Viscosity model (temperature-dependent)	$0.1414 \cdot \mathrm{e}^{\frac{640.23}{t+89.074}}$	mPa·s
Nominal oil temperature (t)	60	°C
Oil inlet pressure (relative)	1, 1.5	bar
Equivalent stiffness of the system	$4.2 \cdot 10^5$	$\mathrm{N{\cdot}m^{-1}}$
Dimple distribution	regular grid	
Centre-to-centre distance	1	mm
Number of dimples	circ. × ax.	
– plain bearing	0×0	
– layout Q2	26×19	
– layout Q3	26×19	
– layout Q23	53×19	

Tab. 9.1: Parameters of the considered journal bearing and bearing layouts

9.1.3 Numerical simulations results

The numerical solution of hydrodynamic lubrication between textured surfaces is affected [97] by several key aspects, including the treatment of cavitation, spatial discretisation and utilised numerical methods. In addition, the importance of mesh generation concerning the position of individual dimples are highlighted in paper [97]. There is also concluded that a mass-conserving treatment is crucial for some theoretical results. However, the influence of the aspects mentioned above on the calculation of the hydrodynamic forces is not addressed, which is closely related to the journal equilibrium points and threshold speed.

The finite difference method with direct solver for hydrodynamic pressure was employed in an in-house software developed to investigate texture effects on system stability. MATLAB function `fsolve` was used for determination of equilibrium points. This work is not concerned with the tribological parameters for which the mass-conserving treatment of flow is essential, such as friction coefficient, frictional losses or side leakage. Thus, on the one hand, employing the Gümbel cavitation condition, which violates mass conservation, is beneficial for CPU time reduction. However, on the other hand, the influence of this condition on the computed lateral hydrodynamic forces has to be sufficiently small.

A mass-conserving problem [16, 17, 98, 99] describes two quantities: the hydrodynamic pressure and fill ratio, which must be complementary. The complementarity problem can also be solved directly or iteratively. A pivoting algorithm [99] for linear complementarity problems available from MathWorks FileExchange was employed. Unfortunately, this algorithm cannot be directly applied to meshes with a high number of nodes because of memory restrictions in modern workstation PCs. Therefore, commercial software AVL Excite was used to

validate developed in-house software and prove properties of mass- and non-mass-conserving problems. AVL Excite is based on the finite element method (FEM) and has a native multigrid solver (MG) for hydrodynamic pressure solution and optional both Gümbel and Elrod cavitation models. The software is still limited by memory access and allows a maximum of relatively dense mesh of 13×13 nodes per mm^2. The texture layout Q2 was chosen for study. Simulations in AVL Excite were performed in cooperation with Ing. Luboš Smolík, Ph.D.

Fig. 9.3 shows that the cavitated regions depicted for the same prescribed equilibrium point (relative eccentricity $\varepsilon = 0.0111$ and attitude angle $\theta = 277.73$ deg) are sensitive to the employed numerical algorithm. Furthermore, the regions are not consistent with the used cavitation model. The Gümbel condition can yield smaller or more extensive areas than the Elrod equation. However, the Gümbel condition tends to underpredict the formation of cavitation in the dimples regardless of the employed numerical algorithm.

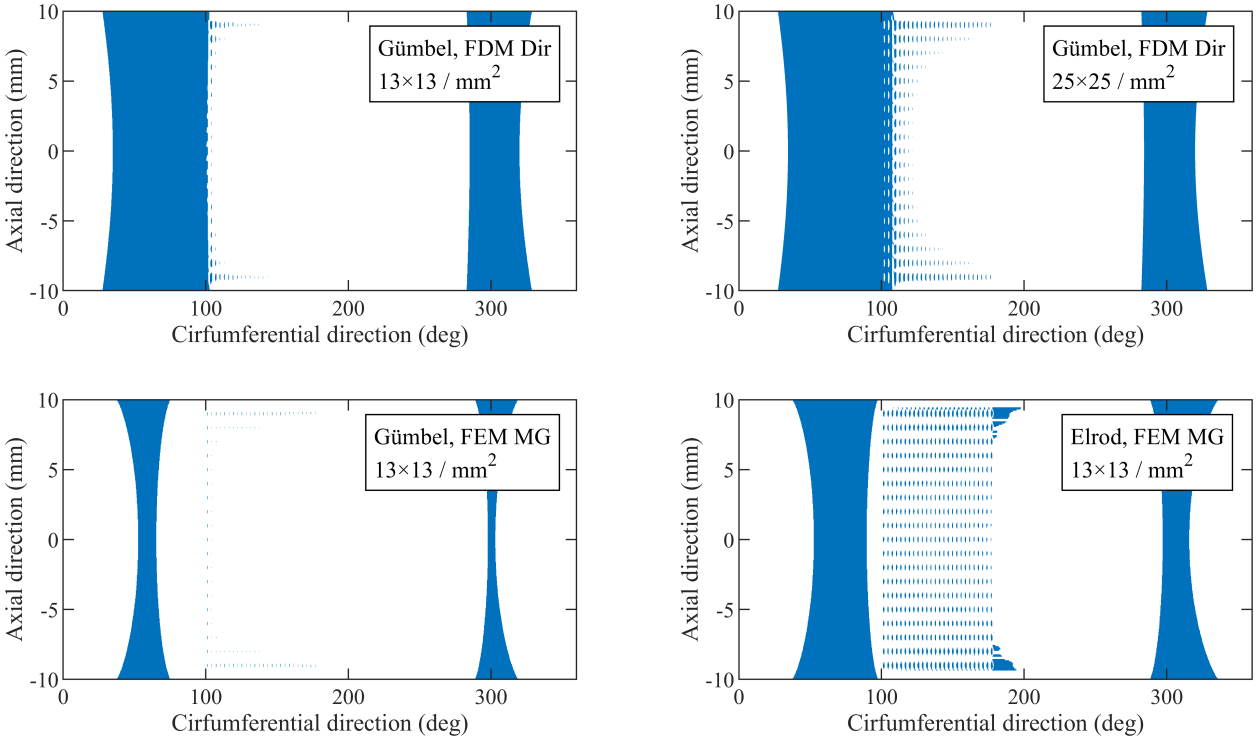

Fig. 9.3: Comparison of cavitated regions (blue) predicted by various cavitation models for layout Q2 (in-house software – upper row, AVL – bottom row)

The cavitated regions also affect the journal equilibrium points, see Fig. 9.4a. Calculated equilibrium points are depicted with a step of 1 krpm for better diagram clarity. At higher eccentricities, the differences due to the numerical methods (direct and multigrid) are more significant than the differences due to the cavitation model (Gümbel and Elrod). At eccentricities close to zero, where the cavitation is more prominent, the equilibrium points form clusters related to the employed cavitation model. However, using very fine meshes, the Gümbel condition predicts equilibrium points close to those predicted by the Elrod model. The importance of the mesh density is highlighted in Fig. 9.4b and c. Coarse meshes can predict considerably different stability thresholds. The threshold speeds are denoted by circles. The results obtained at meshes with at least 23×23 nodes per mm^2 converge to limit

values in terms of both equilibrium points and threshold speeds. However, this observation is limited to the studied texture and should not be generalised to textures with dimples of different shapes.

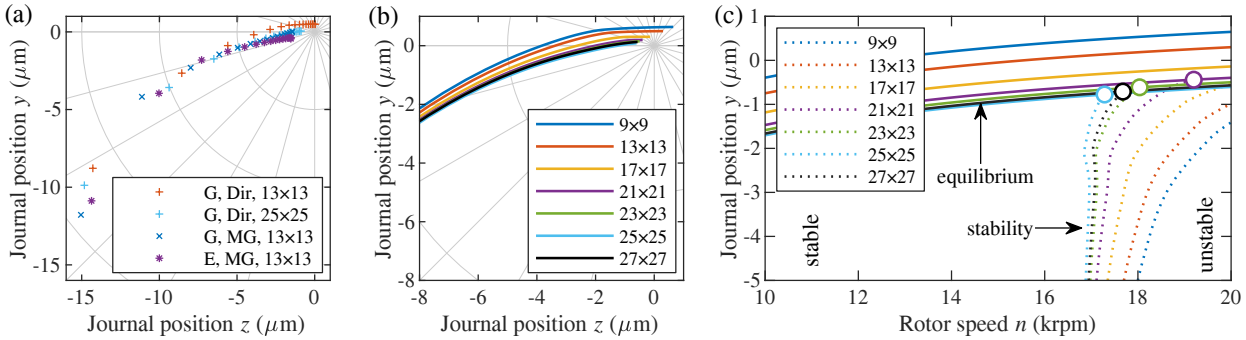

Fig. 9.4: Loci of equilibrium points of layout Q2: a) various numerical algorithms, b) various mesh densities per per mm^2, c) stability thresholds and threshold speeds for various mesh densities

Based on performed sensitivity analyses, the results presented hereafter are obtained only using developed in-house software employing FDM with the Gümbel condition on a fine computational mesh with 25×25 nodes per mm^2, i.e. 2861×481 nodes in total. Determined equilibrium points for the investigated journal bearing with various texture layouts, static bearing loads and relative supply pressures are shown in Fig. 9.5. The texture located in the third quadrant (layouts Q3 and Q23) has a moderate influence on the loci, corresponding to the change of load capacity. This influence is particularly noticeable at higher eccentricities and higher bearing load. However, the texture layout Q2 affects the equilibrium locus almost negligibly compared to the plain bearing. This phenomenon is likely caused by the location of the hydrodynamic pressure gradient (active pressure region) in the third quadrant, where the bearing gap is minimum.

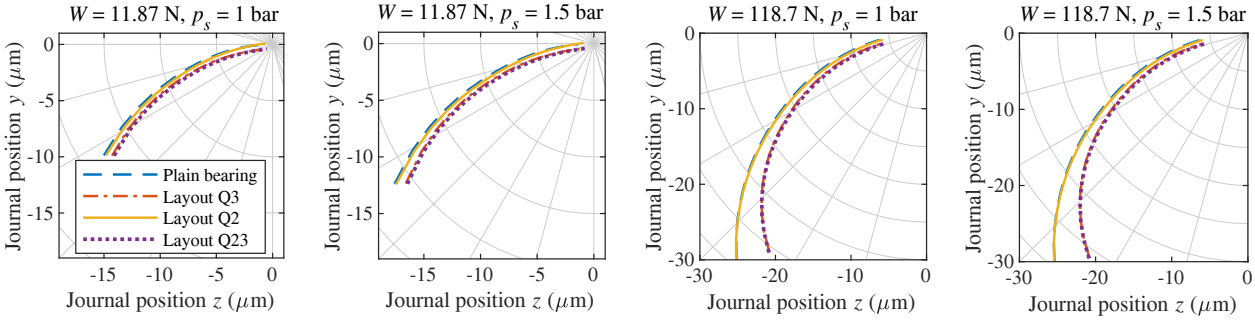

Fig. 9.5: Equilibrium points of the investigated journal bearing with various texture layouts, static bearing loads and relative supply pressures

The texture layouts influence similarly also the threshold speeds. Fig. 9.6 shows that the texture in the second bearing quadrant (layout Q2) has almost negligible effect on the stability of lightly loaded bearing. However, the texture in the third bearing quadrant (layout Q3) shifts the threshold speed from 17 krpm (plain bearing) to 19.7 krpm, and the texture layout Q23 shifts the threshold speed even more. Nevertheless, the effects of the textures are

negligible in the case of higher static loads. The vertical axes are depicted in the logarithmic scale for better loci distinguishing.

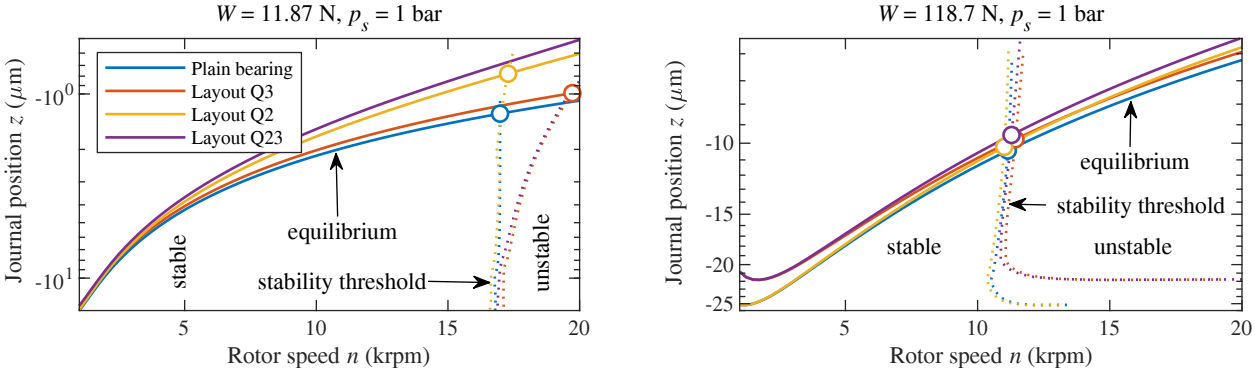

Fig. 9.6: Stability analysis of the investigated journal bearing with various texture layouts and bearing loads at relative supply pressure 1 bar

Corresponding linearised stiffness and damping coefficients calculated in determined equilibrium points are shown in Fig. 9.7 and Fig. 9.8, respectively, for nominal static bearing loads 11.87 N (solid lines) and 118.7 N (dashed lines) at relative supply pressure 1 bar.

For all examined layouts, cross-coupling stiffness coefficients k_{yz}, k_{zy} dominate over the direct stiffness coefficients. Similarly to the static analysis results, the influence of the texture located in the third quadrant (layouts Q3 and Q23) and lower static load is more significant than in the second quadrant (layout Q2). However, the stiffness coefficients are not affected identically, and cross-coupling stiffness k_{yz} remains almost unaffected in all cases. Interestingly, the texture located in the third quadrant behaves similarly to a pressure dam at really low eccentricities (low loads and high speeds), where the bearing can potentially have negative vertical stiffness k_{yy}.

The damping coefficients significantly differ at lower rotor speeds due to increased applied load, but their nominal differences are negligible for different texture layouts. However, damping coefficients are comparable at higher rotor speeds regardless of the applied load or texture layout. The only noticeable difference is in the case of coefficient b_{zz} (horizontal direction), which is increased at the nominal load by application of a texture close to the maximum hydrodynamic pressure (layouts Q3 and Q23).

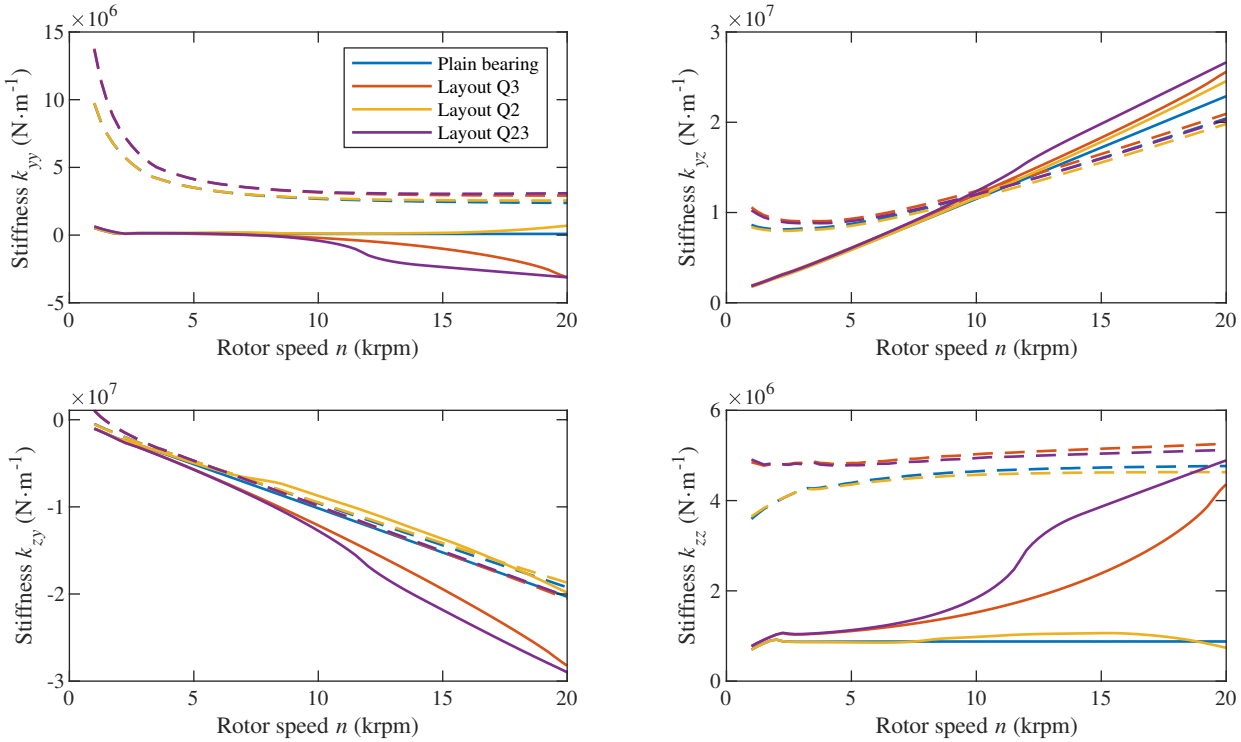

Fig. 9.7: Linearised stiffness coefficients computed for nominal load 11.87 N (solid lines) and increased load 118.7 N (dashed lines) at relative supply pressure 1 bar

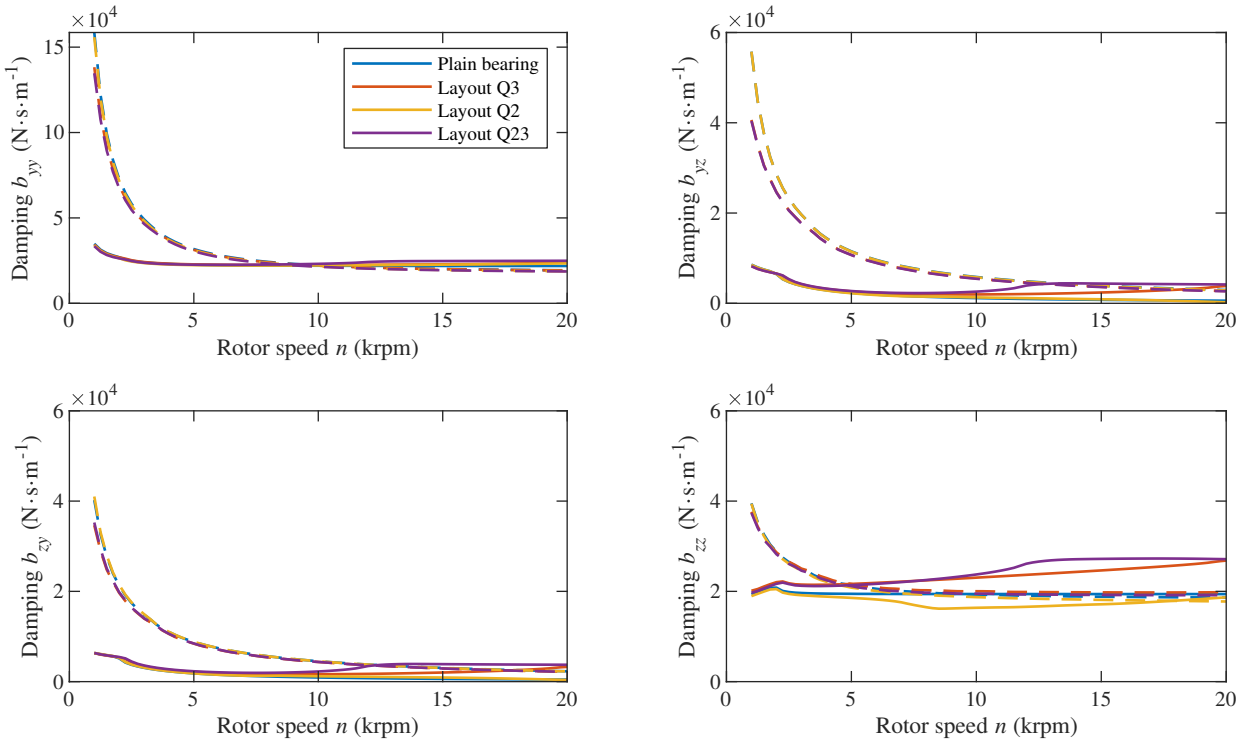

Fig. 9.8: Linearised damping coefficients computed for nominal load 11.87 N (solid lines) and increased load 118.7 N (dashed lines) at relative supply pressure 1 bar

9.2 Experimental validation

The theoretical results of this research were validated using a test rig built during the project of the Czech Science Foundation No. 17-15915S entitled *Nonlinear dynamics of rotating systems considering fluid film instabilities with the emphasis on local effects*. The test rig was built and experimental measurements were performed by cooperating colleagues at Brno University of Technology. The recorded data were postprocessed and analysed by author and colleagues from University of West Bohemia.

9.2.1 Experimental apparatus and materials

The test rig depicted in Fig. 9.9 consists of a rigid steel shaft supported on two journal bearings composed of horizontally divided shells. The shells can be replaced, which allows for testing with various texture configurations. A flexible coupling connects the shaft to an electric motor controlled by a frequency inverter which enables operation up to 20 krpm. Hydraulic oil (ISO VG 22) is pumped from a lubrication unit to each bearing through a bore in the lower shell. This unusual bearing layout, also employed by another authors [79, 100], enables external loading and easy accommodation of a unit for optical measurements. The drained oil flows back into the reservoir of the lubrication unit, which provides a continuous oil supply with adjustable oil inlet temperature and pressure.

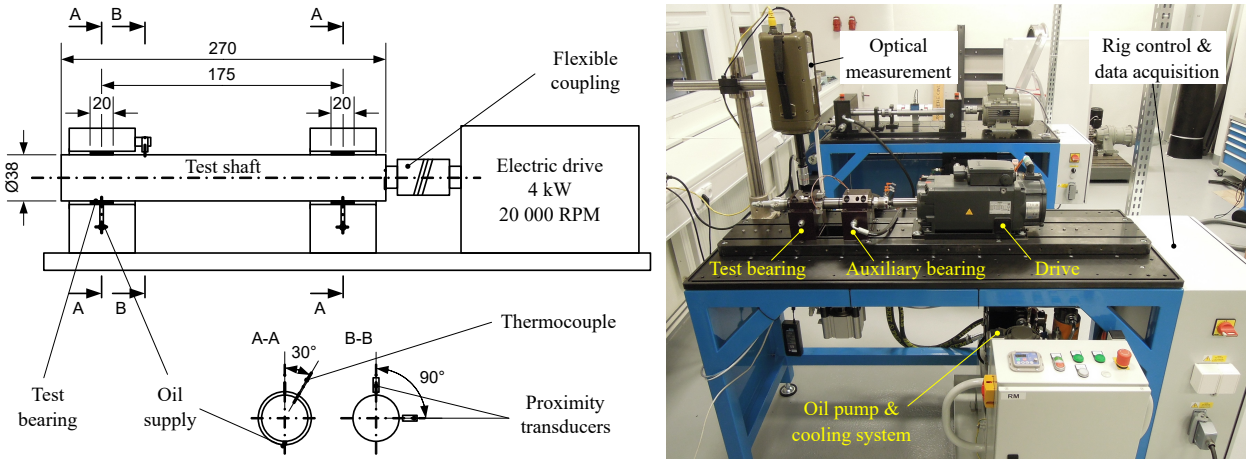

Fig. 9.9: Schematic draw of the test rig and photo of the experimental setup

The test rig is equipped with several sensors. A pair of eddy-current displacement transducers PR 6422 positioned 90° apart are situated close to the non-drive end bearing and connected to 20 kHz eddy current signal converters for measuring the rotor displacement in the horizontal and vertical directions. Bearing temperatures are measured at the outer side of the upper shells employing type K thermocouples. The oil pressure and oil temperature are measured at the inlet to the bearings with a relative pressure transmitter and thermocouple, respectively. Finally, the test rig angular speed and angular position are measured with a built-in rotary encoder in the motor. All signals are acquired by an analogue input multifunction DAQ and processed in the Labview platform.

9.2.2 Test bearings

Presented experiments are conducted using A22E bimetal bearing shells, which are usually used in main bearings of internal combustion engines and whose dimensions are shown above in Tab. 9.1. The shell of 2 mm thickness consists of back steel and Al-12Sn-3Si-1Cu alloy lining. The inner shell surface contains third-order irregularities due to the machining process, as shown in Fig. 9.10a. These irregularities are circumferential grooves of depth ca. 3.5 μm, which are ca. 150 μm apart in the axial direction.

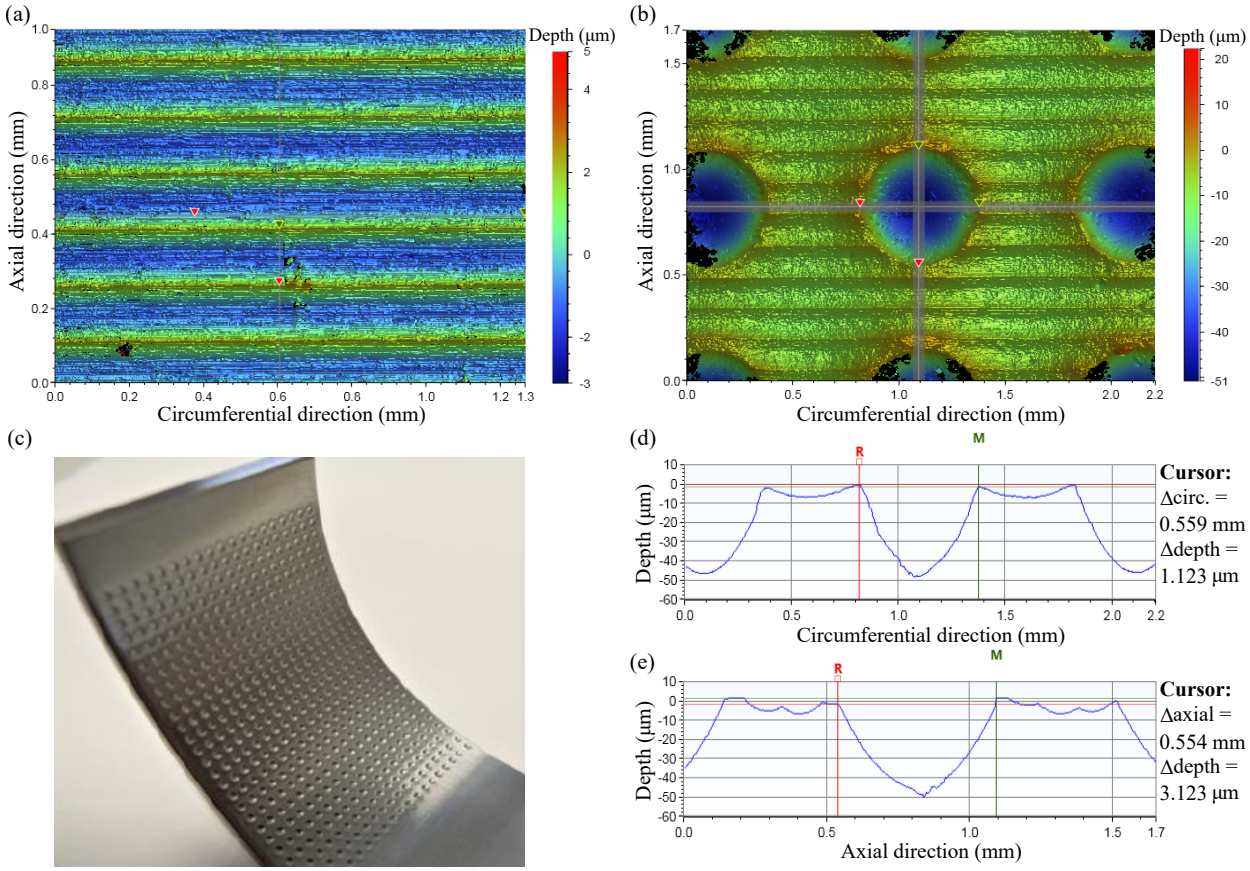

Fig. 9.10: a) Scan of the plain shell with irregularities due to machining process, b) Scan of the textured area of the shell, c) Bearing shell after mechanical indentation, d), e) Typical circumferential and axial profiles of one dimple

Mechanical indentation with a steel ball of 1.2 mm diameter is employed to produce surface texture. This procedure results in dimples shown in Fig. 9.10b and c. Each dimple has roughly 555 μm in diameter and is 45–50 μm deep. The indentation procedure leaves some excessive material at the edge of each dimple, as can be seen in Fig. 9.10d–e. This excessive material was not removed before experiments.

Tested bearing layouts are shown in Fig. 9.11. In all presented cases, the lower shell is plain and accommodates a bore for oil supply. The dimples in textured areas are arranged regularly, with centres 1 mm apart both axially and circumferentially. Such a pattern results in the approximate coverage area rate of 27 %. Fig. 9.10c indicates that the area up to 12° from the shell edge is not textured because of shell mounting in an indentation machine.

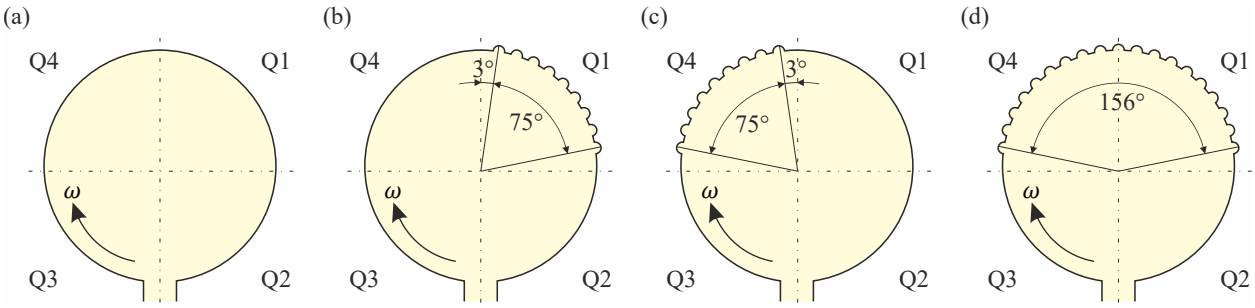

Fig. 9.11: Experimental bearing layouts: a) plain bearing, b) layout Q1, c) layout Q4, d) layout Q14.

9.2.3 Experimental procedure

The main experiment objective was to determine the threshold speed of the tested bearing layouts in a controlled and reproducible manner. Moreover, the threshold speed is influenced [101] by the oil inlet temperature. Therefore, the following steps were proposed to ensure that the test rig is warmed up thoroughly and the temperatures are stabilised:

1. Determine the bearing centre; set offsets (zero positions) of the proximity transducers.
2. Start the oil circulation system and run up the motor to a moderate speed (1 krpm). Operation at this speed ensures that the bearing gap is fully flooded, and the influence of mixed lubrication is negligible.
3. Adjust the oil inlet pressure and temperature, wait until the desired temperature is reached and the bearing shell temperature stabilises.
4. Start data recording.
5. Increase the rotor speed up to 20 krpm with angular acceleration 20 krpm·min^{-1}.
6. Decrease the rotor speed to 1 krpm and wait until the temperatures are stabilised.
7. Stop data recording and save the data.
8. Repeat or stop the experiment.

9.2.4 Experimental results

Experimental results are depicted in Fig. 9.12 – Fig. 9.16. Each figure consists of records from both run-up and coast-down, including spectrograms and peak-to-peak envelopes of relative rotor displacement and time series of bearing and oil temperatures and spectrograms. Similar procedure of subsynchronous order tracking for threshold speed detection as presented in Sec. 8.3 was employed.

The journal oscillates synchronously with relatively small and almost constant magnitudes caused due to out-of-balance force until it reaches the threshold speed. After surpassing the threshold speed, oscillations increase, and a subsynchronous component close to 0.5 of the rotor speed appears. The subsynchronous component can be interpreted as self-excited

vibration due to the oil whirl. Upon slowly reducing the rotor speed from 20 krpm to 1 krpm, the oil whirl disappears at a lower threshold speed than developed during the run-up. This difference indicates possible hysteresis behaviour of the system which has been studied in [19, 37] and it was proposed an analytical approach for predicting the hysteresis using the Hopf bifurcation theory. The hysteresis behaviour was previously numerically simulated and experimentally validated on the laboratory Rotor Kit RK4 in this work in Chap. 8.

It was proved that the hysteresis occurs only in some journal bearings. Here, it is not entirely possible to conclude whether hysteresis occurs or not because the bearing temperatures differ significantly between the run-up and cost-down. Although the oil inlet temperature remains practically constant during the experiment, the bearing shell temperature evolves rapidly due to viscous friction which grows with increasing speed.

In the case of the bearing with layout Q1, there is an apparent subsynchronous resonance between 3000 and 4000 rpm, see Fig. 9.13 and Fig. 9.15. The resonance is accompanied by the forward rotor motion. The exact nature of this resonance is not entirely clear and may be caused due to fluctuations in the oil inlet pressure [A6] or due to transition from mixed to fully hydrodynamic lubrication [100]. Incidentally, the subsynchronous resonance was suppressed at higher oil supply pressures, see Fig. 9.16.

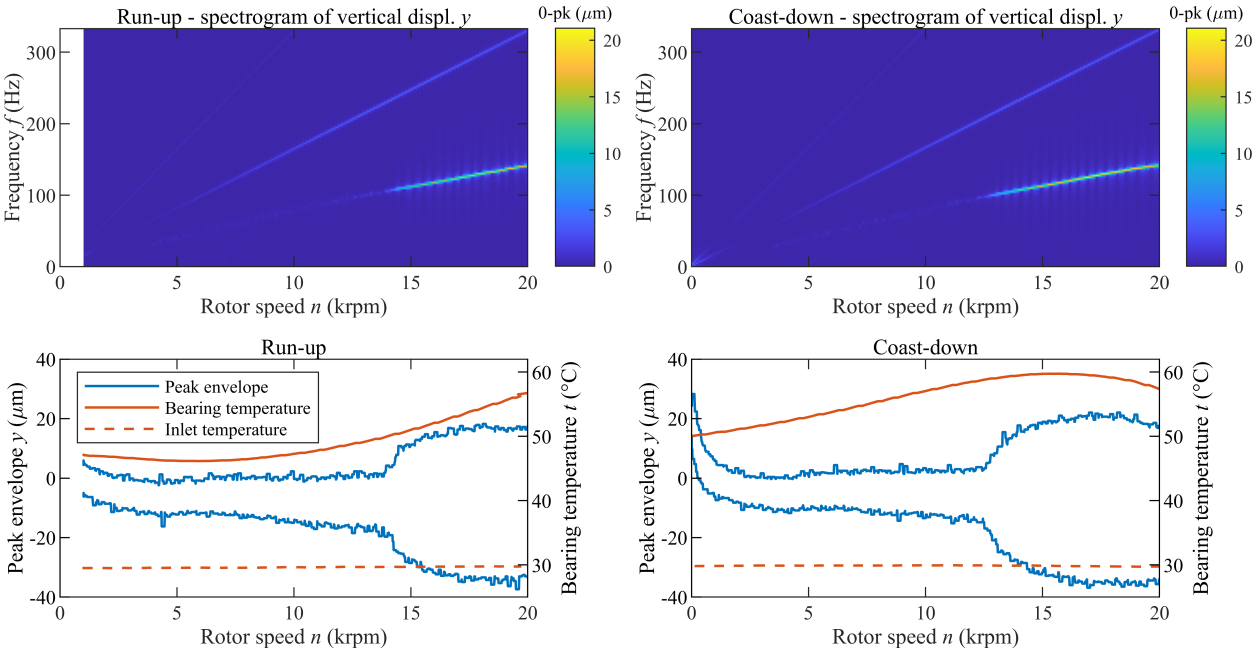

Fig. 9.12: Spectrograms of journal vertical displacement and time series of peak-to-peak envelope and shell temperature for plain bearing and nominal inlet pressure 1 bar

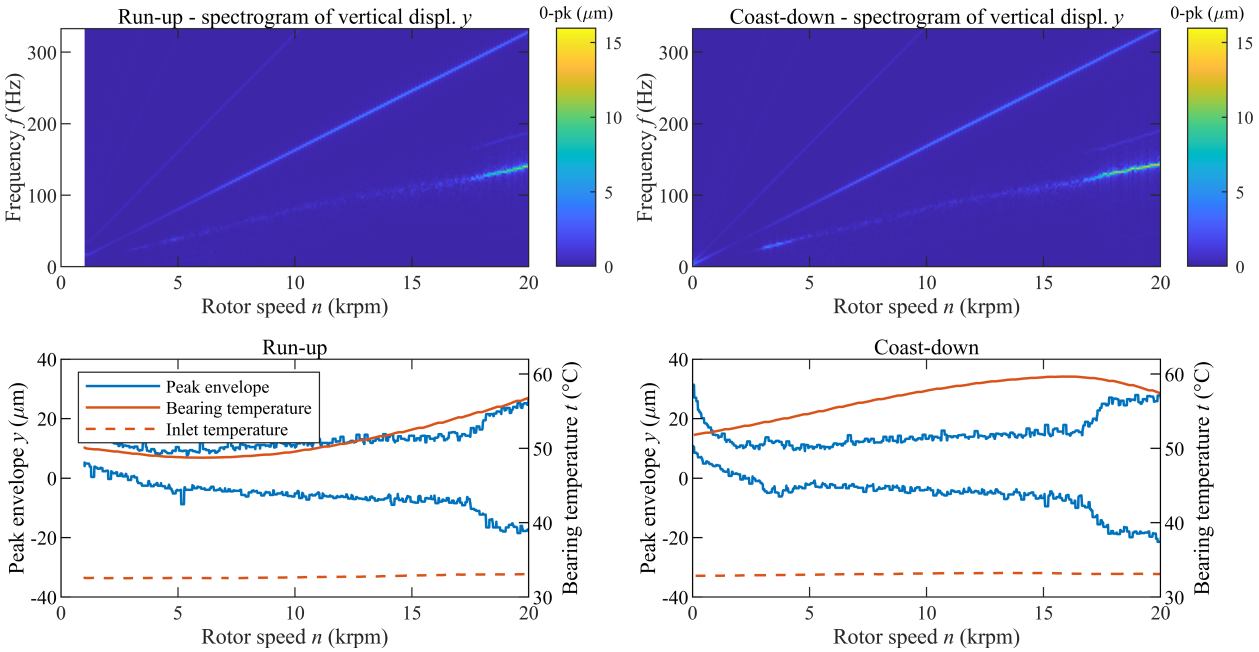

Fig. 9.13: Spectrograms of journal vertical displacement and time series of peak-to-peak envelope and shell temperature for bearing with layout Q1 and nominal inlet pressure 1 bar

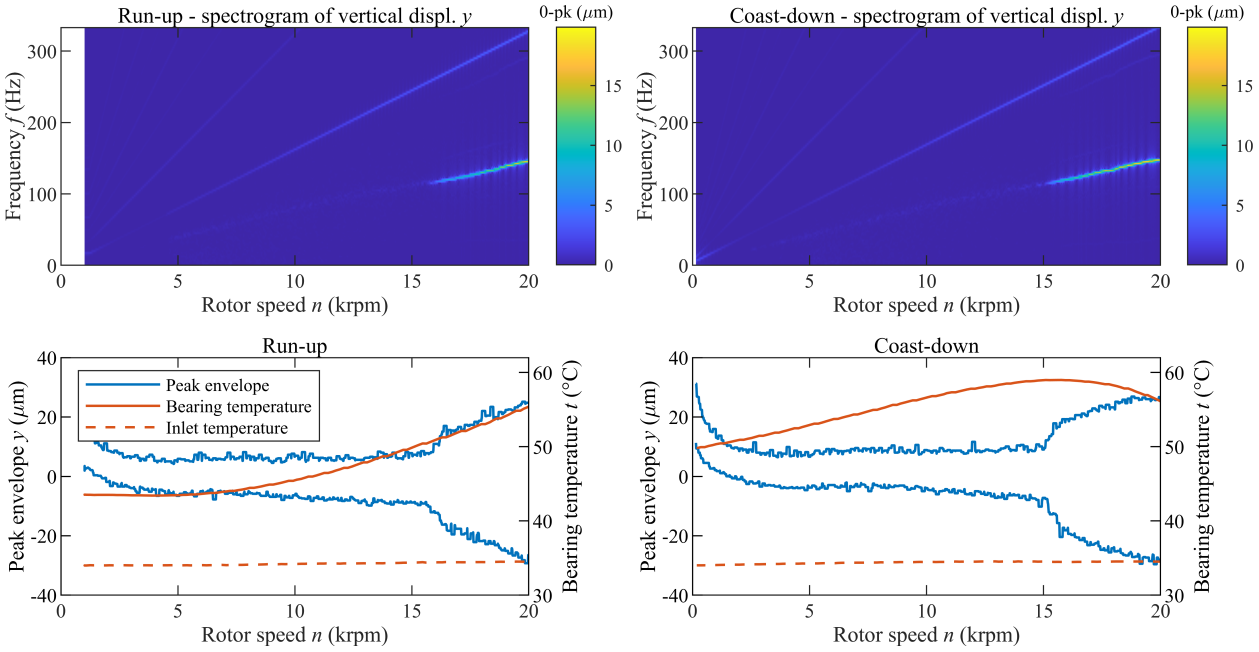

Fig. 9.14: Spectrograms of journal vertical displacement and time series of peak-to-peak envelope and shell temperature for bearing with layout Q4 and nominal inlet pressure 1 bar

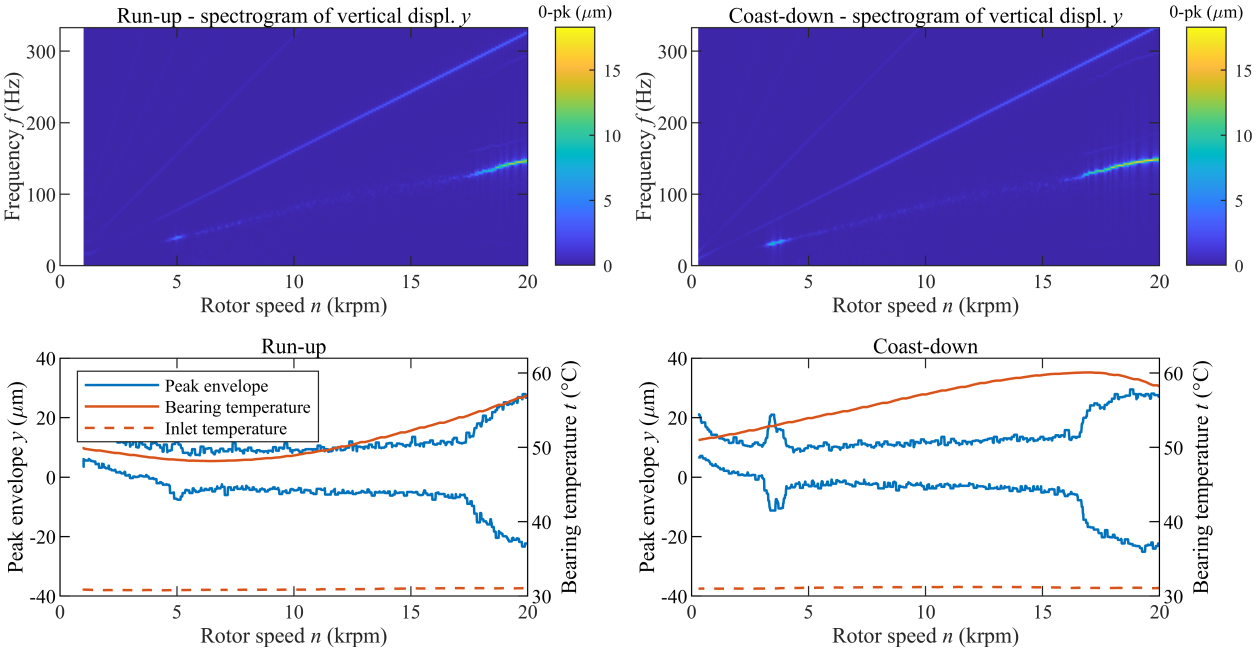

Fig. 9.15: Spectrograms of journal vertical displacement and time series of peak-to-peak envelope and shell temperature for bearing with layout Q14 and nominal inlet pressure 1 bar

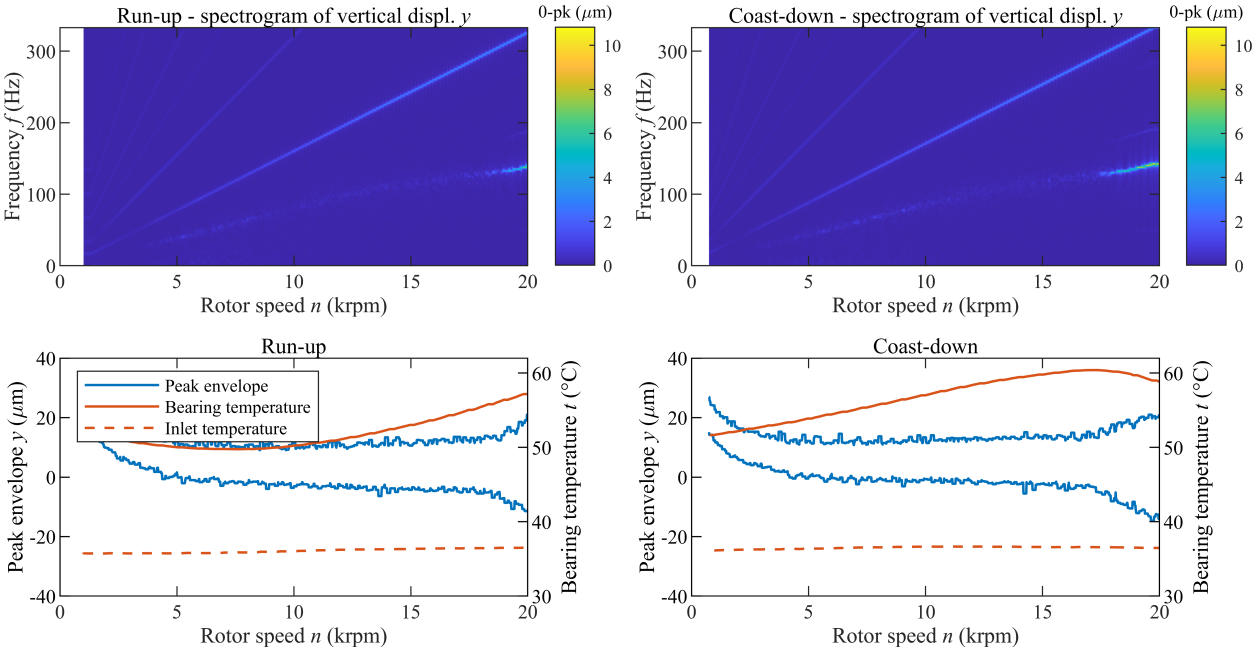

Fig. 9.16: Spectrograms of journal vertical displacement and time series of peak-peak envelope and shell temperature for bearing with layout Q14 and nominal inlet pressure 1.5 bar

Maximum bearing temperatures are summarised in Fig. 9.17 in dependence on the average oil inlet temperature. The oil in the circulation system was heating up during the experiment because the maximum bearing temperature is notably higher than the oil inlet temperature. The difference is ca. 25 °C during run-ups and ca. 30 °C during coast-downs. In theory, these diagrams can reveal the influence of the texture on the total friction in the system. Here, the results are difficult to interpret, although it appears that layout Q1 (i.e. the texture in the loaded area of the bearing) might reduce the friction losses. On the contrary, the bearings with the texture in the unloaded area (layouts Q14, Q4) performed similarly to the plain bearing.

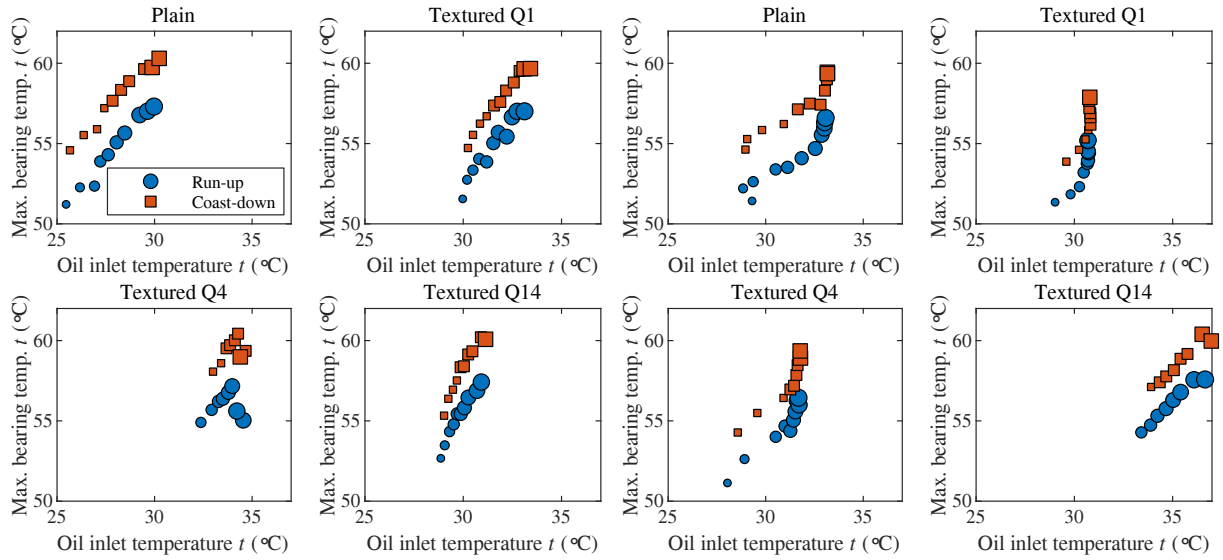

(a) Inlet nominal pressure 1 bar (b) Inlet nominal pressure 1.5 bar

Fig. 9.17: Comparison of maximum measured bearing temperature in dependence on oil inlet temperature for different nominal inlet pressure and distinguished for run-up and coast-down operation. Increasing size of markers denotes the index of repeated measurement

The textures positively influence the peak-to-peak displacement when the fluid-induced instability is developed. Maximum peak-to-peak displacements are depicted in Fig. 9.18. As in the previous case, the results are strongly dependent on the bearing temperatures. The texture in the loaded area (layouts Q1, Q14) of the bearing can reduce vibration by more than 10 % at the given bearing temperature. The texture in the unloaded area (layout Q4) has certain effect only at the higher oil inlet pressure. Moreover, the fluid-induced instability was not fully developed in the bearing with layout Q1 supplied at 1.5 bar. In this configuration, the depicted peak-to-peak displacement corresponds with the synchronous response due to out-of-balance forces. This behaviour was also observed during several initial measurements with layouts Q4 and Q14, see Fig. 9.18b.

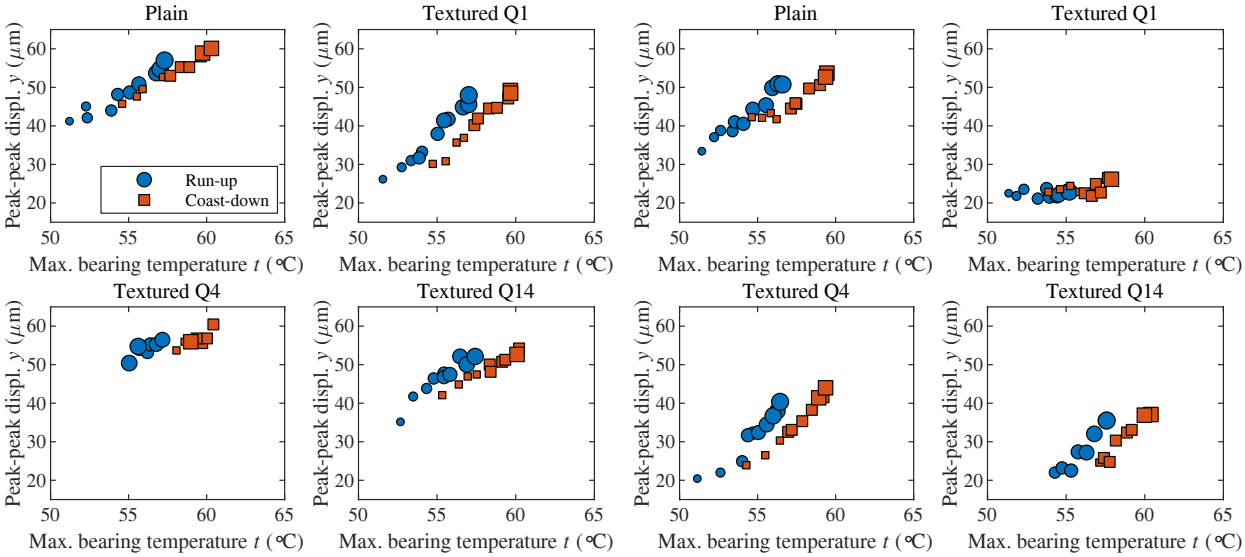

(a) Inlet nominal pressure 1 bar (b) Inlet nominal pressure 1.5 bar

Fig. 9.18: Diagram of maximum peak-peak envelope and maximum bearing temperature for different nominal inlet pressure and distinguished for run-up and coast-down operation. Increasing size of markers denotes the index of repeated measurement

9.2.5 Comparison of numerical and experimental results

Direct comparison of the threshold speeds obtained computationally and experimentally is shown in Fig. 9.19. Here, the results are depicted in dependence on both the bearing shell temperature and the oil inlet pressure. Since both these parameters evolve during the experiment, the displayed data represent current values when the threshold speed is detected.

Constant journal speed is assumed for the numerical assessment of the stability to reduce computational costs. Since the experimental results are obtained with the changing journal speed, the experimental results differ from the numerical results. Influence of the journal angular acceleration on the threshold speed is studied in previous Sec. 5.5 and it is concluded that the threshold speed under unsteady conditions is higher than under the steady-state conditions. This conclusion is in line with the presented comparison in Fig. 9.19.

Threshold speed shift during experimental run-up relatively to computational results is apparent in the case of the plain bearing and layouts Q1 and Q4. Moreover, the experimental data show the same relationships between the temperatures and threshold speeds as the theoretical prediction. The system also exhibits the hysteresis behaviour mentioned above and discussed in [37]. The hysteresis phenomenon is likely present also in the case of the Q14 layout. In this case, however, some experimentally determined threshold speeds are lower than expected. The oil inlet pressures partially caused this discrepancy because they were measured lower than nominal values 1.0 and 1.5 bar used in simulations. Other inaccuracies are probably present due to the isoviscous approximation. The isoviscous approximation returns a reasonable estimate of rotor dynamics if the converging part of the bearing gap is smooth and the oil inlet flow is higher than the bearing leakage. Here, thermodynamic effects due to the texture are apparently not negligible.

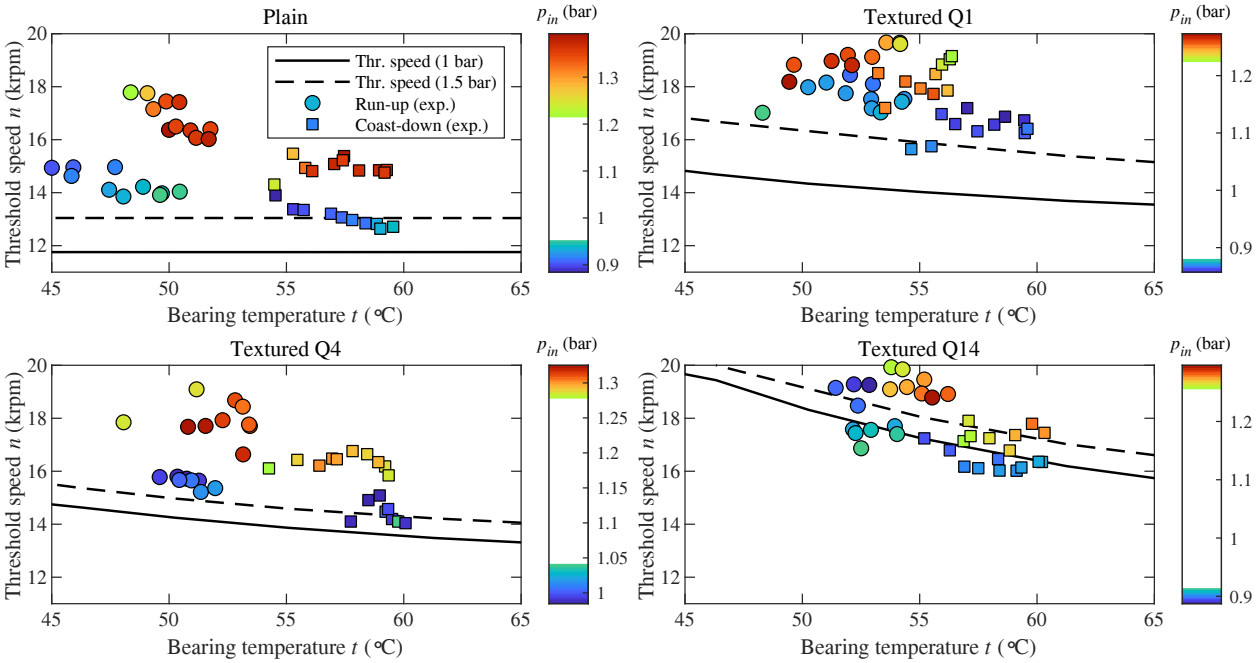

Fig. 9.19: Comparison of calculated threshold speeds with detected rotor speed at the beginning of fluid-induced instability during experiments for various bearing geometries. Run-up and coast-down operations are distinguished by different marker. Colour order depicts the value of inlet pressure at the moment of threshold speed detection

9.3 Results summary

Although the use of the Gümbel condition for cavitation modelling might appear inappropriate, it is demonstrated that errors due to non-conservation of mass are of the same magnitude as uncertainties due to employed numerical methods. Furthermore, the results converge to their limit values at very fine meshes at which the solution of the Elrod equation is very time-consuming. Therefore, the Gümbel condition can be used only for dynamics simulation and not for mass-related tribological parameters such as bearing leakage or power losses.

Based on the theoretical results, the textures produced by the indentation method can be used to improve the stability of lightly loaded journal bearings. The most effective tested layouts are textured close to the minimum oil film thickness. This observation qualitatively corresponds with works [63, 64, 102]. The theoretical threshold speed depends strongly on the density of the computational mesh. The presented simulations employ the mesh with $1.38 \cdot 10^6$ nodes, which is ten to a hundred times more than in other contemporary works employing the finite difference method [64, 103, 67].

Theoretical results have been successfully validated experimentally. The experimental results suggest that some textured bearings cannot be considered isoviscous even if they are well lubricated and only lightly loaded. In summary, the experiments show that texturing in the loaded area (tested layouts Q1, Q14) noticeably improves the stability of the lightly loaded journal bearings. Effects of textures in the unloaded area (tested layout Q4) are minor, although they also improve stability.

10 Conclusions

Several key points of this dissertation were stated in the introduction. This final chapter summarises each research topic and concludes obtained results.

10.1 A unified and comprehensive model for various bearing types

The basis of the hydrodynamic lubrication theory is introduced and briefly described in Chap. 2. It includes various Reynolds equation forms, boundary and cavitation conditions, integration of the pressure field to evaluate the hydrodynamic force and, finally, the process of hydrodynamic force linearisation to estimate dynamic coefficients. The stability analysis of the 2 DoF rotor-bearing model is performed based on the Routh-Hourwitz criterion.

The theoretical background for cylindrical bearings is extended and applied for various journal bearing types, including fixed-bearing geometry and tilting pad journal bearings. This unified and comprehensive modelling of various journal bearing types is presented in Chap. 3. This thesis proposed a general planar model of the bearings with rigid bearing shells (pads) carried by flexible pivots or fixedly oriented concerning the bearing centre. The model is developed using two key features which allow a simplistic formulation of the mathematical model without compromising its nonlinear properties:

- Equations of motion for each pad are formulated in an auxiliary coordinate system with the origin in a pivot point. The usage of the auxiliary coordinate system enables direct modelling of elastic contact between the journal and the pad, which simplifies the formulation of equations of motion.

- The Reynolds equation describing the pressure field on the particular pad is defined in a local coordinate system that moves together with the pad. The system origin is positioned so that simple formula for the gap in the cylindrical journal bearing can describe the gap between the journal and the pad. This simple formula can also be employed if the pad is preloaded and supported on the flexible pivot.

A detailed step-by-step discussion regarding the model formulation is provided. However, this work does not discuss other possible topics, including hydrodynamic lubrication in the turbulent regime, thermodynamics, influence of elastic deformations and kinematics of some advanced pivot designs such as ball-in-socket. Nevertheless, the proposed approach can be easily reproduced and further extended because the role of these phenomena in the cylindrical journal bearings have been extensively discussed.

10.2 Development of the complex in-house software

The presented generalised computational model for various bearing types is implemented into an in-house software written in MATLAB. The software is based on the finite difference method to solve the hydrodynamic pressure, evaluate the hydrodynamic force and estimate the linearised dynamic coefficients. In addition, it also contains several alternative modules resulting from the analytical solution of the hydrodynamic force and stiffness and damping coefficients. The software can perform static and stability analysis, time domain simulations, including steady-state simulations or run-up and coast-down operations simulations.

Chap. 4 is focused on the analytical closed-form solutions and numerical implementation of hydrodynamic lubrication problems employing the finite difference method.

The analytical software module consists of adopted closed-forms of the hydrodynamic force of limit bearing cases and finite length bearings, corresponding linearised dynamic coefficients and linearised stiffness and damping coefficients for finite length bearings originally derived by author (Appendix A).

The numerical procedure implementation is introduced very instructively and quickly reproducible. Despite analytical approach modelling, the numerical approach allows various boundary conditions, e.g. oil supply represented by supplied pressure. The properties of the finite difference method are investigated in Chap. 5. In the case of the fixed coordinate system used for the Reynolds equation formulation, the jumps related to the mesh density in the circumferential direction occur in equilibrium points and linearised dynamic coefficients. The computational time costs were improved with the compiling into the `mex` format.

All numerical simulations presented in this thesis were performed in the developed in-house software.

10.3 Numerical simulations for various bearing types

The linearised dynamic coefficients of the cylindrical journal bearing calculated by the analytical and numerical approach and the threshold speed resulting from the stability analysis are compared in Chap. 5. The results show that the infinitely short journal bearing model and its correction for the finite length bearings satisfy the solution by the finite difference method across a wide range of length-to-diameter ratios and rotor speed. The analytical models based on the infinitely long journal bearing differ from other solutions for relative eccentricity lower than 0.5. In addition, analytical models have significantly reduced computational demands compared to the finite difference method.

Next, a simple 2 DoF rotor-bearing system with cylindrical journal bearing is investigated in transient simulations with various design parameters, angular accelerations, and static unbalances, see Chap. 5. The threshold speeds are distinguished into two boundaries: first, the speed when the instability starts to develop, and second, the speed when the instability is fully developed. The threshold speed detection is provided automatically from the time series. The fluid-induced instability is developed at higher rotor speed with increasing angular acceleration. The area width between both threshold speeds continually decreases with decreasing angular acceleration. Theoretically, for infinitely long run-up, the threshold speed identifies with the analytically established borderline. In the case of applied static

unbalance, a period-doubling region occurs before reaching threshold speed. The bifurcation then disappears with increased rotor speed. The width of this region and oscillations increase with the increasing magnitude of static unbalance. In addition, the static unbalance in the system also influences the threshold speed of the fluid-induced instability.

The fixed-profile journal bearing, such as elliptical and offset halves bearings, are analysed in Chap. 6. Firstly, the computational model of elliptical journal bearings based on the generalised planar model is successfully validated with reference data [38]. Then, the steady-state simulations is performed to analyse the stability. Interestingly, the system response to the harmonic excitation due to applied static unbalance significantly differ for various static loads. The unstable regime's response irregularly changes from quasiperiodic motion to N-periodic motion, and occasionally multiple period-doubling occurs after surpassing the threshold speed. Presented bifurcation diagrams, spectrograms, phase portraits and Poincaré maps describe this behaviour. For several static loads and unbalances cases, the quasiperiodic motion has a dominant subsynchronous variable component in the range ca. 0.42X–0.51X with increasing rotor speed. Examined period-doubling bifurcation in cylindrical journal bearings also exists in elliptical and offset halves journal bearing before reaching the threshold speed.

The proposed comprehensive approach in journal bearing modelling is used to investigate the behaviour of tilting pad journal bearings in Chap. 7 where the four-segment tilting pad journal bearing in load-between pad configuration with flexible pivots is analysed. First, similar to the fixed-profile journal bearings, the model is successfully validated with reference data [38] and other research journal articles. Next, the steady-state response to harmonic excitation is shown. An obtained complex pad's motion is analysed with spectrograms, bifurcation diagrams, Lyapunov exponents, phase trajectories and waveforms of the interaction forces. It is observed that the excessive pad preload strengthen interactions between individual subsystems. Interestingly, the preloaded upper pads exhibit period-doubling or chaotic motion. The motion of the upper pads depends on the position of pivots and undesirable single-sided impacts of the pad's edge to the journal occur. Decreased assembled clearance has a stabilising effect on lightly loaded pad 2 and pad fluttering disappears.

10.4 Textured journal bearing and stability analysis

The previously developed models and methods are extended for the modelling of textured journal bearings. Cylindrical textured journal bearings with dimples produced by ball indentation are investigated in Chap. 9. Several texture layouts are analysed for the texture influence on the stability threshold speeds. Based on the numerical simulations, it is stated that the proposed texture positively influence the threshold speed. If the texture is located in the convergent part of the bearing gap close to minimum film thickness, the trajectory is significantly different and the instability develops at a higher rotor speed. Another observation is stated for computational demands in textured bearing modelling. It is necessary to use a very dense mesh for hydrodynamic pressure calculation compared to plain cylindrical bearings. For this reason, the transient simulations are ineffective in computational time costs as well as employing of time-consuming mass-conserving cavitation conditions.

10.5 Experimental validation

The first experimental validation is performed on the Bently Nevada RK 4 Rotor Kit in Chap. 8. This experimental measurement is focused on the influence of angular acceleration and deceleration on unstable behaviour development and threshold speed hysteresis behaviour. For direct comparison with numerical simulations, two models, a simplified 2 DoF rotor-bearing model and a comprehensive model with a flexible shaft and other couplings, are implemented in the in-house software. The hysteresis loop widths obtained from both experimental and computational approaches are comparable. The nominal experimental threshold speeds are lower than examined from numerical simulations. However, the difference is still reasonable due to the problematic test-rig parameter identification, test-rig assembling misalignment, the supply pressure fluctuation, temperature-dependent lubricant parameters.

The second experimental validation of the proposed computational model is provided for textured journal bearing stability investigation. The results of the analyses with detailed test-rig descriptions are written in Chap. 9. The experimental measurements and the numerical results qualitatively show that the texturing close to minimum film thickness noticeably improves the fluid-induced instability but the angular acceleration effect should be considered. Furthermore, the texture present in the loaded area reduces the vibrations when the fluid-induced instability is developed. The textures located in the unloaded area still but minorly positively affect the stability. Finally, the experimental results reveal that the isoviscous lubricant approximation in texturing applications is not negligible.

10.6 Original contributions of this thesis

The presented thesis focuses on developing and implementing the comprehensive model of various journal bearing types and investigating their behaviour in terms of mutual interaction with the rotor and system stability assessment. The original contributions in the research of the rotating systems supported on the various journal bearing are summarised as follows:

- The unified and comprehensive modelling approach of various journal bearing types with possible elastic contact between the journal and the bearing parts was developed and described in detail. This modelling approach was successfully validated with reference data [38], and also peer-reviewed in the author's journal article [A7].
- Based on the presented theory in the thesis, the complex in-house software was implemented to determine the equilibrium points, assess the system stability based on various criteria (tools) and perform the transient simulations.
- Original contribution in the field of analytical approach is the derivation of the closed-form linearised stiffness and damping coefficients for plain cylindrical finite length bearings. These formulae were also published by the author in [A2] and then used to assess the stability of turbochargers supported on the floating-ring bearings [A5].
- The analytical and numerical (finite difference method) methods were compared and studied their properties and suitability for chosen applications. The influence of angular acceleration on the fluid-induced instability was published in journal article [A8].

- The influence of the angular acceleration/deceleration and hysteresis behaviour was experimentally validated using the Bently Nevada RK 4 Rotor Kit.
- The period-doubling bifurcation in the fixed profile journal bearing before reaching the threshold speed was investigated. In addition, the irregular changes between the N-periodic motion and quasiperiodic journal response were documented.
- The pad fluttering phenomenon with single-sided impacts and its origin and characteristic was analysed and described in the thesis. The simulations reveal that the tilting pad journal bearings can be operated above pad fluttering, and new equilibrium branches of the system can be found during the operations. This topic was also investigated and published in author's publications [A7, A9].
- Contrary to research articles related to the journal bearing texturing, the numerical simulations performed in the dissertation show that using a significantly denser computational mesh in evaluating the hydrodynamic force and threshold speeds is necessary to converge to their limit values.
- It was computationally and experimentally validated that the proposed texture produced by ball indentation and located close to the minimum film thickness positively influenced the system stability and shifted the thresholds speed upwards. The texture present also reduced the rotor vibrations when fluid-induced instability was developed.

The author published particular research topics at the conferences, in the proceedings and their list is attached in the dedicated part of the bibliography.

10.7 Future research

Based on the presented topics and actual research, this work can be further enhanced and specified by the following research tasks:

- Implementation of mass-conserving algorithm and enhanced cavitation modelling
- Temperature-dependent lubricant parameters and heat exchange with solid parts
- Calculation of tribological parameters, e.g. friction losses, bearing leakage, oil film starvation etc.
- Suppression of undesirable phenomena in tilting pad journal bearings that cause fatal damage to their parts
- Improvement of numerical methods to reduce computational costs, e.g. using artificial neural networks [B16]
- Application of developed computational tools in thrust bearings and combined bearings

Bibliography

[1] W. J. Chen, Practical Rotordynamics and Fluid Film Bearing Design, Trafford Publishing, 2015.

[2] H. Nguyen-Schäfer, Rotordynamics of Automotive Turbochargers, Springer-Verlag, Berlin, 2012.

[3] R. Gasch, R. Nordman, H. Pfützner, Rotordynamik, Springer-Verlag, Berlin, 2006.

[4] E. Krämer, Dynamics of Rotors and Foundations, Springer-Verlag, Berlin Heidelberg, 1993.

[5] J. Vance, F. Zeidan, B. Murphy, Machinery Vibration and Rotordynamics, Wiley, New Jersey, 2010.

[6] M. Byrtus, M. Hajžman, V. Zeman, Dynamika rotujících soustav, Západočeská univerzita v Plzni, Plzeň, 2010.

[7] P. Flores, J. Ambrósio, J. Pimenta Claro, H. M. Lankarani, Kinematics and Dynamics of Multibody Systems with Imperfect Joints: Models and Case Studies, Springer-Verlag, Berlin, 2008.

[8] A. Muszyńska, Rotordynamics, Taylor & Francis, Boca Raton, 2005.

[9] O. Reynolds, On the theory of lubrication and its application to mr. beauchamp tower's experiments, including an experimental determination of the viscosity of olive oil 177 (1886) 157–234.

[10] A. Sommerfeld, Zur hydrodynamischen theorie der schmiermittelreibung, Z. Math. Phys. 50 (1-2) (1904) 97–155.

[11] F. W. Ocwirk, Short-bearing approximation for full journal bearings, Tech. rep., Cornell University (1952).

[12] D. Sfyris, A. Chasalevris, An exact analytical solution of the reynolds equation for the finite journal bearing lubrication, Tribology International 55 (2012) 46 – 58.

[13] G. W. Stachowiak, A. W. Batchelor, Engineering Tribology, Butterworth-Heinemann, Boston, 2014.

[14] S. Wen, P. Huang, Principles of Tribology, Wiley, Boston, 2012.

[15] J. Larsen, I. Santos, Efficient solution of the non-linear reynolds equation for compressible fluid using the finite element method, Journal of the Brazilian Society of Mechanical Sciences and Engineering 37 (3) (2015) 945—-957.

[16] F. Profito, M. Giacopini, D. Zachariadis, D. Dini, A general finite volume method for the solution of the reynolds lubrication equation with a mass-conserving cavitation model, Tribology Letters 60 (18) (2015) 1–21.

[17] F. Profito, On the development of advanced techniques for mixed-elastohydrodynamic lubrication modelling of journal and sliding bearing systems, Ph.D. thesis (11 2015).

[18] M. M. Khonsari, E. R. Booser, Applied Tribology, Wiley, New Delhi, 2017.

[19] J. K. Wang, M. M. Khonsari, Thermodynamic Instability in Fluid-Film Bearings, Wiley, Chichester, 2016.

[20] Y. Hori, Hydrodynamic Lubrication, Springer-Verlag, Tokyo, 2006.

[21] T. Okazaki, Y. Hori, The theory of oil-whip in journal bearings, Transactions of the Japan Society of Mechanical Engineers 21 (102) (1955) 125–130.

[22] J. W. Lund, B. Sternlicht, Rotor-bearing dynamics with emphasis on attenuation, Journal of Basic Engineering 84 (4) (1962) 491–498.

[23] G. G. Vignolo, B. D. O., L. M. Quinzani, Approximate analytical solution to reynolds equation for finite length journal bearings, Tribology International 44 (1) (2011) 1089–1099.

[24] J. V. Fedor, Half sommerfeld approximation for finite journal bearings, Journal of Basic Engineering 85 (3) (1963) 435–438.

[25] P. C. Warner, Static and dynamic properties of partial journal bearings, Journal of Basic Engineering 85 (2) (1963) 247–257.

[26] L. E. Barrett, P. Allaire, E. Gunter, A finite length bearing correction factor for short bearing theory, Journal of Lubrication Technology 102 (3) (1980) 283–287.

[27] H. Hirani, K. Athre, S. Biswas, Dynamically loaded finite length journal bearings: Analytical method of solution, Journal of Tribology 121 (4) (1999) 844–852.

[28] Y. Bastani, M. Queiroz, A New Analytic Approximation for the Hydrodynamic Forces in Finite-Length Journal Bearings, Journal of Tribology 132 (1) (2009).

[29] J. W. Lund, Review of the Concept of Dynamic Coefficients for Fluid Film Journal Bearings, Journal of Tribology 109 (1) (1987) 37–41.

[30] J.-R. Lin, Linear stability analysis of rotor-bearing system: couple stress fluid model, Computers & Structures 79 (8) (2001) 801 – 809.

[31] S. M. A. Akers, A. Cameron, Stability contours for a whirling finite journal bearing, Journal of Lubrication Technology 93 (1) (1971) 177–183.

[32] J. K. Wang, M. M. Khonsari, Bifurcation analysis of a flexible rotor supported by two fluid-film journal bearings, Journal of Tribology 128 (3) (2006) 594–603.

[33] M. T. M. Crooijmans, H. J. H. Brouwers, D. H. van Campen, A. de Kraker, Limit cycle predictions of a nonlinear journal-bearing system, Journal of Engineering for Industry 112 (2) (2008) 168–171.

[34] Y, Huang, Z. Tian, R. Chen, C. Haiyin, A simpler method to calculate instability threshold speed of hydrodynamic journal bearings, Mechanism and Machine Theory 108 (2017) 209 – 216.

[35] M. Chouchane, A. Amamou, Bifurcation of limit cycles in fluid film bearings, International Journal of Non-Linear Mechanics 46 (9) (2011) 1258 – 1264.

[36] A. Boyaci, Numerical continuation applied to nonlinear rotor dynamics, Procedia IUTAM 19 (Supplement C) (2016) 255 – 265, iUTAM Symposium Analytical Methods in Nonlinear Dynamics.

[37] J. K. Wang, M. M. Khonsari, On the hysteresis phenomenon associated with instability of rotor-bearing systems, Journal of Tribology 128 (1) (2006-01-01) 188–196.

[38] T. Someya, Journal-Bearing Databook, Springer-Verlag, Berlin, 1989.

[39] G. Daniel, K. Cavalca, Investigation of the influence of thermal effects in the dynamic coefficients of a tilting pad journal bearing, Institution of Mechanical Engineers - 10th International Conference on Vibrations in Rotating Machinery (2012) 479–489.

[40] T. W. Dimond, A. A. Younan, P. E. Allaire, Comparison of tilting-pad journal bearing dynamic full coefficient and reduced order models using modal analysis, in: inproceedings of the ASME Turbo Expo 2009: Power for Land, Sea, and Air, 2009, pp. 1043–1053.

[41] Z. Yan, L. Wang, G. Qiao, T. Zheng, An analytical model for complete dynamical coefficients of a tilting-pad journal bearing, Tribology International 43 (1) (2010) 7 – 15.

[42] R. D. Flack, C. J. Zuck, Experiments on the stability of two flexible rotors in tilting pad bearings, Tribology Transactions 31 (2) (1988) 251–257.

[43] R. Brancati, E. Rocca, R. Russo, Non-linear stability analysis of a rigid rotor on tilting pad journal bearings, Tribology International 29 (7) (1996) 571 – 578.

[44] A. M. Haugaard, I. F. Santos, Stability of multi orifice active tilting-pad journal bearings, Tribology International 43 (9) (2010) 1742 – 1750.

[45] D. Hargreaves, M. Fillon, Analysis of a tilting pad journal bearing to avoid pad fluttering, Tribology International 40 (2007) 607–612.

[46] M. Adams, S. Payandeh, Self-excited vibration of statically unloaded pads in tilting-pad journal bearings, Journal of Tribology 105 (3) (1983) 377–383.

[47] S. H. Yang, C. Kim, Y.-B. Lee, Experimental study on the characteristics of pad fluttering in a tilting pad journal bearing, Tribology International 39 (7) (2006) 686 – 694.

[48] P. Pennacchi, A. Vania, S. Chatterton, E. Pesatori, Case history of pad fluttering in a tilting-pad journal bearing, in: inproceedings of ASME Turbo Expo 2010: Power for Land, Sea and Air, 2010, pp. 1–7.

[49] K. Ikeda, T. Hirano, T. Yamashita, M. Mikami, H. Sakakida, An experimental study of static and dynamic characteristics of a 580mm(22.8in.) diameter direct lubrication tilting pad journal bearing, Journal of Tribology 128 (1) (2006) 146–154.

[50] J. W. Lund, Spring and damping coefficients for the tilting-pad journal bearing, ASLE Transactions 7 (4) (1964) 342–352.

[51] J. C. Nicholas, E. J. Gunter, P. E. Allaire, Stiffness and damping coefficients for the five-pad tilting-pad bearing, A S L E Transactions 22 (2) (1979) 113–124.

[52] W. J. Chen, Bearing dynamic coefficients of flexible-pad journal bearings, Tribology Transactions 38 (2) (1995) 253–260.

[53] J. Kim, A. Palazzolo, R. Gadangi, Dynamic Characteristics of TEHD Tilt Pad Journal Bearing Simulation Including Multiple Mode Pad Flexibility Model, Journal of Vibration and Acoustics 117 (1) (1995) 123–135.

[54] P. Dang, S. Chatterton, P. Pennacchi, The effect of the pivot stiffness on the performances of five-pad tilting pad bearings, Lubricants 61 (2019) 1–24.

[55] S.-H. Jeung, J. Suh, H. Yoon, Performance of tilting pad journal bearings with the same sommerfeld number, Applied Sciences 10 (3529) (1995) 1–15.

[56] Z. Shi, Y. Jin, X. Yuan, Influence of pivot design on nonlinear dynamic analysis of vertical and horizontal rotors in tilting pad journal bearings, Tribology International 140 (2019) 105859.

[57] Y. Jin, F. Chen, F. Zhang, X. Yuan, Nonlinear dynamic performance of tilting-pad journal bearing with adjustable elastic pivot design, Tribology International 136 (2019) 533 – 547.

[58] R. G. Kirk, S. W. Reedy, Evaluation of Pivot Stiffness for Typical Tilting-Pad Journal Bearing Designs, Journal of Vibration, Acoustics, Stress, and Reliability in Design 110 (2) (1988) 165–171.

[59] S. M. Mehdi, K. E. Jang, T. H. Kim, Effects of pivot design on performance of tilting pad journal bearings, Tribology International 119 (2018) 175 – 189.

[60] I. Etsion, L. Burstein, A model for mechanical seals with regular microsurface structure, Tribology Transactions 39 (3) (1996) 677–683.

[61] N. Tala-Ighil, P. Maspeyrot, M. Fillon, A. Bounif, Effects of surface texture on journal-bearing characteristics under steady-state operating conditions, inproceedings of the Institution of Mechanical Engineers, Part J: Journal of Engineering Tribology 221 (6) (2007-09-20) 623–633.

[62] N. Tala-Ighil, M. Fillon, Surface texturing effect comparative analysis in the hydrodynamic journal bearings, Mechanics & Industry 16 (3) (2015) 1–12.

[63] N. Tala-Ighil, M. Fillon, P. Maspeyrot, Effect of textured area on the performances of a hydrodynamic journal bearing, Tribology International 44 (3) (2011) 211–219.

[64] V. Brizmer, Y. Kligerman, A laser surface textured journal bearing, Journal of Tribology 134 (3) (2012-07-01).

[65] S. Kango, R. Sharma, R. Pandey, Comparative analysis of textured and grooved hydrodynamic journal bearing, Proceedings of the Institution of Mechanical Engineers, Part J: Journal of Engineering Tribology 228 (1) (2013-08-02) 82–95.

[66] B. Manser, I. Belaidi, A. Hamrani, S. Khelladi, F. Bakir, Texture shape effects on hydrodynamic journal bearing performances using mass-conserving numerical approach, Tribology - Materials, Surfaces & Interfaces 14 (1) (2020-01-02) 33–50.

[67] Y. Jiang, Y. Gao, Q. An, Dynamic analysis of the rotor supported by journal bearing with micro-spherical surface texturing, inproceedings of the Institution of Mechanical Engineers, Part K: Journal of Multi-body Dynamics 228 (4) (2014-06-19) 355–365.

[68] T. S. R. Ganji, S. K. Kakoty, Effect of cylindrical texture on dynamic characteristics of journal bearing, International Journal of Recent advances in Mechanical Engineering 3 (4) (2014-11-30) 105–117.

[69] S. Matele, K. Pandey, Effect of surface texturing on the dynamic characteristics of hydrodynamic journal bearing comprising concepts of green tribology, inproceedings of the Institution of Mechanical Engineers, Part J: Journal of Engineering Tribology 232 (11) (2018-01-12) 1365–1376.

[70] S. Sharma, G. Jamwal, R. K. Awasthi, Dynamic and stability performance improvement of the hydrodynamic bearing by using triangular-shaped textures, Proceedings of the Institution of Mechanical Engineers, Part J: Journal of Engineering Tribology 234 (9) (2020) 1436–1451.

[71] G. Jamwal, S. Sharma, R. Awasthi, The dynamic performance analysis of chevron shape textured hydrodynamic bearings, Industrial Lubrication and Tribology 72 (1) (2019-07-22) 1–8.

[72] G. H. Jang, J. W. Yoon, Stability analysis of a hydrodynamic journal bearing with rotating herringbone grooves, Journal of Tribology 125 (2) (2003-04-01) 291–300.

[73] S. Sharma, A. Sharma, G. Jamwal, R. K. Awasthi, The effect of v-shape protruded and dimple textured on the load-carrying capacity and coefficient of friction of hydrodynamic journal bearing, Proceedings of the Institution of Mechanical Engineers, Part J: Journal of Engineering Tribology (2020) 1–15.

[74] X. Lu, M. M. Khonsari, An experimental investigation of dimple effect on the stribeck curve of journal bearings, Tribology Letters 27 (2) (2007-6-25) 169–176.

[75] S.-C. Vlădescu, M. Fowell, L. Mattsson, T. Reddyhoff, The effects of laser surface texture applied to internal combustion engine journal bearing shells – an experimental study, Tribology International 134 (2019) 317–327.

[76] A. Dadouche, M. J. Conlon, W. Dmochowski, W. Koszela, L. Galda, P. Pawlus, Effect of surface texturing on the steady-state properties and dynamic coefficients of a plain journal bearing, Volume 6: Structures and Dynamics, Parts A and B (2011-06-06) 695–704.

[77] J. Zhang, G. Li, X. Wang, X. Xin, Z. Hua, Experimental study on the effect of surface texture on the dynamic performance of journal bearing, Advanced Manufacturing and Automation VII (2018) 131–142.

[78] Z. Xie, Y. Zhang, J. Zhou, W. Zhu, Theoretical and experimental research on the micro interface lubrication regime of water lubricated bearing, Mechanical Systems and Signal Processing 151 (2021) 107422.

[79] H. Yamada, H. Taura, S. Kaneko, Numerical and experimental analyses of the dynamic characteristics of journal bearings with square dimples, Journal of Tribology 140 (1) (2018-01-01).

[80] C. Chen, X. Wang, Y. Shen, Z. Li, J. Dong, Experimental investigation for vibration reduction of surface-textured journal bearings, Industrial Lubrication and Tribology 71 (2) (2019-03-11) 232–241.

[81] J. Ma, H. Zhang, S. Lou, F. Chu, Z. Shi, F. Gu, A. D. Ball, Analytical and experimental investigation of vibration characteristics induced by tribofilm-asperity interactions in hydrodynamic journal bearings, Mechanical Systems and Signal Processing 150 (2021) 107227.

[82] L. I. Ramos, D. J. Ramos, G. B. Daniel, Evaluation of textured journal bearings under dynamic operating conditions in rotating machinery, inproceedings of the Institution of Mechanical Engineers, Part J: Journal of Engineering Tribology 234 (6) (2020) 842–857.

[83] D. J. Ramos, L. I. Ramos, G. B. Daniel, Stability analysis of rotating systems supported by textured journal bearings, Journal of Tribology 142 (3) (2020-03-01).

[84] J. Zapoměl, Počítačové modelování příčného kmitání rotorů uložených v hydrodynamických ložiskách a squeeze filmových tlumičích, Vysoká škola báňská - Technická univerzita Ostrava, Ostrava, 2007.

[85] J. S. Rao, Instability of Rotors in Fluid Film Bearings, Journal of Vibration, Acoustics, Stress, and Reliability in Design 105 (3) (1983) 274–279.

[86] J. E. Hensley, D. Childs, Measurements versus predictions for rotordynamic characteristics of a flexure pivot-pad tilting pad bearing in an lbp condition at higher unit loads, in: inproceedings of the ASME Turbo Expo 2008: Power for Land, Sea, and Air. Volume 5: Structures and Dynamics, Parts A and B, 2008, pp. 873–881.

[87] K. Thomsen, P. Klit, A. Vølund, Discontinuity effects in dynamically loaded tilting pad journal bearings, inproceedings of the Institution of Mechanical Engineers, Part J: Journal of Engineering Tribology 225 (7) (2011) 663–669.

[88] J. F. Booker, A Table of the Journal-Bearing Integral, Journal of Basic Engineering 87 (2) (1965) 533–535.

[89] P. Přikryl, Numerické metody matematické analýzy, SNTL – Nakladatelsví technické literatury, Praha, 1988.

[90] K. Rektorys, Přehled užité matematiky II, Prometheus, Praha, 1995.

[91] Y. Altman, Accelerating MATLAB Performance – 1001 tips to speed up MATLAB programs, Taylor & Francis, Boca Raton, 2015.

[92] L. Smolík, R. Pašek, J. Rendl, autofft - time-frequency analysis in matlab, Tech. rep. (11 2021).

[93] P. E. Allaire, D. F. Li, K. C. Choy, Transient unbalance response of four multilobe journal bearings, Journal of Lubrication Technology 102 (3) (1980) 300–306.

[94] Chien-Hsin Chen, Cha'O-Kuang Chen, The influence of fluid inertia on the operating characteristics of finite journal bearings, Wear 131 (2) (1989) 229–240.

[95] S. Pagano, E. Rocca, M. Russo, R. Russo, Instability threshold of a rigid rotor-tilting pad journal bearings system, International Journal of Rotating Machinery 3 (3) (1997) 199–213.

[96] A. Wolf, J. B. Swift, H. L. Swinney, J. A. Vastano, Determining lyapunov exponents from a time series, Physica D: Nonlinear Phenomena 16 (3) (1985) 285–317.

[97] D. Gropper, L. Wang, T. J. Harvey, Hydrodynamic lubrication of textured surfaces, Tribology International 94 (2016) 509–529.

[98] H. G. Elrod, A Cavitation Algorithm, Journal of Lubrication Technology 103 (3) (1981) 350–354.

[99] A. Almqvist, J. Fabricius, R. Larsson, P. Wall, A new approach for studying cavitation in lubrication, Journal of Tribology 136 (1) (2013) 011706.

[100] J. Tůma, M. Kozubková, M. Pawlenka, M. Mahdal, J. Šimek, Theoretical and experimental analysis of the bearing journal motion due to fluid force caused by the oil film, MM Science Journal 2018 (2018) 2466 – 2472.

[101] J. K. Wang, M. M. Khonsari, Influence of inlet oil temperature on the instability threshold of rotor-bearing systems, Journal of Tribology 128 (2) (2006-04-01) 319–326.

[102] H. Taura, Effect of texture region on the static and dynamic characteristic of partially textured journal bearings, in: inproceedings of the 10th International Conference on Rotor Dynamics – IFToMM, Springer International Publishing, Cham, 2019, pp. 422–436.

[103] A. EL-Said, B. EL-Souhily, W. Crosby, H. EL-Gamal, The performance and stability of three-lobe journal bearing textured with micro protrusions, Alexandria Engineering Journal 56 (4) (2017) 423–432.

Author's publications cited in the thesis

[A1] J. Rendl, Numerické řešení Reynoldsovy rovnice pro kluzná ložiska, Bachelor's thesis, Západočeská univerzita v Plzni, Plzeň (2015).

[A2] Š. Dyk, J. Rendl, L. Smolík, M. Byrtus, Dynamic coefficients and stability analysis of finite-length journal bearings considering approximate analytical solutions of the Reynolds equation, Tribology International 130 (3) (2019) 229–244.

[A3] J. Rendl, Výpočtové modelování kluzných ložisek pro úlohy dynamiky rotorů, Master's thesis, Západočeská univerzita v Plzni, Plzeň (2017).

[A4] L. Smolík, J. Rendl, M. Hartl, P. Polach, Limitations of finite difference methods in the computation of coupling forces prescribed by the Reynolds equation, The 5th Joint International Conference on Multibody System Dynamics, 2018.

[A5] Š. Dyk, L. Smolík, J. Rendl, Predictive capability of various linearization approaches for floating-ring bearings in nonlinear dynamics of turbochargers, Mechanism and Machine Theory 149 (2020) 103843.

[A6] L. Smolík, J. Rendl, J. Stifter, M. Omasta, Sub-synchronous shaft oscillations due to oil supply, in: Proceedings of the ASME Design Engineering Technical Conference, 2018.

[A7] J. Rendl, Š. Dyk, L. Smolík, Nonlinear dynamic analysis of a tilting pad journal bearing subjected to pad fluttering, Nonlinear Dynamics 105 (08 2021).

[A8] L. Smolík, J. Rendl, Š. Dyk, P. Polach, M. Hajžman, Threshold stability curves for a nonlinear rotor-bearing system, Journal of Sound and Vibration 442 (3) (2019) 698–713.

[A9] J. Rendl, L. Smolík, Š. Dyk, M. Hajžman, Impact dynamics in four-segment tilting pad journal bearings subjected to pad fluttering, in: Proceedings of the ASME Design Engineering Technical Conference, 2021.

Author's publications related to the topic

[B1] J. Rendl, M. Hajžman, L. Smolík, Numerical solver for journal bearing dynamics, in: Applied Mechanics 2016 : Book of Abstracts, Bratislava: Slovenská technická univerzita, 2016, pp. 49–50.

[B2] L. Smolík, J. Rendl, Numerical investigation of dynamics of rotor with fluid-induced instability, in: Applied Mechanics 2017 Conference inproceedings, Brno, Czech Republic: Ústav fyziky materiálů AV ČR, v.v.i., 2017, pp. 109–112.

[B3] P. Polach, L. Smolík, J. Rendl, M. Hartl, M. Omasta, Š. Dyk, Investigation of rotor dynamics with fluid film instabilities II, in: Engineering Mechanics 2018, 2018, pp. 689–692.

[B4] P. Polach, L. Smolík, J. Rendl, M. Hajžman, Influence of plain journal bearing parameters on the rotor nonlinear behaviour, in: Awrejcewicz, J. Engineering Dynamics and Life Sciences, Lodź: Department of Automation, Biomechanics and Mechatronics, 2017, pp. 441–451.

[B5] L. Smolík, J. Rendl, Analýza stability testovacího zařízení. část II: Zařízení pro výzkum víření oleje, Tech. rep., Grantová Agentura České republiky (2018).

[B6] J. Rendl, L. Smolík, Numerical and Experimental Investigation of the Hysteresis Phenomenon Associated with Instability of Rotor-Bearing Systems, in: Proceedings DYMAMESI 2019, Praha: Ústav termomechaniky AV ČR, v. v. i., 2019.

[B7] J. Rendl, Software for Investigation of Dynamic Behaviour of Rotating Systems Supported on Journal Bearings, in: Applied Mechanics 2019 – Conference inproceedings, Ostrava: Vysoká škola báňská – Technická univerzita Ostrava, 2019, pp. 184–188.

[B8] L. Smolík, P. Polach, J. Rendl, Sub-Synchronous Vibrations of a Rotor Supported on Poorly Lubricated Journal Bearings, in: Engineering Mechanics 2019, Praha: Ústav termomechaniky AV ČR, v. v. i., 2019, pp. 339–342.

[B9] J. Rendl, L. Smolík, M. Byrtus, Fluid-induced instability of rotor systems with journal bearings and investigation of different behaviour during the run-up and run-down process, 14th International Conference on Vibration Problems, Hersonissos, 2019.

[B10] J. Rendl, Galerkin method for approximate modelling of finite-length journal bearings, in: Proceedings of Computational Mechanics 2019, Plzeň: University of West Bohemia, 2019, pp. 164–165.

[B11] Š. Dyk, J. Rendl, L. Smolík, Methods for linearized analysis of floating ring bearings, in: Proceedings of Computational Mechanics 2019, Plzeň: University of West Bohemia, 2019, pp. 50–51.

[B12] P. Polach, L. Smolík, J. Rendl, M. Hajžman, Self-excited and flow-induced vibrations of a rotor supported on journal bearings, in: Proceedings of Computational Mechanics 2019, Plzeň: University of West Bohemia, 2019, pp. 156–159.

[B13] J. Rendl, Výpočtové metody používané pro analýzu rotorových systémů s kluznými ložisky, in: Výpočty konstrukcí metodou konečných prvků 2019, Liberec, 2019.

[B14] J. Rendl, Š. Dyk, Dynamics of Jeffcott rotor supported by tilting-pad journal bearings, in: Proceedings DYMAMESI 2020, Praha: Ústav termomechaniky AV ČR, v. v. i., 2019.

[B15] J. Rendl, Š. Dyk, L. Smolík, M. Hajžman, Numerical investigation of dynamic behaviour of jeffcott rotor supported by tilting-pad journal bearings, International Conference on Engineering Vibration 2020, Aberdeen, 2020.

[B16] L. Smolík, J. Rendl, R. Bulín, Application of feedforward networks to evalute joint forces in multibody systems, in: International Conference on Engineering Vibration 2020, Aberdeen, 2020.

[B17] M. Hajžman, L. Smolík, J. Rendl, Ověření a zpřesnění výsledků hydrodynamických výpočtů softwarem COMBROS A, Tech. rep., GTW BEARINGS s.r.o. (2020).

[B18] J. Rendl, On the development of the software for tilting pad journal bearing dynamics, in: Applied Mechanics 2021 : 22nd International Science Conference for Young Researchers, Book of Full Texts, Česká společnost pro mechaniku, z.s., 2021, pp. 46–49.

[B19] J. Rendl, L. Smolík, Influence of mesh density on the analysis of textured journal bearings, in: Proceedings of Computational Mechanics 2021, Plzeň: University of West Bohemia, 2021, pp. 204–206.

A Appendix – analytical methods

Polynomial functions in (4.7) – (4.10) were derived [28] for both limited cases of journal bearings as follows

$$f_1^{IS}(\lambda) = 0.5298\,\lambda^3 - 2.983\,\lambda^2 + 6.084\,\lambda - 5.046, \tag{A.1a}$$
$$f_2^{IS}(\lambda) = 0.2610\,\lambda^4 - 2.122\,\lambda^3 + 6.673\,\lambda^2 - 10.13\,\lambda + 7.252, \tag{A.1b}$$
$$f_3^{IS}(\lambda) = 0.1934\,\lambda^3 - 1.135\,\lambda^2 + 2.633\,\lambda - 2.933, \tag{A.1c}$$
$$f_4^{IS}(\lambda) = -0.0261\,\lambda^3 + 0.2953\,\lambda^2 - 1.070\,\lambda + 1.517, \tag{A.1d}$$
$$g_1^{IS}(\lambda) = 0.3479\,\lambda^4 - 1.983\,\lambda^3 + 3.913\,\lambda^2 - 2.595\,\lambda - 0.5057, \tag{A.1e}$$
$$g_2^{IS}(\lambda) = -0.1890\,\lambda^4 + 0.9467\,\lambda^3 - 1.417\,\lambda^2 + 0.2101\,\lambda + 0.6514, \tag{A.1f}$$
$$g_3^{IS}(\lambda) = 0.0592\,\lambda^3 - 0,2005\,\lambda^2 - 0.1118\,\lambda + 0.9485, \tag{A.1g}$$

$$f_1^{IL}(\lambda) = 0.4818\,\lambda^5 - 3.361\,\lambda^4 + 9.014\,\lambda^3 - 11.07\,\lambda^2 + 4.365\,\lambda + 0.8131, \tag{A.2a}$$
$$f_2^{IL}(\lambda) = -0.512\,\lambda^5 + 3.501\,\lambda^4 - 9.102\,\lambda^3 + 10.48\,\lambda^2 - 2.509\,\lambda - 1.38, \tag{A.2b}$$
$$f_3^{IL}(\lambda) = 0.0518\,\lambda^3 - 0.0079\,\lambda^2 - 1.3\,\lambda + 0.8953, \tag{A.2c}$$
$$f_4^{IL}(\lambda) = -0.1161\,\lambda^2 + 0.7893\,\lambda - 0.2410, \tag{A.2d}$$
$$g_1^{IL}(\lambda) = -0.2022\,\lambda^4 + 1.241\,\lambda^3 - 2.757\,\lambda^2 + 2.38\,\lambda - 0.0929, \tag{A.2e}$$
$$g_2^{IL}(\lambda) = 0.1420\,\lambda^4 - 0.8147\,\lambda^3 + 1.622\,\lambda^2 - 1.141\,\lambda - 0.0513, \tag{A.2f}$$
$$g_3^{IL}(\lambda) = -0.0336\,\lambda^3 + 0.0855\,\lambda^2 + 0.2418\,\lambda - 0.0267, \tag{A.2g}$$

where $\lambda = L/(2R)$. Stiffness and damping coefficients determined by linearisation process are written in the closed form for all analytical computational models, i.e. infinitely short (IS – formulae (A.3)), infinitely long (IL – formulae (A.4)) and their corrected models (IScor – formulae (A.5), ILcor – formulae (A.6)).

$$k_{yy}^{IS} = -\frac{L^3 R\,\mu}{c^3}\left\{\frac{\varepsilon|\omega|\left[\,1-\varepsilon^2+(3\,\varepsilon^2+1)\sin^2\gamma\,\right]}{(\varepsilon^2-1)^3}+\frac{3\,\varepsilon^2\,\omega\,\pi\sin(2\,\gamma)}{8\,(1-\varepsilon^2)^{\frac{5}{2}}}\right\}, \tag{A.3a}$$

$$k_{yz}^{IS} = -\frac{L^3 R\,\mu}{2\,c^3}\left\{\frac{\omega\,\pi\left[\,\varepsilon^2\left(2-3\,\sin^2\gamma\right)+1\,\right]}{2\,(1-\varepsilon^2)^{\frac{5}{2}}}+\frac{\varepsilon|\omega|\,(3\,\varepsilon^2+1)\sin(2\,\gamma)}{(\varepsilon^2-1)^3}\right\}, \tag{A.3b}$$

$$k_{zy}^{IS} = \frac{L^3 R\,\mu}{2\,c^3}\left\{\frac{\omega\,\pi\left[\,1-\varepsilon^2\left(1-3\sin^2\gamma\right)\,\right]}{2\,(1-\varepsilon^2)^{\frac{5}{2}}}-\frac{\varepsilon|\omega|\,(3\,\varepsilon^2+1)\sin(2\,\gamma)}{(\varepsilon^2-1)^3}\right\}, \tag{A.3c}$$

$$k_{zz}^{IS} = -\frac{L^3 R\,\mu}{c^3}\left\{\frac{\varepsilon|\omega|\left[\,2\,\varepsilon^2+2-(3\,\varepsilon^2+1)\sin^2\gamma\,\right]}{(\varepsilon^2-1)^3}-\frac{3\,\varepsilon^2\,\omega\,\pi\sin(2\,\gamma)}{8\,(1-\varepsilon^2)^{\frac{5}{2}}}\right\}, \tag{A.3d}$$

$$b_{yy}^{IS} = \frac{L^3 R\,\mu}{c^3}\left[\frac{\pi\cos^2\gamma}{2\,(1-\varepsilon^2)^{\frac{3}{2}}}+\frac{\pi\,(2\,\varepsilon^2+1)\sin^2\gamma}{2\,(1-\varepsilon^2)^{\frac{5}{2}}}-\frac{\varepsilon\,(1+\mathrm{sign}\,(\omega))\sin(2\,\gamma)}{(\varepsilon^2-1)^2}\right], \tag{A.3e}$$

$$\begin{aligned} b_{yz}^{IS} = {} & \frac{L^3 R\,\mu\,\varepsilon}{4\,c^3\,(1-\varepsilon^2)^{\frac{9}{2}}}\left[8\left(1-\varepsilon^2\right)^{\frac{5}{2}}\left(\mathrm{sign}\,(\omega)\,\sin^2\gamma-\cos^2\gamma\right)+\right. \\ & \left.+\,3\,\varepsilon\,\pi\left(\varepsilon^4-2\,\varepsilon^2+1\right)\sin(2\,\gamma)\right], \end{aligned} \tag{A.3f}$$

$$\begin{aligned} b_{zy}^{IS} = {} & \frac{L^3 R\,\mu\,\varepsilon}{4\,c^3\,(1-\varepsilon^2)^{\frac{9}{2}}}\left[8\left(1-\varepsilon^2\right)^{\frac{5}{2}}\left(\sin^2\gamma-\mathrm{sign}\,(\omega)\,\cos^2\gamma\right)+\right. \\ & \left.+\,3\,\varepsilon\,\pi\left(\varepsilon^4-2\,\varepsilon^2+1\right)\sin(2\,\gamma)\right], \end{aligned} \tag{A.3g}$$

$$b_{zz}^{IS} = \frac{L^3 R\,\mu}{c^3}\left[\frac{\pi\sin^2\gamma}{2\,(1-\varepsilon^2)^{\frac{3}{2}}}+\frac{\pi\,(2\,\varepsilon^2+1)\cos^2\gamma}{2\,(1-\varepsilon^2)^{\frac{5}{2}}}+\frac{\varepsilon\,(1+\mathrm{sign}\,(\omega))\sin(2\,\gamma)}{(\varepsilon^2-1)^2}\right], \tag{A.3h}$$

$$k_{yy}^{IL} = -\frac{3LR^3\mu\,\varepsilon}{c^3\left(\varepsilon^4+\varepsilon^2-2\right)^2}\left\{\frac{3\,\omega\,\pi\,\varepsilon^3\left(\varepsilon^4-2\,\varepsilon^2+1\right)\sin\left(2\,\gamma\right)}{\left(1-\varepsilon^2\right)^{\frac{3}{2}}} - \right. \tag{A.4a}$$
$$\left. - 4|\omega|\left[4+2\,\varepsilon^4-\left(3\,\varepsilon^4+\varepsilon^2+2\right)\cos^2\gamma\right]\right\},$$

$$k_{yz}^{IL} = \frac{6LR^3\mu}{c^3}\left[\frac{\varepsilon\,|\omega|\left(3\,\varepsilon^4+\varepsilon^2+2\right)\sin\left(2\,\gamma\right)}{\left(\varepsilon^4+\varepsilon^2-2\right)^2}+\frac{\omega\,\pi\left(\varepsilon^2-2-2\,\varepsilon^4+3\,\varepsilon^4\sin^2\gamma\right)}{\left(1-\varepsilon^2\right)^{\frac{3}{2}}\left(\varepsilon^2+2\right)^2}\right], \tag{A.4b}$$

$$k_{zy}^{IL} = \frac{6LR^3\mu}{c^3}\left[\frac{\varepsilon\,|\omega|\left(3\,\varepsilon^4+\varepsilon^2+2\right)\sin\left(2\,\gamma\right)}{\left(\varepsilon^4+\varepsilon^2-2\right)^2}+\frac{\omega\,\pi\left(2-\varepsilon^2-\varepsilon^4+3\,\varepsilon^4\sin^2\gamma\right)}{\left(1-\varepsilon^2\right)^{\frac{3}{2}}\left(\varepsilon^2+2\right)^2}\right], \tag{A.4c}$$

$$k_{zz}^{IL} = \frac{3LR^3\mu\,\varepsilon}{c^3\left(1-\varepsilon^2\right)^{\frac{7}{2}}\left(\varepsilon^2+2\right)^2}\left\{3\,\omega\,\pi\,\varepsilon^3\left(\varepsilon^4-2\,\varepsilon^2+1\right)\sin\left(2\,\gamma\right)+\right. \tag{A.4d}$$
$$\left. + 4|\omega|\left(1-\varepsilon^2\right)^{\frac{3}{2}}\left[2\,\varepsilon^4+4-\left(3\,\varepsilon^4+\varepsilon^2+2\right)\sin^2\gamma\right]\right\},$$

$$b_{yy}^{IL} = \frac{6LR^3\mu}{c^3}\left[\frac{\pi\sin^2\gamma}{\left(1-\varepsilon^2\right)^{\frac{3}{2}}}+\frac{2\,\pi\cos^2\gamma}{\sqrt{1-\varepsilon^2}\left(\varepsilon^2+2\right)}+\frac{2\sin\left(2\,\gamma\right)}{\varepsilon^2-1}\left(\frac{1}{\varepsilon+1}+\frac{\varepsilon\,\mathrm{sign}\left(\omega\right)}{\varepsilon^2+2}\right)\right], \tag{A.4e}$$

$$b_{yz}^{IL} = \frac{3LR^3\mu}{c^3}\left[\frac{\pi\sin\left(2\,\gamma\right)}{\left(1-\varepsilon^2\right)^{\frac{3}{2}}}-\frac{2\,\pi\sin\left(2\,\gamma\right)}{\sqrt{1-\varepsilon^2}\left(\varepsilon^2+2\right)}-\frac{8\,\varepsilon\,\mathrm{sign}\left(\omega\right)\,\sin^2\gamma}{\left(\varepsilon^2-1\right)\left(\varepsilon^2+2\right)}+\frac{8\cos^2\gamma}{\left(\varepsilon^2-1\right)\left(\varepsilon+1\right)}\right], \tag{A.4f}$$

$$b_{zy}^{IL} = \frac{3LR^3\mu}{c^3}\left[\frac{\pi\sin\left(2\,\gamma\right)}{\left(1-\varepsilon^2\right)^{\frac{3}{2}}}-\frac{2\,\pi\sin\left(2\,\gamma\right)}{\sqrt{1-\varepsilon^2}\left(\varepsilon^2+2\right)}+\frac{8\,\varepsilon\,\mathrm{sign}\left(\omega\right)\,\cos^2\gamma}{\left(\varepsilon^2-1\right)\left(\varepsilon^2+2\right)}-\frac{8\sin^2\gamma}{\left(\varepsilon^2-1\right)\left(\varepsilon+1\right)}\right], \tag{A.4g}$$

$$b_{zz}^{IL} = \frac{6LR^3\mu}{c^3}\left[\frac{\pi\cos^2\gamma}{\left(1-\varepsilon^2\right)^{\frac{3}{2}}}+\frac{2\,\pi\sin^2\gamma}{\sqrt{1-\varepsilon^2}\left(\varepsilon^2+2\right)}-\frac{2\sin\left(2\,\gamma\right)}{\varepsilon^2-1}\left(\frac{1}{\varepsilon+1}+\frac{\varepsilon\,\mathrm{sign}\left(\omega\right)}{\varepsilon^2+2}\right)\right], \tag{A.4h}$$

$$k_{yy}^{IScor} = -\frac{L^3 R\,\mu\,\varepsilon}{c^3}\left\{\frac{\omega\,\pi\,(dY_2 + 3\,\varepsilon\,Y_2 - \varepsilon^2\,dY_2)\sin(2\gamma)}{8\,(1-\varepsilon^2)^{\frac{5}{2}}} + \right. \tag{A.5a}$$
$$\left. + \frac{|\omega|\left[\,Y_1\,(1-\varepsilon^2) - (\varepsilon^3\,dY_1 - 3\,\varepsilon^2\,Y_1 - \varepsilon\,dY_1 - Y_1)\sin^2\gamma\,\right]}{(\varepsilon^2-1)^3}\right\},$$

$$k_{yz}^{IScor} = -\frac{L^3 R\,\mu}{2\,c^3}\left\{\frac{\varepsilon|\omega|\,(Y_1 + \varepsilon\,dY_1 + 3\,\varepsilon^2\,Y_1 - \varepsilon^3\,dY_1)\sin(2\gamma)}{(\varepsilon^2-1)^3} + \right. \tag{A.5b}$$
$$\left. + \frac{\omega\,\pi\left[\,\varepsilon\,(\varepsilon^2\,dY_2 - 3\,\varepsilon\,Y_2 - dY_2)\sin^2\gamma + Y_2\,(1+2\,\varepsilon^2) + \varepsilon\,dY_2\,(1-\varepsilon^2)\,\right]}{2\,(1-\varepsilon^2)^{\frac{5}{2}}}\right\},$$

$$k_{zy}^{IScor} = \frac{L^3 R\,\mu}{2\,c^3}\left\{\frac{\omega\,\pi\left[\,\varepsilon\,(dY_2 + 3\,\varepsilon\,Y_2 - \varepsilon^2\,dY_2)\sin^2\gamma + Y_2\,(1-\varepsilon^2)\,\right]}{2\,(1-\varepsilon^2)^{\frac{5}{2}}} - \right. \tag{A.5c}$$
$$\left. - \frac{\varepsilon|\omega|\,(Y_1 + \varepsilon\,dY_1 + 3\,\varepsilon^2\,Y_1 - \varepsilon^3\,dY_1)\sin(2\gamma)}{(\varepsilon^2-1)^3}\right\},$$

$$k_{zz}^{IScor} = \frac{L^3 R\,\mu\,\varepsilon}{c^3}\left\{\frac{\omega\,\pi\,(dY_2 + 3\,\varepsilon\,Y_2 - \varepsilon^2\,dY_2)\sin(2\gamma)}{8\,(1-\varepsilon^2)^{\frac{5}{2}}} - \right. \tag{A.5d}$$
$$\left. - \frac{|\omega|\left[\,(\varepsilon^3\,dY_1 - 3\,\varepsilon^2\,Y_1 - \varepsilon\,dY_1 - Y_1)\sin^2\gamma + 2\,Y_1\,(1+\varepsilon^2) + \varepsilon\,dY_1\,(1-\varepsilon^2)\,\right]}{(\varepsilon^2-1)^3}\right\},$$

$$b_{yy}^{IScor} = \frac{L^3 R\,\mu}{c^3}\left[\frac{\pi\,Y_2\cos^2\gamma}{2\,(1-\varepsilon^2)^{\frac{3}{2}}} + \frac{\pi\,Y_1\,(2\,\varepsilon^2+1)\sin^2\gamma}{2\,(1-\varepsilon^2)^{\frac{5}{2}}} - \frac{\varepsilon\,(Y_2 + Y_1\,\mathrm{sign}\,(\omega))\sin(2\,\gamma)}{(\varepsilon^2-1)^2}\right], \tag{A.5e}$$

$$b_{yz}^{IScor} = \frac{L^3 R\,\mu}{c^3}\left[\frac{\pi\,Y_1\,(2\,\varepsilon^2+1)\sin(2\,\gamma)}{4\,(1-\varepsilon^2)^{\frac{5}{2}}} - \frac{\pi\,Y_2\sin(2\,\gamma)}{4\,(1-\varepsilon^2)^{\frac{3}{2}}} + \right. \tag{A.5f}$$
$$\left. + \frac{2\,\varepsilon\left(Y_1\,\mathrm{sign}\,(\omega)\,\sin^2\gamma - Y_2\cos^2\gamma\right)}{(\varepsilon^2-1)^2}\right],$$

$$b_{zy}^{IScor} = \frac{L^3 R\,\mu}{c^3}\left[\frac{\pi\,Y_1\,(2\,\varepsilon^2+1)\sin(2\,\gamma)}{4\,(1-\varepsilon^2)^{\frac{5}{2}}} - \frac{\pi\,Y_2\sin(2\,\gamma)}{4\,(1-\varepsilon^2)^{\frac{3}{2}}} + \right. \tag{A.5g}$$
$$\left. + \frac{2\,\varepsilon\left(Y_2\sin^2\gamma - Y_1\,\mathrm{sign}\,(\omega)\cos^2\gamma\right)}{(\varepsilon^2-1)^2}\right],$$

$$b_{zz}^{IScor} = \frac{L^3 R\,\mu}{c^3}\left[\frac{\pi\,Y_2\sin^2\gamma}{2\,(1-\varepsilon^2)^{\frac{3}{2}}} + \frac{\pi\,Y_1\,(2\,\varepsilon^2+1)\cos^2\gamma}{2\,(1-\varepsilon^2)^{\frac{5}{2}}} + \frac{\varepsilon\,(Y_2 + Y_1\,\mathrm{sign}\,(\omega))\sin(2\,\gamma)}{(\varepsilon^2-1)^2}\right], \tag{A.5h}$$

$$Y_1(\lambda,\varepsilon) = f_1^{IS}\varepsilon^3 + f_2^{IS}\varepsilon^2 + f_3^{IS}\varepsilon + f_4^{IS}, \qquad dY_1(\lambda,\varepsilon) = \frac{\partial Y_1(\lambda,\varepsilon)}{\partial\varepsilon}, \tag{A.5i}$$

$$Y_2(\lambda,\varepsilon) = g_1^{IS}\varepsilon^2 + g_2^{IS}\varepsilon + g_3^{IS}, \qquad dY_2(\lambda,\varepsilon) = \frac{\partial Y_2(\lambda,\varepsilon)}{\partial\varepsilon}, \tag{A.5j}$$

$$k_{yy}^{ILcor} = \frac{3LR^3\mu\,\varepsilon}{c^3}\left\{\frac{8\,Z_1|\omega|\,(\varepsilon^4+2)\sin^2\gamma}{\left(\varepsilon^4+\varepsilon^2-2\right)^2} - \right. \tag{A.6a}$$
$$\left. - \frac{\omega\,\pi\,[\;dZ_2\,(2-\varepsilon^2-\varepsilon^4)+3\,Z_2\,\varepsilon^3\;]\sin(2\gamma)}{(1-\varepsilon^2)^{\frac{3}{2}}\,(\varepsilon^2+2)^2} - \frac{4|\omega|\left(Z_1\cos^2\gamma+\varepsilon\,dZ_1\sin^2\gamma\right)}{(\varepsilon^2-1)\,(\varepsilon^2+2)}\right\},$$

$$k_{yz}^{ILcor} = \frac{6LR^3\mu}{c^3}\left\{\frac{\varepsilon|\omega|\,[Z_1\,(2+\varepsilon^2+3\,\varepsilon^4)+dZ_1\,(2\,\varepsilon-\varepsilon^3-\varepsilon^5)]\sin(2\gamma)}{\left(\varepsilon^4+\varepsilon^2-2\right)^2} - \right. \tag{A.6b}$$
$$\left. - \omega\left[\frac{\varepsilon\,\pi\,dZ_2\cos^2\gamma+\pi\,Z_2\sin^2\gamma}{\sqrt{1-\varepsilon^2}\,(\varepsilon^2+2)} + \frac{\pi\,Z_2\,(2\,\varepsilon^4-\varepsilon^2+2)\cos^2\gamma}{(1-\varepsilon^2)^{\frac{3}{2}}\,(\varepsilon^2+2)^2}\right]\right\},$$

$$k_{zy}^{ILcor} = \frac{6LR^3\mu}{c^3}\left\{\frac{\varepsilon|\omega|\,[Z_1\,(2+\varepsilon^2+3\,\varepsilon^4)+dZ_1\,(2\,\varepsilon-\varepsilon^3-\varepsilon^5)\,]\sin(2\gamma)}{\left(\varepsilon^4+\varepsilon^2-2\right)^2} + \right. \tag{A.6c}$$
$$\left. + \omega\left[\frac{\varepsilon\,\pi\,dZ_2\sin^2\gamma+\pi\,Z_2\cos^2\gamma}{\sqrt{1-\varepsilon^2}\,(\varepsilon^2+2)} + \frac{\pi\,Z_2\,(2\,\varepsilon^4-\varepsilon^2+2)\sin^2\gamma}{(1-\varepsilon^2)^{\frac{3}{2}}\,(\varepsilon^2+2)^2}\right]\right\},$$

$$k_{zz}^{ILcor} = \frac{3LR^3\mu\,\varepsilon}{c^3}\left\{\frac{8\,Z_1|\omega|\,(\varepsilon^4+2)\cos^2\gamma}{\left(\varepsilon^4+\varepsilon^2-2\right)^2} + \right. \tag{A.6d}$$
$$\left. + \frac{\omega\,\pi\,[\;dZ_2\,(2-\varepsilon^2-\varepsilon^4)+3\,Z_2\,\varepsilon^3\;]\sin(2\gamma)}{(1-\varepsilon^2)^{\frac{3}{2}}\,(\varepsilon^2+2)^2} - \frac{4|\omega|\left(Z_1\sin^2\gamma+\varepsilon\,dZ_1\cos^2\gamma\right)}{(\varepsilon^2-1)\,(\varepsilon^2+2)}\right\},$$

$$b_{yy}^{ILcor} = \frac{6LR^3\mu}{c^3}\left[\frac{\pi\,Z_1\sin^2\gamma}{(1-\varepsilon^2)^{\frac{3}{2}}} + \frac{2\,\pi\,Z_2\cos^2\gamma}{\sqrt{1-\varepsilon^2}\,(\varepsilon^2+2)} + \frac{2\sin(2\,\gamma)}{\varepsilon^2-1}\left(\frac{Z_2}{\varepsilon+1}+\frac{\varepsilon\,Z_1\,\mathrm{sign}\,(\omega)}{\varepsilon^2+2}\right)\right], \tag{A.6e}$$

$$b_{yz}^{ILcor} = \frac{3LR^3\mu}{c^3}\left[\frac{\pi\,Z_1\sin(2\,\gamma)}{(1-\varepsilon^2)^{\frac{3}{2}}} - \frac{2\,\pi\,Z_2\sin(2\,\gamma)}{\sqrt{1-\varepsilon^2}\,(\varepsilon^2+2)} - \frac{8\,\varepsilon\,Z_1\,\mathrm{sign}\,(\omega)\,\sin^2\gamma}{(\varepsilon^2-1)\,(\varepsilon^2+2)} + \right. \tag{A.6f}$$
$$\left. + \frac{8\,Z_2\cos^2\gamma}{(\varepsilon^2-1)\,(\varepsilon+1)}\right],$$

$$b_{zy}^{ILcor} = \frac{3LR^3\mu}{c^3}\left[\frac{\pi\,Z_1\sin(2\,\gamma)}{(1-\varepsilon^2)^{\frac{3}{2}}} - \frac{2\,\pi\,Z_2\sin(2\,\gamma)}{\sqrt{1-\varepsilon^2}\,(\varepsilon^2+2)} + \frac{8\,\varepsilon\,Z_1\,\mathrm{sign}\,(\omega)\,\cos^2\gamma}{(\varepsilon^2-1)\,(\varepsilon^2+2)} - \right. \tag{A.6g}$$
$$\left. - \frac{8\,Z_2\sin^2\gamma}{(\varepsilon^2-1)\,(\varepsilon+1)}\right],$$

$$b_{zz}^{ILcor} = \frac{6LR^3\mu}{c^3}\left[\frac{\pi\,Z_1\cos^2\gamma}{(1-\varepsilon^2)^{\frac{3}{2}}} + \frac{2\,\pi\,Z_2\sin^2\gamma}{\sqrt{1-\varepsilon^2}\,(\varepsilon^2+2)} - \frac{2\sin(2\,\gamma)}{\varepsilon^2-1}\left(\frac{Z_2}{\varepsilon+1}+\frac{\varepsilon\,Z_1\,\mathrm{sign}\,(\omega)}{\varepsilon^2+2}\right)\right], \tag{A.6h}$$

$$Z_1(\lambda,\varepsilon) = f_1^{IL}\varepsilon^3 + f_2^{IL}\varepsilon^2 + f_3^{IL}\varepsilon + f_4^{IL}, \qquad dZ_1(\lambda,\varepsilon) = \frac{\partial Z_1(\lambda,\varepsilon)}{\partial\varepsilon}, \tag{A.6i}$$

$$Z_2(\lambda,\varepsilon) = g_1^{IL}\varepsilon^2 + g_2^{IL}\varepsilon + g_3^{IL}, \qquad dZ_2(\lambda,\varepsilon) = \frac{\partial Z_2(\lambda,\varepsilon)}{\partial\varepsilon}. \tag{A.6j}$$

B Appendix – solution strategy

A flowchart describing the solution strategy and the order of calculation steps inside the used solver is depicted in Fig. B.1. The depicted flowchart shows only the inner part of the loop in the k-th iteration step. An output function is different for each type of each analysis and has the following form with respect to the notation used in (3.1):

1. Static analysis – Static equilibrium points $\mathbf{q} = [\mathbf{q}_r, \mathbf{q}_p]^T$ are determined if $\mathbf{f}(\mathbf{q}) = \mathbf{0}$. The residuum function is defined as follows

$$\mathbf{f}(\mathbf{q}) = \begin{bmatrix} \mathbf{f}_{g,r} + \mathbf{f}_{c,r} \\ \mathbf{f}_{g,r} + \mathbf{f}_{c,p} \end{bmatrix}. \tag{B.1}$$

2. Analysis of dynamics – The system of the second order differential equations (3.1) is transformed to the system of the first order differential equations using the mass identity

$$\begin{bmatrix} \mathbf{M}_r & \mathbf{0} \\ \mathbf{0} & \mathbf{M}_p \end{bmatrix} \begin{bmatrix} \dot{\mathbf{q}}_r \\ \dot{\mathbf{q}}_p \end{bmatrix} - \begin{bmatrix} \mathbf{M}_r & \mathbf{0} \\ \mathbf{0} & \mathbf{M}_p \end{bmatrix} \begin{bmatrix} \dot{\mathbf{q}}_r \\ \dot{\mathbf{q}}_p \end{bmatrix} = \begin{bmatrix} \mathbf{0} \\ \mathbf{0} \end{bmatrix}. \tag{B.2}$$

   The resulting system is solved for state-space vector $\mathbf{x}(t) = [\dot{\mathbf{q}}_r(t), \dot{\mathbf{q}}_p(t), \mathbf{q}_r(t), \mathbf{q}_p(t)]^T$. The derivative of the state-space vector, which is evaluated in each iteration step of solver `ode15s`, can be written in the matrix form

$$\dot{\mathbf{x}}(t) = \begin{bmatrix} \begin{bmatrix} \mathbf{M}_r & \mathbf{0} \\ \mathbf{0} & \mathbf{M}_p \end{bmatrix}^{-1} \left(\begin{bmatrix} \mathbf{f}_{g,r} \\ \mathbf{f}_{g,p} \end{bmatrix} + \begin{bmatrix} \mathbf{f}_{un} \\ \mathbf{0} \end{bmatrix} + \begin{bmatrix} \mathbf{f}_{c,r} \\ \mathbf{f}_{c,p} \end{bmatrix} \right) \\ \dot{\mathbf{q}}_r \\ \dot{\mathbf{q}}_p \end{bmatrix}. \tag{B.3}$$

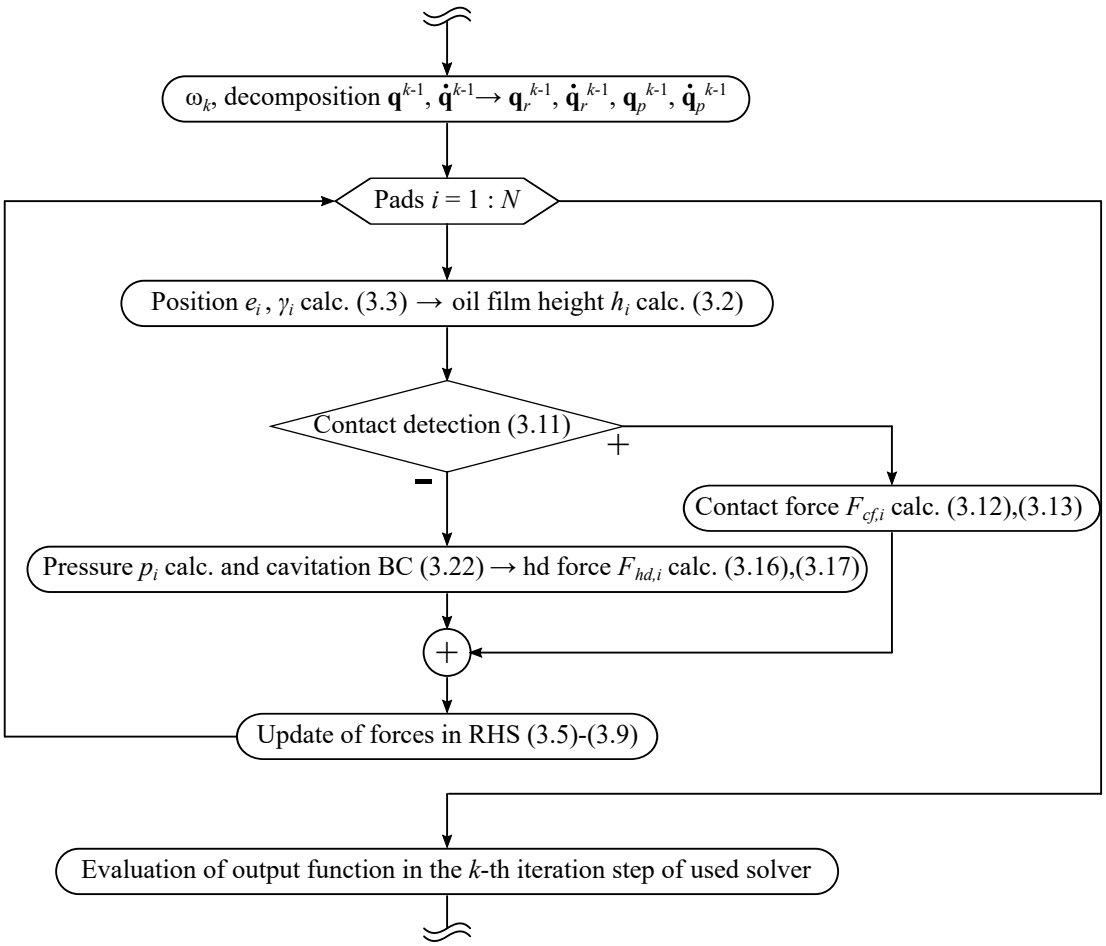

Fig. B.1: Flowchart of solution strategy inside of used numerical solver

Shrnutí

Disertační práce je zaměřena na matematické modelování rotorových systému s kluznými ložisky a detailní vyšetřování vlivu jednotlivých typů ložisek a jejich vlastností na výsledné chování rotorového systému. V práci je představen komplexní model radiálního kluzného ložiska, jehož vhodnou modifikací lze modelovat všechny běžně používané typy ložisek. Současně je formulována metodika modelování interakce mezi rotorem a částmi ložiska a metodika vyšetřování stability systému.

V úvodní části práce je postupně odvozen komplexní model radiálního kluzného ložiska. V případě ložiska s naklápěcími segmenty je pohyb dokonale tuhých segmentů uložených viskoelastickou vazbou k rámu předpokládán jako rovinný. Proudění maziva v ložiskové mezeře je popsáno Reynoldsovou rovnicí, jejímž řešením je neznámé tlakové pole. Tlakové pole je pro každý segment nebo dílčí pánev pevného ložiska řešeno zvlášť. Díky vhodně zavedeným souřadnicovým systémům pevně spojených se segmenty a transformací polohy rotoru je ložisková mezera aproximována předpisem pro mezeru válcového ložiska. Pokud není mezi rotorem a segmentem vytvořen nosný olejový film, tak jsou hydrodynamické síly od tlakového pole nahrazeny elastickými silami, které vzniknou v důsledku vzájemného kontaktu pevných částí systému. Posuzování stability systému je realizováno s využitím koeficientů tuhosti a tlumení plynoucích z linearizace hydrodynamické síly.

Hlavní metodou pro řešení Reynoldsovy rovnice v této práci je metoda konečných diferencí, kterou je možné aplikovat na všechny typy ložisek, tj. válcová, eliptická, přesazená a ložiska s naklápěcími segmenty. Vlastnosti této metody jsou vyšetřovány pro válcové ložisko. Metoda konečných diferencí umožňuje zahrnout do výpočtového modelu přívodní drážky a otvory včetně změny profilu pánve získané například texturováním. Pro limitní případy Reynoldsovy rovnice, tj. aproximace nekonečně krátkým a dlouhým válcovým ložiskem, existuje řešení v uzavřeném tvaru. K výpočtu hydrodynamických sil pro ložisko konečné délky jsou využity korekční polynomy. Z korigovaných hydrodynamických sil jsou pak nově odvozeny koeficienty tuhosti a tlumení pro ložisko konečné délky.

Modely válcového ložiska, texturovaného válcového ložiska, ložiska s pevným profilem i naklápěcími segmenty byly implementovány do vlastního programového vybavení vytvořeného v systému MATLAB. Pomocí softwaru jsou prováděny statické analýzy, posuzovaní stability a simulace odezvy systému v časové oblasti na harmonické buzení od rotující nevývahy ale i přechodové simulace pro rozběh a doběh systému. Simulované odezvy jsou analyzovány pomocí nástrojů: detekce prahových rychlostí, bifurkační diagramy, rychlá Fourierova transformace, fázové portréty a Poincarého zobrazení. Výsledky z vlastního programu jsou pro ložiska s pevným profilem a naklápěcími segmenty validovány pomocí referenčních dat z odborné literatury. Model válcového ložiska a texturovaného ložiska je porovnán s experimentálním měřením na Bently Nevada RK 4 Rotor Kit, resp. na zkušebním zařízení vyrobeném v rámci projektu GA ČR.

Vytvořený model a metodika modelování různých typů ložisek je snadno rozšiřitelná a může být zpřesněna o další jevy vyskytující se při hydrodynamickém mazání.

Résumé

This thesis is focused on the mathematical modelling of rotating systems with journal bearings and detailed investigation of particular journal bearing types and their effects on rotating system's behaviour. First, a complex model of a radial journal bearing is introduced for modelling of typically used journal bearing types. Concurrently, the modelling methodology of mutual interaction between the rotor and bearing parts and methodology of system stability assessment are formulated.

The complex model of a radial journal bearing is derived step-by-step in the first part of the thesis. For the case of tilting pad journal bearings, the motion of the rigid pad supported on the visco-elastic support is supposed to be planar. The Reynolds equation governs unknown pressure field in the lubricant circulating in the bearing gap. The pressure field is calculated for each pad or particular bearing shell separately. Defined coordinate systems fixedly attached to the pads allow the description of the bearing gap by formulae for cylindrical journal bearings. If the load-carrying oil film between the rotor and the pad is missing, the hydrodynamic forces are substituted by elastic forces, which are developed due to solid contact of rigid parts of the system. System stability assessment is realised using stiffness and damping coefficients resulting from the linearisation of the hydrodynamic force.

The primary method for solving the Reynolds equation in the thesis is the finite difference method applicable for all bearing types, i.e. cylindrical, elliptical, offset halves and tilting pad journal bearings. Properties of this method are investigated for the cylindrical journal bearing. In addition, the finite difference method is suitable for computationally implementing supply bores and grooves and bearing profile changes produced by bearing shell texturing. For limit cases of the Reynolds equation, i.e. approximation by the infinitely short and long bearing, the solution in the closed-form exists. Evaluating the hydrodynamic force for the finite-length bearing is performed using the correction polynomial functions. The stiffness and damping coefficients for the finite-length bearings are derived based on the corrected hydrodynamic forces.

Computational models of cylindrical bearing, textured cylindrical bearing, bearings with fixed-profile and tilting pads were implemented into an in-house software written in MATLAB. The software can perform the static analysis, system stability assessment and simulations in the time domain of the rotor response to the harmonic excitation due to out-of-balance force and transient simulations for run-up and coast-down operations. Simulated responses are analysed using the following tools: threshold speed detection, bifurcation diagrams, fast Fourier transform, phase portraits and Poincaré maps. Results obtained from the in-house software are validated for fixed-profile journal bearings and tilting pad journal bearings with reference data in research publications. The cylindrical bearing and textured bearing models are validated with experimental measurement of the Bently Nevada RK 4 Rotor Kit and test rig built during the Czech Science Foundation project, respectively.

The presented model and modelling methodology of various bearing types is extendable and can be specified by other phenomena related to hydrodynamic lubrication.